UNIVERSITY OF
BIRMINGHAM

MULTI-LAYER PERIODIC SURFACES AND METASURFACES FOR HIGH-GAIN ANTENNAS

by

KONSTANTINOS KONSTANTINIDIS

A thesis submitted to the University of Birmingham for the degree of DOCTOR OF PHILOSOPHY

School of Electronic, Electrical and Systems Engineering

College of Engineering and Physical Sciences

University of Birmingham

May 2015

ABSTRACT

MULTI-LAYER PERIODIC SURFACES AND METASURFACES FOR HIGH-GAIN ANTENNAS

KONSTANTINOS KONSTANTINIDIS

Doctorate of Philosophy

School of Electronic, Electrical and Systems Engineering

University of Birmingham

Novel highly-directive Fabry-Perot (FP) type antennas with significantly enhanced bandwidth performance based on periodic metasurfaces are presented in this thesis. The proposed antennas are formed by multiple layers of periodic surfaces and metasurfaces placed over a ground plane and a low directivity primary source. Initially, multi-layer FP antennas of half wavelength air cavities are investigated as an effort to achieve broadband highly-directive response and generalize the concept of the directivity-bandwidth product enhancement by adding appropriately designed Partially Reflective Surface (PRS) layers in FP type antennas. Subsequently, the limitations of this technique are investigated by studying the dispersion characteristics of the modes supported in multi-layer FP Leaky-Wave Antenna (LWAs)**,** providing a full interpretation of the operation of multi-layer Fabry-Perot LWAs. Moreover, a new concept of designing sub-wavelength profile multi-layer FP antennas by replacing the conventional PRSs with optimized composite metasurfaces is proposed outperforming previous designs of the same profile. Finally, a FP antenna operating at sub-millimetre wave frequencies is designed and presented based on micromachined fully metalized SU8 at around 300GHz. An in-house fabrication process is employed for the implementation of a prototype and measurement results are also presented in this thesis. This work offers an interesting new solution for planar high-gain low cost antennas for such high frequencies.

To my family,

To Marina.

Acknowledgements

First and foremost, I would like to profoundly thank my thesis supervisor, Dr. Alexandros Feresidis, for his support and guidance throughout my PhD. His passion and encouragement during these years were very important factor for the completion of my work.

I would like to acknowledge Prof. Peter S. Hall, Dr. Peter Gardner and Prof. Mike Lancaster for their support and useful advices during my research endeavour.

I would also like to thank the technicians of the Department of Electronic, Electrical and Systems Engineering Alan Yates and Donna Johnson whose help with the fabrication of many antenna prototypes has been really valuable.

Special thanks go to the PhD and postdoctoral researchers of my group Marina Mavridou, Elena Abdo, Rashad Mahmud, Xiaobang Shang and Yingtao Tian.

Also, I would like to acknowledge the financial support from the school and from EPRSC.

List of Publications

Journal papers:

1. **K. Konstantinidis**, A. P. Feresidis, P. S. Hall, "Multi-layer Partially Reflective Surfaces for Broadband Fabry-Perot Cavity Antennas" *IEEE Trans. Antennas and Propag.,* vol.62, no.7, pp.3474-3481, July 2014.

2. **K. Konstantinidis**, A. P. Feresidis, P. S. Hall, "Dual Sub-wavelength Fabry-Perot Cavities for Broadband Highly-Directive Antennas", *IEEE Antennas and Wireless Propag. Lett.,* vol.13, no., pp.1184-1186, 2014.

3. **K. Konstantinidis**, A. P. Feresidis, P. S. Hall, "Dual-Slot Feeding Technique for Broadband Fabry-Perot Cavity Antennas", *IET Microw. Antennas and Propag.,* January 2015.

4. **K. Konstantinidis**, A. P. Feresidis, P. S. Hall, "Broadband Sub–Wavelength Profile High-Gain Antennas Based on Multi-layer Metasurfaces", *IEEE Trans. Antennas and Propag.,* January 2015.

5. **K. Konstantinidis**, A. P. Feresidis, Y. Tian, X. Shang, and M. J. Lancaster, "Micromachined Terahertz Fabry-Perot Cavity Highly Directive Antennas", *IET Microw. Antennas and Propag.,* (accepted).

6. **K. Konstantinidis**, A. P. Feresidis, "Broadband Near-Zero Index Metamaterials", *Journal of Optics* (accepted).

7. M. Mavridou, **K. Konstantinidis**, A. P. Feresidis, "Tunable milimitre-wave HIS and application for beam-scanning antenna", *IEEE Trans. Antennas and Propag.,* (awaiting).

8. **K. Konstantinidis**, A. P. Feresidis, P. S. Hall, "Dispersion Analysis of Multi-Layer Fabry-Perot Leaky-Wave Antennas", *IEEE Trans. Antennas and Propag.,* (in preparation).

International conferences:

1. **K. Konstantinidis**, A. P. Feresidis, P. S. Hall, M. J. Lancaster, "Design of Fabry-Perot cavity antenna at 94 GHz," *Antennas and Propagation Conference (LAPC)*, 2012 Loughborough, UK.

2. A. P. Feresidis, **K. Konstantinidis**, M. J. Lancaster, P. S. Hall, "Waveguide-Fed High Gain Antenna at Sub-millimeter Wave Frequencies", *IET Workshop on Millimetre Wave Technologies for Gigabit per Second Wireless Communications*, Belfast, September, 2012.

3. **K. Konstantinidis**, A. P. Feresidis, P. S. Hall, "Multiple Layer Fabry-Perot Cavity Antennas", *7th European Conference on Antennas and Propagation*, Gothenburg, Sweden, Apr. 8-12, 2013.

4. **K. Konstantinidis**, A. P. Feresidis, P. S. Hall, "Multi-Layer Optimised Periodic Surfaces for Broadband Fabry-Perot Cavity Antennas", *IEEE Antennas and Propagation Society International Symposium*, Orlando, FL, USA, Jul. 7-13, 2013.

5. **K. Konstantinidis**, A. P. Feresidis, M. J. Lancaster, P. S. Hall, P. Gardner, "Design of a submillimetre wave Fabry–Perot cavity antenna", *European Microwave Week 2013*, Nuremberg, Germany, October 6-11, 2013.

6. **K. Konstantinidis**, A. P. Feresidis, P. S. Hall, "Dispersion Characteristics of Multi-Layer Fabry-Perot Leaky-Wave Antennas", *8th European Conference on Antennas and Propagation*, The Hague, Netherlands, Apr. 6-11, 2014.

7. **K. Konstantinidis**, A. P. Feresidis, P. S. Hall, M. J. Lancaster, "Micromachined Periodic Surfaces for Planar Terahertz Antennas", *8th European Conference on Antennas and Propagation*, The Hague, Netherlands, Apr. 6-11, 2014.

8. **K. Konstantinidis**, A. P. Feresidis, "Novel Meta-Surfaces for the Design of Broadband Highly Directive Antennas", *8th International Congress on Advanced Electromagnetic Materials in Microwaves and Optics – Metamaterials 2014* Copenhagen, Denmark, 25-30 August 2014.

9. **K. Konstantinidis**, A. P. Feresidis, P. S. Hall, "Multi-Layer Sub–Wavelength Profile Broadband Leaky–Wave Antenna", *European Microwave Week 2014*, Rome, Italy, October 5-10, 2014.

10. **K. Konstantinidis**, A. P. Feresidis, P. S. Hall, "Broadband Dual-Slot-Fed Multi-layer Fabry-Perot Cavity Antenna", *Antennas and Propagation Conference (LAPC)*, 2014 Loughborough, UK.

11. **K. Konstantinidis**, A. P. Feresidis, M. J. Lancaster, "Design of sub-millimetre wave Fabry–Perot cavity antenna", *IET 2nd Annual Active and Passive RF Devices Seminar*, Birmingham, UK, 29 October 2014.

12. M. Mavridou, **K. Konstantinidis**, A. P. Feresidis, P. Gardner, "Reconfigurable Beams from Millimetre-Wave Leaky-Wave Antennas", *9th European Conference on Antennas and Propagation*, Lisbon, Portugal, Apr. 12-17, 2015.

13. **K. Konstantinidis**, A. P. Feresidis, P. S. Hall, "Broadband Fabry-Perot Type Sub–Wavelength Profile Antenna", *9th European Conference on Antennas and Propagation*, Lisbon, Portugal, Apr. 12-17, 2015.

CONTENTS

List of Figures

CHAPTER 1

INTRODUCTION

1.1 BACKGROUND AND OBJECTIVES

1.1.1 High-Gain Antennas

Gain is a figure of merit that describes the ability of an antenna to radiate efficiently the input energy through space [1-3]. Consequently, modern communication systems have increasing demands of high gain antennas to enhance the overall system gain and the signal to noise ratio (SNR). Moreover, to obtain precise signal targeting between two communication devices, complying with standard protocols, it is necessary to use directional antennas enabling line of sight (LOS) transmission. Directional antennas reduce signal interference by sending fewer signals from/to a direction other than the main beam.

Different implementations of high gain antennas have been extensively studied over the past years. A brief review of general antenna types will be presented below. The antenna's gain is directly related to its radiation aperture size, i.e. the larger the effective area is, the narrower the beamwidth which is translated to high directivity values due to the inverse relationship of directivity and beamwidth. This implies that typically, high gain antennas are electrically large [1].

Fig.1.1.1 Parabolic satellite communication antenna in Raisting, Bavaria, Germany (courtesy: Richard Bartz).

Parabolic reflector antennas (Fig. 1.1.1) are used as high gain antennas for point-to-point communications and satellite communications. As their name indicates they are formed by a parabolic "dish", and an external feed antenna. Their operation is based on reflecting in phase the waves emerging from the feed antenna which is placed at the focus point of the reflector. Although their performance is broadband since it is not related to resonant elements [2], their disadvantages are their large size and the external feeding mechanism. The same mechanism describes the operation of **lens antennas** (Fig. 1.1.2). The difference lies in the degrees of freedom, which number four in the case of lenses while there is just one for the reflector

antenna [2, 3]. One of the advantages of a lens antenna over a parabolic antenna is the ability to steer the radiated beam by moving the external feed, due to the spherical symmetry of the lens, avoiding rotating the whole antenna. Nevertheless, it still requires mechanical steering, it is bulky and fed externally. A good candidate for the primary source for parabolic reflector antennas and lenses are **horn antennas** (Fig. 1.1.3)**.** They are characterized by a broadband operation since they don't have resonant elements and high gain is possible by increasing their size [2]. Electronically steerable beams can be obtained from a **phased array** (Fig. 1.1.4)**.** It consists of a network of radiating elements arranged on a support. Each element is individually fed. Controlling the amplitude and phase of each element will result in a desired radiation beam shape and angle. However, the cost of a phased array antenna its high, due to the phase controller and power amplifier required for each antenna element [2]. In Fig.1.1.4, a phased array reconfigures the beam pointing direction during operation to monitor targets over a wide area of the sky.

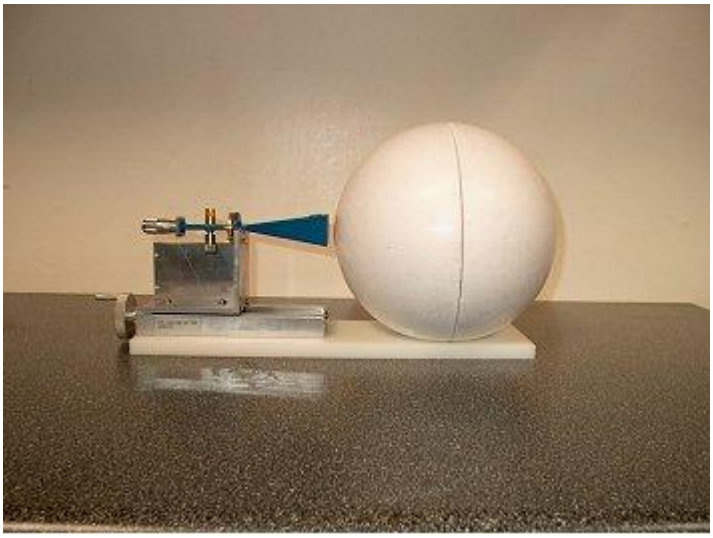

Fig.1.1.2 Luneburg lens antenna (courtesy: Rozendal Associates Inc.).

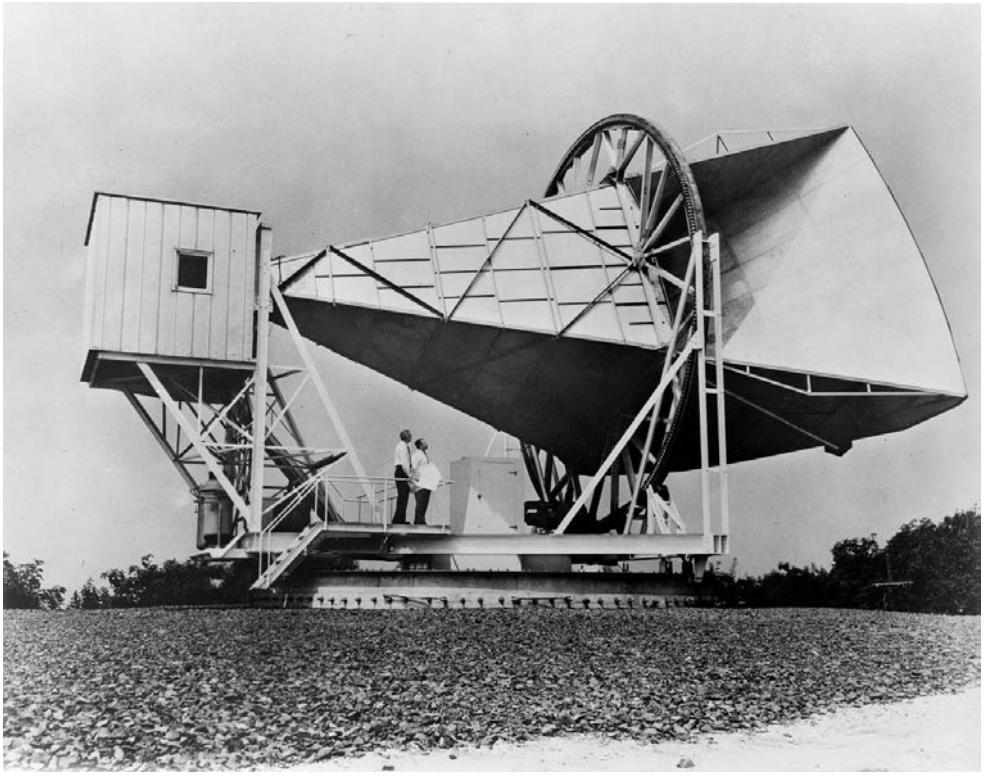

Fig. 1.1.3 This horn antenna was built in 1959 at Bell Telephone Laboratories for pioneering work in communication satellites for NASA at Holmdel, New Jersey (courtesy: Great Images in NASA).

Fig. 1.1.4 Phased array inter-continental missile detection radar (courtesy: Alaska District).

Reflectarrays (Fig. 1.1.5) consist of a planar reflecting surface patterned with an array of elements illuminated by an external feed. Control of the elements' reflection phase provides a control of the reflected radiation pattern [4, 5]. One of the main advantages of reflectarrays is the reconfigurability of the elements which in turn results in a dynamic steering of the reflected beam. This could be achieved using tunable components such as diodes [6] or MEMS [7] or tunable substrates such as liquid crystals [8] or ferroelectric/ferromagnetic materials [9]. Although they offer the advantage of simplicity and they are less bulky than reflectors and lens antennas, they have narrowband performance related to their inherit resonance based operation.

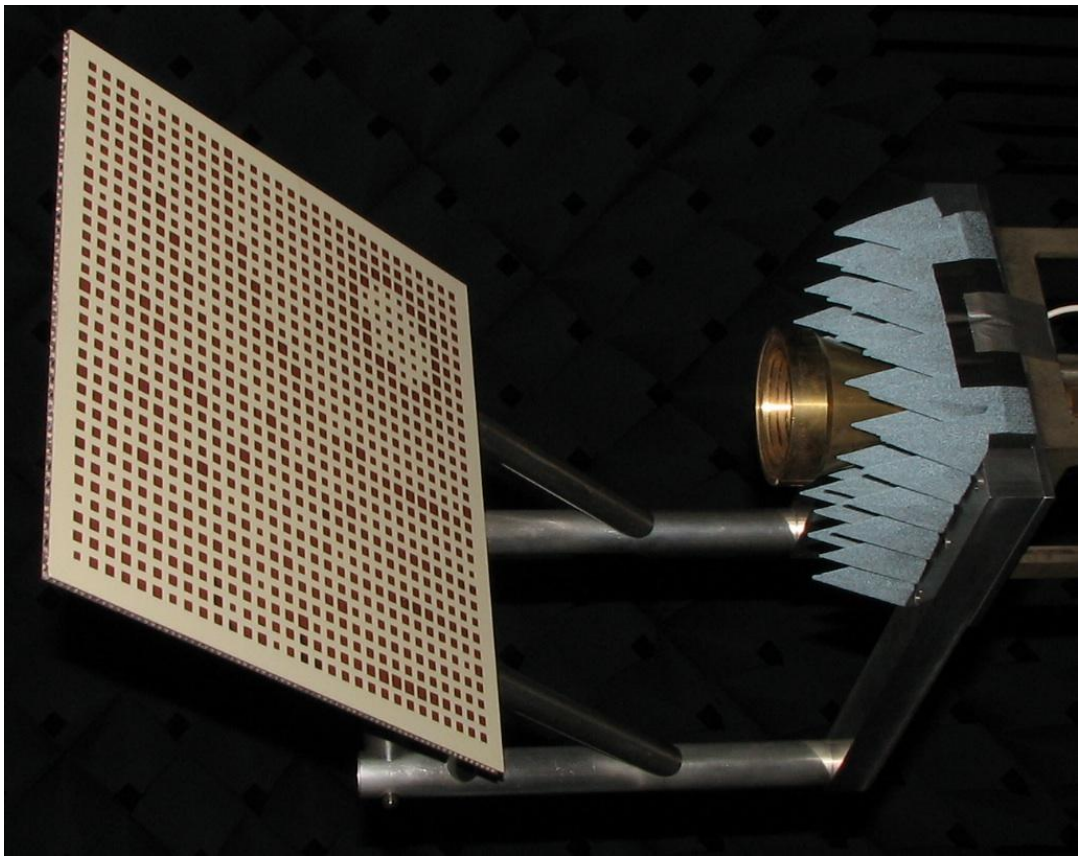

Fig.1.1.5 Printed reflectarray antenna (courtesy: TICRA).

Furthermore, there has been a strong demand over the last years for high gain, highly efficient and low profile planar antennas working up to millimetre wave frequencies. Potential applications include wireless local area networks (WLAN), mobile communication systems and satellite communications. **Microstrip patch arrays** have been actively used in recent years for applications such as satellite communications due to their low profile, light weight and low cost. However, their complicated feeding mechanisms led to low efficiency, low gain and pattern deterioration due to their high resistive losses and spurious feed radiation [10-12]. **Slotted waveguide arrays** are a good alternative for high gain and highly efficient planar antennas. Several types have been proposed by Ando et al.[13, 14], with Radial Line Slot Arrays (RLSA) being one of them. They are available commercially in the 12GHz band for direct broadcast from a satellite (DBS) [15]. However the high manufacturing cost at millimetre wave frequencies and the necessity of perfect flatness of the plates are major disadvantages.

Fabry-Perot (FP) type Leaky-Wave Antennas (LWAs) employing doubly periodic arrays of conducting elements, or apertures in a conducting sheet, have been investigated in recent years [16-18], as they provide high-gain, high efficiency and a simple feeding network. Their name is derived from the classical Fabry-Perot interferometer which is widely used in optics. The latter is based on multiple reflections of waves between two parallel reflecting surfaces placed in close proximity creating a resonant cavity [19]. This optical resonant cavity exhibits sharp resonances at discrete frequencies, and thus behaves as narrowband frequency filter. FP LWAs consist of a metallic or metallo-dielectric periodic array placed at approximately half wavelength distance over a metallic ground plane and a low-directivity primary source (e.g. dipole). The passive array acts as a Partially Reflective Surface (PRS), [16-18], creating a

Fabry-Perot type resonant cavity that significantly increases the gain and directivity of the primary source.

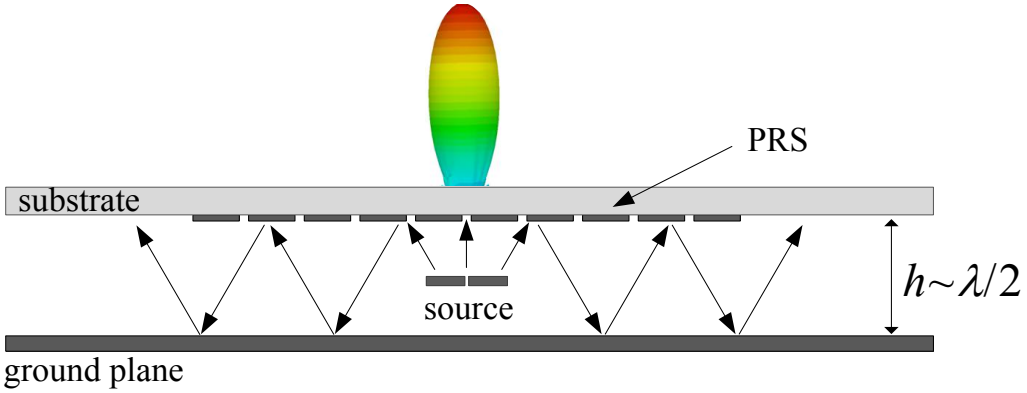

Fig. 1.1.6 Schematic diagram of a PRS LWA.

The concept of FP antennas was first demonstrated by Trentini who studied how several types of PRSs can increase the directivity of a waveguide aperture in the ground plane. He was also the first to employ a ray optics approximation to describe the antenna operation by means of the multiple reflections between the ground plane and the PRS [16]. The operating frequency is defined by the cavity distance which is typically half-wavelength in order to achieve constructive interference of the waves bounced between the PRS and the ground. Later, different configurations were proposed employing one or more dielectric layers with different dielectric constants and thicknesses replacing the PRS layer [20-23]. Since the operation of these antennas is based on the reflection characteristics of the PRS, high dielectric constant values were chosen to achieve high reflectivity values. However, a large number of layers is necessary in order to obtain comparable directivity values with the conventional PRS antenna. Other implementations were investigated over the last few years comprising periodic PRSs with different geometries [17, 24-26]. Moreover, a leaky-wave approach has also been successfully employed in order to analyse and design this type of antennas. This is due to the

partial electromagnetic transparency of the PRS at frequencies near the resonance which causes a Leaky Wave (LW) action [27].

The reduction of the profile of FP type antennas has also been studied extensively, by replacing the ground plane with a new type of surface, named Artificial Magnetic Conductors (AMC) (see section 1.1.2). Their key property is that they reflect electromagnetic waves with zero phase shift at a specific frequency. This property has been exploited in [28-31] where quarter wavelength profile highly directive antennas have been presented. In both half-wavelength and sub-wavelength implementations based on a FP resonant cavity, the directivity performance of a primary source increases when placed in the middle of the cavity. However this leads inherently to a narrow operational bandwidth.

Modern wireless communication systems require highly directive antennas with a wide operational frequency range due to the increase in demand for data capacity. Therefore, the design of broadband high gain FP LWAs remains an important challenge. Over the last few years, several authors have proposed different techniques to improve the bandwidth of these antennas. In [32-34] an array of multiple sources was employed replacing the single feed in the ground plane, in order to increase the radiating aperture of the antenna. This led to an increase of the bandwidth for a fixed gain value and therefore an increase of the gain-bandwidth product. More recently, a technique for bandwidth improvement was introduced [35], using the coupling between two PRSs of dissimilar array dimensions. This design exploited the different reflectivity values of the PRS layers to obtain a positive reflection phase gradient that satisfied the resonance condition of the antenna cavity for a certain frequency range. The proposed technique led to a double layer PRS design with half-wavelength separation between the PRSs and the ground plane, achieving a significant bandwidth enhancement compared to a single layer FP PRS antenna. The technique was

further investigated in more recent work employing different configurations [36-38]. In [36] a double-layer square ring geometry was presented obtaining an increasing phase. In [37] a positive phase gradient was achieved employing dipoles printed on both sides of a dielectric substrate. Finally, design guidelines to tailor the antenna bandwidth and directivity of two metallodielectric arrays over a ground plane were presented in [38]. In all the above cases the antenna radiation bandwidth was enhanced.

1.1.2 Periodic Structures

Frequency Selective Surfaces (FSS) have been subject of extensive work from the beginning of the twentieth century [39]. Their study increased exponentially due to the potential for military applications [40-46]. The versatility of these surfaces is wide due to dependence of their reflection and transmission coefficients on the frequency of operation, polarization and angle of incidence [46, 47]. FSS have been applied in many areas such as quasi optical beam splitters [48], dual or multi-banding Cassegrain reflectors [49], metallic radomes [50], phase screens for beam steering [51], dual-band arrays [52] and absorbers [53]. FSS are two dimensional (2-D) periodic arrays of metallic elements or apertures that exhibit stop-band and pass-band characteristics when excited by an electromagnetic wave at an angle arbitrary to the plane of the array. They exhibit total reflection (patch FSS) or total transmission (aperture FSS) at the resonant frequency and act as Partially Reflective Surfaces (PRS) at frequencies near the resonance.

Artificial Magnetic Conductors (AMC) are as indicated from their name, engineered metamaterial surfaces that in a specific frequency range act as Perfect Magnetic Conductors (PMC), i.e. they reflect incident waves in phase resulting in no tangential component of the magnetic field. This type of structure was first introduced by Sievenpiper [54], which

employed 2D periodic arrays of mushroom type elements on a grounded dielectric substrate. These elements are essentially metallic patches printed on the substrate and connected with vias to the ground. Later, in [28] it was proven that simpler designs could be implemented achieving the AMC response without the need of vias.

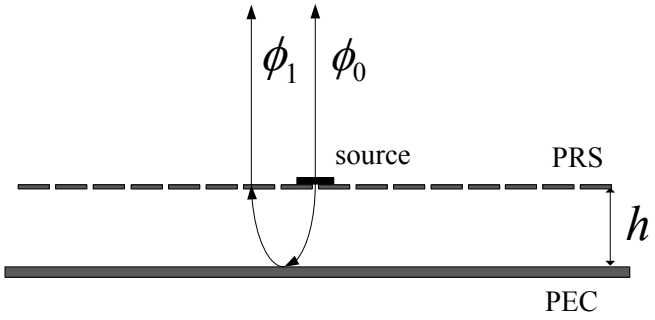

Fig. 1.1.7 Resonant cavity formed by PEC and PRS with the excitation outside the cavity.

The basic principle of the AMC operation can be described using ray optics theory. If a 2D periodic array of metallic elements is considered, placed at a distance *h* from a ground plane as shown in Fig. 1.1.7, then in order to obtain an AMC response, the direct and reflected rays should be in phase, i.e. the resonance condition (1.1-1) must be satisfied. This is obtained for the appropriate values of the transmission phase of the PRS surface ϕ_T and the cavity distance *h* for a specific frequency.

$$\phi_1 - \phi_0 = 2 \cdot \phi_T - \frac{2\pi}{\lambda} \cdot 2h - \pi = 2N\pi\,, \quad N=0,\ 1,\ 2.... \tag{1.1-1}$$

Thus, as explained above, for a specific frequency these types of structures exhibit a reflection phase of zero acting as an Artificial Magnetic Conductor (AMC), but they can also be operated at various reflection phase values giving an engineered impedance. In this case they are called Artificial Impedance Surfaces (AIS) which are useful for different applications. They can be applied as ground planes in printed [54] or in cavity antennas for profile

reduction [28, 29] as mentioned in the previous section, but they have also been employed for their phase shifting properties in applications such as reflectarrays [4], polarisation converters [55], holographic surfaces [56] etc.

1.1.3 Metasurfaces

Over the past years metamaterials have been the subject of extensive study due to their extraordinary electromagnetic properties. They are engineered materials synthesized by a periodic arrangement of elements and offer great flexibility for manipulating their electromagnetic and optical properties such as their effective refractive index. Metasurfaces [57, 58] are a 2D implementation of metamaterial structures, typically created by arrays of sub-wavelength scatterers. Compared to 3D metamaterials, they have the advantage of occupying less physical area and thus offer the possibility of lower loss structures. As they are composed of elements whose size and periodicity are smaller than the wavelength, they can be considered as a homogeneous material with an effective permittivity and permeability. Knowledge of these constitutive parameters can give information of the macroscopic behaviour of the metasurfaces.

Different types of metamaterials have been investigated, achieving properties not available in nature such as negative refractive index or near zero index. Negative-index materials (NIM) have been realised and experimentally demonstrated [59, 60]. Metamaterials of this type, exhibit simultaneously negative effective permittivity and effective permeability over a frequency range. More recently, numerous reports have appeared for metamaterials with near-zero refractive index (NZI) [61] and epsilon-near-zero (ENZ) [62, 63] for visible and infrared wavelengths. Electromagnetic waves inside such materials experience no spatial phase change and extremely large phase velocity. Near-zero refractive index materials can be obtained from

three possible combinations of electric permittivity and magnetic permeability values. The first case occurs when the permittivity approaches zero, resulting in high effective impedance values and a reflection coefficient close to +1. This means that the incident and reflected waves are in phase. The second case is obtained when the permeability approaches zero, which implies that the material acts as a Perfect Electric Conductor (PEC) with a reflection coefficient close to -1. Finally, in the third case, both the permittivity and the permeability of the structure are close to zero. This means that the metamaterial is matched to free space for the NZI frequency region. These unique properties pave the way for a number of applications such as cloaking [64-66], super-reflection [67], tunnelling [68-70] and funnelling [71].

1.2 MOTIVATIONS AND OBJECTIVES

In the previous section, we have presented a brief overview of different types of high gain antennas, an introduction to leaky wave antennas and periodic surfaces and a brief background on metasurfaces. The focus of this PhD thesis is to study the use of periodic metasurfaces in the design of **novel highly-directive Fabry Perot type antennas with significantly enhanced bandwidth performance**. As mentioned previously, these antennas offer numerous advantages over other antenna types. They are planar and easy to fabricate. They are characterized by a simple feeding mechanism, high directivity and efficient performance, but they suffer from a narrow bandwidth. A significant amount of work has been conducted in the field of FP LWAs so far towards two goals: the increase of the radiation bandwidth and the reduction of the profile. It has been shown [51] that by adding an extra layer and therefore creating a double-layer FP antenna the bandwidth could be significantly improved. Although extensive work had already been done for double layer configurations, there was no study in the literature about the possibility of using additional layers to further increase the bandwidth which would lead to a generalization of the concept.

For this reason, **one of the objectives of this thesis was to explore the possibility of creating multiple PRS layers FP antennas and thereby generalize the bandwidth enhancement concept.** The introduction of multiple layers of PRS implies extra complexity, more design parameters and increase of the computational time in design work. Efficient tools were used to analyse and estimate the antenna performance reducing the computational time. Among these tools were the periodic analysis using ray optics and reciprocity, and an equivalent circuit approach. Additionally, **in this dissertation the limitations of this technique will be presented, these were determined by studying the dispersion characteristics of the modes supported in multi-layer FP LWAs.** The implementation of multi-layer FP antennas addresses the issue of inherent narrow band performance but at the expense of increasing the antenna profile. In an effort to achieve improved bandwidth performance while keeping a low antenna profile, **a new concept of designing sub-wavelength profile multi-layer FP antennas by replacing the conventional PRSs with optimized composite metasurfaces was introduced.** All these designs were implemented to operate at frequencies around 15GHz as a proof of concept. Finally, as a last step of this thesis, **a first report of FP antenna operating at submillimetre wave frequencies is presented**. The FP antenna was based on micromachined fully metalized SU8 at around 300GHz. An in-house fabrication process was employed imposing several design considerations which make this antenna different to the lower frequency prototypes reported in the literature. Finally the design incorporates two back to back H bends to facilitate the interconnection with a waveguide flange. This work offers an interesting new solution for planar high-gain low cost antennas for such high frequencies.

1.3 OUTLINE OF CHAPTERS

This thesis deals with the analysis and design of planar periodic surfaces and metasurfaces for broadband and directive emission at millimetre and sub-millimetre wave frequencies. A brief introduction of high gain antennas as well as their advantages and disadvantages has been given. The aim of this research is highlighted and the concept of increasing the radiation bandwidth by incorporating additional layers was mentioned.

The rest of the dissertation is structured in six further chapters as follows:

In Chapter 2, the theoretical background of the thesis is presented. Different analysis tools used to design the proposed antenna structures are described. These include a ray optics approach, periodic analysis, dispersion analysis for leaky wave antennas and reciprocity. The ray optics approach gives an estimation of the directivity performance calculating the reflection characteristics of the proposed PRS structures under normal plane wave incidence assuming an infinite structure. Periodic full wave analysis is used to reduce the calculations from the infinite structure to the analysis of a single unit cell. Moreover, a leaky wave analysis together with reciprocity is presented. This provides a better insight of the function of the antennas and valuable design guidelines by estimating the antennas' performance. Finally, a different approach to characterize sub-wavelength profile metasurfaces is described based on a retrieval parameter extraction method. This gives information about the metamaterial nature of these structures by calculating their effective constitutive parameters.

In Chapter 3, initially a FP LWA with double-layer PRS is studied. An optimization is performed extracting the reflection coefficients of the double-layer PRS for high gain and broadband performance. Later, we present for the first time the design and implementation of a three-layer PRS for enhancement of the directivity – bandwidth (BW) product of FP

antennas and thereby generalize the concept of broadband FP antennas with multiple PRS layers. The three-layer PRS is studied and optimized to produce a reflection phase increasing with frequency over a wide range by virtue of the resonances of the two cavities formed between the three PRSs. In addition we present a simple equivalent circuit model for the design of the proposed multi-layer PRSs. A novel three-layer FP antenna has been designed achieving broadband high gain performance. This antenna outperforms previous antenna designs based on two-layer PRSs. Initially, a simple waveguide-fed slot was used as a primary source. Subsequently, an alternative feeding technique was investigated achieving improved matching and increase of the directivity through microstrip-line-fed slots. Antenna prototypes are designed for frequencies around 15GHz to validate their performance and characteristics. Two prototypes have been fabricated and measured for both feeding techniques validating the expected simulation results.

In Chapter 4, we study the dispersion characteristics of broadband periodic multilayer FP antennas employing full wave analysis tools. Initially, reciprocity is applied to estimate the far field radiation patterns of the antennas by measuring the electric field strength in the middle of the first cavity upon a plane wave illumination. Then a dipole source is used to excite the cavity modes and extract the complex propagation constant of the leaky modes. In both cases periodic boundary conditions are applied to reduce the calculations. Moreover, a simple and rigorous analysis procedure combining array theory and reciprocity validates the leaky-mode propagation constant values derived from the full wave simulations. Finally, finite size antennas based on the results of the periodic analysis are presented achieving a broadband directivity response. This dispersion analysis technique that is carried out for multi-layer FP LWAs reveals the limitations in these antennas in terms of performance through the extraction of the leaky modes.

In Chapter 5, a new concept for designing sub-wavelength profile and broadband high-gain leaky-wave antennas is introduced. This design technique allows for the implementation of broadband antennas with profiles of less than half wavelength. Initially, two double-layer periodic arrays of dissimilar dimensions are designed, each double-layer array consisting of an Artificial Magnetic Conductor (AMC) and a PRS printed on either side of a dielectric substrate. They are placed a quarter wavelength from a ground plane and from each other. Thus, two air cavities are created with a total profile of half wavelength, with a dipole, placed in the middle of the first cavity, used as a primary source. This antenna outperforms the design of a conventional one-layer FP antenna with $\lambda/2$ profile, in respect to both size and directivity-bandwidth performance. Furthermore, this concept is extended to achieve further profile reduction. A different approach to characterize this type of structures is through the retrieval parameter extraction. We propose multiple layers of closely spaced metasurfaces designed to manipulate the constitutive parameters of the effective metamaterial. The retrieval parameters are extracted using the reflection and transmission characteristics of the metasurfaces demonstrating a broadband ε-near zero (ENZ) effect.

In Chapter 6, we extend the FP type antenna concept into the Terahertz spectrum. The chapter begins with a brief introduction of the applications at sub-millimetre wavelengths. A review of the most promising micromachining fabrication techniques follows. The in-house SU-8 micromachining process is explained. A planar highly-directive and highly-efficient THz antenna based on novel cost-efficient micromachining of metalized polymer SU8, is designed. The absence of dielectric substrates and the creation of air cavities lead to significant increase in the antenna efficiency and gain. An antenna prototype operating at 267GHz has been fabricated using a multiple-layer metal coated SU8 substrate incorporating a waveguide H-bend. Moreover, measurements of the antenna's performance were performed and are

presented. Further improvements of the proposed antenna design, including a broadband matching technique and beam-steering application are introduced. Finally, design considerations for a broadband FP antenna based on multiple micromachined metalized SU-8 polymer layers operating at 300GHz are presented.

Finally, in Chapter 7 we present the main conclusions and achievements of this dissertation. Guidelines for future work will be proposed as well.

REFERENCES

[1] C. A. Balanis, "*Antenna Theory Analysis and Design*", Wiley-Interscience, ISBN 978-047-1667-82-7, Hoboken (NJ), USA, 2005.

[2] R.C. Johnson (ed.) "*Antenna Engineering Handbook*", third edition, McGraw-Hill, New York, 1993.

[3] C. A. Balanis, "*Modern Antenna Handbook*", John Wiley & Sons, Inc., 1680, 2008.

[4] J. Huang and J. A. Encinar, "*Reflectarray Antennas*", Institute of Electrical and Electronics Engineers, John Wiley & Sons, 2008.

[5] R. E. Collin, "*Foundations for Microwave Engineering*", 2nd ed. New York: Wiley-IEEE press, 2000.

[6] D. Sievenpiper, J. Schaffner, H. Song, R. Loo, and G. Tangonan, "Two-Dimensional Beam Steering Using an Electrically Tunable Impedance Surface", *IEEE Trans. Antennas and Propag.,* vol. 51, no. 10, pp. 2713 – 2722, Oct. 2003.

[7] J. Perruisseau-Carrier and A. K. Skrivervik, "Monolithic MEMS Based Reflectarray Cell Digitally Reconfigurable over a 360° Phase Range*" IEEE Antennas Wireless Propag. Lett.,* vol. 7, pp. 138-141, 2008.

[8] W. Hu; R. Cahill, J.A. Encinar, R. Dickie, H. Gamble, V. Fusco and N. Grant, "Design and Measurement of Reconfigurable Millimeter Wave Reflectarray Cells With Nematic Liquid Crystal", *IEEE Trans. Antennas and Propag.,* vol. 56, no.10, pp.3112-3117, Oct. 2008.

[9] R. Romanofsky, "Special Issues and Features of a Scanning Reflectarray Antenna Based on Ferroelectric Thin Film Phase Shifters", in *1st European Conference on Antennas and Propagation (EuCAP 2006)*, Nice, France, 2006.

[10] J.R. James and P. S. Hall, "*Handbook of Microstrip Antennas*", Peter Peregrinus Ltd. London, 1989.

[11] D. M. Pozar and D. H. Schaubert, "*Microstrip Antennas*", New York: IEEE Press, 1995.

[12] P. S. Hall and C. M. Hall, "Coplanar Corporate Feed Effects in Microstrip Patch Arrays Design", *IEE Proc., Microw., Antennas & Propag.,* pt. H, vol. 135, June 1988, pp. 180-186.

[13] J. Hirokawa, M. Ando and N. Goto, "Waveguide-Fed Parallel Plate Slot Array Antenna", *IEEE Trans. Antennas and Propag.,* vol.40, No.2, pp.218-223, 1992.

[14] M. Ando, J. Hirokawa, T. Yamamoto, A. Akiyama, Y. Kimura and N. Goto, "Novel Single-Layer Waveguides for High-Efficiency Millimeter-Wave Arrays", *IEEE Trans. Microwave Theory Tech.,* vol. MTT-46, No. 6, June 1998, pp. 792-799.

[15] M. Ando, K. Sakurai and N. Goto, "Characteristics of a Radial Line Slot Antenna for 12GHz Band Satellite TV Reception", *IEEE Trans. Antennas and Propag.,* vol., AP-34, No.10, pp.1269-1272, 1986.

[16] G.V. Trentini, "Partially Reflecting Sheet Array", *IRE Trans. Antennas Propag.*, vol. AP-4, pp. 666-671, 1956.

[17] J. R. James, S. J. A. Kinany, P. D. Peel, and G. Andrasic, "Leaky-wave multiple dichroic beamformers", *Electron. Lett.*, vol. 25, 1989.

[18] A. P. Feresidis, and J. C. Vardaxoglou, "High-Gain Planar Antenna Using Optimized Partially Reflective Surfaces", *IEE Proc. Microw. Antennas Propag.*, vol. 148, no. 6, Feb. 2001.

[19] S. Kartalopoulos, "Optical Spectral Filters and Gratings", in Introduction to DWDM Technology: Data in a Rainbow, Wiley-IEEE Press eBook Chapters, 2000.

[20] D. R. Jackson and N. G. Alexopoulos, "Gain Enhancement Methods for Printed Circuits Antennas", *IEEE Trans. Antennas Propag.*, vol. AP-33, no. 9, pp. 976–987, Sep. 1985.

[21] H. Y. Yang and N. G. Alexopoulos, "Gain Enhancement Methods for Printed Circuits Antennas Through Multiple Superstrates," *IEEE Trans. Antennas Propag.*, vol. AP-35, no. 7, pp. 860–864, Jul. 1987.

[22] D. R. Jackson, A. A. Oliner, and A. Ip, "Leaky-Wave Propagation and Radiation for a Narrow-Beam Multiple-Layer Dielectric Structure," *IEEE Antennas Propag.*, vol. AP-41, no. 3, pp. 344–348, Mar. 1993.

[23] T. Zhao, D. R. Jackson, J. T.Williams, and A. A. Oliner, "Simple CAD Model for a Dielectric Leaky-Wave Antenna", *IEEE Antennas Wireless Propag.*, vol. 3, pp. 243–245, April 2004.

[24] Y. J. Lee, J. Yeo, R. Mittra, and W. S. Park, "Design of a High-Directivity Electromagnetic Bandgap (EBG) Resonator Antenna Using a Frequency Selective Surface (FSS) Superstrate", *Microwave and Optical Technology Letters*, vol. 43, no. 6, pp. 462-467, Dec. 2004.

[25] T. Zhao, D. R. Jackson, J. T. Williams, Hung-Yu D. Yang, and A. A. Oliner, "2-D Periodic Leaky-Wave Antennas-Part I: Metal Patch Design", *IEEE Trans. Antennas and Propag.*, vol. 53, no. 11, pp.3505-3514, Nov. 2005.

[26] T. Zhao, D. R. Jackson, J. T. Williams, Hung-Yu D. Yang, and A. A. Oliner, "2-D Periodic Leaky-Wave Antennas-Part II: Slot Design", *IEEE Trans. Antennas and Propag.*, vol. 53, no. 11, pp. 3515-3524, Nov. 2005.

[27] A. A. Oliner, "*Leaky-Wave Antennas*", in Antenna Engineering Handbook, 3rd ed, R. C. Hansen, Ed. New York: McGraw-Hill, 1993, ch.10.

[28] S. Wang, A.P. Feresidis, G. Goussetis, J.C. Vardaxoglou, "Low-Profile Resonant Cavity Antenna with Artificial Magnetic Conductor Ground Plane", *Electron. Lett.*, vol.40, no.7, pp.405,406, 1 April 2004.

[29] A. P. Feresidis, G. Goussetis, S. Wang, and J. C. Vardaxoglou, "Artificial Magnetic Conductor Surfaces and Their Application to Low-Profile High- Gain Planar Antennas", *IEEE Trans. Antennas Propag.*, vol. 53, no. 1, pp. 209-215, Jan. 2005.

[30] J. R. Kelly, T. Kokkinos, and A. P. Feresidis, "Analysis and Design of Sub-wavelength Resonant Cavity Type 2-D Leaky-Wave Antennas", *IEEE Trans. Antennas and Propagation*, vol. 56, no. 9, pp. 2817-2825, Sept. 2008.

[31] C. Mateo-Segura, G. Goussetis, A. P. Feresidis, "Sub-Wavelength Profile 2-D Leaky-Wave Antennas With Two Periodic Layers", *IEEE Trans. Antennas Propag.*, vol.59, no.2, pp. 416-424, Feb. 2011.

[32] Y.J. Lee, J. Yeo, R. Mittra, and W. S. Park, "Application of electromagnetic bandgap (EBG) superstrates with controllable defects for a class of patch antennas as spatial angular filters", *IEEE Trans. Antennas Propag.,* vol. 53, no. 1, pp. 224-235, Jan. 2005.

[33] R. Gardelli, M. Albani, F. Capolino, ”Array Thinning by Using Antennas in a Fabry-Perot Cavity for Gain Enhancement”, *IEEE Trans. Antennas Propag.,* vol.54, no.7, pp.1979-1990, July 2006.

[34] A.R.Weily, K.P. Esselle, T.S. Bird and B.C. Sanders, “Dual Resonator 1-D EBG Antenna with Slot Array Feed for Improved Radiation Bandwidth”, *IET Microwaves, Antennas Propag.,* vol. 1, no. 1, pp. 198-203, February 2007.

[35] A. P. Feresidis, J. C. Vardaxoglou, “A Broadband High-Gain Resonant Cavity Antenna with Single Feed”, *Proc. EuCAP* 2006, Nice, France, 2006.

[36] L. Moustafa and B. Jecko, “EBG Structure with Wide Defect Band for Broadband Cavity Antenna Applications”, *IEEE Antenna Wireless Propag., Lett.*, vol.7, pp.693-696, Nov.2008.

[37] Ge Yuehe, K.P. Esselle, and T.S. Bird, “The Use of Simple Thin Partially Reflective Surfaces With Positive Reflection Phase Gradients to Design Wideband, Low-Profile EBG Resonator Antennas”, *IEEE Trans. Antennas Propag.*, vol. 60, no. 2, pp. 743-750, Feb. 2012.

[38] C. Mateo-Segura, A. P. Feresidis, G. Goussetis, “Bandwidth Enhancement of 2-D Leaky-Wave Antennas With Double-Layer Periodic Surfaces”, *IEEE Trans. Antennas Propag.*, vol.62, no.2, pp.586,593, Feb. 2014.

[39] G. Marconi and C.S. Franklin, “Reflector for Use in Wireless Telegraphy and Telephony”, *US Patent* 1,301,473, April 1919.

[40] B. A. Munk, R. G. Kouyoumjian, and L. Peters, Jr., “Reflection Properties of Periodic Surfaces of Loaded Dipoles”, *IEEE Trans. Antennas Propag.,* vol. AP-19, no. 5, pp. 612-617, Sept. 1971.

[41] B. A. Munk, “Periodic Surface for Large Scan Angles”, *United States Patent* 3,789,404, Jan. 1974.

[42] J. H. Richmond, “Radiation and Scattering by Thin-Wire Structures in the Complex Frequency Domain”, *Nat. Aeron. Space Admin.*, NASA CR-2396, May 1974.

[43] E. L. Pelton and B. A. Munk, “Periodic Antenna Surface of Tripole Slot Elements”, *United States Patent* 3,975,738, Aug. 1976.

[44] B. A. Munk, G. A. Burrell, and T. W. Kornbau, “A General Theory of Periodic Surfaces in Stratified Media”, Tech. Rept. 7 3 6-1, Ohio State Univ. Electro Science Lab., Dept. of Electrical Eng., *prepared under contract* AFAL-TR-77-2 19, Nov. 1977.

[45] R. Mittra, C.H. Chan, T. Cwik, “Techniques for Analyzing Frequency Selective Surfaces-a Review”, *Proceedings of the IEEE*, Vol. 76, pp.593- 615, Dec. 1988.

[46] B. A. Munk, “*Frequency Selective Surfaces: Theory and Design*”, Wiley-Interscience, 2005.

[47] J.C. Vardaxoglou, “*Frequency Selective Surfaces Analysis and Design*”, John Wiley, 1997.

[48] R. Ulrich, “Far-infrared Properties of Metallic Mesh and its Complementary Structure”, *Infrared Physics*, vol. 7, pp.37-55, 1967.

[49] V. D. Agrawal, and F.A. Pelow, “Design of a Dischroic Casegrain Subreflector”, *IEEE Trans. Antennas Propag.,* AP-27, no. 4, pp.466-473, July 1979.

[50] C. J. Larson, “Modified Center Layer Metallic Biplanar Radome Design”, Tech. Rept. AFAL-TR-78-28, Ohio State Univ. ElectroScience Lab. Rept. RF 4346-2, Columbus, March 1978.

[51] H. D. Griffiths, A. M. Vernon, and K. Milne, "Planar Phase Shifting Structures for Steerable DBS Antennas", *Proc. 6th International Conference on Antennas and Propagation (ICAP 89),* 1989, pp. 45-49.

[52] F. C. Seman, R. Cahill, V. F. Fusco, and G. Goussetis, "Design of a Salisbury Screen Absorber Using Frequency Selective Surfaces to Improve Bandwidth and Angular Stability Performance", *IET Microw. Antennas Propag.,* vol. 5, no. 2, pp. 149-156, Jan. 2011.

[53] J. Romeu, and Y. Rahmat-Samii, "Fractal FSS: A Novel Dual-Band Frequency Selective Surface", *IEEE Trans. Antennas and Propag.*, Vol. 48, no. 7, pp. 1097-1105, July 2000.

[54] D. Sievenpiper, Z. Lijun, R. F. Broas, N. G. Alexopoulos, and E. Yablonovitch, "High-Impedance Electromagnetic Surfaces with a Forbidden Frequency Band", *IEEE Trans. Microw. Theory Tech.*, vol. 47, no. 11, pp. 2059–2074, Nov. 1999.

[55] E. Doumanis, G. Goussetis, J.-L. Gomez-Tornero, R. Cahill, and V. Fusco, "Anisotropic impedance surfaces for linear to circular polarization conversion," *IEEE Trans. Antennas Propag.,* vol. 60, no. 1, pp. 212–219, Jan. 2012.

[56] B. H. Fong, J. S. Colburn, J. J. Ottusch, J. L. Visher, and D. F. Sievenpiper, "Scalar and tensor holographic artificial impedance surfaces," *IEEE Trans. Antennas and Propag.,* vol. 58, no. 10, pp. 3212–3221, Oct. 2010.

[57] N. Yu and F. Capasso, "Flat Optics with Designer Metasurfaces", *Nature Materials*, 13, 139, 2014.

[58] F. Falcone, T. Lopetegi, M. A. G. Laso, J. D. Baena, J. Bonache, R. Marqués, F. Martín, and M. Sorolla, "Babinet principle applied to the design of metasurfaces and metamaterials", *Phys. Rev. Lett*., vol. 93, pp. 197401–4, Nov. 2004.

[59] S. Zhang, W. Fan, N. C. Panoiu, K. J. Malloy, R. M. Osgood, and S. R. Brueck, "Experimental demonstration of near-infrared negative index metamaterials," *Phys. Rev. Lett*., 95, 1374041, (2005).

[60] X. H. Zhang, M. Davanço, Y. Urzhumov, G. Shvets, and S. R. Forrest, "From scattering parameters to Snell's law: a subwavelength near-infrared negative-index metamaterial", *Phys. Rev. Lett*., 101(26), 267401, (2008).

[61] P. Moitra, Y. Yang, Z. Anderson, I. Kravchenko, D. Briggs, and J. Valentine,"Realization of an All-dielectric Zero-index Optical Metamaterial", *Nature Photonics*, 7, 791-795, (2013).

[62] R. Maas, J. Parsons, N. Engheta, and A. Polman, "Experimental realization of an epsilon-near-zero metamaterial at visible wavelengths", *Nature Photonics*, 7, 907–912, (2013).

[63] R. J. Pollard, A. Murphy, W. R. Hendren, P. R. Evans, R. Atkinson, G. A. Wurtz, and A.V. Zayats, "Optical Nonlocalities and AdditionalWaves in Epsilon-Near-Zero Metamaterials", *Phys. Rev. Lett*., 102, 127405, (2009).

[64] T. Ergin, N. Stenger, P. Brenner, J. B. Pendry, and M. Wegener, "Three-Dimensional Invisibility Cloak at Optical Wavelengths", *Science* 328, 337, (2010).

[65] E. Kallos, C. Argyropoulos, Y. Hao, and A. Alú, "Comparison of frequency responses of cloaking devices under nonmonochromatic illumination", *Phys. Rev., B* 84, 045102, (2011).

[66] P. Y. Chen, C. Argyropoulos, and A. Alù, "Broadening the Cloaking Bandwidth with Non-Foster Metasurfaces", *Phys. Rev. Lett*., 111, 233001, (2013).

[67] J. Hao, W. Yan, and M. Qiu, "Super-reflection and cloaking based on zero index metamaterial", *Appl. Phys. Lett*., 96, 101109, (2010).

[68] M Silveirinha and N. Engheta, "Tunneling of Electromagnetic Energy through Subwavelength Channels and Bends using ε-Near-Zero Materials", *Phys. Rev. Lett*., 97**,** 157403, (2006).

[69] R. Liu, Q. Cheng, T. Hand, J. J. Mock, T. J. Cui, S. A. Cummer, and D. R. Smith, "Experimental Demonstration of Electromagnetic Tunneling Through an Epsilon-Near-Zero Metamaterial at Microwave Frequencies", *Phys. Rev. Lett*., 100, 023903, (2008).

[70] B. Edwards, A. Alù, M. G. Silveirinha, and N. Engheta, "Reflectionless sharp bends and corners in waveguides using epsilon-near-zero effects", *J. Appl. Phys*., 105, 044905, (2009).

[71] D. C. Adams, S. Inampudi, T. Ribaudo, D. Slocum, S. Vangala, N. A. Kuhta, W. D. Goodhue, V. A. Podolskiy, and D. Wasserman, "Funneling Light through a Subwavelength Aperture with Epsilon-Near-Zero Materials", *Phys. Rev. Lett*., 107, 133901, (2011).

CHAPTER 2

THEORETICAL BACKGROUND

This chapter covers all the theoretical approaches used for the design of the proposed antenna structures throughout this thesis. Initially, a geometric optics analysis is used to describe the multiple reflections between the PRS and the ground plane and give an estimation of the directivity performance calculating the reflection characteristics of the proposed PRS structures under normal plane wave incidence assuming an infinite structure. In section 2.2, periodic full wave analysis is described which is based on Floquet theorem and is employed by the simulation software to reduce the calculations from an infinite structure into the analysis of a single unit cell. This will result in a good approximation for the performance of the proposed periodic structures and significantly decrease the computational time. Section 2.3 is focused on leaky wave theory and its implementation on FP antennas. The leaky-wave approach, together with reciprocity which is also explained in this section, will provide a better insight into the function of the antennas and valuable design guidelines by estimating the antennas' performance. Finally, in section 2.4 a different approach to characterize sub-wavelength profile metasurfaces is described based on a retrieval parameter extraction method. This method will be utilized to obtain the constitutive parameters of these metasurfaces taking into account both isotropic and anisotropic cases.

2.1 RAY OPTICS

A geometrical optics (or ray optics) approach has been used to describe mathematically the operation of FP antennas. It is adopted to describe the ray paths between transmitting and reflecting rays [1]. This approximate method assumes an infinite extent of the structure and thus is not taking into account diffraction effects while it also ignores higher order mode coupling. The approach was first presented by Trentini [2], where he has shown how adding various types of partially reflective sheets placed in front of the reflecting screen can increase the directivity and gain of a waveguide aperture.

Let's assume the simple case when we have a single layer PRS placed at a distance *h* in front of completely reflective plane. The same concept can be applied for the case when we have multiple PRSs printed on dielectric substrates and superimposed over a ground plane. The PRS and the ground plane are assumed to have infinite size while the cavity distance is at the order of the wavelength. A waveguide-fed slot is used as a primary source to excite the waves inside the cavity. This will introduce multiple reflections between the two planes with decreasing amplitudes. A phase shift is introduced by the optical path length, the total reflection at the ground and the partial reflection at the PRS. Let's assume that a ray is emitted from the waveguide slot which has a radiation pattern *f(θ)*. The reflection coefficient of the PRS will be $R \cdot e^{i\phi_R}$, where R is the magnitude and ϕ_R the phase. If we assume no transmission losses, the amplitude of the transmitted ray will be proportional to $\sqrt{1-R^2}$; the amplitude of the once-reflected ray is proportional to $R\sqrt{1-R^2}$; the amplitude of the twice-reflected ray is proportional to $R^2\sqrt{1-R^2}$ and so on. The electric field intensity in the Fraunhofer zone is the summation of the partial rays, and we may write:

$$E = \sum_{n=0}^{\infty} f(\theta) E_0 R^n \sqrt{1-R^2}\, e^{i\phi_n} \tag{2.1-1}$$

where ϕ_n the phase angle composed of the total phase variations during reflections from the ground and the PRS, and of the path differences of the partial rays. From Fig. 2.1.1:

$$\phi_0 - \phi_1 = \frac{2\pi}{\lambda}(\Delta l) - \pi + \phi_R = \frac{2\pi}{\lambda} 2h\left(\tan\theta \cdot \sin\theta - \frac{1}{\cos\theta} \right) - \pi + \phi_R$$

$$= \frac{2\pi}{\lambda} 2h\left(\frac{\sin^2\theta}{\cos\theta} - \frac{1}{\cos\theta} \right) - \pi + \phi_R = \frac{2\pi}{\lambda} 2h\left(\frac{\sin^2\theta - (\sin^2\theta + \cos^2\theta)}{\cos\theta} \right) - \pi + \phi_R$$

$$= -\frac{2\pi}{\lambda} 2h \cdot \cos\theta - \pi + \phi_R \tag{2.1-2}$$

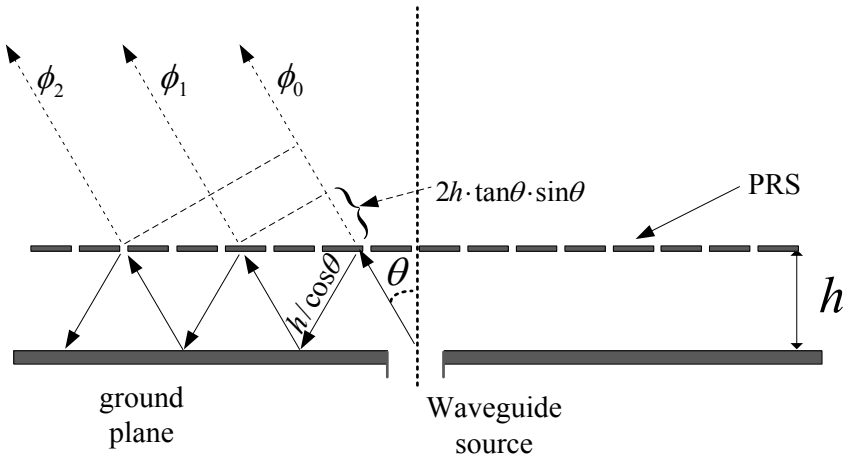

Fig. 2.1.1 Schematic diagram of a single layer FP antenna showing the multiple reflections between the ground and the PRS.

Thus,

$$\phi_n = n(\Delta\phi) = n\left(-\frac{2\pi}{\lambda} 2h \cdot \cos\theta - \pi + \phi_R \right) \tag{2.1-3}$$

Since 0<*R*<*1*, (2.1-1) is now written

$$\sum_{n=0}^{\infty}(R(\theta)e^{i\Delta\phi})^n = \frac{1}{1-R(\theta)e^{i\Delta\phi}} \tag{2.1-4}$$

Substituting equation (2.1-4) into (2.1-1) the absolute value of electric field strength is

$$|E| = |E_0| f(\theta)\sqrt{\frac{1-R^2}{1+R^2-2R\cos(\Delta\phi)}} \tag{2.1-5}$$

Therefore the power pattern becomes

$$P = \frac{|E|^2}{|E_0|^2} = \frac{1-R^2}{1+R^2-2R\cos\left(\phi_R - \pi - \frac{4\pi}{\lambda}h\cos\theta\right)} f^2(\theta) \tag{2.1-6}$$

where the amplitude R and the reflection phase on the PRS ϕ_R depend on the angle of incident θ. Maximum power at boresight ($\theta = 0$) is obtained when the following phase condition is satisfied:

$$\phi_R(0) - \pi - \frac{4\pi}{\lambda}h = 2N\pi \quad \text{where } N=0, 1, 2,.. \tag{2.1-7}$$

Rearranging (2.1-7), the equation that determines the resonant distance h between the PRS and the ground plane is

$$h = \frac{\lambda}{4}\left(\frac{\phi_R}{\pi} - 1\right) + N\frac{\lambda}{2} \tag{2.1-8}$$

Assuming an infinite extent of the array and the ground and also a uniform illumination of the PRS we can derive an expression for the boresight directivity in respect of the primary source by replacing (2.1-8) into (2.1-6).

$$D = \frac{P}{F} = \frac{1+R}{1-R} \tag{2.1-9}$$

From equation (2.1-9) it can be seen that the directivity increases with R, which means that a highly reflecting PRS placed at the resonant distance will result to a high-directivity antenna. Regarding the reflection phase of the PRS, we can rearrange the equation (2.1-8) as

$$\phi_R = \frac{4\pi h}{c} f - (2N-1)\pi \tag{2.1-10}$$

In order to obtain high directivity values for a broad frequency range the phase must satisfy the resonant condition within this range. This means that a phase should have a linearly increasing response with frequency as derived from the equation (2.1-10), for the frequency range of interest. To sum up, the reflection magnitude of the PRS will define the directivity maximum while the reflection phase will determine the bandwidth performance. This technique although is an approximation, will give valuable information for the design of high-directivity broadband FP antennas as we will see in the next chapter.

2.2 PERIODIC ANALYSIS

A structure can be characterized as periodic if it can be produced by an infinite repetition of a basic unit which is called “unit cell”, shifted by one or more (up to three) translation vectors. Depending on the number of translation vectors, 1-D, 2-D or 3-D structures can be obtained. The magnitude of the translation vector defines the periodicity of the structure in each dimension. The electromagnetic field in a periodic structure has the same amplitude in each unit cell with a phase shift added in successive unit cells. This means that the analysis of an infinite structure can be simplified and reduced into the analysis of a single unit cell, taking into account the appropriate phase shift. In a practical case, only finite size structures exist.

Nevertheless, an array can be considered periodic if it is large enough, and periodic analysis can be employed giving a good approximation of the actual behaviour of the structure. This will significantly reduce the computational time and calculations.

2.2.1 Frequency Selective Surfaces

As explained in Chapter 1.1.1, FSS are two dimensional (2-D) periodic arrays of metallic elements or apertures that exhibit stop-band and pass-band characteristics respectively when excited by an Electric field at an angle arbitrary to the plane of the array [3, 4]. If a plane wave with $\vec{E}_i$ is incident on a lossless FSS array, the transmitted electric field $\vec{E}_t$, and the reflected electric field $\vec{E}_r$, are related to $\vec{E}_i$ as:

$$E_i = E_r + E_t \tag{2.2-1}$$

$$R = \frac{E_r}{E_i} \text{ and } T = \frac{E_t}{E_i} \tag{2.2-2}$$

where R and T the reflection and transmission coefficients respectively.

Various elements with different geometries such as dipoles, cross dipoles, square loops and square patches can be used as FSS. Each element exhibits different reflection and transmission characteristics depending on the geometry. Metallic elements on a dielectric substrate give stop-band characteristics whereas pass-band characteristics are obtained with apertures on a conducting plane.

Complementary arrays may be defined as arrays with elements of the same shape such that if the two arrays are put on top of each other, a complete perfectly conducting plane is obtained (Fig. 2.1.1). The transmission coefficient of conducting arrays is equal to the reflection coefficient of the complementary aperture arrays and vice versa. This is a simple case of Babinet's principle [3, 4].

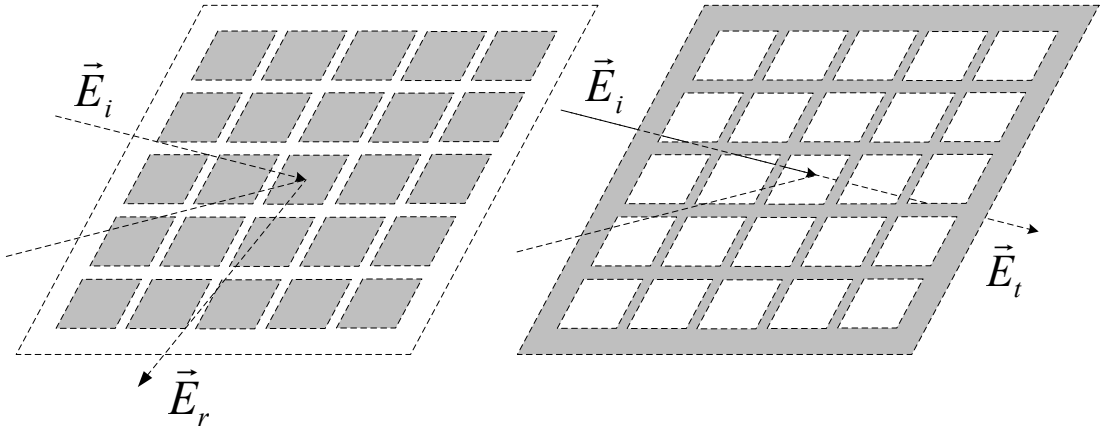

Fig. 2.2.1 Complementary arrays. Reflection of the capacitive array is equal with the transmission of the inductive array at the resonance.

2.2.2 Propagation in periodic surfaces

As mentioned earlier, propagation in periodic structures can be described using periodic analysis which is based on Floquet's theorem [5]. This is an expansion Fourier series applied for periodic functions.

Let's assume a FSS array of arbitrary elements that lies in the x-y plane. The array is excited by a linearly polarized plane wave with an angle of incidence θ with respect to the z axis. The lattice vectors $\vec{D}_v$ and $\vec{D}_u$ (Fig. 2.2-2) are expressed with respect to x and y axis as:

$$\vec{D}_u = D_u\left(\cos a_1\hat{x} + \sin a_1\hat{y}\right)$$

$$\vec{D}_v = D_v\left(\cos a_2\hat{x} + \sin a_2\hat{y}\right) \qquad (2.2\text{-}3)$$

where α the angle between the vectors $\vec{D}_v$ and $\vec{D}_u$, α_1 the angle between $\vec{D}_u$ and the x-axis, and α_2 the angle between $\vec{D}_v$ and the x-axis. Also, $D_u = \left|\vec{D}_u\right|$ $D_v = \left|\vec{D}_v\right|$.

The modal representation of the field of a periodic array in scalar Floquet modes [4, 6] is given as: $\Xi_{pq}(x,y,z) = \Psi_{pq}(x,y)e^{\pm j\beta_{pq}Z} = e^{-j\vec{k}_{tpq}\vec{r}} \cdot e^{\pm j\beta_{pq}Z}$ (2.2-4)

where $p,q = 0,\pm1,\pm2,....$, and $\vec{r} = x\hat{x} + y\hat{y}$

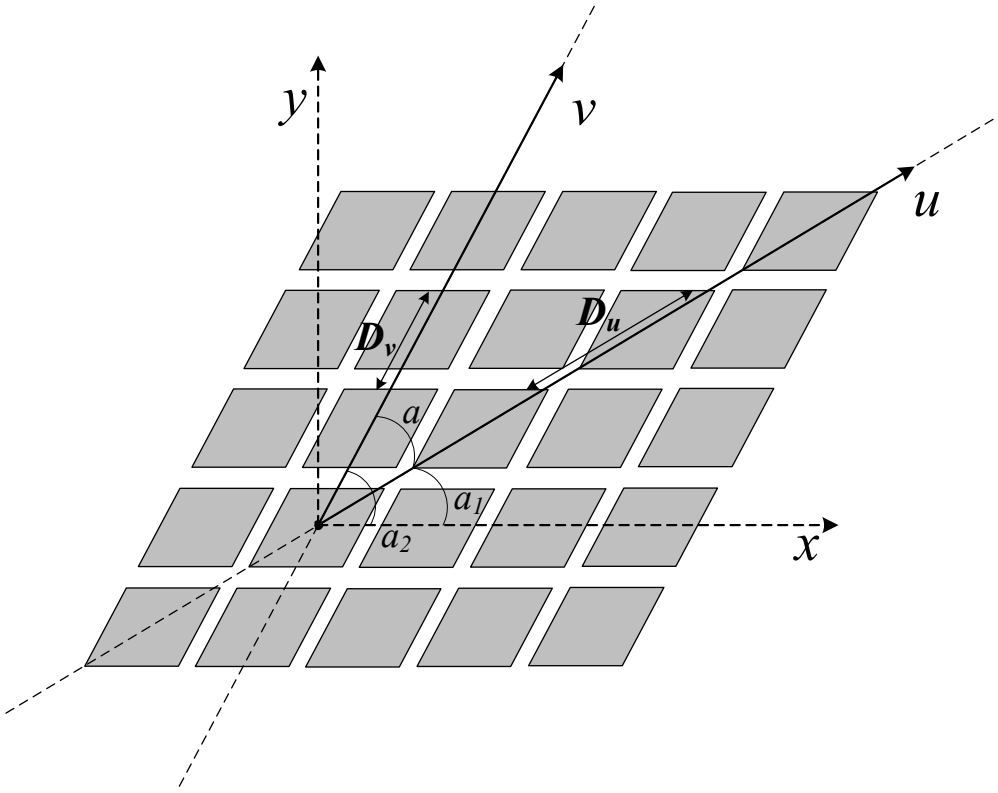

Fig. 2.2.2 Arbitrary lattice geometry of a 2D periodic infinite array.

$$\vec{k}_{tpq} = k_{tx}\hat{x} + k_{ty}\hat{y}$$

$$\vec{k}_{tpq} = \vec{k}_{t00} + p\vec{k}_1 + q\vec{k}_2$$

$$= (k_{0x} + pk_{1x} + qk_{2x})\hat{x} + (k_{0y} + pk_{1y} + qk_{2y})\hat{y} \quad (2.2\text{-}5)$$

where

$$\vec{k}_{t00} = \vec{k}_{00x} + \vec{k}_{00y}$$

and

$$\vec{k}_{t00} = k_0 \sin\theta\cos\phi \cdot \hat{x} + k_0 \sin\theta\sin\phi \cdot \hat{y}$$

with

$$k_0 = \frac{2\pi}{\lambda},$$

$$\vec{k}_1 = -\frac{2\pi}{A}\hat{z} \times \vec{D}_v$$

$$\vec{k}_2 = -\frac{2\pi}{A}\hat{z} \times \vec{D}_u$$

$A = \left|\vec{D}_v \times \vec{D}_u\right| = D_u D_y \sin a$, the area of the unit cell

$$\vec{k}_1 = k_{1x}\hat{x} + k_{1y}\hat{y}$$

$$\vec{k}_2 = k_{2x}\hat{x} + k_{2y}\hat{y}$$

$$\vec{k}_{1x} = \frac{2\pi}{D_u}\frac{\sin a_2}{\sin a}\ \vec{k}_{2x} = -\frac{2\pi}{D_v}\frac{\sin a_1}{\sin a}$$

$$\vec{k}_{1y} = -\frac{2\pi}{D_u}\frac{\sin a_2}{\sin a}\ \vec{k}_{2y} = \frac{2\pi}{D_v}\frac{\sin a_1}{\sin a}$$

The propagation constant β_{pq} is given from equation (2.2-6)

$$\beta_{pq} = \sqrt{k^2 - \vec{k}_{tpq} \cdot \vec{k}_{tpq}} \qquad (2.2\text{-}6)$$

where $k = k_0\sqrt{\varepsilon_r}$.

In order to have a propagating wave, β_{pq} should have a real and positive value, i.e.

$$k^2 > \vec{k}_{tpq} \cdot \vec{k}_{tpq}$$

On the other hand

$$k^2 < \vec{k}_{tpq} \cdot \vec{k}_{tpq}$$

$$\beta_{pq} = -j\sqrt{\vec{k}_{tpq} \cdot \vec{k}_{tpq} - k^2}$$

corresponds to evanescent waves.

2.2.3 Commercial electromagnetic solvers

Many techniques have been employed to solve the electromagnetic fields for periodic structures. The most popular numerical methods are based on Time domain-Differential equations such as Finite Difference Time Domain (FDTD) [7, 8], Finite Element Method (FEM) [9] or Transmission Line Matrix (TLM) [10] and Frequency domain-Integral Equations methods such as Method of Moments (MoM) [11]. These numerical technique are employed by commercial simulation software packages. In this dissertation CST Microwave Studio^{TM} has been used which is based on FDTD method.

CST Microwave Studio^{TM} is a 3-D full-wave numerical tool, which integrates various electromagnetic solvers. The two solvers that were used in this thesis are briefly described here. The finite integral time-domain solver employs a technique similar to FDTD which uses the integral form of Maxwell equations instead of the differential ones. It is based on non-orthogonal meshing schemes, that allow the tool to efficiently and rigorously model complicated structures. Since it is a time-domain solver, it is ideal for analysing the structures under investigation for a broadband frequency range. However it is not suitable for highly resonant structures. The finite-element frequency-domain solver on the other hand, is appropriate for the analysis of such highly resonant structures. Moreover it contains a special feature for analysing periodic structures applying periodic boundary conditions to the unit cell of the structure under investigation. The periodic boundary implementation creates the boundaries for arbitrarily shaped unit cells assuming infinite size structures where an appropriate phase shift is introduced between consecutive periodic elements.

2.3 ANALYSIS TECHNIQUE FOR LEAKY-WAVE ANTENNAS

Apart from ray optics theory, FP antennas can be described using leaky wave theory. This is due to the partial electromagnetic transparency of the PRS at frequencies near the resonance which causes a Leaky Wave (LW) action. This leaky-wave approach is explained in this subsection. Furthermore an estimation tool for the antenna's performance based on the theorem of reciprocity is also presented. As explained below, this tool can be employed to obtain radiation patterns for infinite size structures. Finally, radiation patterns can also be obtained using the array theory approach. Applying these tools, a better insight of the function of LWAs is provided along with a dispersion characterization of antennas of this type.

2.3.1 Leaky waves

Leaky waves are excited when leakage in a waveguiding structure occurs. Due to this leakage they are characterized by a complex propagation wavenumber [12]:

$$k = \beta - j\alpha \tag{2.3-1}$$

where β is the phase constant and α the leakage rate or attenuation constant. Leaky waves are fast waves i.e. waves whose propagation constant is smaller than the free space wave number $\beta < k_0$ as will be explained later on. They are typically produced from surface waves that are excited in the structure, due to discontinuities along one side of the structure. In 2-D FP antennas, the waveguiding structure is formed by the ground plane and the PRS. Therefore, the discontinuities occur in the PRS due to the uniform periodic modulation.

As indicated by its name, the attenuation constant defines the amplitude decrease per meter of the propagating wave. A large α implies that the wave is attenuated at fast rate, i.e. a short effective aperture is produced. Conversely, a low value of α, will produce a large effective

aperture. Consequently, α controls the beamwidth of the radiated beam. The phase constant β on the other hand, represents the phase variation per meter of the propagating wave. The latter controls the angle of the radiating beam as obtained from:

$$\sin\theta = \frac{\beta}{k_0} \tag{2.3-2}$$

where θ the angle of the main beam of the radiation pattern with respect to the normal direction and $k_0 = \frac{2\pi}{\lambda}$.

This equation is extracted from simple trigonometry and ray optics (Fig. 2.3.1). Again, from trigonometry it is known that

$$\left|\sin\theta\right| \le 1 \Rightarrow \left|\frac{\beta}{k_0}\right| \le 1. \tag{2.3-3}$$

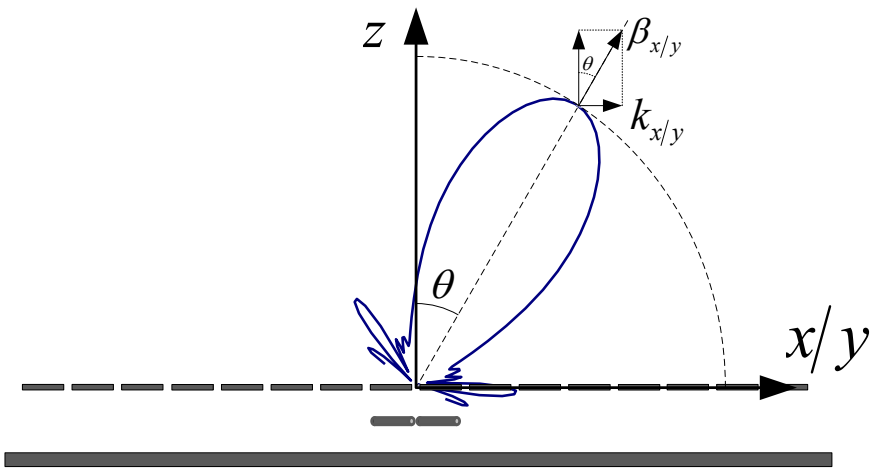

Fig. 2.3.1 Schematic representation of LW radiation.

From this, the condition for leaky-wave radiation is produced, since no radiation can occur if $\beta > k_0$. It must be emphasised that the waves that satisfy the equation (2.3-3) are called "fast waves" due to the fact that their phase velocity is greater than the one of the light. On the other hand, waves whose phase constant is greater than k_0, don't radiate and so they are called "slow waves".

2.3.2 Reciprocity

One way to calculate the power pattern of the antenna is using the theory of reciprocity. This theory is based on the principle that a source placed at a point A in the far field will provoke an electric field strength at a point B inside the structure, equal to the one that would be provoked at point A, from a source at point B (Fig. 2.3.2). Thereby, in the case of FP LWA, the theory of reciprocity can be employed to avoid the calculation of the far field which will significantly reduce the computational time. Instead, the near field is calculated at an observation point inside the cavity formed between the ground plane and the PRS. The radiation pattern at a fixed frequency can be obtained by scanning the near fields for different angles (θ,ϕ) of the incoming plane wave [13].

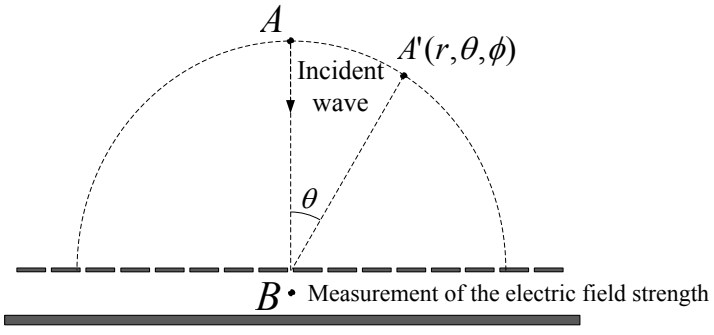

Fig. 2.3.2 Schematic diagram of reciprocity technique.

By considering an infinite array model the complexity in computational analysis is reduced. This means that the analysis of the whole structure is simplified to the analysis of one unit cell. The reciprocity technique is described in [13] for single layer periodic antennas and exploits the fact that the receiving and transmitting field patterns for an antenna are identical [14]. Consequently, a unit cell of the structure under study can be considered, employing periodic boundary conditions. By scanning the relative field strength Ex or Ey (polarization makes no difference for both x and y directions due to symmetry), the radiation pattern of the antenna can be obtained. Once the 3- D radiation pattern is determined, the integration of the obtained values can be used as a reference in order to obtain the directivity pattern, so that,

$$D(\theta,\phi) = \frac{4\pi \cdot \left|E(\theta,\phi)^2\right|}{\iint\limits_{\theta,\phi} \left|E(\theta,\phi)\right|^2 \cdot \sin(\theta) \cdot d\theta \cdot d\phi} \tag{2.3-4}$$

where $\mathrm{D}(\theta,\phi)$ is the directivity of the antenna in the direction (θ,ϕ) and $\mathrm{E}(\theta,\phi)$ is the electric field strength at the observation point in the middle of the cavity, when excited by a plane wave incident from (θ,ϕ).

Apart from the radiation pattern and directivity response estimation, calculation of the near-field inside the cavity in conjunction with reciprocity arguments can be employed towards a more accurate procedure for determining the antenna profile for a specific desired operating frequency. Reciprocity suggests that for an antenna radiating at broadside, the fields at the observation point are maximised for a given normally incident wave at the central operating frequency.

Therefore, scanning the fields over the frequency yields the central operating frequency of the antenna at the peak of the observed curve. It is then possible to tune the design to the specified frequency by modifying the antenna profile.

2.3.3 Array Factor Approach

Leaky wave antennas can be characterized using array factor (AF) theory. The array factor approach provides an alternative method to compute the radiation characteristics of periodic arrays. The AF is a function of the geometry of the array and the excitation phase. By varying the separation or/and the phase between the elements, the characteristics of the array factor and of the total field of the array can be controlled [14, 15]. For 2-D arrays, the AF is given by:

$$AF(\theta,\phi) = \left[\sum_{m=-\frac{M}{2}}^{m=\frac{M}{2}} I_{m1} e^{i(m-1)(k_0 D_x \sin\theta\cos\phi)+i\xi_m}\right]\cdot\left[\sum_{m=-\frac{N}{2}}^{m=\frac{N}{2}} I_{1n} e^{i(n-1)(k_0 D_y \sin\theta\sin\phi)+i\xi_n}\right] \tag{2.3-5}$$

where D_x and D_y the periodicity in x-y axis and M and N the number of cells along x and y directions respectively.

The angles θ and ϕ are the elevation and azimuthal angles of the radiated beam respectively. The elevation angle is given by:

$$\theta = \sin^{-1}\left[\frac{\beta(\omega)}{k_0}\right] \tag{2.3-6}$$

where $\beta(\omega)$ the propagation constant in the direction of propagation.

The parameters ξm and ξn in (2.3-5) represent the phase shift that the excitation undergoes for the mth or nth element with respect to the element at the origin. This relative phase shift is

defined by (2.3-7) and is related to the propagation constant, $\beta_{x/y}$ for the x- and y- directions respectively:

$$\xi_m = -(m-1)\beta_x D_x,\ \xi_n = -(n-1)\beta_y D_y \tag{2.3-7}$$

On the other hand, the magnitude of the excitation at each element is determined by the exponential function:

$$I_{m1} = I_0 e^{-a_x (m-1) D_x},\ I_{1n} = I_0 e^{-a_y (n-1) D_y} \tag{2.3-8}$$

where $a_{x/y}$ the leakage rate.

Substituting (2.3-7) and (2.3-8) in (2.3-5) the radiation pattern of a LWA can be given from (2.3-9), if the antenna's dispersion characteristics α and β are known.

$$AF = \sum_{n=0}^{N-1} e^{-na \cdot D} e^{jn\left(\frac{2\pi D \cos\gamma}{\lambda} - \beta \cdot D\right)} \tag{2.3-9}$$

where γ is the angle from the axis of propagation, i.e. the complementary of angle θ.

This theory assumes infinite size structures and therefore it is not taking into account the edge effects. Moreover it only considers fundamental Floquet modes, with the higher modes assumed to be evanescent.

2.4 RETRIEVAL PARAMETER APPROACH FOR METASURFACES

A metamaterial can be characterized by its effective permittivity and permeability. Various methods have been proposed for retrieving the effective parameters of metamaterials. One approach that has been extensively investigated is based on averaging the electromagnetic fields [16, 17] inside the metamaterial structure; however this cannot be applied to obtain

experimental results. Another method that has been considered is to estimate the effective constitutive parameters using analytical models [18, 19] to approximate the metamaterial structures. Although it has been proven to be more suitable for practical cases than the previous one, it demands an increased complexity for more complicated structures. Finally, a very commonly used technique to retrieve ε and μ is based on the S-parameters. This method is well established and has the advantage that it can be applied to all kinds of structures independently of their complexity. Moreover, it can be used in both simulation and measurements. A version of this technique, known as the Nicolson – Ross – Weir [20, 21]method has been employed in this work and is going to be analyzed for both isotropic and anisotropic metasurfaces.

2.4.1 Isotropic Parameter Retrieval Technique

Let's consider a homogeneous slab whose effective permittivity and permeability we desire to retrieve. In this case, we can retrieve the permittivity and permeability from the reflection (S_{11}) and transmission (S_{21}) values [22-27].

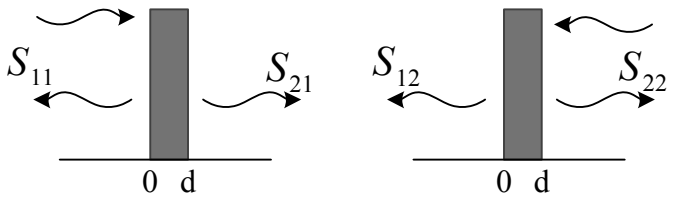

Fig. 2.4.1 S-parameters on a homogeneous 1D slab of thickness d.

In order to describe the retrieval approach from the S-parameters of the material, initially we define the transfer matrix which is given in (2.4-1) that relates the fields on both sides of the material.

$$F' = TF \tag{2.4-1}$$

where $F = \begin{pmatrix} E \\ H \end{pmatrix}$ and E and H are the electric and magnetic field amplitudes on both sides of the slab.

In this case, the transfer matrix is given from

$$T = \begin{pmatrix} \cos(nkd) & -\frac{z}{k}\sin(nkd) \\ \frac{k}{z}\sin(nkd) & \cos(nkd) \end{pmatrix} \tag{2.4-2}$$

where k is the wavenumber, d is the thickness of the slab (or in the case of a metamaterial structure the size of the unit cell), n the refractive index and z the wave impedance of the slab. The electric permittivity and magnetic permeability of the slab are in turn defined by (2.4-3)

$$\varepsilon = \frac{n}{z}, \mu = nz \tag{2.4-3}$$

For a homogeneous slab, the S matrix is symmetric and the matrix elements are expressed as

$$S_{21} = S_{12} = \frac{1}{T_s + \frac{1}{2}\left(ikT_{12} + \frac{T_{21}}{ik}\right)} \tag{2.4-4}$$

$$S_{11} = S_{22} = \frac{\frac{1}{2}\left(\frac{T_{21}}{ik} - ikT_{12}\right)}{T_s + \frac{1}{2}\left(ikT_{12} + \frac{T_{21}}{ik}\right)}$$

where $T_s = T_{11} = T_{22}$. Thus, combining (2.4-2) and (2.4-4) we get

$$S_{21} = S_{12} = \frac{1}{\cos(nkd) - \frac{i}{2}\left(z + \frac{1}{z}\right)\sin(nkd)} \tag{2.4-5}$$

$$S_{11} = S_{22} = \frac{i}{2}\left(\frac{1}{z} - z\right)\sin(nkd) \tag{2.4-6}$$

So we can solve the above equations to find n and z as follows.

$$n = \frac{1}{kd}\cos^{-1}\left[\frac{1}{2S_{21}}(1 - S_{11}^2 + S_{21}^2)\right] \tag{2.4-7}$$

$$z = \sqrt{\frac{(1+S_{11})^2 - S_{21}^2}{(1-S_{11})^2 - S_{21}^2}} \tag{2.4-8}$$

However, both (2.4-7) and (2.4-8) create ambiguities due to the multiple solutions of the inverse cosine and the two branches of the square root in (2.4-7) and (2.4-8) respectively. These ambiguities are solved by choosing the correct branch so that the conditions $\mathrm{Re}(z) \geq 0$ and $\mathrm{Im}(n) \geq 0$ are satisfied.

2.4.2 Anisotropic Parameter Retrieval Technique

The equations that have been shown above can produce the constitutive parameters of a material that is considered isotropic. However, in many cases anisotropic materials are investigated [28]. For such materials the constitutive parameters are tensors given by:

$$\bar{\bar{\varepsilon}} = \varepsilon_0 \bar{\bar{\varepsilon}}_r = \varepsilon_0 diag\left[\varepsilon_{xx}, \varepsilon_{yy}, \varepsilon_{zz}\right] \tag{2.4-9}$$

$$\bar{\bar{\mu}} = \mu_0 \bar{\bar{\mu}}_r = \mu_0 diag\left[\mu_{xx}, \mu_{yy}, \mu_{zz}\right] \tag{2.4-10}$$

where ε_0 and μ_0 the permittivity and permeability of free space respectively.

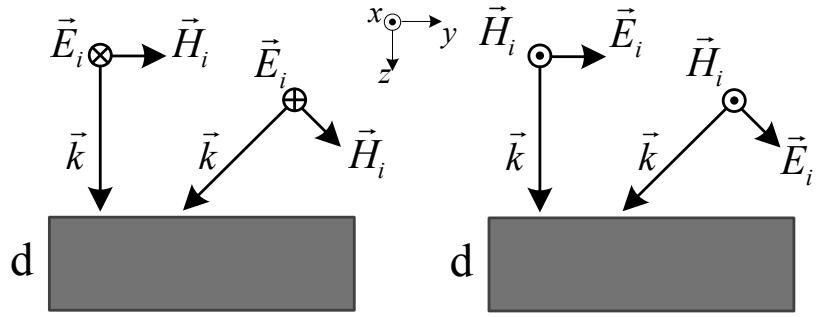

Fig. 2.4.2 Schematic of a homogeneous anisotropic slab with thickness d, illuminated by TE (left) and TM (right) polarised plane waves for normal and oblique incidence.

We assume that a plane wave is illuminating the anisotropic slab, incident at an angle θ_i with respect to the normal direction $\hat{z}$ (Fig. 2.4.2), where the plane wave vectors are in the y-z plane for both transverse electric (TE) and transverse magnetic (TM) polarized waves. The dispersion relations inside the material TE and TM polarizations respectively are given by

$$\frac{\beta_y^2}{\mu_{zz}} + \frac{\beta_{zTE}^2}{\mu_{yy}} = k_0^2 \varepsilon_{xx} \tag{2.4-11}$$

$$\frac{\beta_y^2}{\varepsilon_{zz}} + \frac{\beta_{zTM}^2}{\varepsilon_{yy}} = k_0^2 \mu_{xx} \tag{2.4-12}$$

where $\beta_y = k_y = k_0 \sin\theta_i$ and k_0 is the free space number.

Assigning boundary conditions on both sides of the slab, the scattering parameters of the slab can be extracted under a plane wave illumination of arbitrary angle of incidence. The scattering parameters corresponding to TE and TM waves can be derived from the following equations

$$S_{11} = \frac{\Gamma_{TE(TM)}\left(1 - e^{i2\beta_{zTE(TM)d}}\right)}{1 - \Gamma_{TE(TM)}^2 e^{i2\beta_{zTE(TM)d}}} \tag{2.4-13}$$

$$S_{21} = \frac{(1-\Gamma_{TE(TM)}^2 e^{i2\beta_{zTE(TM)d}}}{1-\Gamma_{TE(TM)}^2 e^{i2\beta_{zTE(TM)d}}} \tag{2.4-14}$$

where

$$\Gamma_{TE(TM)} = \frac{Z_{TE(TM)}-1}{Z_{TE(TM)}+1} \tag{2.4-15}$$

the reflection coefficient at one side of the slab. The normalized wave impedances for TE and TM waves respectively, are calculated by

$$Z_{TE} = \frac{k_z \mu_{yy}}{\beta_{zTE}} \tag{2.4-16}$$

$$Z_{TM} = \frac{\beta_{zTM}}{k_z \varepsilon_{yy}} \tag{2.4-17}$$

where $k_z = k_0 \cos\theta_i$

For the retrieval of all the components of the constitutive parameters, we use the scattering parameters for two cases corresponding to different incident angle of plane wave illumination. The tensor parameters $\varepsilon_{xx}, \mu_{yy}$ and μ_{zz} are active when the slab is illuminated by TE waves and the tensor parameters $\varepsilon_{yy}, \mu_{xx}$ and ε_{zz} are active when the slab is illuminated by TM waves. Initially, we obtain the S-parameters for two TE incident waves with angles of incidence θ_{i1} and θ_{i2} with $\theta_{i1} \neq \theta_{i2}$. These will be S_{TE11-1}, S_{TE21-1}, S_{TE11-2} and S_{TE21-2} corresponding to the two angles of incidence and will be given by equations (2.4-13) and (2.4-14). Solving these four equations we obtain the z components of the refractive indices and the wave impedances for both angles of incidence by the following equations (2.4-18) and (2.4-19), where l =1, 2. Again, ambiguities arise when solving these equations as in the isotropic

case, which are solved by choosing the correct branch taking into account the conditions mentioned there.

$$\cos(n_{zTE-l}k_0 d) = \frac{1 - S_{TE11-l}^2 + S_{TE21-l}^2}{2S_{TE21-l}} \tag{2.4-18}$$

$$Z_{TE-l} = \pm\sqrt{\frac{(1+S_{TE11-l})^2 - S_{TE21-l}^2}{(1-S_{TE11-l})^2 - S_{TE21-l}^2}} \tag{2.4-19}$$

Thus, using (2.4-11), (2.4-16), as well as (2.4-18) and (2.4-19) we obtain the equations (2.4-20), (2.4-21) and (2.4-22) from which can calculate the tensors $\varepsilon_{xx}, \mu_{yy}$ and μ_{zz}.

$$\mu_{yy} = \frac{n_{zTE-l} Z_{TE-l}}{\cos\theta_{il}} \tag{2.4-20}$$

$$\varepsilon_{xx} = \frac{n_{zTE-1}\left[\frac{\cos\theta_{i1}}{Z_{TE-1}}\right]\sin^2\theta_{i2} - n_{zTE-2}\left[\frac{\cos\theta_{i2}}{Z_{TE-2}}\right]\sin^2\theta_{i1}}{\sin^2\theta_{i2} - \sin^2\theta_{i1}} \tag{2.4-21}$$

$$\mu_{zz} = \frac{\sin^2\theta_{i2} - \sin^2\theta_{i1}}{n_{zTE-1}\left[\frac{\cos\theta_{i1}}{Z_{TE-1}}\right] - n_{zTE-2}\left[\frac{\cos\theta_{i2}}{Z_{TE-2}}\right]} \tag{2.4-22}$$

Similarly, for the other three tensor, we need the S-parameters for two TM incident waves with angles of incidence θ_{i1} and θ_{i2} which will be S_{TM11-1}, S_{TM21-1}, S_{TM11-2} and S_{TM21-2}. Following the same procedure we get the z components of the refractive indices and wave impedances

$$\cos(n_{zTM-l}k_0 d) = \frac{1 - S_{TM11-l}^2 + S_{TM21-l}^2}{2S_{TM21-l}} \tag{2.4-23}$$

$$Z_{TM-l} = \pm\sqrt{\frac{(1+S_{TM11-l})^2 - S_{TM21-l}^2}{(1-S_{TM11-l})^2 - S_{TM21-l}^2}} \tag{2.4-24}$$

with l=1, 2.

In this case, we use (2.4-12), (2.4-17), (2.4-23) and (2.4-24) we obtain the equations (2.4-25), (2.4-26) and (2.4-27) from which can calculate the tensors $\varepsilon_{yy}, \mu_{xx}$ and ε_{zz}.

$$\varepsilon_{yy} = \frac{n_{zTM-l}}{Z_{TM-l}\cos\theta_{il}} \tag{2.4-25}$$

$$\mu_{xx} = \frac{n_{zTM-1}Z_{TM-1}\cos\theta_{i1}\sin^2\theta_{i2} - n_{zTM-2}Z_{TM-2}\cos\theta_{i2}\sin^2\theta_{i1}}{\sin^2\theta_{i2} - \sin^2\theta_{i1}} \tag{2.4-26}$$

$$\varepsilon_{zz} = \frac{\sin^2\theta_{i2} - \sin^2\theta_{i1}}{n_{zTM-1}Z_{TM-1}\cos\theta_{i1} - n_{zTM-2}Z_{TM-2}\cos\theta_{i2}} \tag{2.4-27}$$

Therefore, with this approach we can obtain all three tensors for each constitutive parameter which can characterize an anisotropic homogeneous medium, i.e. a material with different electromagnetic properties at each axis.

2.5 CONCLUSIONS

In this Chapter, a brief description of the theoretical tools used throughout this thesis was provided. The contents of section 2.1 and 2.2 are applied for the design and analysis of the antennas presented in Chapter 3, 5, 6. The analysis in section 2.3 is applied in Chapter 4 while the one in section 2.4 is applied in Chapter 5.

REFERENCES

[1] J. D. Krauss, "*Electromagnetics*", McGraw Hill Inc, 1953.

[2] G.V. Trentini, "Partially Reflecting Sheet Array", *IRE Trans. Antennas Propag.*, vol. AP-4, pp. 666-671, 1956.

[3] B. A. Munk, "*Frequency Selective Surfaces: Theory and Design*", Wiley-Interscience, 2005.

[4] J.C. Vardaxoglou, "*Frequency Selective Surfaces Analysis and Design*", John Wiley, 1997.

[5] M. G. Floquet, "Sur les équations différentielles linéaires à coefficients périodiques", *Annales scientifiques de l'École Normale Supérieure,* pp. 47-88, 1883.

[6] D. M. Pozar, "*Microwave Engineering*", 2nd edition, New York: John Wiley & Sons Inc, 1998.

[7] K.S. Yee, "Numerical Solutions of Initial Boundary Value Problems Involving Maxwell's Equations in Isotropic Media", *IEEE Trans. Antennas Propag.*, vol. 14(5), pp. 302-307, May 1966.

[8] A. Monorchio, and R. Mittra, "Time-Domain (FE/FDTD) Technique for Solving Complex Electromagnetic Problems", *IEEE Microw. and guided waves Lett.*, vol 8, no. 2, pp. 93-95, Feb. 1998.

[9] M.N.O. Sadiku, "A Simple Introduction to Finite Element Analysis of Electromagnetic Problems", *IEEE Trans. Educ.,* vol. 32, no. 2, May 1989, pp. 85–93.

[10] C. Christopoulos, "*The Transmission-Line Modeling Method in Electromagnetics*", Morgan & Claypool publishers, 2006.

[11] R.F. Harrington, "*Field Computation by Moment Method*", New York, NY: Macmillan, 1968.

[12] A. A. Oliner, "*Leaky-Wave antennas*", in Antenna Engineering Handbook, 3rd ed, R. C. Hansen, Ed. New York: McGraw-Hill, 1993, ch.10.

[13] T. Zhao, D. R. Jackson, J. T. Williams, Hung-Yu D. Yang, and A. A. Oliner, "2-D Periodic Leaky-Wave Antennas-Part I: Metal Patch Design", *IEEE Trans. Antennas and Propag.*, vol. 53, no. 11, pp.3505-3514, Nov. 2005.

[14] C. A. Balanis, "*Antenna Theory: Analysis and Design*", Second edition, New York: John Wiley & Sons Inc, 1997.

[15] C. Caloz and T. Itoh, "Array factor approach of leaky-wave antennas and application to 1D/2D composite right/left-handed (CRLH) structures", *IEEE Microwave and Wireless Comp. Lett.*, vol.14, No.6, July 2006, pp. 274-276.

[16] J. B. Pedry, A. J. Holden, D. J. Robbins, and W. J. Stewart, "Magnetism from conductors and enhanced nonlinear phenomena", *IEEE Microwave Theory and Techniques*, vol.47, No.11, November 1999, pp. 2075-2084.

[17] B. I. Popa and S. A. Cummer, "Determining the effective electromagnetic properties of negative-refractive-index metamaterials from internal fields", *Phys. Rev. B* 72, 165102, (2005).

[18] R. Marqués, F. Medina, and R. Rafii-El-Idrissi, "Role of bianisotropy in negative permeability and left-handed metamaterials", *Phys. Rev. B* 65, 144440, (2002).

[19] R. Marqués, F. Mesa, J. Martel, F. Medina, "Comparative Analysis of Edge- and Broadside Coupled Split Ring Resonators for Metamaterial Design-Theory and Experiments", *IEEE Trans. Antennas and Propag.*, vol. 51, no. 10, pp.2572-2581, Oct. 2003.

[20] A. M. Nicolson and G. F. Ross, "Measurement of the Intrinsic Properties of Materials by Time Domain Tech niques", *IEEE Transactions on Instrumentation and Measurement*, IM-19, 1970, pp. 377-382.

[21] W. B. Weir, “Automatic Measurement of Complex Dielectric Constant and Permeability at Microwave Frequencies,” *Proceedings of the IEEE*, 62, 1974, pp. 33-36.

[22] D. R. Smith, S. Schultz, P. Markoš, and C. M. Soukoulis, “Determination of Effective Permittivity and Permeability from Reflection and Transmission Coefficients”, *Phys. Rev. B* 65, 195104, (2002).

[23] R. W. Ziolkowski, “Design, Fabrication, and Testing of Double Negative Metamaterials”, *IEEE Transactions on Antennas and Propagation*, 51, 7, pp. 1516-1528, July, 2003.

[24] X. Chen, T. M. Grzegorzyk, B.-I. Wu, J. Pacheco, Jr., and J. A Kong, “Robust Method to Retrieve the Constitutive Effective Parameters of Metamaterials”, *Phys. Rev. E*, 70, 0166081, (2004).

[25] D. R. Smith, D. C. Vier, Th. Koschny, and C. M. Soukoulis, “Electromagnetic Parameter Retrieval from Inhomogeneous Metamaterials”, *Phys. Rev. E*, 71, 0366171, (2005).

[26] D. R. Smith, “Analytic expressions for the constitutive parameters of magnetoelectric metamaterials”, *Phys Rev E*, 81, 036605, (2010).

[27] S. Arslanagić, T. V. Hansen, N. A. Mortensen, A. H. Gregersen, O. Sigmund, R. W. Ziolkowski, and O. Breinbjerg, “A review of the scattering-parameter extraction method with clarification of ambiguity issues in relation to metamaterial homogenization,” *IEEE Antennas Propag. Mag*., vol. 55, no. 2, pp. 91–106, Apr. 2013.

[28] Z. H. Jiang, J. A. Bossard, X. Wang, and D. H. Werner, “Synthesizing metamaterials with angularly independent effective medium properties based on an anisotropic parameter retrieval technique coupled with a genetic algorithm”, *J. Appl. Phys*., 109, 013515, (2011).

CHAPTER 3

MULTI-LAYER PERIODIC SURFACES FOR BROADBAND HIGH-GAIN ANTENNAS

Fabry-Perot cavity (FPC) antennas are characterized by inherently narrow operational bandwidth as already discussed in Chapter 1. A technique for enhancing the bandwidth of FPC antennas has been recently proposed [1]. An optimized double layer PRS FPC antenna has been presented which achieves a significant bandwidth enhancement compared to a single layer PRS FPC antenna.

In this chapter, high-gain broadband Fabry-Perot type antenna designs are proposed, based on multi-layer periodic Partially Reflective Surfaces (PRSs), extending the previously reported work and significantly enhancing the FPC antenna directivity-bandwidth performance. A double-layer and a three-layer PRS antenna are investigated. Initially, the double layer antenna is studied, consisting of two PRS layers placed in front of a ground plane. Then, three layers of PRSs are employed, consisting of metallic patches printed on thin dielectric substrates and placed in front of a ground plane, forming three open cavities. The antenna performance is based on the reflection characteristics of the PRS array, which are obtained using periodic analysis. We present for the first time the design and implementation of a three-layer PRS for enhancement of the directivity – bandwidth (BW) product of FPC antennas and thereby generalize the concept of broadband FPC antennas with multiple PRS layers. An equivalent circuit approach is also presented for the design of the multi-layer PRSs showing very good agreement with full-wave analysis. The geometry has been optimized using full wave simulations (CST Microwave Studio^{TM}). A prototype has been fabricated and

tested, validating the simulation results. Furthermore, a dual-slot feeding technique is proposed for broadband multi-layer periodic Fabry-Perot cavity antennas achieving enhanced directivity as well as broadband radiation and matching performance. In order to demonstrate the feeding technique, two FPC antennas are presented formed by two- and three-layer periodic Partially Reflective Surfaces (PRSs) respectively placed in front of a ground plane. Measurements of a fabricated three-layer PRS antenna prototype are presented validating the simulation results.

3.1 UNIT CELL ANALYSIS FOR MULTI-LAYER PRS

3.1.1 Double-Layer PRS

Initially, a double-layer PRS is designed which is then employed in front of a ground plane in the double-layer antenna described in 3.2.1. Two periodic PRS layers are used, printed on a 1.6mm thick dielectric substrate with relative permittivity of 2.55 and tangent loss of 0.0019. The unit cell structure is shown in Fig. 3.1.1. Metallic square elements have been chosen for the proposed design. In Fig. 3.1.1 (a) the dimensions of each layer are depicted with the periodicity P=11mm and the dimensions of the elements d_1=10mm and d_2=6mm. The cross section of the unit cell is shown in Fig. 3.1.1 (b), where the distance between the two PRS layers is h_2=11mm. These dimensions have been chosen, so that a positive gradient in the reflection phase response would be obtained, since as explained in Chapter 2.1, a positive gradient in the phase of the reflection coefficient with frequency is required to achieve high gain for a broad frequency range. Periodic boundary conditions have been employed in CST Microwave Studio^{TM} in order extract the reflection coefficients and to optimize the dimensions following this design procedure which was first reported in [1].

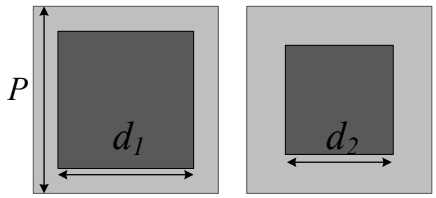

(a)

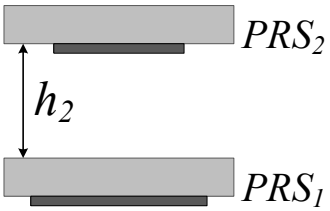

(b)

Fig. 3.1.1 (a) Unit cell dimensions of the two-layer PRS, (b) Cross section of the double-layer PRS.

In Fig. 3.1.2, the complex reflection coefficients are presented with the optimum phase derived from (2.1-10) also included considering a distance h_1=11.3mm from the ground plane. It can be observed that, a minimum occurs in the reflection magnitude at 13.7GHz. This implies that at the resonant frequency the transmission is slightly increased. It is expected from (2.1-9), that the observed high reflection magnitude values will result in a high directivity antenna, implemented using the proposed double-layer PRS. Moreover, a phase increase is obtained in the reflection phase between 13.3GHz to 14.1GHz. Finally, the two phase curves intersect at 13.8GHz which indicates high directivity values around this frequency.

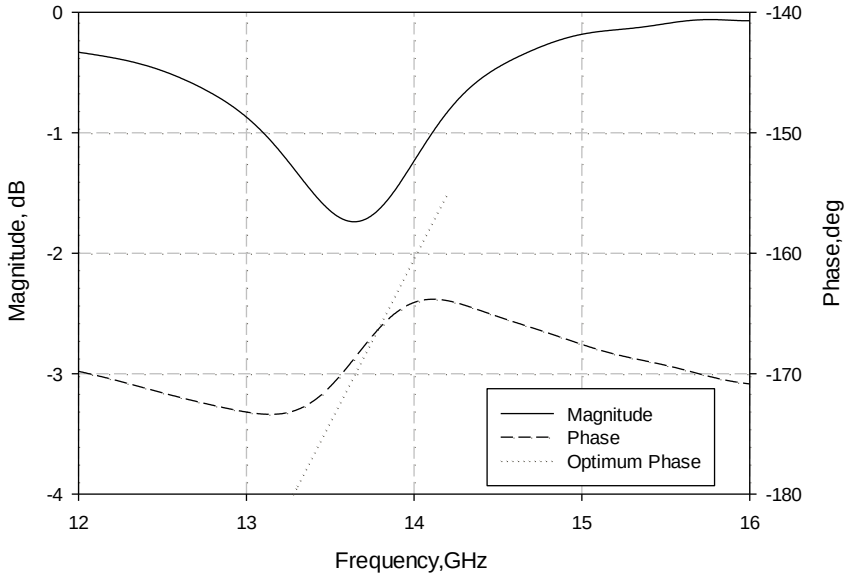

Fig. 3.1.2 Complex Reflection Coefficients of the two-layer PRS with h_2=11mm, d_1=10mm, d_2=6mm.

3.1.2 Three-Layer PRS

In this section a parametric study and optimization of a three layer PRS is carried out with the aim of achieving a reflection phase response increasing with frequency in a wider frequency band compared with the two-layer PRS design. Each layer consists of a metallic square patch PRS array printed on a 1.6mm thick dielectric substrate with permittivity ε_r=2.55 and tangent loss of 0.0019. As mentioned in Chapter 2.1, a positive gradient in the phase of the reflection coefficient with frequency is required to achieve high gain for a broad frequency range. The values of the parameters for the desired behavior in the phase of the reflection coefficient i.e. approaching the optimum phase derived from equation (2.1-10) were found after a parametric optimization procedure. Nevertheless, for the derivation of the optimum phase the distance h_1 between the ground and the first layer is needed, and was selected to be h_1=10.7mm. The unit cell of the three-layer PRS is presented in Fig. 3.1.3, with the top view of each layer shown in Fig. 3.1.3 (a) and a cross section in Fig. 3.1.3 (b). The unit cell dimensions, as shown in the

figure and starting from the layer closer to the ground plane, are d_1=9.16mm, d_2=10mm and d_3=6mm. The periodicity for all three layers is P=11mm. Finally the cavity distances are h_2=9.5mm and h_3=10mm.

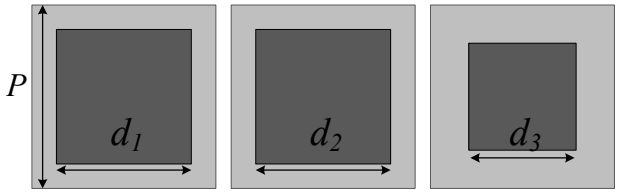

(a)

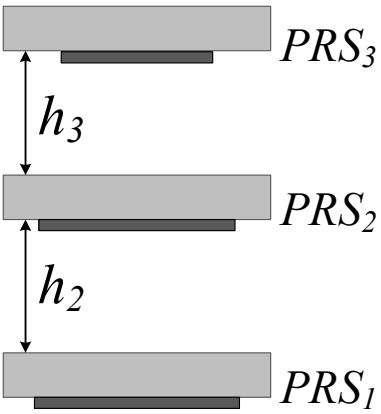

(b)

Fig. 3.1.3 (a) Unit cell dimensions of the three-layer PRS, (b) Cross section of the three-layer PRS.

Two resonances are obtained from the three-layer PRS due to the two formed air cavities. At each resonant frequency the magnitude of the reflection coefficient has a minimum and the phase is increasing for a frequency range around the resonance. To achieve a broadband phase increase, the two resonances have to be brought close together but not overlap.

In Fig. 3.1.4 and Fig. 3.1.5 the complex reflection coefficients are presented for three different

values of each of the structure's parameters and the optimum phase is also included. The optimized case for the selected values is shown as a reference in all the graphs (solid line). In the optimized case, two minimums occur in the reflection magnitude at 14.4GHz and 14.9GHz. An increase in the positive gradient range of the phase is obtained, extending between 14.1GHz to 15.1GHz. This is a significant improvement over the optimized two-layer PRS case (see Fig. 3.1.2). Again, the positive gradient phase response leads to high antenna directivity in this frequency range according to the ray analysis, if the proposed PRSs are employed in the design of an FPC antenna. It is expected that at the frequencies where the optimized phase value is equal to that of the optimum phase, maximum directivity will be achieved since the cavity resonance condition, (2.1-10), is satisfied.

In Fig. 3.1.4 (a, b) the effect of the two cavity heights on the reflection coefficients is shown. It can be observed that the first cavity (the cavity formed between the first and the second PRS layers) has a stronger effect than the second. Varying h_2 by half millimeter below and above the selected value (h_2 =9.5mm) only one resonance occurs with a significant shift at higher or lower frequency respectively from the center frequency which is 14.6GHz. The same behavior is obtained with variation of h_3 but with a smaller frequency shift. In Fig. 3.1.5 (a, b and c) the effect of the PRS size of each layer is studied. Variation in the size is much less significant than in the height of the cavities. As d_1 increases, although two resonances take place, the resonance at the lower frequency becomes dominant. For the selected value d_1=9.16mm, the two resonances have the same strength and the phase is closer to the optimum. For d_2, it is observed that for smaller values the two resonances move apart, while for larger values they overlap. Finally, when d_3 is increased the resonance at the higher frequency becomes stronger. For d_3=5.5mm the two resonances overlap again.

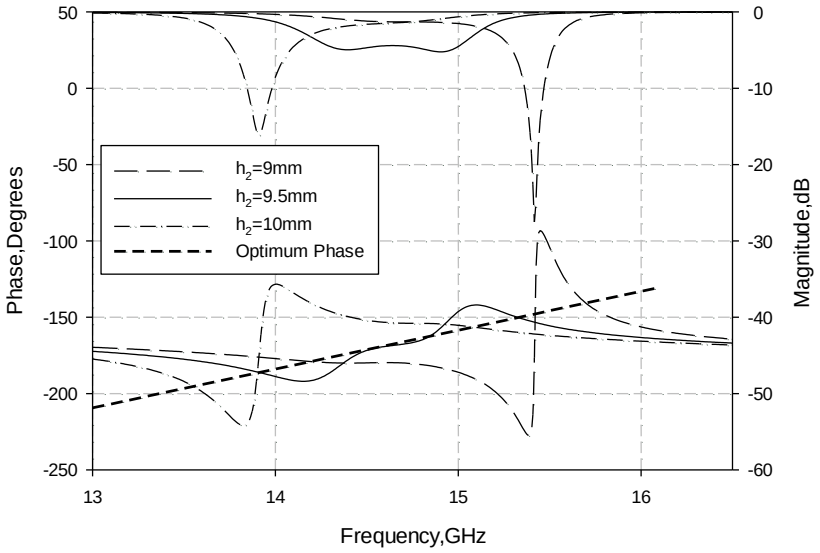

(a)

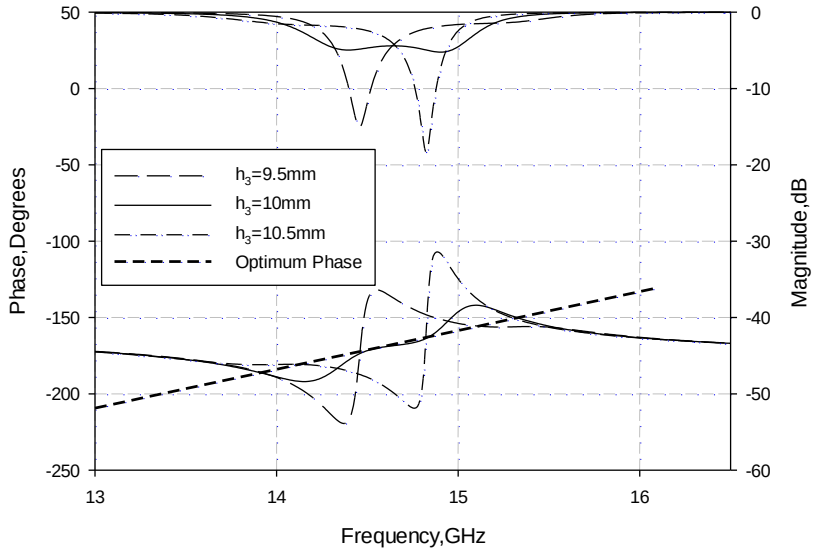

(b)

Fig. 3.1.4 Complex Reflection Coefficients of the three-layer PRS changing (a) the cavity distance h_2 (h_3=10mm, d_1=9.16mm, d_2=10mm, d_3=6mm), (b) the cavity distance h_3 (h_2=9.5mm, d_1=9.16mm, d_2=10mm, d_3=6mm).

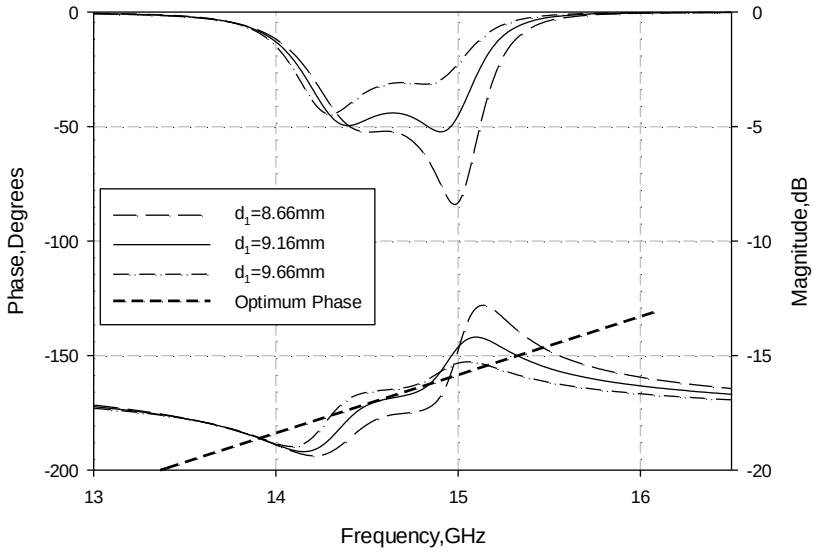
0
-50
-100
-150
-200
13
14
15
16
Phase,Degrees
Magnitude,dB
0
-5
-10
-15
-20
Frequency,GHz
d1=8.66mm
d1=9.16mm
d1=9.66mm
Optimum Phase

(a)

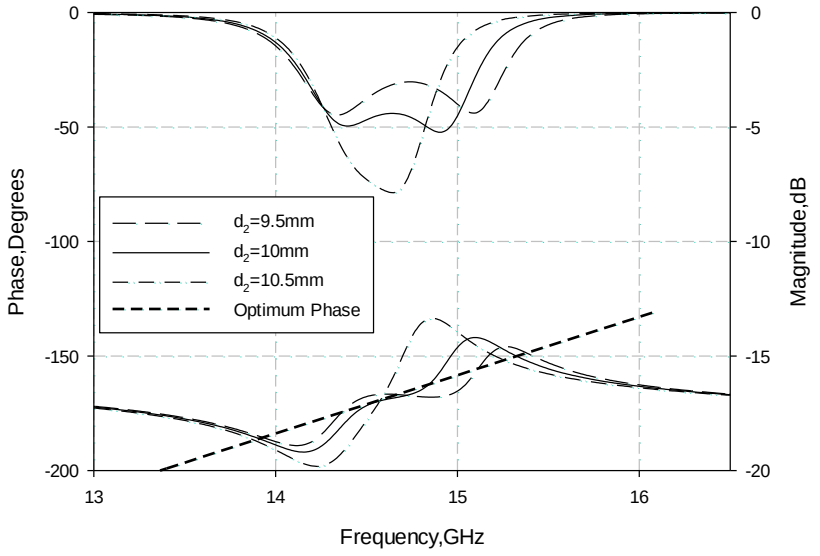
0
-50
-100
-150
-200
13
14
15
16
Phase,Degrees
Magnitude,dB
0
-5
-10
-15
-20
Frequency,GHz
d2=9.5mm
d2=10mm
d2=10.5mm
Optimum Phase

(b)

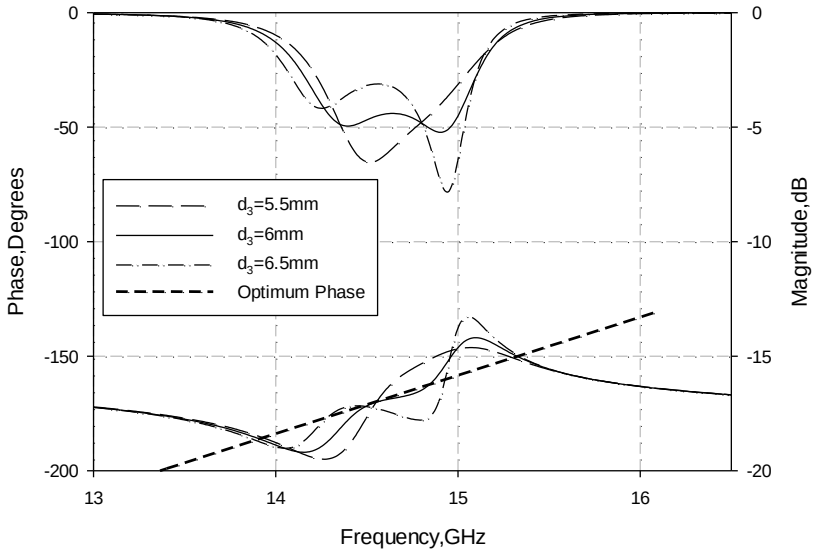

(c)

Fig. 3.1.5 Complex Reflection Coefficients of the three-layer PRS changing (a) the first layer patch dimensions d_1 (h_2=9.5mm, h_3=10mm, d_2=10mm, d_3=6mm), (b) the second layer patch dimensions d_2 (h_2=9.5mm, h_3=10mm, d_1=9.16mm, d_3=6mm) and (c) the third layer patch dimensions d_3 (h_2=9.5mm, h_3=10mm, d_1=9.16mm, d_2=10mm).

3.1.3 Equivalent Circuit Model

Multi-layer PRS arrays are studied in this section using an equivalent circuit approach which allows for a fast optimization of the design. In order to demonstrate the equivalent circuit approach and its accuracy in modelling the proposed multi-layer PRSs working examples of a single-layer, a two-layer and a three-layer PRS are employed. The three-layer design is based on the optimised design that was presented in section 3.1.2.

The unit cell of a periodic metallic patch array printed on a dielectric substrate can be modeled with the equivalent circuit shown in Fig. 3.1.6 (a) [2, 3]. In order to model the metallic patches as equivalent electrical parameters, the electric and magnetic fields should be considered. Strong electric field is generated on the surface of the metallic patches due to

electromagnetic excitation. The established electric field between two adjacent elements causes a capacitive behavior and is modeled with a shunt capacitor C_i. The inductor in series L_i represents the current flowing through the patches. The dielectric substrate can be modeled as a transmission line with the length of the line t_i being equal to the substrate's thickness and the characteristic impedance is calculated from $Z_i = Z_0 / \sqrt{\varepsilon_r}$, where Z_0=377 Ω is the free space impedance and ε_r is the dielectric constant of the material. The two terminals represent the free space on both sides of the PRS and have characteristic impedance equal to Z_0.

An initial calculation of the electrical parameters C_i and L_i from the physical dimensions of the unit cell can be realized using equations (3.1-1) and (3.1-2) [3, 4] where P is the periodicity, $s=P-d$ is the separation between two adjacent patches, d is the width of the patch and $\varepsilon_{eff} = \varepsilon_r$.

$$C = \varepsilon_0 \varepsilon_{eff} \frac{2P}{\pi} \ln\left(\frac{1}{\sin\left(\frac{\pi s}{P} \right)} \right) \tag{3.1-1}$$

$$L = \mu_0 \frac{P}{2\pi} \ln\left(\frac{1}{\sin\left(\frac{\pi d}{2P} \right)} \right) \tag{3.1-2}$$

For multiple layer structures, the equivalent circuit of each layer is cascaded, adding a transmission line to model the air cavity between the layers. The length of the line is equal to the cavity distance and the impedance is that of the free space. In Fig. 3.1.6 (b) the three-layer equivalent circuit is presented.

To validate the model the complex reflection coefficients have been obtained for single, double and three-layer PRS using both circuit analysis software (AWR Microwave Office)

and full-wave simulations (CST Microwave Studio^{TM}). In CST, periodic boundary conditions are applied to the unit cell of the structure, which assume an infinite extend of the surface, and reduce the calculations of the complete structure into a single unit cell. Simulations have been carried out for six different values of the physical dimension of the patch (d) for a single PRS. Different combinations were then investigated for double and three-layer PRSs. The periodicity and the material properties are the ones used in section 3.1. In Fig. 3.1.7 one case for a single, a double and a three-layer PRS is shown for brevity.

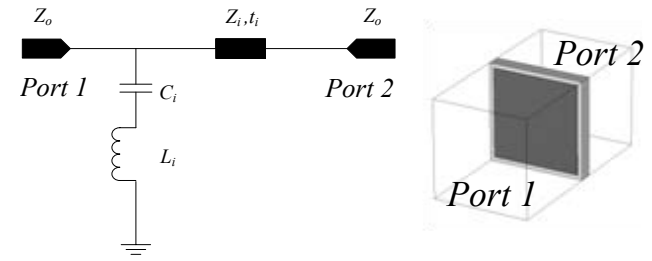

(a)

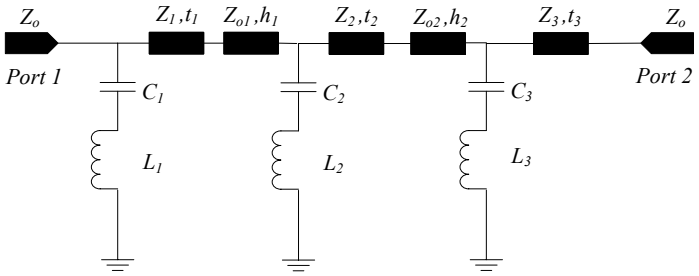

(b)

Fig. 3.1.6 Equivalent circuit for (a) single-layer PRS, (b) three-layer PRS.

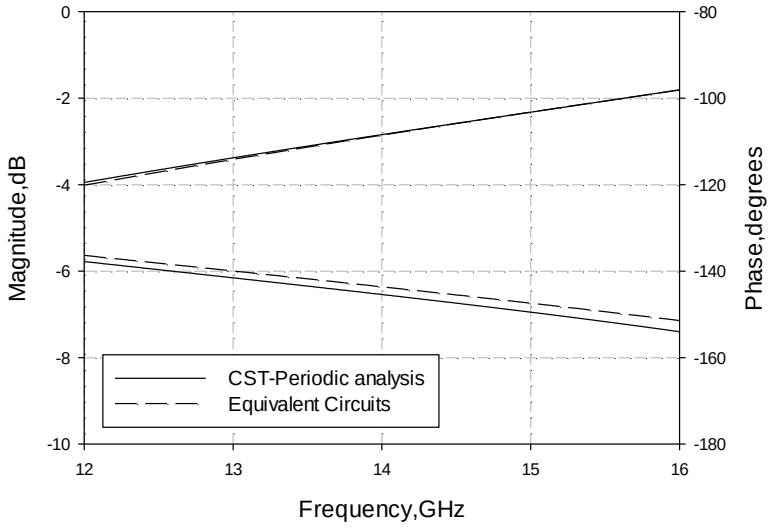
0
-2
-4
-6
-8
-10
-80
-100
-120
-140
-160
-180
12
13
14
15
16
Magnitude,dB
Phase,degrees
Frequency,GHz
CST-Periodic analysis
Equivalent Circuits

(a)

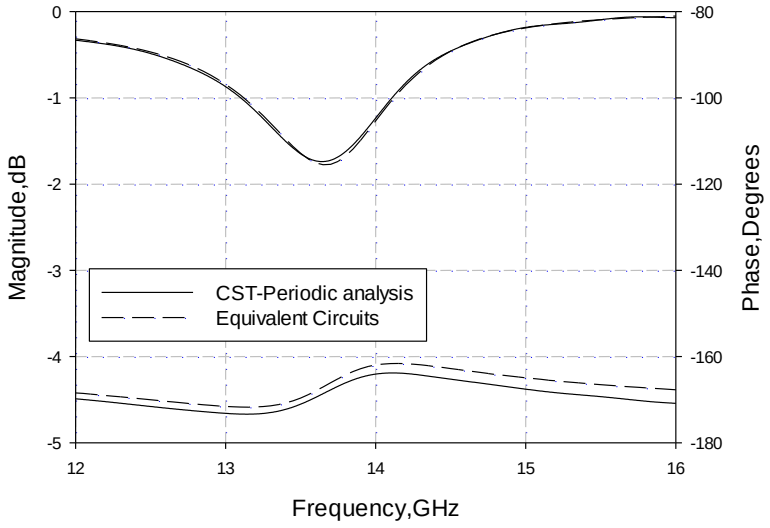
0
-1
-2
-3
-4
-5
-80
-100
-120
-140
-160
-180
12
13
14
15
16
Magnitude,dB
Phase,Degrees
Frequency,GHz
CST-Periodic analysis
Equivalent Circuits

(b)

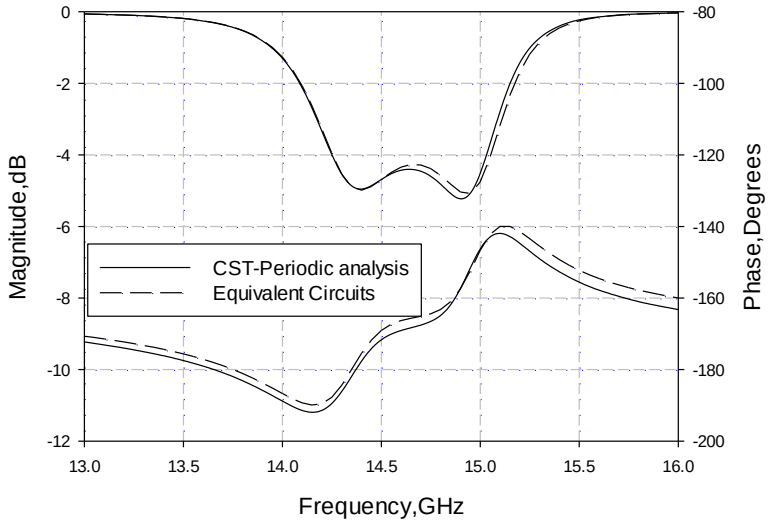

(c)

Fig. 3.1.7 Complex Reflection Coefficients for (a) single-layer PRS for d=6mm, (b) double-layer PRS for d_1=10mm, d_2=6mm and h_2=11mm, (c) three-layer PRS for the proposed design dimensions, obtained from the equivalent circuit model and periodic full-wave analysis.

TABLE I

PHYSICAL AND ELECTRICAL PARAMETERS

FOR SINGLE-LAYER PRS

d (mm)	C (pF)	L (nH)
10	0.2101	0.088
9.16	0.1301	0.27
9	0.1251	0.263
8	0.0751	0.66
7	0.0481	1.14
6	0.0292	1.959

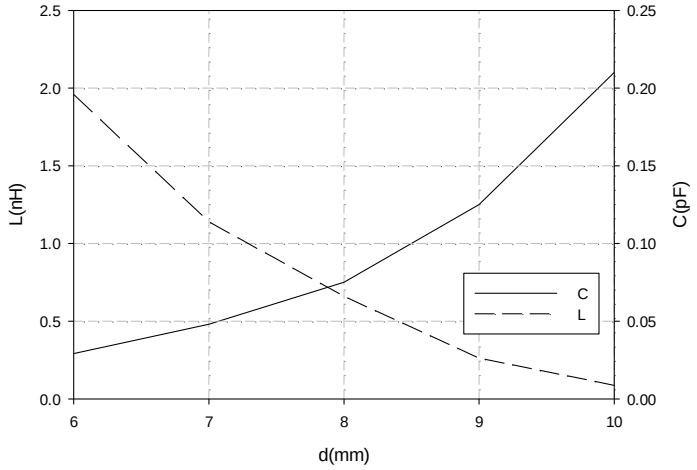

Fig. 3.1.8 Variation of equivalent capacitance and inductance with the physical dimensions of the single-layer PRS.

Good agreement has been achieved after fine tuning of the values obtained from equations (3.1-1) and (3.1-2) of the electrical parameters (Fig. 3.1.7). The values used for *C* and *L* are presented in Table I. The good agreement can be attributed to the fact that the separation between the layers in the proposed design is in the order of half wavelength, hence the effects of the higher order evanescent Floquet harmonics are minimal.

In Fig. 3.1.8 the variation of the equivalent capacitance and inductance as the patch dimensions increase is depicted. It is evident that increasing the patch size, leads to increased capacitance and reduced inductance. This behavior can be justified taking into account that as the patch increases the separation between the adjacent elements decreases causing an increase of the electric coupling. On the other hand, decreasing the patch dimension, the induced currents become stronger leading to larger inductance values.

3.2 ANTENNA DESIGN

3.2.1 Double-Layer PRS Antenna

Based on the optimized PRS designs, a double-layer finite size FPC antenna is initially produced. The structure has been formed using the double-layer PRS placed in front of a metallic ground plane (Fig. 3.2.1). A waveguide – fed slot inside the ground plane is used as a single feeder of the antenna. The dimensions of the slot are 10x2.5mm^2, which have been selected so that a good matching in the frequency range of interest is achieved. The overall lateral dimensions of the antenna are 80x80mm^2, which corresponds to about 4λ at 14.5GHz. A total of 5x5 array elements are printed on each dielectric layer. The distance between the ground and the first PRS layer is h_1=11.3mm while the rest of the parameters are h_2=11mm, d_1=10mm and d_2=6mm, as described in section 3.1.1.

The antenna's simulated directivity is depicted in Fig. 3.2.2 (solid line), showing a maximum of 19.9dBi at 14.4GHz. The 3dB directivity bandwidth is calculated at approximately 10.6%. Two peaks are observed the directivity of the antenna corresponding to the two resonant cavities. These two peaks provide the broadband directivity behavior, which is expected since the reflection phase response of the PRSs is close to the optimum phase in this frequency range, i.e. the resonant condition is satisfied (see Fig. 3.1.2). Moreover, the gain and S_{11} are presented in Fig. 3.2.2, showing good matching of the antenna and very small discrepancies between the directivity and the gain.

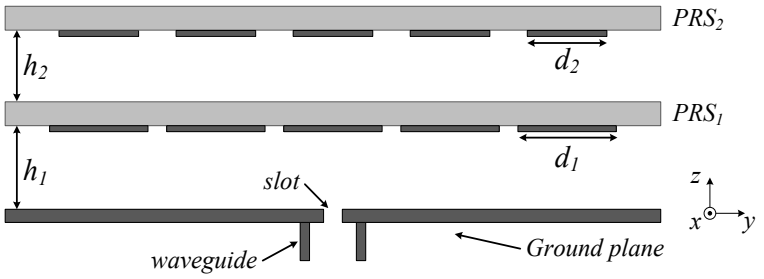

Fig. 3.2.1 Schematic diagram of the double-layer PRS antenna.

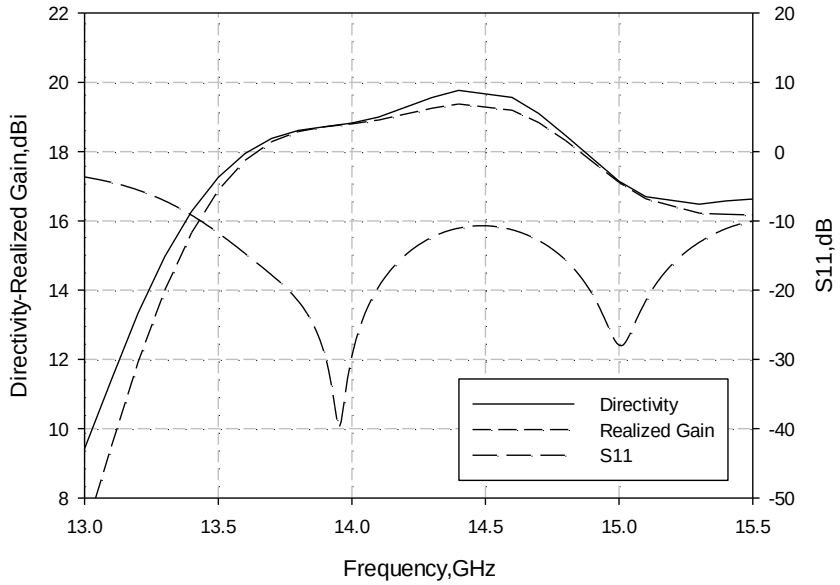

Fig. 3.2.2 Simulated directivity, realized gain and S_{11} of the two-layer PRS antenna.

3.2.2 Three-Layer PRS Antenna

In this section a realistic three-layer PRS finite size antenna structure is simulated based on the optimized designs obtained in section 3.1.2. Furthermore, a comparison with the optimized two-layer antenna described in the previous section is presented in order to validate the improvement in the directivity-bandwidth product by virtue of the proposed three-layer design.

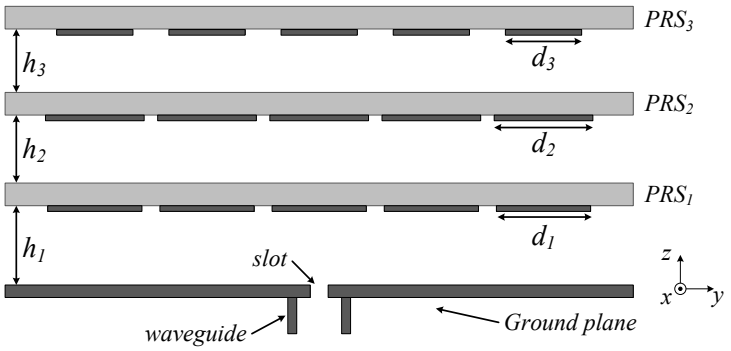

Fig. 3.2.3 Schematic diagram of the three-layer PRS antenna.

The structure is formed using the optimized three-layer PRS placed in front of a metallic ground plane (Fig. 3.2.3). Again, a waveguide – fed slot inside the ground plane is used for the feeding of the antenna with the same dimensions that have been used for the double-layer antenna. Also, in order to have a fair comparison between the two designs, the overall lateral dimensions of the antenna are the same, with 5x5 array elements printed on each dielectric layer. For this finite size structure, the distance h_1 was changed to 11.3mm instead of 10.7mm which was used for an infinite size antenna. The rest of the parameters are h_2=9.5mm, h_3=10mm, d_1=9.16mm, d_2=10mm and d_3=6mm, as described in section 3.1.2.

The antenna's simulated directivity is shown in Fig. 3.2.4. A maximum directivity of around 21dBi is observed at 13.7GHz and it is kept over 18dBi for frequencies between 13.5GHz to 15.7GHz. The 3dB directivity bandwidth is calculated at approximately 15%. It is interesting to note that three peaks appear in the directivity of the antenna at three closely spaced frequencies corresponding to a third order cavity resonance response, which in turn is attributed to the three formed cavities. Moreover, these three peaks coincide with the frequencies where the resonant condition is satisfied, i.e. where the reflection phase of the PRSs crosses the optimum phase line (see Fig. 3.1.4). The directivity of the optimized two-layer antenna is also shown in Fig. 3.2.4. It is evident that the three-layer antenna outperforms

the two-layer one. In Table II a more detailed comparison between the two antennas, a single-layer antenna with similar maximum directivity value and resonant frequency, as well as the waveguide slot source is presented.

In Fig. 3.2.5, two other cases are compared with the optimized one, corresponding to different h_2=9mm and h_3=9.5mm. It can be observed that, after changing the first cavity distance, a deep drop occurs at 15.6GHz that deteriorates the antenna performance by significantly reducing the operating bandwidth. This behaviour is justified from the corresponding reflection coefficient in Fig. 3.1.4 (a). A similar effect is observed after reducing h_3 where the average directivity drops over the operating bandwidth compared with the optimized case, with a minimum of around 17dBi at 15GHz and the antenna bandwidth is thus significantly reduced. It should be noted that the radiation patterns in both of the above cases are also distorted at out-of-band frequencies (approximately over 15 GHz).

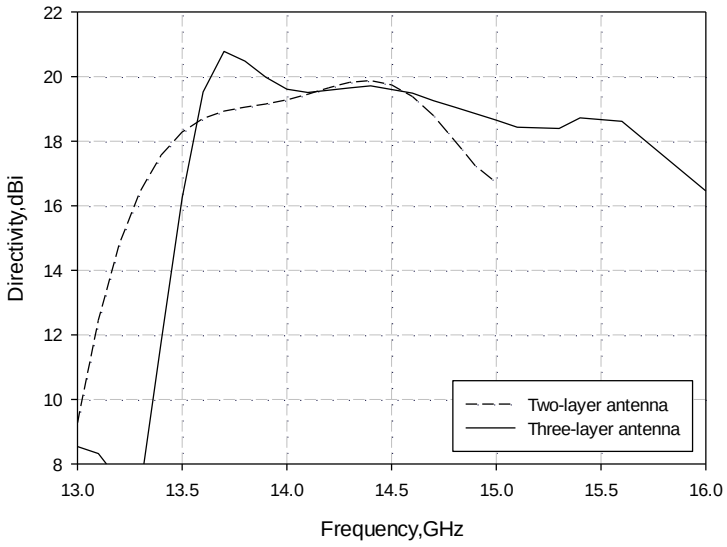

Fig. 3.2.4 Directivity comparison between three-layer and two-layer antenna.

TABLE II

COMPARISON BETWEEN DOUBLE LAYER AND THREE LAYER ANTENNA

Antenna Design	Maximum Directivity (dBi)	-3dB Radiation Bandwidth (%)	Directivity - Bandwidth Product
Waveguide slot	5.8	N/A	N/A
Single-layer	18.6	5.89	427
Double layer	19.88	10.6	1031
Three layer	20.8	15.1	1815

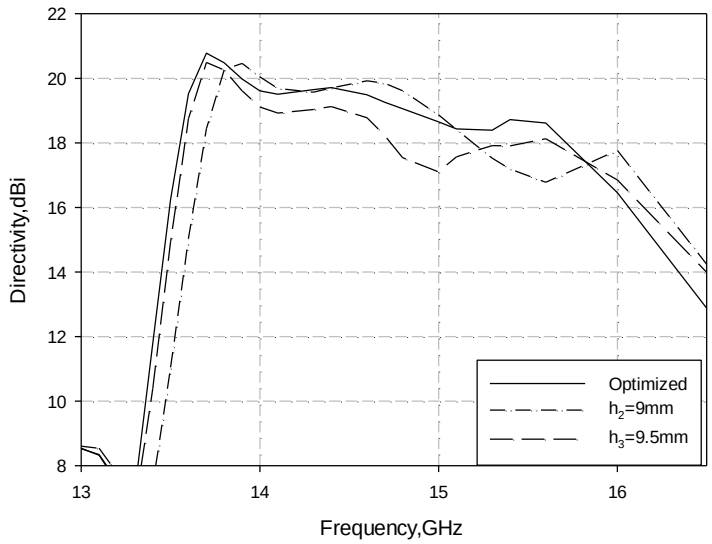

Fig. 3.2.5 Simulated directivity versus frequency for different cavity distances h_2 and h_3.

Two shapes have been investigated for the feeding slot (Fig. 3.2.6), in order to achieve good matching, namely a simple rectangular slot with the dimensions mentioned in the beginning of this section (slot A) and a bow tie one (slot B). The simulated S_{11} and gain for both cases are shown in Fig. 3.2.7. It can be observed that slot B gives a slightly improved S_{11} and gain

respectively. The antenna exhibits broadband performance with a maximum gain of 20dBi and bandwidth of 15%. There is a slight deterioration of the S_{11} assuming a maximum value of -8.5dB at approximately 13.7GHz. However this only reduces the gain at that frequency by less than 1dB (compared to the directivity).

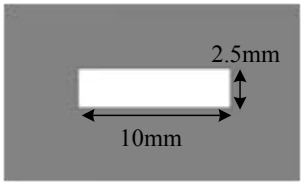

(a)

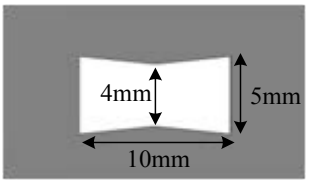

(b)

Fig. 3.2.6 Schematic diagram of the two slot designs: (a) Slot A and (b) Slot B.

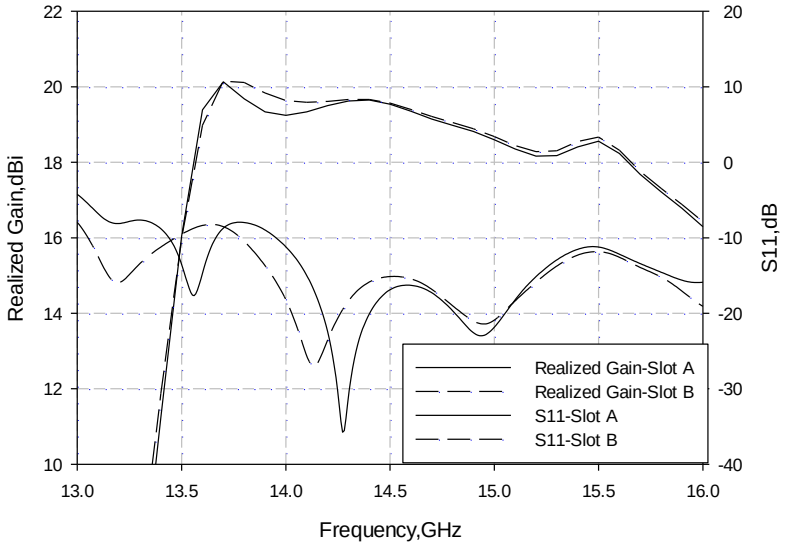

Fig. 3.2.7 Simulated S_{11} and gain for the two slot designs.

3.2.3 Practical Implementation and Measurements

Because of fabrication limitations, slot A has been selected for the final prototype. A prototype of the proposed antenna has been fabricated and measured in a full anechoic chamber (Fig. 3.2.8). Plastic screws and spacers were used for the mounting of the antenna. Due to fabrication inaccuracies the dimensions of the slot in the ground plane were 10.7x2.5mm^2 (instead of 10x2.5mm^2).

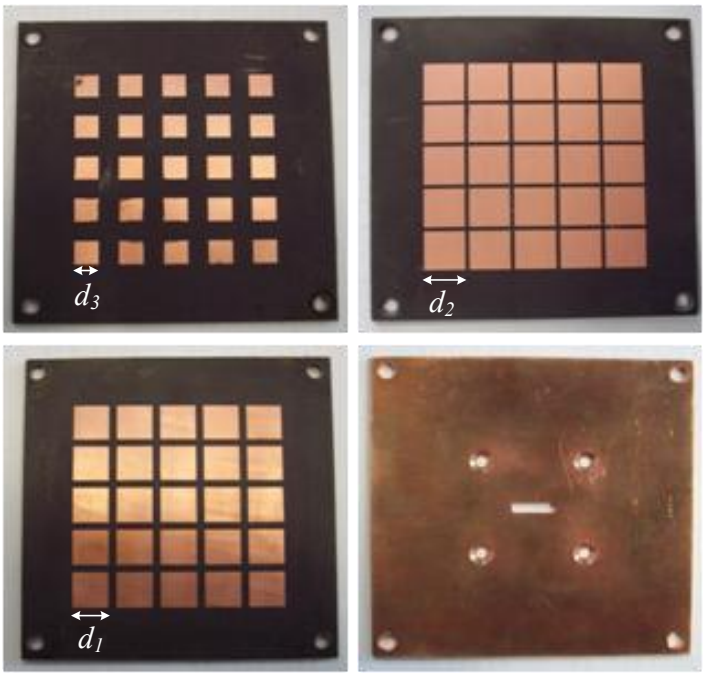

(a)

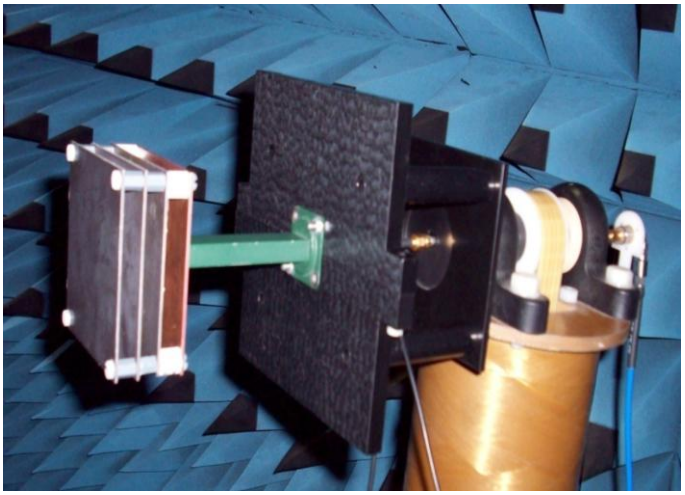

(b)

Fig. 3.2.8 Photograph of (a) three PRS layers and ground plane, (b) complete antenna.

The simulated and measured return loss of the antenna with the new slot dimensions is presented in Fig. 3.2.9. A minimum occurs at 13.95GHz, with satisfactory matching within the 3dB radiation bandwidth. At the edges of the band the measured matching deteriorates slightly due to the narrowband operation of the feeding slot. Fig. 3.2.10 shows the simulated and measured gain versus frequency. A good agreement is obtained with a maximum measured value of 19.5dBi at 13.7GHz. The small discrepancy between simulation and measurement is attributed to fabrication tolerances. Moreover the well known gain transfer method was employed in order to measure the prototype antenna's gain which implies a ±0.5dB error introduced by the gain of the reference broadband horn antenna used. The gain values are approximately 1dB lower than the directivity values due to the imperfect matching and material losses.

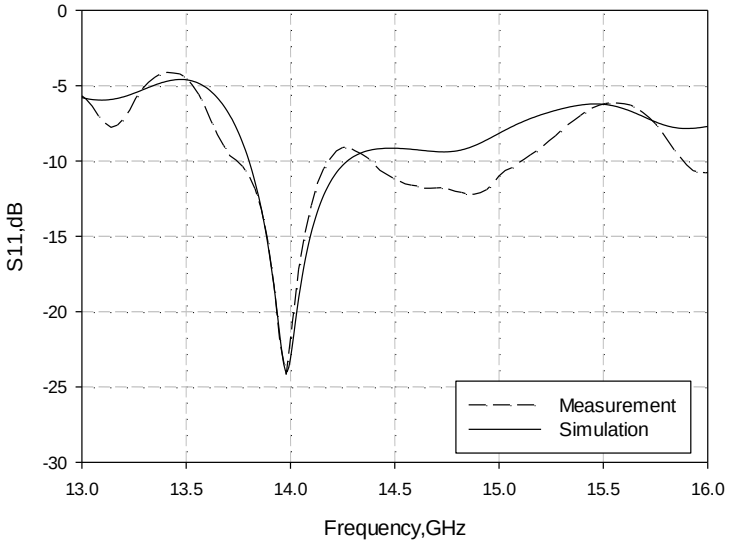

Fig. 3.2.9 Simulated and measured return loss for slot dimensions 10.7x2.5mm^2.

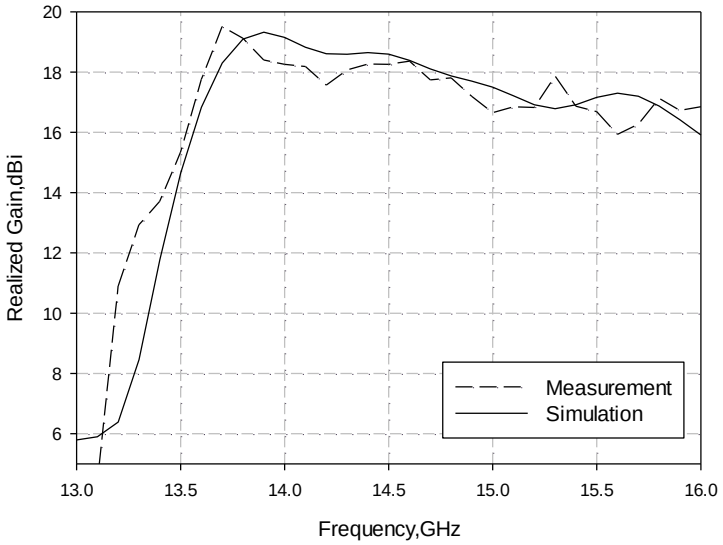

Fig. 3.2.10 Simulated and measured realized gain for the final antenna.

The H- and E-plane patterns were measured in five different frequencies within the operating band. Simulated and measured results are presented in Fig. 3.2.11. In all frequencies the sidelobe level is below -10dB. There are some discrepancies between simulation and measurement especially at around 60^o. It was found that these are caused by the large plastic

supporting base of the waveguide that can be seen in the photo of Fig. 3.2.8 (b). The results presented here were obtained after a thin layer of absorbers were placed around the support behind the antenna which improved the sidelobe level at these angles by at least 3dBs compared to the patterns obtained without absorbers.

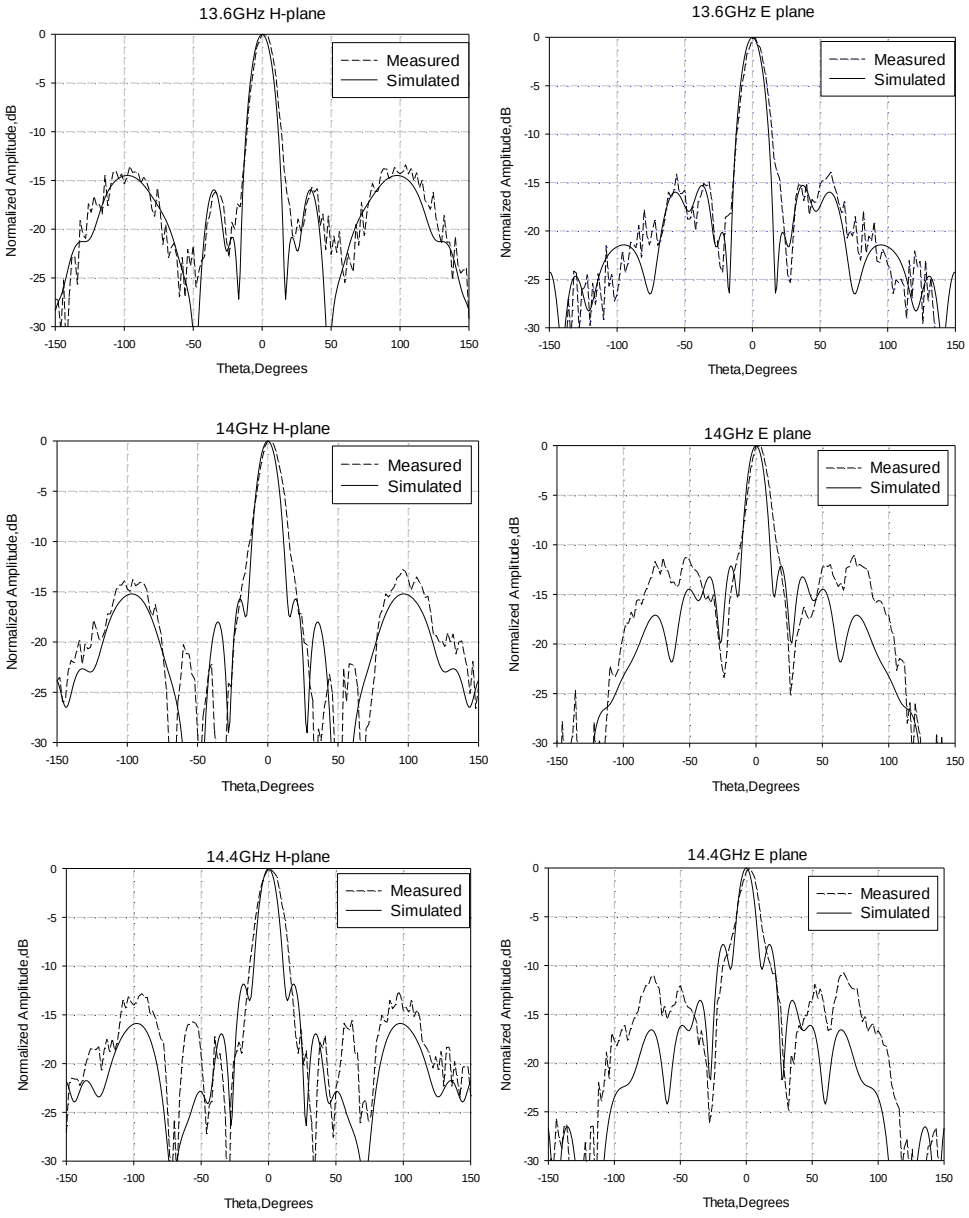

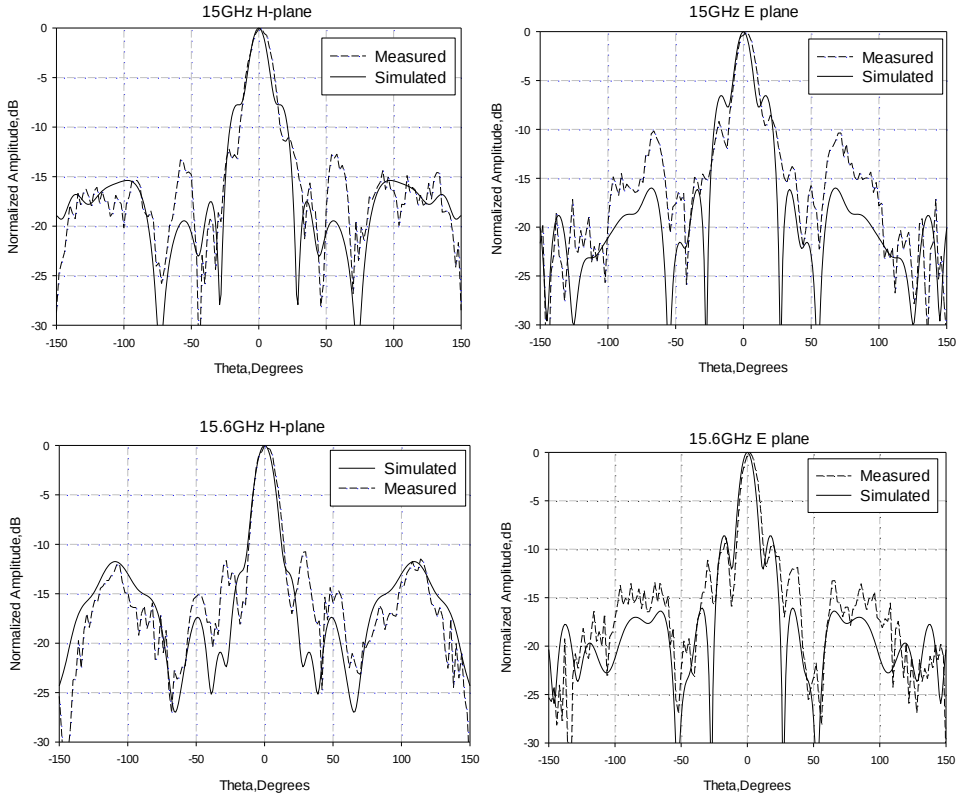

(a) (b)

Fig. 3.2.11 Simulated and measured patterns for the (a) H-plane and (b) E-plane in five frequencies over the operational bandwidth of the antenna.

3.3 DUAL-SLOT FEEDING TECHNIQUE FOR BROADBAND FABRY-PEROT CAVITY ANTENNAS

In this section, we present a new dual-slot dual-resonant feeding technique for the double- and three-layer-PRS broadband FP antennas, achieving a broadband matching performance as well as increased directivity and gain. It must be emphasized that the proposed optimized feeding slots are of different length and they exhibit two significant enhancements in the antenna performance, namely broadband input matching and increase of the directivity. Moreover, as they are excited by a microstrip line, they are based on printed layer fabrication process and thus they are directly scalable to higher frequencies. Full wave periodic

simulations are initially carried out using CST Microwave Studio™ in order to optimize the antenna design. Measurement results of a fabricated prototype are also presented.

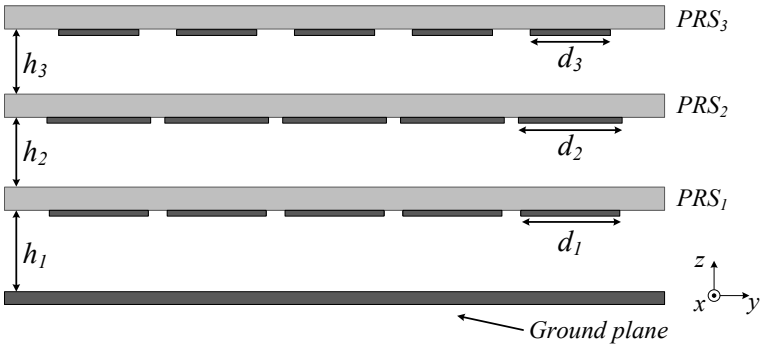

(a)

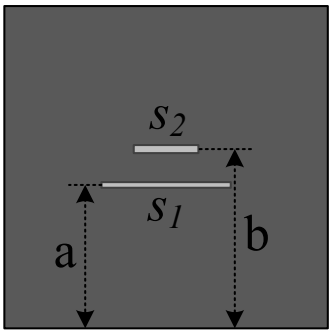

(b)

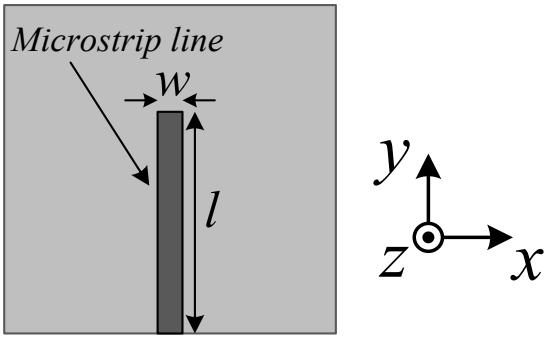

(c)

Fig. 3.3.1 Schematic diagram of the proposed antenna, (a) Cross section of the structure, (b) Front view of ground plane with slots of length s_{xi} and width s_{yi} and (c) Back view of the ground plane (microstrip line).

3.3.1 Design of the Feeding Structure

The design of the proposed dual-slot feeding structure that is used in later sections in broadband FP antennas is presented in this section. As already mentioned, we have chosen a microstrip fed slot antenna design which is easily scalable to higher frequencies. A microstrip line is printed on a 1.6mm thick dielectric substrate with an electric permittivity ε_r=2.2 and a tangent loss tanδ=0.009 (Fig. 3.3.1c). The ground plane is printed on the other side of the substrate and the feeding slot/s are etched off it. This structure is based on chemical etching printed circuit board fabrication process. In order to evaluate the operation frequency and bandwidth of the proposed feeding structure, the latter has been simulated. Initially an approximately half wavelength rectangular slot was etched on the ground plane located in the centre of the plane, above the microstrip line. The dimensions of the slot were selected such that a resonance would occur within the frequency range of interest and are presented in Table III. In the same table the dimensions of the microstrip line are also included. The S_{11} response for the single slot feeding is shown in Fig. 3.3.2. It can be observed that the S_{11} is below -10dB from 13.8GHz to 15.2GHz corresponding to a fractional bandwidth of 10%, with a minimum occurring at 14.5GHz which is the central frequency of the multi-layer antenna.

Subsequently, a second slot of different dimensions has been added as shown in Fig. 3.3.1 (b), introducing extra coupling which in turn is expected to cause a more broadband response. The dimensions (length s_{xi} and width s_{yi}) and the distance between the slots are shown again in Table III. The S_{11} response for the dual slot feeding is also shown in Fig. 3.3.2. It is evident that indeed a more broadband (tripled) matching is achieved with the S_{11} being below -10dB from 12.8GHz to 17GHz corresponding to about 30% fractional bandwidth. Two minima occur in this case, at 13GHz and 15.5GHz related to the dual resonance of the structure. It must be noted that the optimisation that led to the design presented here was also carried out

in the presence of the entire FP antennas in order to ensure a successful operation of the final antenna prototypes.

TABLE III

PARAMETER VALUES (MM) FOR FEEDING STRUCTURE

Parameter (single slot)	a		w	l	s_x		s_y	
Value	40		4.8	50.5	14.8		1	
Parameter (dual slot)	a	b	w	l	s_{x1}	s_{x2}	s_{y1}	s_{y2}
Value	37.6	42.5	4.8	50.5	18.5	8.2	1	1.5

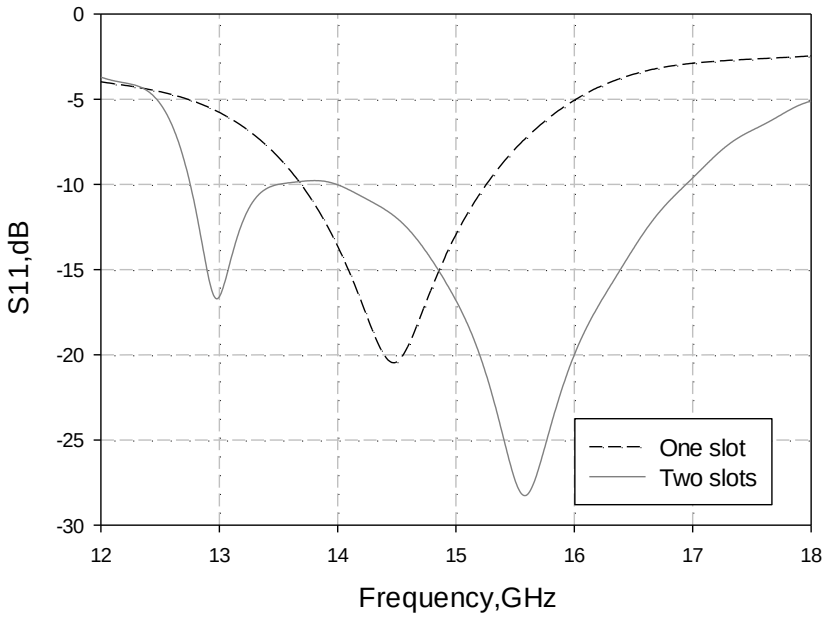

Fig. 3.3.2 Comparison of the S_{11} between one and two microstrip fed slots as primary source.

In order to further evaluate the advantages of the dual-slot feeding structure, an inspection of the near-field distribution is carried out. In Fig. 3.3.3, a cross section of the electric field for the single slot and the dual-slot is presented at 14GHz. It is evident that in the case of the two coupled slots a more uniform near field distribution is obtained than in the case of the single

slot. This effect is particularly advantageous in the case of the FP antennas studied in section 3.3.2, as it contributes to a significant enhancement of the overall antenna directivity.

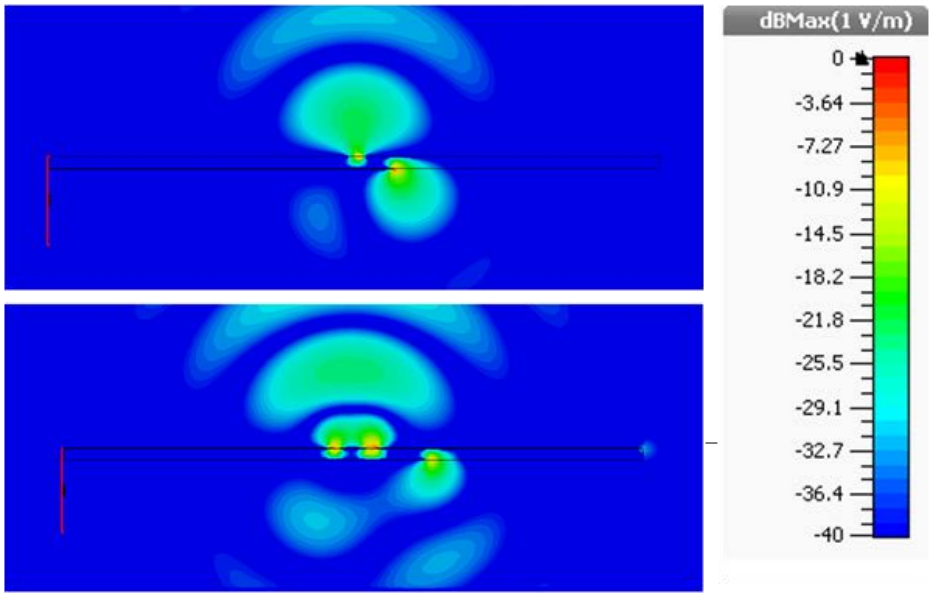

Fig. 3.3.3 Cross section of the electric field distribution (YZ plane) for the ground plane with one (top) and two (bottom) slots.

3.3.2 Antenna Design

3.3.2.1 *Double-Layer Antenna*

Initially, a double layer PRS antenna is designed. Two periodic PRS layers are used, printed on a 1.6mm thick dielectric substrate (Taconic TLY–5) with relative permittivity of 2.2. Following the same procedure as the one explained in 3.1.1 and 3.2.1, the layers are placed in front of a ground plane forming two air cavities of approximately half wavelength each. The complete structure is similar to the one presented in Fig. 3.3.1 (a) with two PRS layers instead of three. The elements and their dimensions as well as the cavity distances are as described in section 3.1.1. The antenna is fed by two rectangular sub-wavelength slots on a ground plane. A 50Ω microstrip line is used to excite the slots, printed on a same thickness substrate. The

two slots are etched on the ground plane which lies on the other side of the substrate (Fig. 3.3.1b, c) as explained in Section 3.3.1.

The complete antenna structure was simulated in CST Microwave Studio. Both the single slot and the dual-slot feeding structures have been incorporated with the multi-layer antenna for comparison. The S_{11} response for the single slot feeding is shown in Fig. 3.3.4 (a). It can be seen that the S_{11} is below -10dB from 13.6GHz to 15.2GHz. The S_{11} response for the optimised dual-slot feeding is also presented in Fig. 3.3.4 (a). With the proposed dual-slot technique, the S_{11} remains below -10dB within a much broader frequency range compared to the single-slot feeding and covers the entire antenna operating bandwidth. Moreover from Fig. 3.3.4 (b), it can be observed that the gain and directivity of the antenna are also improved with the dual-slot feeding, achieving a maximum gain of around 18.7dBi at 14.5GHz, compared to 17.1dBi for the single slot case. Also, the difference between the directivity and gain is less in the case of the dual-slot feeding due to the improved matching performance. The -3dB directivity-bandwidth of the antenna is around 12.2%.

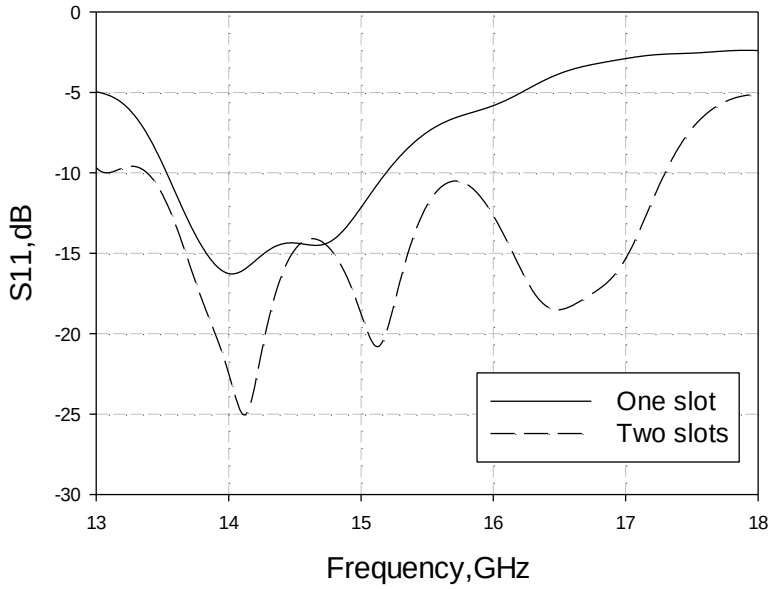

(a)

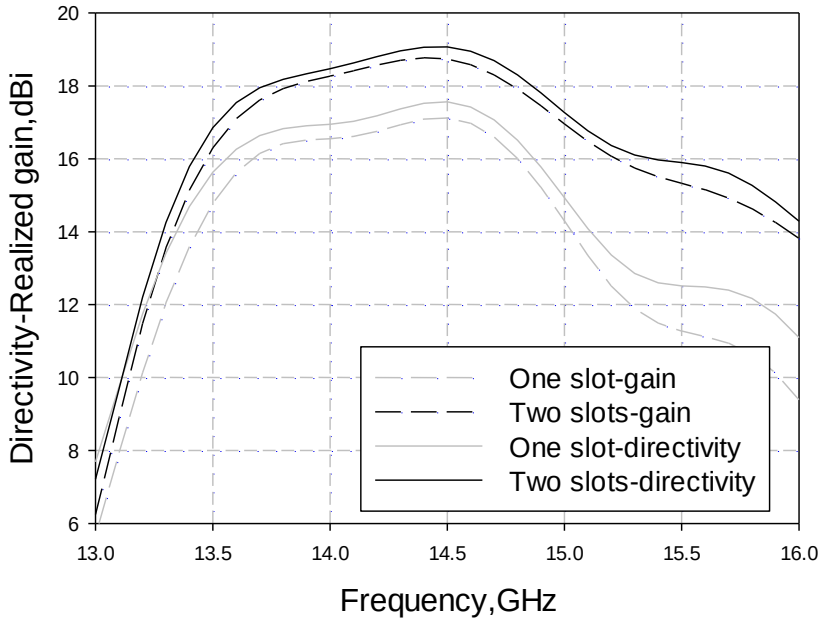

(b)

Fig. 3.3.4 Comparison between one and two microstrip fed slots as primary source of the double layer PRS antenna in terms of (a) S_{11} and (b) Realized Gain and Directivity.

3.3.2.2 *Three-Layer Antenna*

Three optimised PRS layers are employed next, to achieve a more broadband antenna performance. The layers are placed again in front of a ground plane forming three air cavities of approximately half wavelength each (Fig. 3.3.1a). The dimensions of the unit cells as well as the distances between the layers are the ones used in the optimised three layer PRS described in section 3.1.2.

The S_{11} response for the case of single slot feeding is shown in Fig. 3.3.5 (a). It is evident that the achieved -10dB matching does not cover all the desired frequency range, causing a deterioration of the realized antenna gain (Fig. 3.3.5b). The introduction of the second slot yields a more broadband input matching that covers all the operational frequency range. From Fig. 3.3.5 (a) it can be seen that for this case the S_{11} is below -10dB from 13.6GHz to

17.4GHz. Moreover from Fig. 3.3.5 (b), it can be observed that there are very small discrepancies between the directivity and the gain in the case of the two slots, as expected. In comparison, for the single slot feeding the difference between the directivity and gain is increased, especially at higher frequencies with a maximum of about 2dB, due to the poor matching at frequencies higher than 15.1GHz. The complete dual-slot-fed antenna structure achieves a maximum gain of around 19dBi (Fig. 3.3.5b) with a -3dB directivity bandwidth of 16%. It is interesting to note that, as in the case of the double-layer PRS antenna, the dual-slot feeding not only improves the input matching but it also increases significantly the antenna directivity.

In order to further investigate the directivity enhancement due to the dual-slot feeding mechanism, the electric near-field distribution for the three layer antenna with one and two feeding slots is shown in Fig. 3.3.6, providing a better insight of the dual-slot operation. For brevity, we present the YZ cross section of the field distribution only at 14GHz and 15GHz. It can be observed that the field distribution is significantly improved (i.e. becomes more uniform) with the proposed feeding technique compared to the single slot at both frequencies as expected from the investigation of the feeding structures. This explains the significant directivity enhancement of more than 3dBs at frequencies over 15GHz (Fig. 3.3.5b).

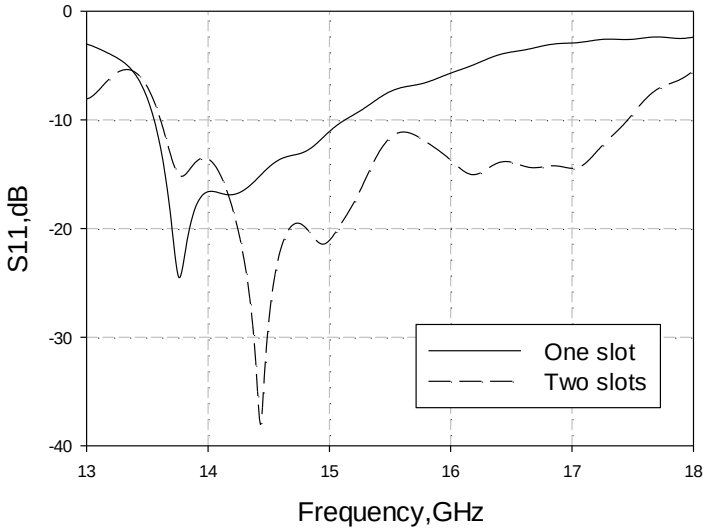

(a)

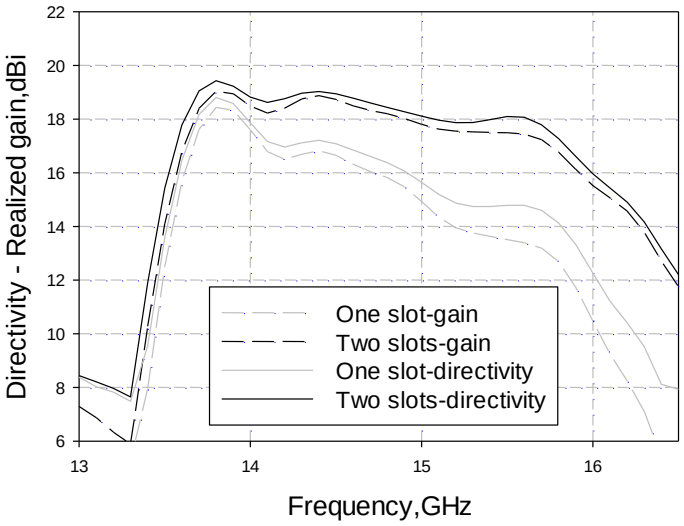

(b)

Fig. 3.3.5 Comparison between one and two microstrip fed slots as primary source of the three layer PRS antenna in terms of (a) S_{11} and (b) Realized Gain and Directivity.

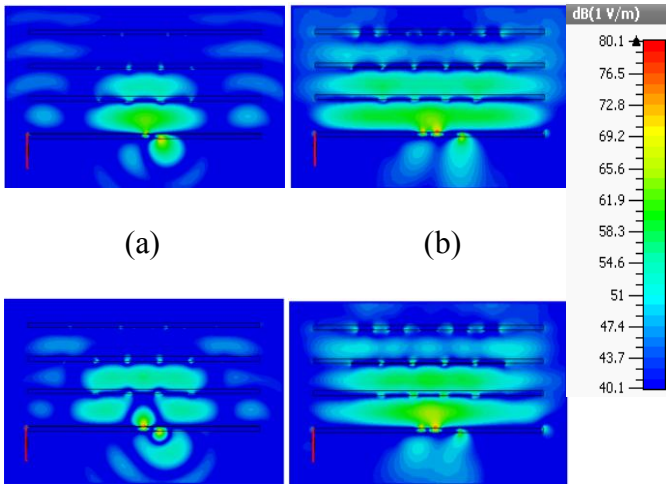

Fig. 3.3.6 Cross section of the electric field distribution (YZ plane) for the three layer antenna (a) One slot at 14GHz, (b) Two slots at 14GHz, (c) One slot at 15GHz and (d) Two slots at 15GHz.

3.3.3 Measurements

A prototype of the proposed antenna has been fabricated and measured in a full anechoic chamber (Fig. 3.3.7). Plastic screws and spacers were used for the mounting of the antenna. The simulated and measured S_{11} of the antenna is presented in Fig. 3.3.8 (a). An S_{11} below -10dB is achieved within the -3dB gain bandwidth of the antenna which is around 15%. The measured gain with a maximum value of 18.7dB is shown in Fig. 3.3.8 (b) and agrees well with the simulation results. The small discrepancy between simulations and measurements is attributed to fabrication tolerances. The H- and E-plane patterns where measured in three different frequencies within the operating band. Simulated and measured results are presented in Fig. 3.3.9. In all frequencies good agreement has been achieved.

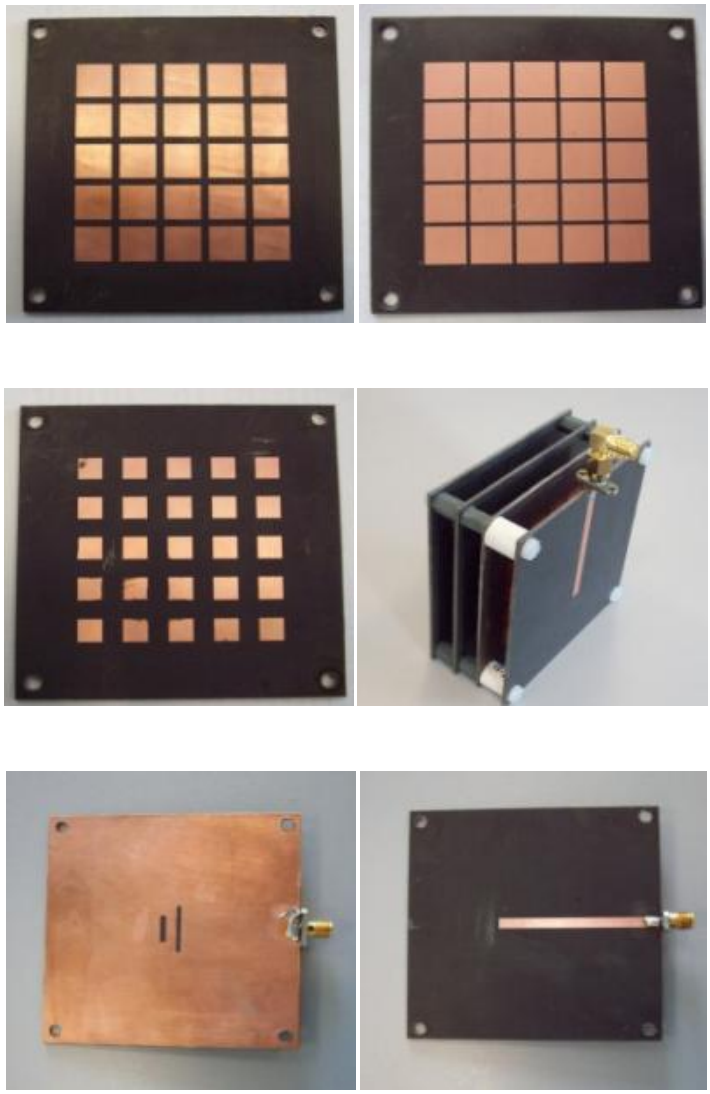

Fig. 3.3.7 Photograph of the fabricated prototype (three PRS layers, assembled antenna and both sides of ground plane).

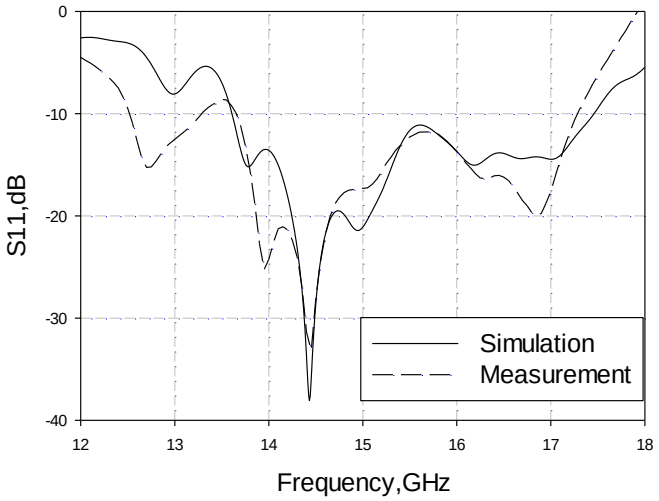

(a)

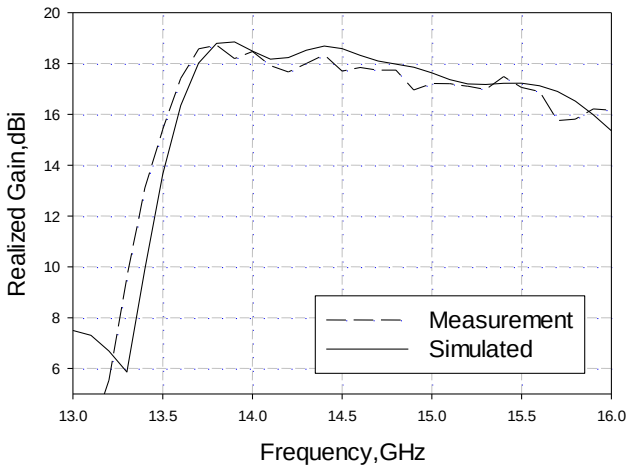

(b)

Fig. 3.3.8 Comparison between measurement and simulation for the proposed antenna for (a) S_{11} and (b) Realized Gain.

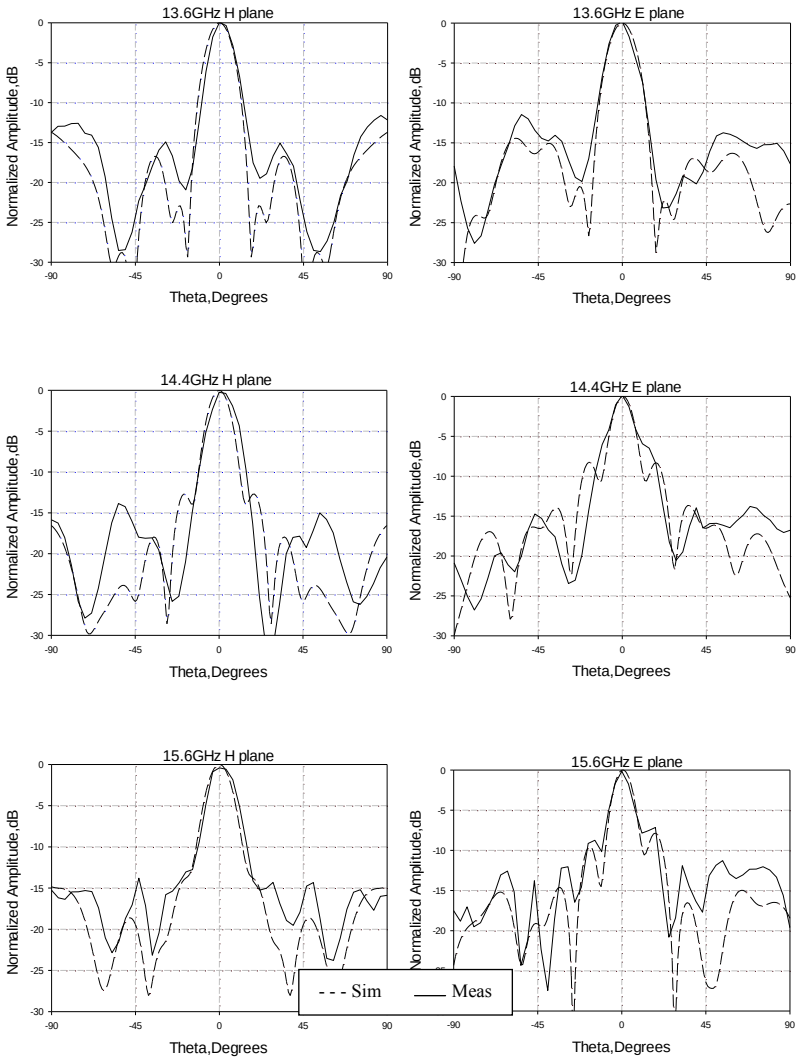

Fig. 3.3.9 Simulated and measured radiation patterns.

3.4 CONCLUSIONS

In this Chapter, broadband multi-layer PRS FP antennas have been investigated and optimized. Two- and three-layer PRSs with reflection phase increasing with frequency over a wide range have been designed and presented. Also, an equivalent circuit model was employed successfully for the PRS design. Two high gain broadband Fabry-Perot type antennas have been proposed, based on the optimized PRSs. A double layer antenna was initially designed as a starting point, achieving a maximum directivity of 19.9dBi with a 3dB bandwidth of 10.6%. Then a three-layer PRS FP antenna was proposed with a directivity of

20.8dBi at a central operating frequency of 14.5GHz and a 3dB bandwidth of about 15%, outperforming earlier antenna designs based on two–layer PRS. Measured results of a fabricated prototype have been presented and are in good agreement with simulation predictions.

Furthermore, a new dual-slot dual-resonant feeding technique for two- and three-layer-PRS FP antennas has been presented achieving a broadband matching performance and an increased directivity and gain. A maximum antenna gain of around 18.7dBi and 19dBi has been achieved for the two- and three-layer antennas respectively with a -3dB directivity bandwidth of 12.2% for the two-layer and 16% for the three-layer case. Measured results for a fabricated prototype of the three-layer antenna have been presented and are in good agreement with simulation predictions.

REFERENCES

[1] A. P. Feresidis, J. C. Vardaxoglou, "A broadband high-gain resonant cavity antenna with single feed", *Proc. EuCAP* 2006, Nice, France, 2006.

[2] B. A. Munk, "*Frequency Selective Surfaces: Theory and Design*", New York: Wiley-Interscience, 2000.

[3] B. A. Munk, "*Finite Antenna Arrays and FSS*", New York: Wiley-Interscience, 2003.

[4] N. Marcuvitz, "*Waveguide Handbook*", Lexington, MA: Boston Technical, 1964, pp.218-285.

CHAPTER 4

DISPERSION ANALYSIS OF MULTI-LAYER LEAKY-WAVE ANTENNAS

Planar leaky-wave antennas (LWA) have attracted a lot of interest since they can achieve high directivity performance and moreover they are suitable for beam-scanning applications due to their inherent dispersive properties [1]. As explained in Chapter 2.3, leaky wave theory can be employed to analyze Fabry-Perot type antennas, implemented by placing a Partially Reflective Surface (PRS) in front of a ground plane creating a Fabry-Perot type cavity (FPC) [2, 3]. Furthermore, it has been proven from the work presented in Chapter 3, that the use of multiple PRS layers produces directivity-bandwidth product enhancement in antennas of this type. This raises the question of how many layers can be added, in order to achieve the maximum directivity-bandwidth product and what are the limitations of these antennas.

In order to address this issue and also to provide a thorough understanding of the multi-layer FPC antenna operation, a leaky-wave analysis is developed in this chapter to study the dispersion characteristics of the antennas employing full wave analysis tools. The analysis of the structure is based on periodic full wave simulations using commercial software (CST Microwave Studio^{TM}). Initially, reciprocity is applied to estimate the far field response of the antennas by measuring the electric field strength in the middle of the first cavity of the structure's unit cell upon a plane wave illumination. This technique has been also employed in [4, 5] where Method of Moments (MoM) spectral domain analysis combined with reciprocity is employed to extract the radiation patterns of a double layer Fabry-Perot LWA. Then a dipole source is used to excite the cavity modes and extract the complex propagation constant

of the leaky modes. In both cases periodic boundary conditions are applied to reduce the calculations. Moreover, a simple and rigorous analysis procedure using array theory is employed to validate the complex leaky-mode propagation constant values derived from the full wave simulations. Finally, finite size antennas based on the results of the periodic analysis are presented achieving a broadband directivity response.

4.1 ANALYSIS OF SUPPORTED MODES USING RECIPROCITY

The structures under investigation in this Chapter are essentially the same type as the ones studied in Chapter 3. They consist of multiple layers of periodic metallodielectric Partially Reflective Surfaces (PRS) placed over a ground plane forming air cavities of about half wavelength each. More specifically double layer and three layer FPC type leaky wave antennas are being studied. Since the proposed structures are considered periodic, full wave periodic analysis is employed in commercial simulation software (CST Microwave Studio^{TM}) to estimate the directivity performance of the antennas through measuring the near field inside the first cavity of the unit cell of the respective structure and using the reciprocity principle as explained in Chapter 2.

4.1.1 Double-Layer PRS

The structure shown in Fig. 4.1.1 (a) consists of two PRS layers printed on a dielectric substrate of permittivity ε_r=2.2 and thickness 1.6mm, placed above a ground plane. Each of the two formed air cavities is approximately half a wavelength thick at the operational frequency which is 14GHz. In particular, the different cavity heights are h_1=11.3mm and h_2= 11mm. Square metallic patches are chosen for this configuration as shown in Fig. 4.1.1 (b). The periodicity of both layers is P=11mm and the dimensions of the elements are d_1=10mm in PRS_1 and d_2=6mm in PRS_2. A dipole source is used as an excitation placed in the middle of

the cavity between the ground plane and PRS_1. Periodic boundary conditions are employed, so a single unit cell is analyzed instead of the complete structure. A good estimation of the antenna's performance can be made by calculating the magnitude of the x-component of the electric field at the centre between the ground plane and the first PRS under x-polarized normal plane wave incidence. By reciprocity, this is proportional to the far-field intensity at broadside as explained in Chapter 2.3.2.

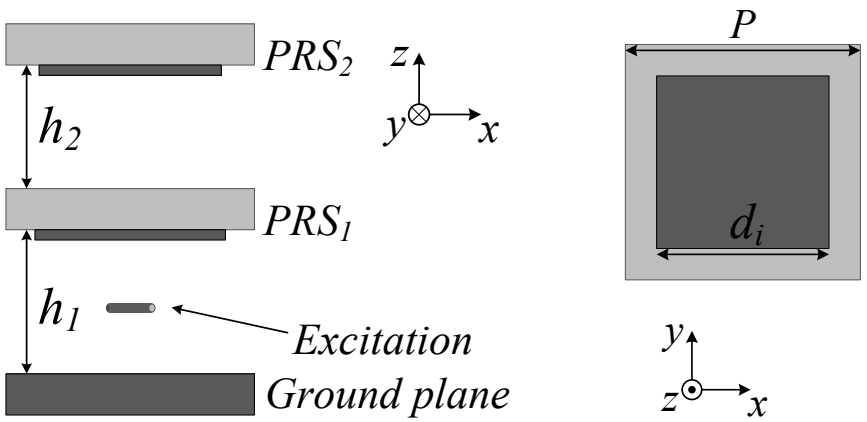

Fig. 4.1.1 (a) Cross section of the double layer Fabry-Perot cavity unit cell, (b) Unit cell of the square patch PRS.

In Fig. 4.1.2, the near-field electric field strength is plotted for frequencies between 12GHz and 15GHz. As mentioned earlier this is proportional to the far field radiation intensity. Two peaks appear attributed to the two resonant modes of the structure at 13.5GHz and 14GHz. It can be observed that the second mode is more strongly excited than the first. The total radiated power of the antenna (i.e. the denominator of equation 2.3-4) at low frequencies (below 13.7GHz) is reduced since at these frequencies the resonant leaky mode of the cavity is close to cut off and thus weakly excited. Consequently, this response of the electric field strength differs to the antenna's directivity, which must be calculated by (2.3-4) and it will

result in a more flat response with frequency. Thus all the dimensions of the structure mentioned earlier, have been chosen accordingly to achieve this desired response.

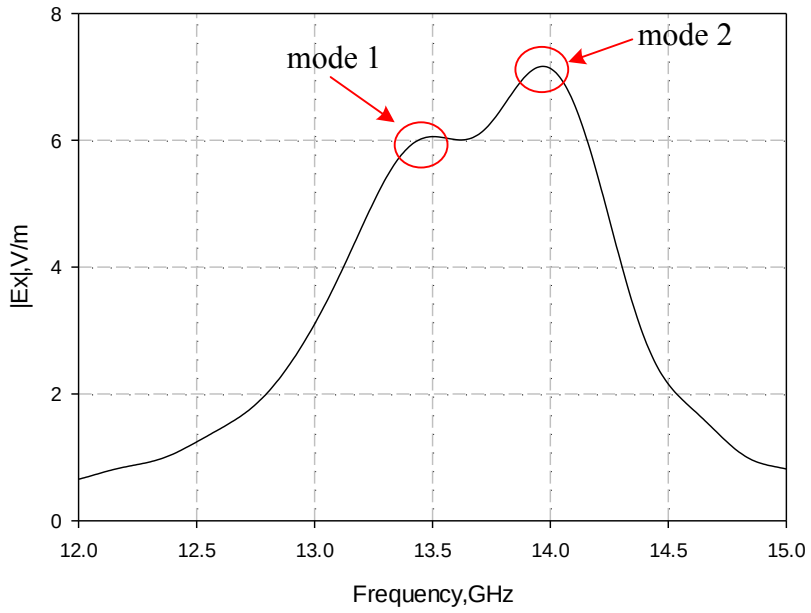

Fig. 4.1.2 Magnitude of E_x in the centre of the unit cell between the ground plane and PRS_1 of the proposed structure.

4.1.2 Three-Layer PRS

Subsequently, the three-layer structure is investigated. The structure is shown in Fig.4.1.3 and consists of three PRS layers printed on a dielectric substrate of the same permittivity and thickness as the PRSs of the double-layer structure. Three air cavities are formed in this case, each being approximately half wavelength thick at 14GHz. Namely, the different cavity heights are h_1=11.17mm, h_2= 10.46mm and h_3=11.65mm. Again, square metallic patches are chosen for this configuration. The periodicity of all three layers is 11mm and the dimensions of the elements are d_1=10.57mm in PRS_1, d_2=8.77mm in PRS_2 and d_3=5.52mm in PRS_3. The dipole source used as an excitation in the middle of the cavity between the ground plane and

PRS_1 is also illustrated in Fig. 4.1.3. Periodic boundary conditions are employed, in the simulation software. The magnitude of the x-component of the electric field is calculated at the centre between the ground plane and the first PRS under x-polarized normal plane wave incidence. As mentioned in the previous subsection, by reciprocity, the calculated electric field is proportional to the far-field intensity at broadside.

The near-field electric field strength is plotted in Fig. 4.1.4 for frequencies between 12GHz and 15GHz. From the figure it can be observed that three peaks appear as expected, attributed to the three resonant modes of the structure. The peaks occur at 12.8GHz, 13.7GHz and 14.1GHz. Similarly to the case of the double layer structure, the second and third modes are more strongly excited than the first.

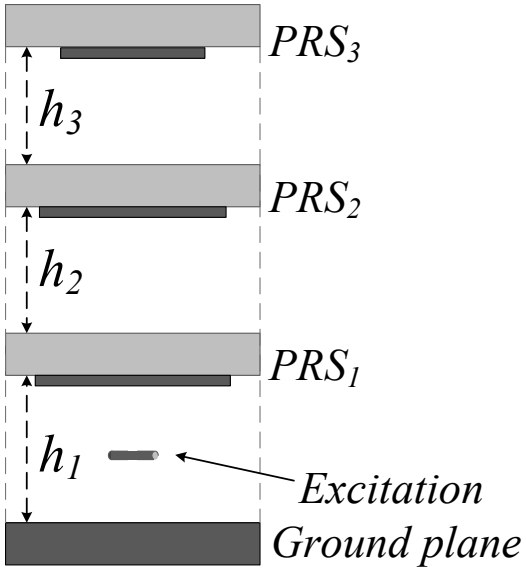

Fig. 4.1.3 Cross section of the three layer Fabry-Perot cavity unit cell.

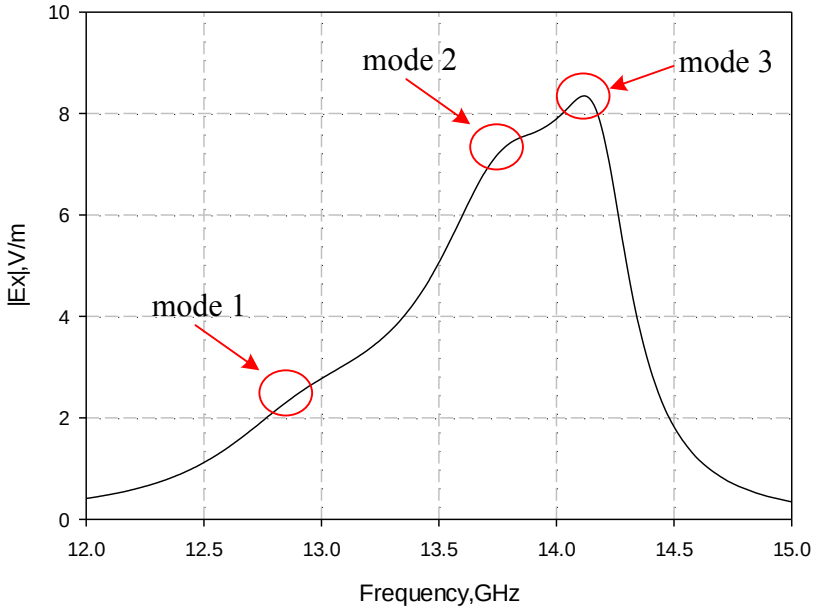

Fig. 4.1.4 Magnitude of E_x in the centre of the unit cell between the ground plane and PRS_1 of the proposed structure.

A visualisation of the exited modes inside the three cavities can be seen in Fig. 4.1.5. The electric fields are presented for three frequencies corresponding to the three resonant modes. For the first mode at 12.8GHz (Fig. 4.1.5a), the fields in the first and second cavities starting from the ground are antiparallel and similarly the fields in the second and third cavities are also antiparallel. Moreover, the fields are stronger in the second cavity compared to the other two. For the second mode at 13.7GHz the fields are stronger at the first cavity and antiparallel with the fields at the other two cavities which are more weakly excited (Fig. 4.1.5b). Finally, the fields for the third mode at 14.1GHz are shown in Fig. 4.1.5 (c). The fields are parallel in the first two cavities with the first cavity being more strongly excited while the third cavity does not have a significant contribution to the overall electric field strength of this mode.

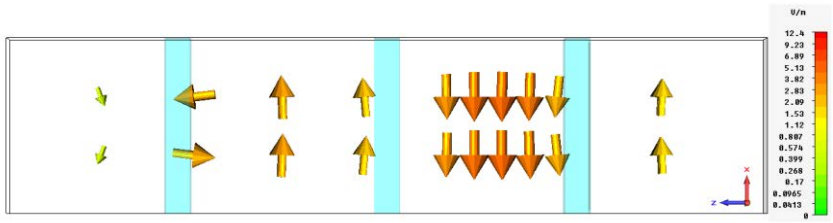

(a)

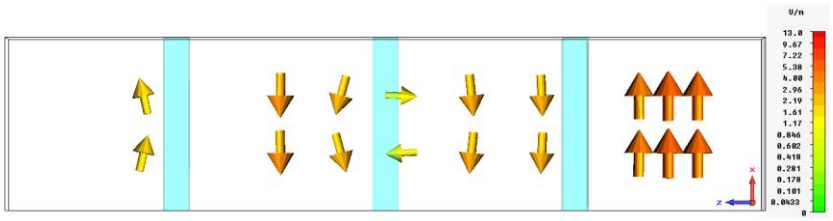

(b)

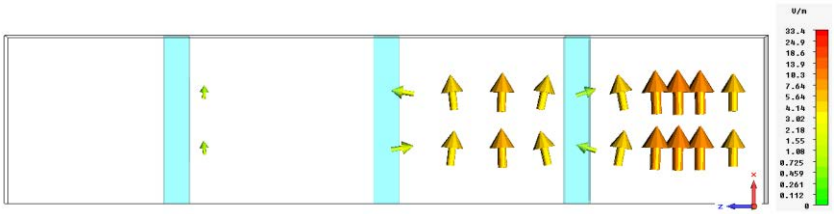

(c)

Fig. 4.1.5 Electric field strength inside the three resonant cavities with the ground plane at the right hand side at (a) 12.8GHz, (b) 13.7GHz, (c) 14.1GHz. The three PRS layers are shown in light blue.

4.2 DISPERSION ANALYSIS

The main information about the operation of leaky wave antennas can be provided by investigating the complex wavenumber, k, of the leaky-modes. As explained in Chapter 2.3.1, the real part of k is the propagation constant β. When $\beta < k_0$, fast waves are supported, i.e. the wave velocity is larger than the speed of light. The angle of the radiated leaky-wave beam is related to β and can be calculated from the equation (2.3-2). Obtaining the values of β will

give an estimation of the angle of the main radiated beams corresponding to the different modes. On the other hand, α is the imaginary part of k and is referred to as the attenuation constant. Knowledge of the values of α, gives information about the beamwidth of the radiated beam for the corresponding leaky mode.

In the past, the dispersion analysis and characterization of periodic LWAs has been carried out [6-8]. However the full wave dispersion analysis techniques that have been developed thus far are limited to a single layer periodic PRS. In this Chapter, a full wave dispersion characterization of multi-layer periodic FPC type structures is being presented for the first time. The values of β are extracted from simulations of the unit cell of the structure applying periodic boundary conditions along the x and y axis. A phase difference is introduced between the boundaries along the x axis in order to study the dispersion properties in this direction. The phase is varied from 0 deg to 180 deg with a step of 10 deg to account for different values of β. A small dipole source (see Fig. 4.1.1a and 4.1.3) in the middle of the first cavity is used in order to excite the structure and sample the supported modes which correspond to the resonances of the cavities and appear as minima in the S_{11} response.

Subsequently, in order to extract the values of α, two consecutive unit cells are designed in the simulation software. This is done so that two dipoles can be placed in the first cavity with a distance of a period between them as shown in Fig. 4.2.1. The dipoles are employed to sample the electric field strength in the two observation points. As explained in [6], the electric field strength is attenuated by a factor of $e^{-\alpha \cdot P}$, where P is the periodicity of the unit cell. Thus, the values of α can be extracted from the ratio of the two sampled electric field strengths (4.2-1) applying periodic boundary conditions and varying the phase shift between them. It should be pointed out here that the applied phase shift at the boundaries has to be double the one used for the extraction of β due to the fact that two unit cells are used.

$$E = E_0 \cdot e^{-\alpha \cdot P} \Rightarrow \alpha = -\frac{1}{P} \cdot \ln\left(\frac{E}{E_0}\right), \tag{4.2-1}$$

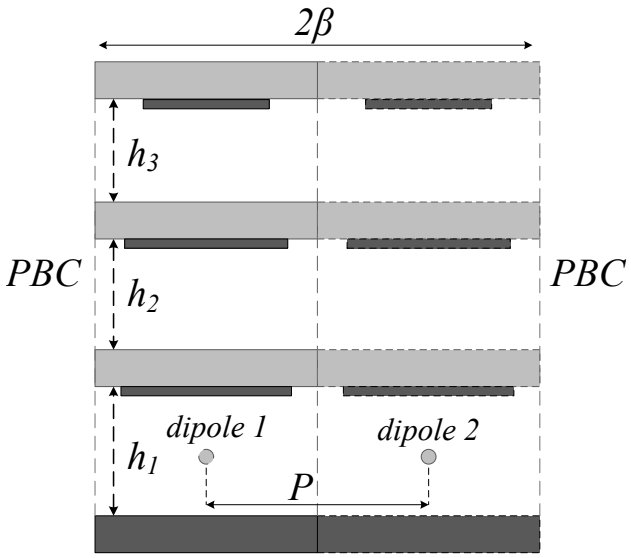

Fig. 4.2.1 Field sampling points one spatial period apart from each other for the calculation of the attenuation constant with (4.2-1) for the three layer Fabry-Perot cavity structure.

4.2.1 Double-Layer LWA

Initially, a dispersion characterization of the double-layer Fabry-Perot structure proposed in section 4.1.1 is carried out which reveals the propagation constant for the two leaky modes at different frequencies (Fig. 4.2.3). This is carried out employing the technique described earlier in this Chapter, i.e. by sampling the cavity resonances using a dipole in the middle of the first cavity. A better understanding of the technique can be provided from Fig. 4.2.2 where the S_{11} response of the dipole is depicted for phase shifts between the boundaries of 20^o and 80^o, corresponding to two different values of β. It can be observed that in both cases two minima occur corresponding to the two modes. From the dispersion diagram of the propagation constant in Fig. 4.2.3, it can be seen that fast waves are supported from the structure as expected, since the two modes are located in the leaky region, above the light line.

The first mode starts at 13.5GHz while the second at 14GHz. These values agree with the peaks that appear in the electric field strength response for normal plane wave incidence shown in Fig. 4.1.2. Moreover, the values of β increase with frequency for both leaky modes corresponding to radiating beams at higher angles. Subsequently, employing the technique described earlier, the attenuation constant values are extracted and depicted in Fig. 4.2.5. For example, for the case of 10^{o} between the boundaries, the sampled electric field strength from the two dipoles is shown in Fig. 4.2.4. The value of α is then calculated at the frequencies where the maxima appear from (4.2-1), substituting E_0 and E_1 which are the fields sampled from the first and second dipole respectively. The values of α are estimated only for angles close to broadside, because for higher angle there is strong coupling between the modes making their determination challenging. However, the small values of the attenuation constant imply that a very large size antenna is required to have significant attenuation of the field at the antenna's edges. Consequently, for a finite size antenna the exact value of α does not considerably affect the radiation pattern.

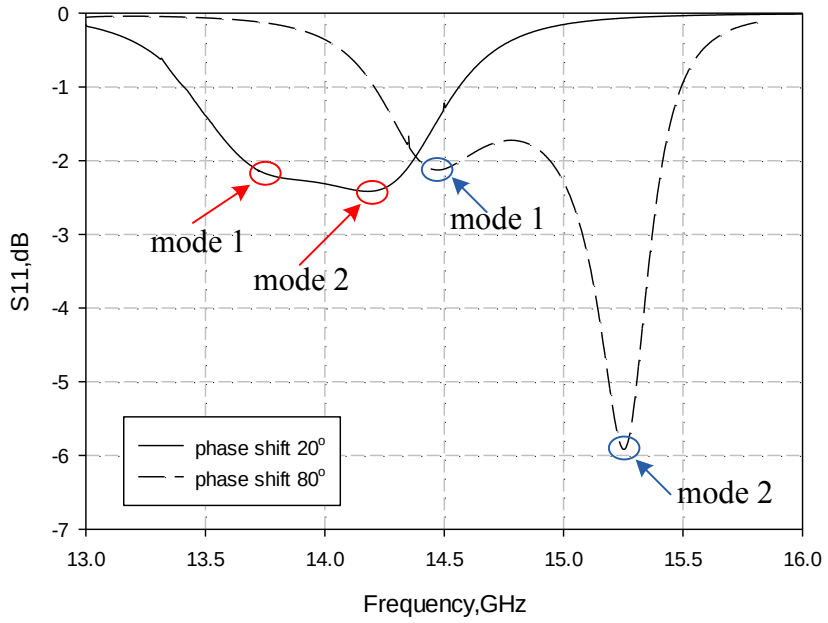

Fig. 4.2.2 S_{11} response versus frequency for two representative cases of phase shifts along the x axis showing the minima corresponding to the frequencies of the two leaky modes.

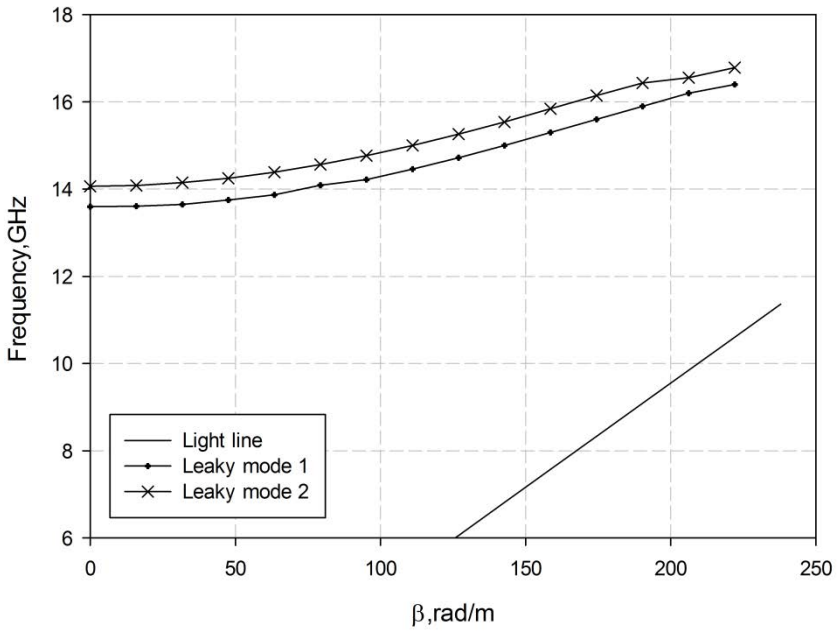

Fig. 4.2.3 Frequency versus propagation constant for the x axis showing the two leaky modes supported from the double-layer Fabry-Perot cavity structure.

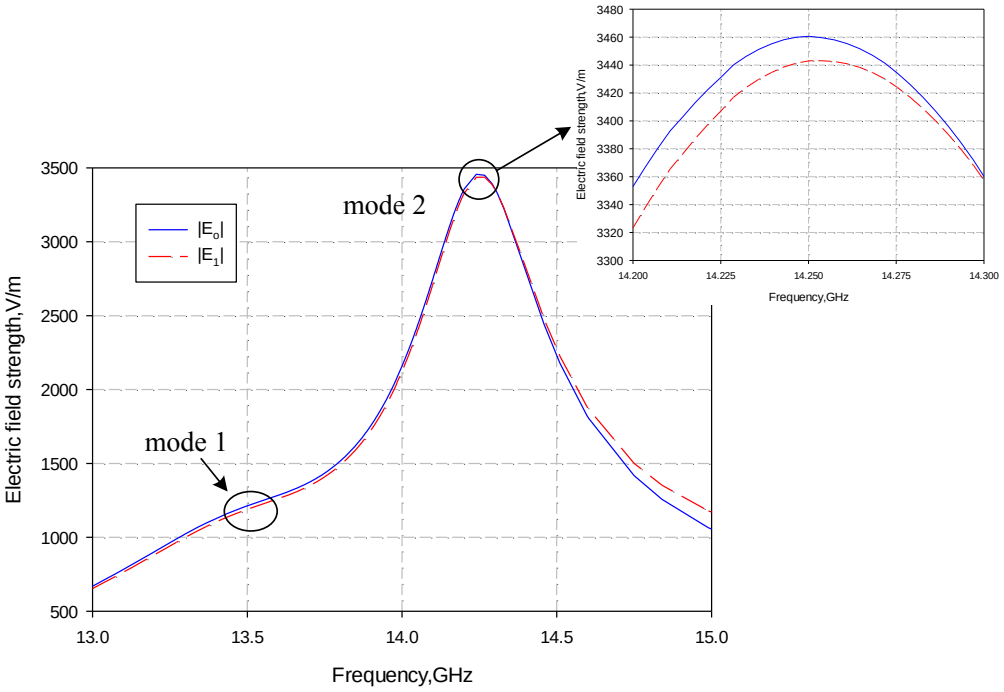

Fig. 4.2.4 Electric field strength for 10^{o} phase shift between the boundaries, as sampled from the two dipoles in the first cavity of the structure for the calculation of the attenuation constant.

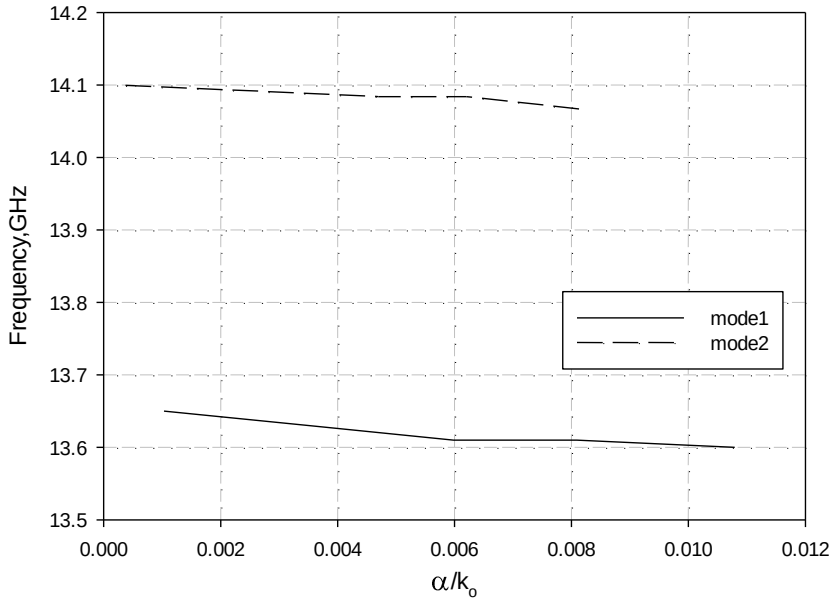

Fig. 4.2.5 Frequency versus normalized attenuation constant for the x axis showing the two leaky modes supported from the double-layer Fabry-Perot cavity structure.

4.2.2 Three-Layer LWA

Subsequently, a dispersion characterization of the three-layer Fabry-Perot structure under investigation described in section 4.1.2, reveals the complex propagation constant for the three leaky modes at different frequencies (Fig. 4.2.6 and 4.2.7). As in the case of the double-layer structure, fast wave propagation is supported in the proposed configuration. This is evident from the dispersion diagram shown in Fig. 4.2.6, since the three modes corresponding to the three resonant cavities are located in the leaky region above the light line. The first mode starts at 12.8GHz, the second at 13.7GHz and the third at 14.1GHz. For low values of β, the three modes are well separated while for higher values of β the second and third modes tend to converge. Furthermore, similarly to the double-layer case the attenuation constant values are calculated just for small angles and depicted in Fig. 4.2.7. Again, due to the small calculated values, a large size antenna is needed in order for the fast waves to significantly attenuate reaching the edge of the structure.

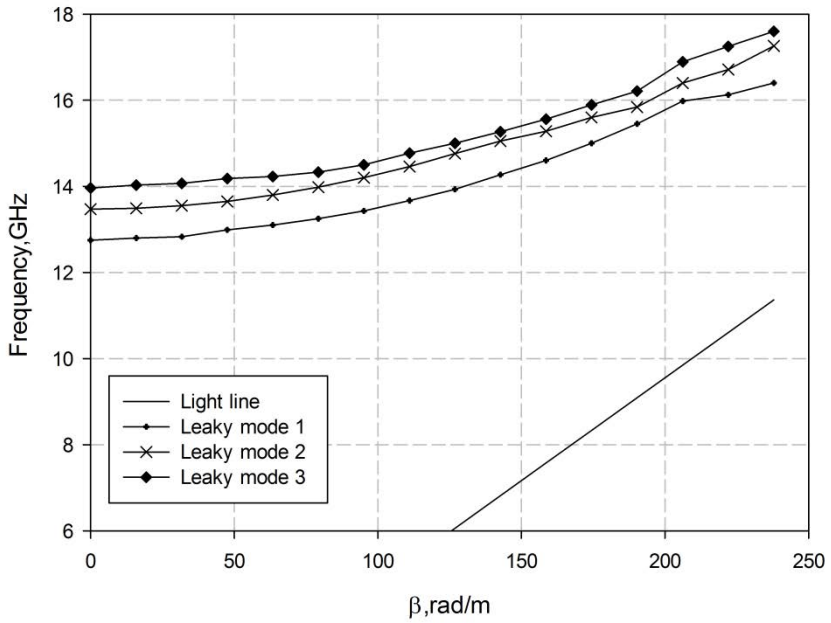

Fig. 4.2.6 Frequency versus propagation constant for the x axis showing the three leaky modes supported from the three-layer Fabry-Perot cavity structure.

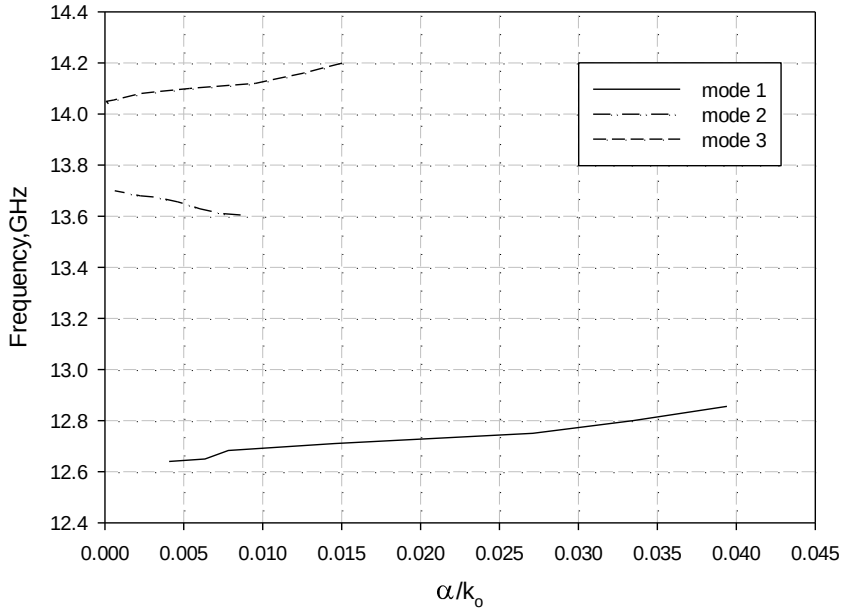

Fig. 4.2.7 Frequency versus normalized attenuation constant for the x axis showing the three leaky modes supported from the three-layer Fabry-Perot cavity structure.

4.3 RADIATION PATTERN CALCULATION USING ARRAY FACTOR APPROACH

As explained in section 2.3.3, at a specific frequency the radiation pattern can be calculated using the array factor (equation 2.3.9). For a structure with more than one leaky modes, the total radiation pattern is the result of superposition of the leaky-wave radiation of all modes. This can give an estimation of the total radiation pattern and thus provide insight for the performance as well as the limitations of this type of antennas. For example at higher frequencies close to the cut off of the higher order modes, the values of β corresponding to the first modes (with lower cut-offs) assume large values. This means that each of these first modes will contribute to the total radiation pattern by giving two beams at large angles $\pm\theta$, where θ will be given by (2.3-6). This effect is common in this type of LWAs as β increases and is expected to distort the total radiation pattern, creating high level sidelobes.

Therefore, in order to validate the analysis and the results for the complex propagation constant presented in sections 4.2.1 and 4.2.2, finite size antennas have been designed and simulation results are presented. Two antennas are investigated corresponding to the double and three-layer structures that have been analyzed. The antenna shown in Fig. 4.3.1, consists of a ground plane, three PRS layers and an ideal dipole feed. The ground plane has been made transparent in the figure to make the feeding dipole visible. A similar structure is designed for the double-layer case, employing two PRS layers instead of three. Despite their finite size, they are large enough to be approximated with an infinite structure. Thus, a good agreement with the infinite analysis results presented in the previous sections is expected.

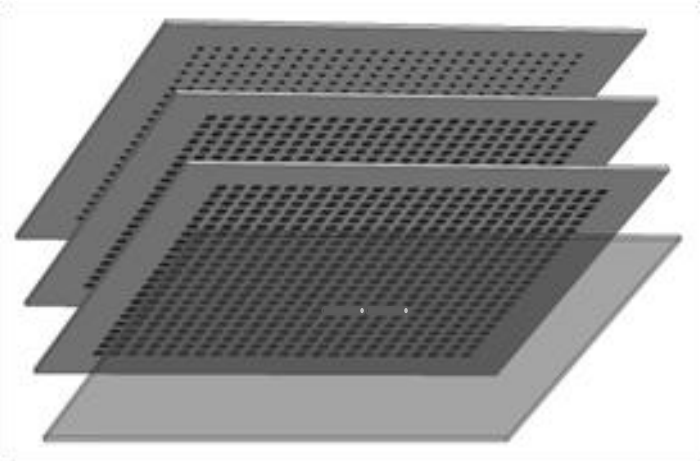

Fig. 4.3.1 3-D view of the three-layer FPC type finite size antenna with excitation source in the middle of the first cavity.

4.3.1 Double-Layer

A double-layer finite size antenna has been designed and simulation results are presented in this section to validate both the reciprocity and leaky-wave analysis. The antenna consists of a ground plane, two PRS layers and an ideal dipole feed. The distances between the layers and the dimensions of the square elements in each layer are as described in section 4.1.1, i.e.

h_1=11.3mm and h_2= 11mm, P=11mm, d_1=10mm and d_2=6mm. The dipole lies in the middle of the first cavity (between the ground plane and the first PRS layer). An array of 13x13 elements is printed on each dielectric layer which corresponds to a size of 7λ x 7λ.

The complete antenna structure was simulated in full-wave simulation software to extract the directivity performance. Due to the size of the proposed design, computational time is very long, which is impractical. In order to address this issue, symmetry planes were employed reducing the calculations in one quarter of the total structure. A magnetic symmetry plane (H_t=0) is introduced in the YZ plane, along the dipole's length and an electric symmetry plane (E_t=0) is introduced in the XZ plane vertical to the dipole's length. Subsequently, the directivity is calculated and is shown in Fig. 4.3.2. A maximum of 19dBi is achieved at 14.3GHz and the 3dB radiation bandwidth is 10.8%. Two peaks appear at 13.4GHz and 14.3GHz. There is a fluctuation of about 2.5dB making the peaks predominant. The peaks correspond to the two resonant leaky modes of the structure as calculated from both the near field response and the dispersion analysis. However there is a small frequency shift towards high frequencies for the second peak compared to the frequency of the second leaky mode (which is 14GHz). This can be attributed to the finite size of the structure. Moreover, it should be noted that the first peak is more broadband with the bandwidth decreasing for the second one. This is in good agreement with the electric field strength response shown in Fig. 4.1.2.

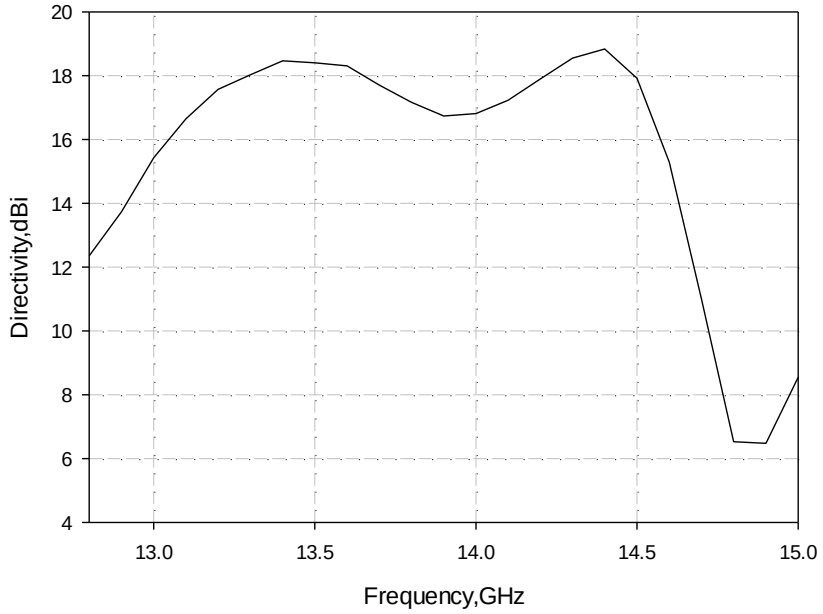

Fig. 4.3.2 Simulated directivity versus frequency of the proposed double-layer antenna.

The H- and E-plane radiation patterns of the proposed antenna are shown in Fig. 4.3.3 for frequencies 13.5GHz, 14.4GHz and 14.6GHz. For each frequency the simulated pattern is compared to the pattern calculated from the array factor approach and more specifically from (4.3-1) where P the periodicity, and γ the angle from the axis of propagation. In this case, the total radiation pattern at a specific frequency is the contribution of the two leaky modes, thus knowing the values of the complex propagation constant can give us full information of the radiation properties at each frequency. It can be observed from Fig. 4.3.3 that good agreement has been obtained between full-wave simulation and the array factor approach for N=13 which is the number of elements of the structure. Moreover, from the pattern at 14.6GHz it is evident that a beam splitting effect occurs which is attributed to the high values of β as the frequency increases. This behavior is typical for LWA as explained at the beginning of section 4.3, but what is more interesting is that from the performed analysis the latter can be

predicted without the need of performing full-wave simulations which require high computational complexity.

$$AF_{tot} = AF_1 + AF_2 = \sum_{n=0}^{N-1} e^{-na_1 \cdot P} e^{jn(\frac{2\pi P \cos\gamma}{\lambda} - \beta_1 \cdot P)} + \sum_{n=0}^{N-1} e^{-na_2 \cdot P} e^{jn(\frac{2\pi P \cos\gamma}{\lambda} - \beta_2 \cdot P)}, \quad (4.3\text{-}1)$$

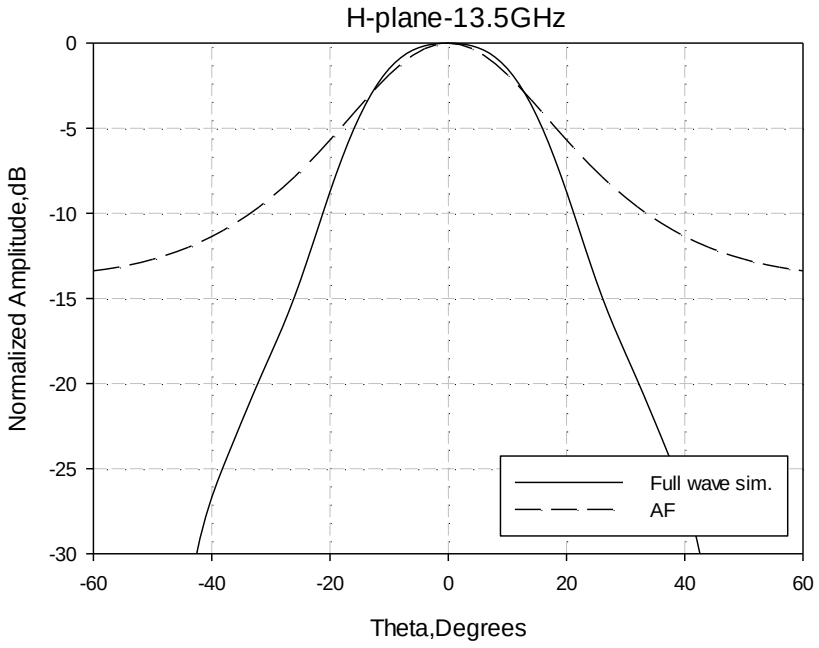

(a)

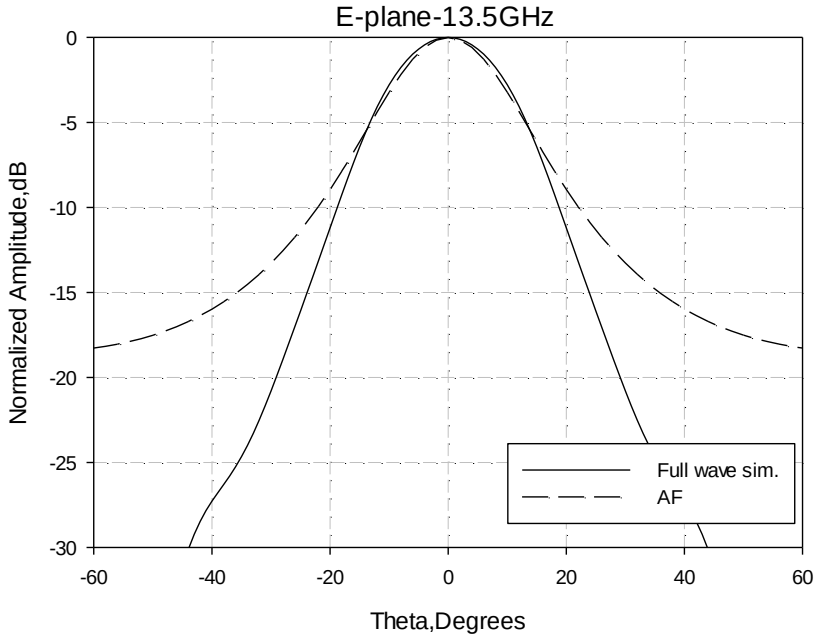
E-plane-13.5GHz
Normalized Amplitude,dB
0
-5
-10
-15
-20
-25
-30
-60
-40
-20
0
20
40
60
Theta,Degrees
Full wave sim.
AF

(b)

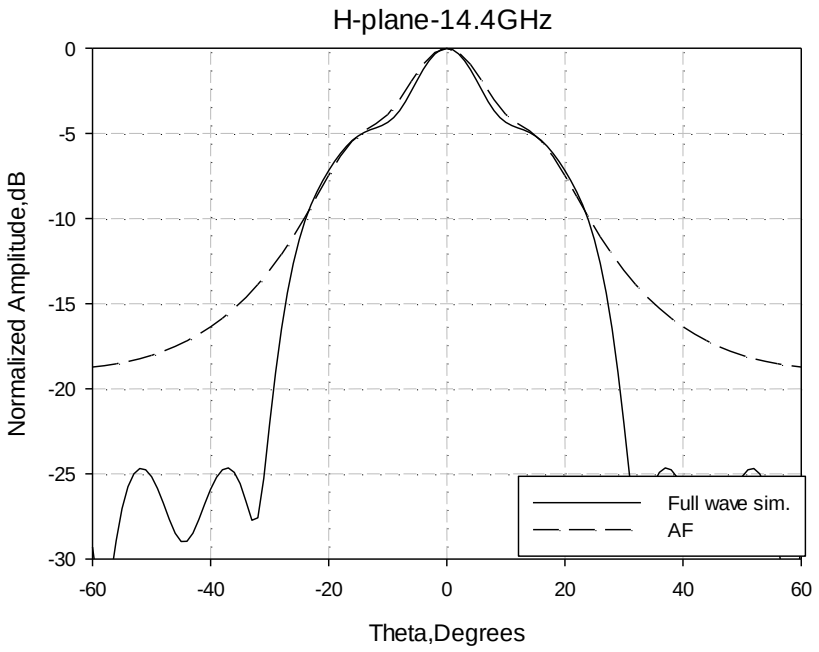
H-plane-14.4GHz
Normalized Amplitude,dB
0
-5
-10
-15
-20
-25
-30
-60
-40
-20
0
20
40
60
Theta,Degrees
Full wave sim.
AF

(c)

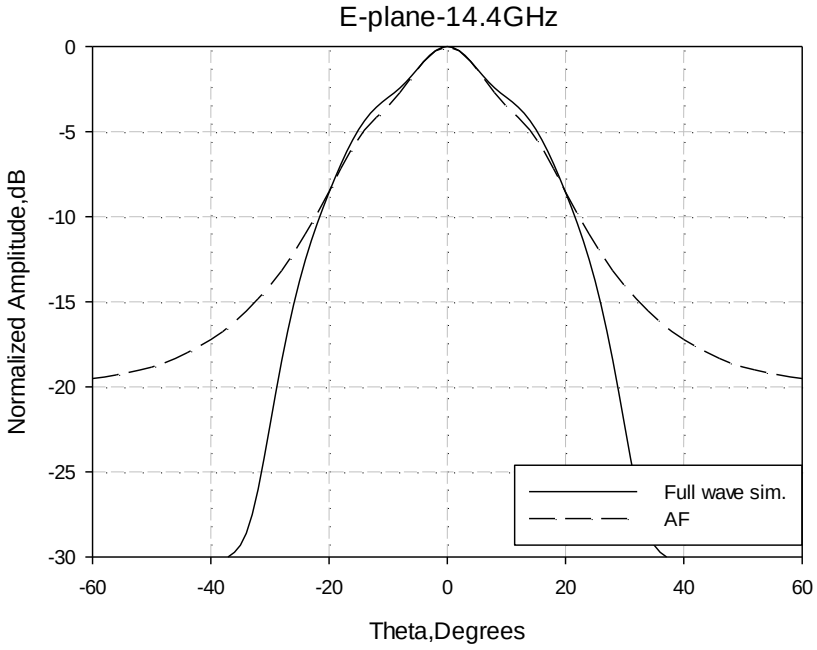
E-plane-14.4GHz
Normalized Amplitude,dB
0
-5
-10
-15
-20
-25
-30
-60
-40
-20
0
20
40
60
Theta,Degrees
Full wave sim.
AF

(d)

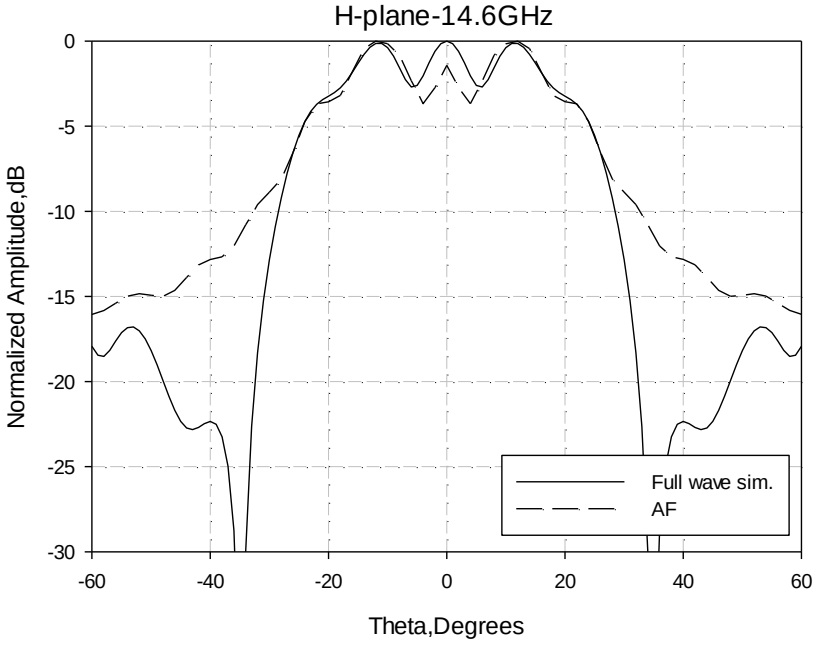
H-plane-14.6GHz
Normalized Amplitude,dB
0
-5
-10
-15
-20
-25
-30
-60
-40
-20
0
20
40
60
Theta,Degrees
Full wave sim.
AF

(e)

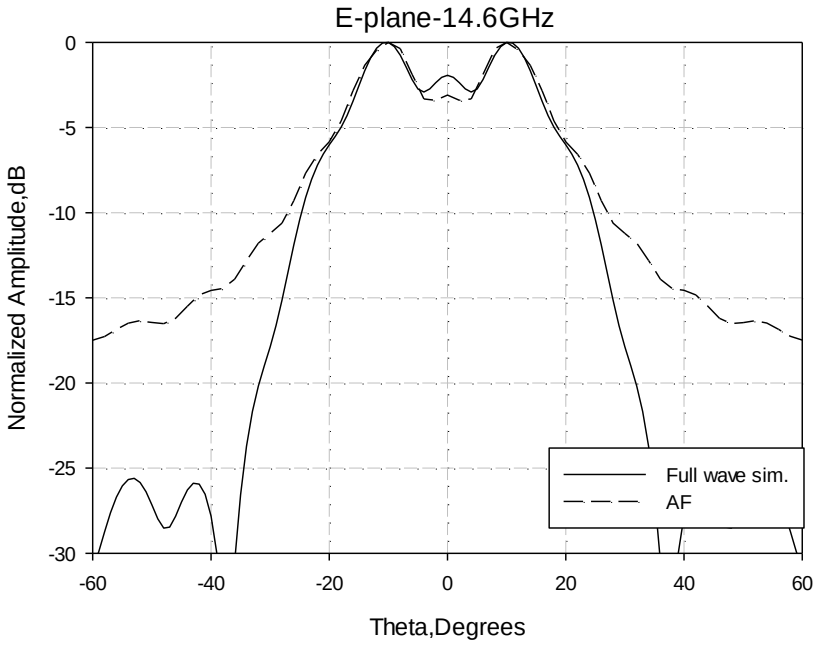

(f)

Fig. 4.3.3 Radiation patterns comparison of the proposed double-layer antenna. H-plane at (a) 13.5GHz, (c) 14.4GHz and (e) 14.6GHz. E-plane at (b) 13.5GHz, (d) 14.4GHz and (f) 14.6GHz.

4.3.2 Three-Layer

In this section, a finite size antenna for the three-layer structure is presented. The antenna is the one shown in Fig. 4.3.1. The antenna consists of a ground plane, the three PRS layers investigated in sections 4.1.2 and 4.2.2, and an ideal dipole feed. The distances between the layers and the dimensions of the square elements in each layer are as described in Section 4.1.2, i.e. h_1=11.17mm, h_2= 10.46mm, h_3=11.65mm, P=11mm, d_1=10.57mm, d_2=8.77mm and d_3=5.52mm. An array of 13x13 elements is printed on each dielectric layer which corresponds to a size of 7λ x 7λ, as in the case of the double-layer antenna.

The complete antenna structure was then simulated in CST to extract the directivity performance and the obtained directivity versus frequency is shown in Fig. 4.3.4. A maximum

of 20.4dBi is achieved and the 3dB radiation bandwidth is 15.4%. Three peaks appear at 12.8GHz, 13.7GHz and 14.2GHz. There is a fluctuation of about 2.5dB making the peaks predominant. The peaks correspond to the three resonant leaky modes of the structure as calculated from both the near field response and the dispersion analysis. Moreover, it should be noted that the first peak is more broadband with the bandwidth decreasing for the second and third peak. This is in good agreement with the electric field strength response shown in Fig. 4.1.4. Furthermore, although the third mode is shown to be more strongly excited, the maximum directivity value corresponds to the first peak. This is attributed to the inverse relation between the directivity and the radiated power. The latter is significantly reduced at lower frequencies where part of the first resonant mode is below the cut off and fields are evanescent. The power then increases as the cavities are more strongly excited resulting in the observed broadband directivity response.

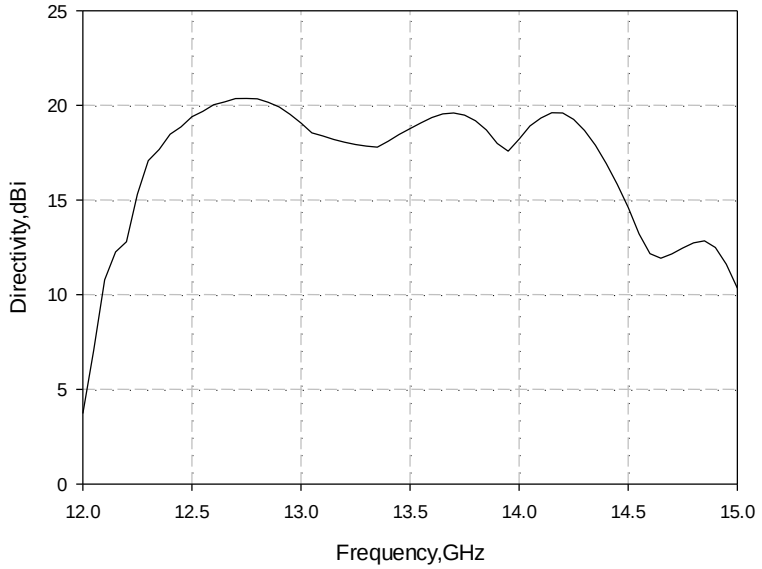

Fig. 4.3.4 Simulated directivity versus frequency of the proposed three-layer antenna.

Following the same procedure as in the case of the double-layer structure, the H- and E-plane radiation patterns of the proposed antenna are calculated using the array factor approach and

compared to the simulated ones in Fig. 4.3.5 for frequencies 13.7GHz, 14.2GHz and 14.4GHz. In this case the total radiation pattern is calculated from (4.3-2), which corresponds to the contribution of the three leaky modes. It is evident from Fig. 4.3.5 that good agreement has been obtained between full-wave simulation and the array factor approach. This result validates the conclusions derived from the analysis carried out in section 4.2.2. As expected, the radiation patterns deteriorate at higher frequencies which can be observed from Fig. 4.3.5 (c-f). Consequently, the performed analysis provides a full interpretation of the operation of multi-layer Fabry-Perot LWAs, and has led to accurate prediction of the radiation patterns through the array factor approach.

$$AF_{tot} = AF_1 + AF_2 + AF_3 =$$
$$= \sum_{n=0}^{N-1} e^{-na_1 \cdot P} e^{jn(\frac{2\pi P \cos\gamma}{\lambda} - \beta_1 \cdot P)} + \sum_{n=0}^{N-1} e^{-na_2 \cdot P} e^{jn(\frac{2\pi P \cos\gamma}{\lambda} - \beta_2 \cdot P)} + \sum_{n=0}^{N-1} e^{-na_3 \cdot P} e^{jn(\frac{2\pi P \cos\gamma}{\lambda} - \beta_3 \cdot P)}, \quad (4.3\text{-}2)$$

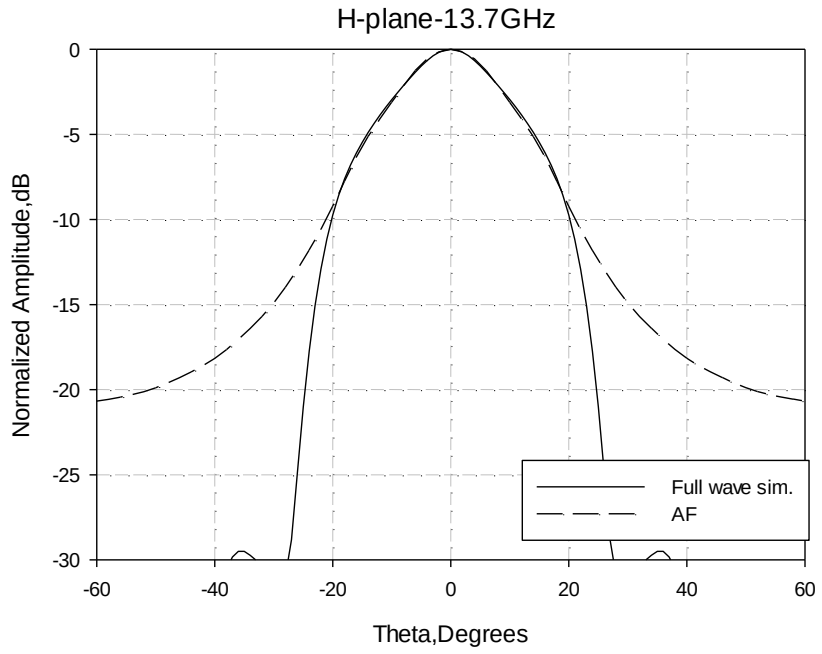

(a)

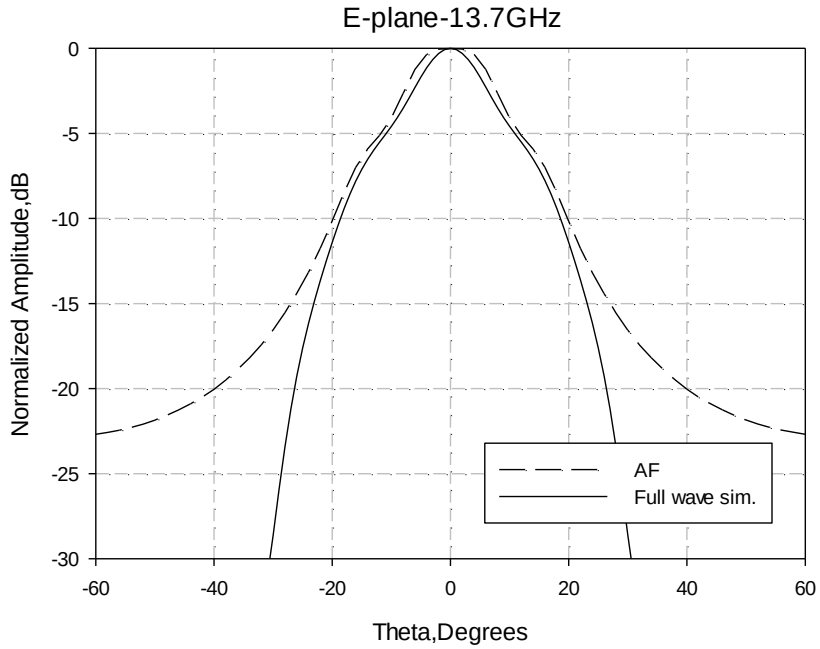
E-plane-13.7GHz
Normalized Amplitude,dB
Theta,Degrees
AF
Full wave sim.
0
-5
-10
-15
-20
-25
-30
-60
-40
-20
0
20
40
60

(b)

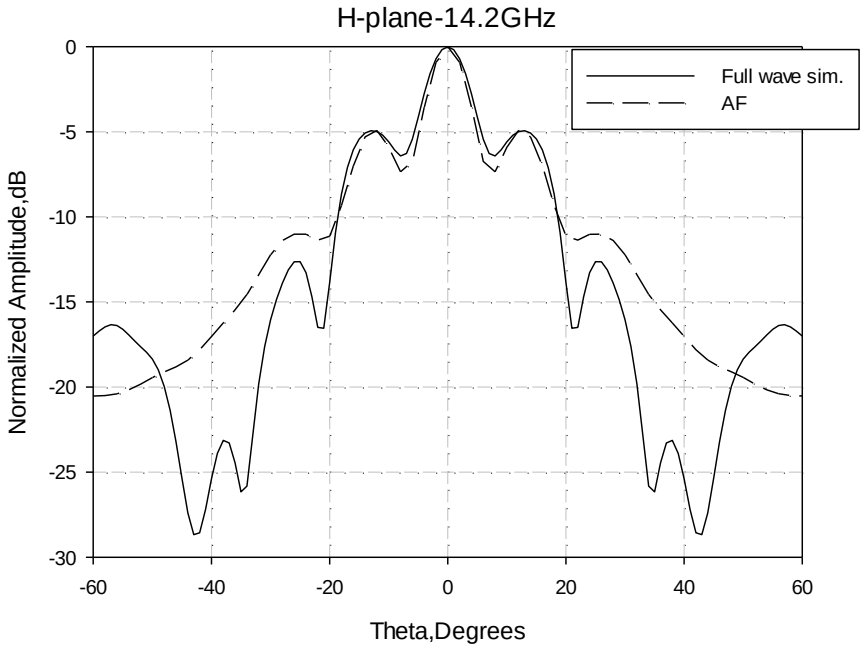
H-plane-14.2GHz
Normalized Amplitude,dB
Theta,Degrees
Full wave sim.
AF
0
-5
-10
-15
-20
-25
-30
-60
-40
-20
0
20
40
60

(c)

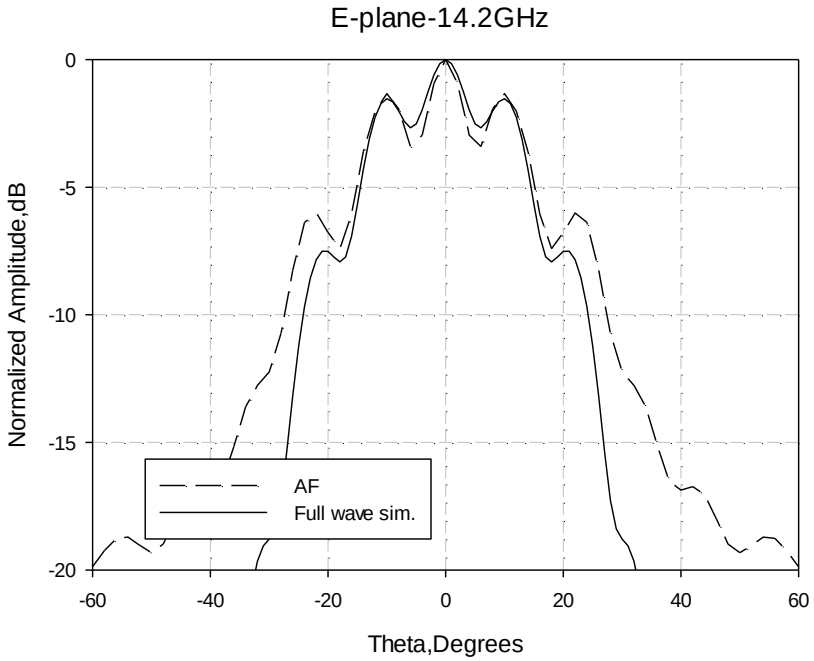
E-plane-14.2GHz
Normalized Amplitude,dB
0
-5
-10
-15
-20
-60
-40
-20
0
20
40
60
Theta,Degrees
AF
Full wave sim.

(d)

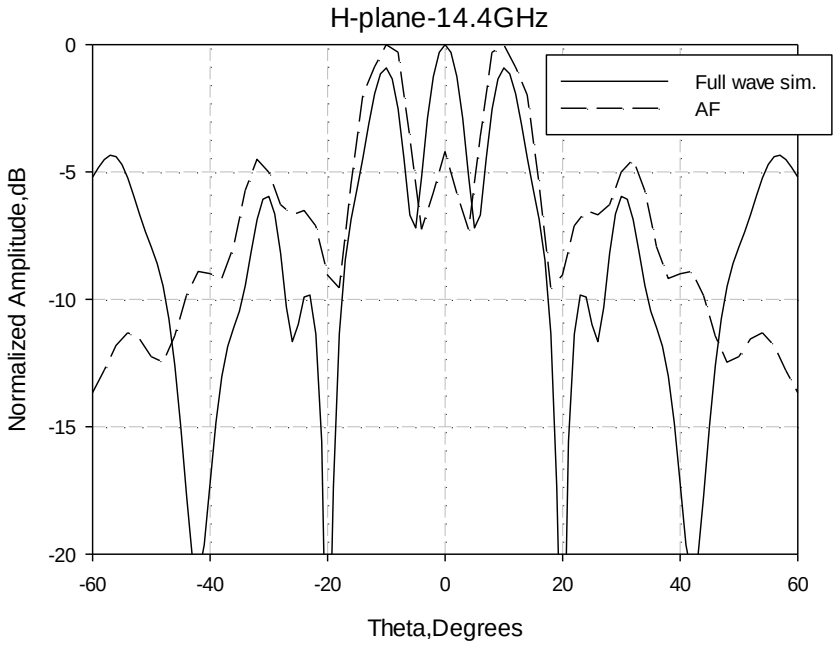
H-plane-14.4GHz
Normalized Amplitude,dB
0
-5
-10
-15
-20
-60
-40
-20
0
20
40
60
Theta,Degrees
Full wave sim.
AF

(e)

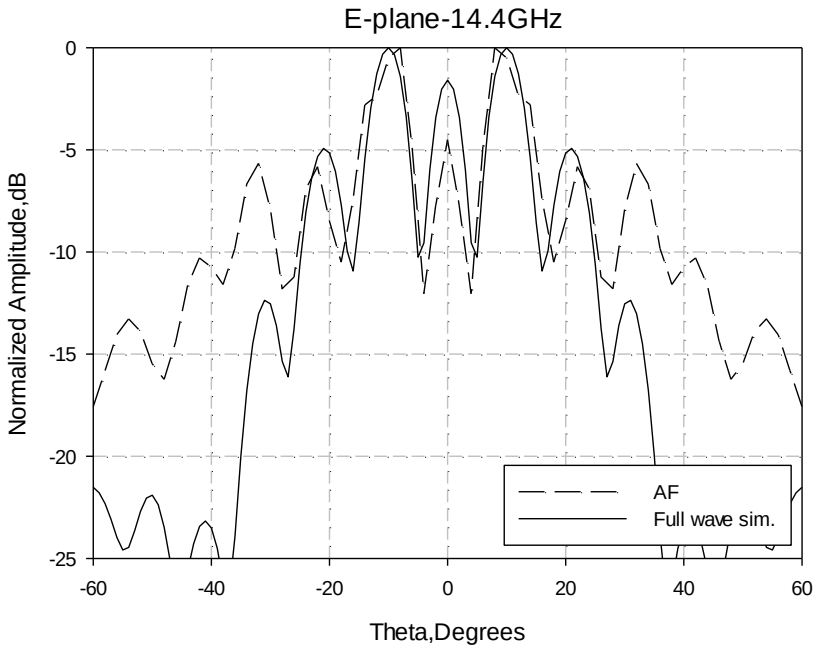

(f)

Fig. 4.3.5 Radiation patterns comparison of the proposed three-layer antenna. H-plane at (a) 13.7GHz, (c) 14.2GHz and (e) 14.4GHz. E-plane at (b) 13.7GHz, (d) 14.2GHz and (f) 14.4GHz.

4.4 CONCLUSIONS

In this chapter, the dispersion properties of broadband 2-D multi-layer Fabry-Perot Leaky-Wave antennas (LWAs) have been presented. The structures under investigation consist of two and three PRS layers and a ground plane separated by half wavelength air cavities. Full wave periodic analysis has been employed to estimate the directivity performance through measuring the near field and using reciprocity. Dispersion analysis of the leaky modes of the structure has also been performed extracting the complex propagation constant for the leaky modes. A dipole source is used for excitation of the cavity modes and the extraction of their complex propagation constant. Finally, finite size antennas have been presented achieving broadband directive performance. A validation of the dispersion analysis has also been

presented by comparing the radiation patterns at different frequencies as extracted through full wave simulations and employing the array factor approach. Good agreement has been achieved between the periodic unit cell analysis and the finite size antenna showing that the performed analysis provides a full interpretation of the operation of multi-layer Fabry-Perot LWAs.

REFERENCES

[1] A. Oliner. "Leaky-wave antennas," in Antenna Engineering Handbook, Third Edition, edited by R. C. Johnson, McGraw Hill, 1993.

[2] G.V. Trentini, "Partially reflecting sheet array", *IRE Trans. Antennas Propag.*, vol. AP-4, pp. 666-671, 1956.

[3] A. P. Feresidis, and J. C. Vardaxoglou, "High-gain planar antenna using optimized partially reflective surfaces," *Proc. Inst. Elect. Microw. Antennas Propag.,* vol. 148, no. 6, Feb. 2001.

[4] C. Mateo-Segura, G. Goussetis, and A. P. Feresidis, "Sub-wavelength Profile 2-D Leaky-Wave Antennas with Two Periodic Layers"*, IEEE Trans. Antennas Propag.*, vol. 59, pp.416- 424, Feb. 2011.

[5] C. Mateo-Segura, A. P. Feresidis, G. Goussetis, "Analysis of broadband highly-directive Fabry-Perot cavity Leaky-Wave antennas with two periodic layers," *Antennas and Propagation Society International Symposium (APSURSI), 2010 IEEE*, vol., no., pp.1,4, 11-17 July 2010.

[6] T. Kokkinos, C.D. Sarris, G.V. Eleftheriades, "Periodic FDTD analysis of leaky-wave structures and applications to the analysis of negative-refractive-index leaky-wave

antennas," *IEEE Transactions on Microwave Theory and Techniques,* , vol.54, no.4, pp.1619,1630, June 2006.

[7] T. Kokkinos, C.D. Sarris, G.V. Eleftheriades, "Periodic finite-difference time-domain analysis of loaded transmission-line negative-refractive-index metamaterials," *IEEE Transactions on Microwave Theory and Techniques,* , vol.53, no.4, pp.1488,1495, April 2005.

[8] P. Kosmas, A.P. Feresidis, G. Goussetis, "Periodic FDTD Analysis of a 2-D Leaky-Wave Planar Antenna Based on Dipole Frequency Selective Surfaces," *IEEE Transactions on Antennas and Propagation,* vol.55, no.7, pp.2006,2012, July 2007.

CHAPTER 5

MULTI-LAYER METASURFACES FOR BROADBAND HIGHLY DIRECTIVE ANTENNAS

In this Chapter, a new concept for designing broadband and sub-wavelength profile Fabry-Perot type antennas is introduced. It is based on the use of Artificial Magnetic Conductor (AMC) surfaces which are formed from doubly periodic arrays of metallic elements printed on a grounded dielectric substrate. Their key property is that they reflect incident electromagnetic waves with zero phase shift at a specific frequency [1]. In [2-4] this property has been exploited for the first time to achieve a FP antenna of sub-wavelength profile, replacing the ground plane with an AMC surface. More recently, a λ/60 profile FPC antenna has been proposed employing an AMC ground plane and a combination of an AMC and a PRS surface to further reduce the profile [5]. Nevertheless, the above profile reduction techniques suffer from a narrowband antenna performance. In this work, a novel multi-layer periodic array design is proposed yielding sub-wavelength profile Fabry-Perot cavities that significantly enhance the bandwidth performance of the resulting highly-directive antennas. Initially, the concept is presented introducing a design based on optimized double-layer periodic arrays of dissimilar dimensions, with each double-layer array consisting of a capacitive Artificial Magnetic Conductor (AMC) layer and an inductive Partially Reflective Surface (PRS) layer printed on either side of a dielectric substrate. They are placed at about quarter wavelength distance from a ground plane and from each other creating sub-wavelength FP type antennas. Subsequently the concept is extended for cavities of λ/6 thickness and three sub-wavelength antennas are presented for one, two and three double-

sided periodic arrays placed at about sixth of a wavelength from a ground plane and from each other. The proposed antennas are simulated using CST Microwave Studio™ and measured. The gain-bandwidth product of the measured prototypes outperforms any previous Fabry-Perot antenna design with the same profile.

The effective material parameters of the proposed multilayer metasurfaces are also calculated using a well known parameter retrieval technique. The parameters are extracted using the reflection and transmission characteristics of the metasurfaces yielding a broadband ε-near zero (ENZ) and near zero index (NZI) effect. This demonstrates that our proposed design concept can be used to develop broadband ENZ metamaterials.

5.1 DESIGN OF PERIODIC AMC-PRS ARRAYS

A novel multi-layer periodic array design is proposed yielding two sub-wavelength profile Fabry-Perot cavities that significantly enhance the bandwidth performance of the resulting low profile antenna (Fig. 5.1.1a). Two double layer arrays of dissimilar dimensions are designed, each one consisting of an AMC and a PRS surface printed on either side of a dielectric substrate. They are placed at about quarter wavelength from a ground plane and from each other. Thus, two quarter-wave air cavities are created with a total profile of about λ/2. The elements on both AMC and PRS surfaces are sub-wavelength and not resonant in the frequency range of interest. A dipole, placed in the middle of the first cavity, is used as a primary source. A periodic analysis at unit cell level is initially carried out to extract and optimise the reflection characteristics of the surfaces. A finite size antenna employing the optimized multi-layer surfaces is simulated and presented in order to validate the advantages of the proposed design.

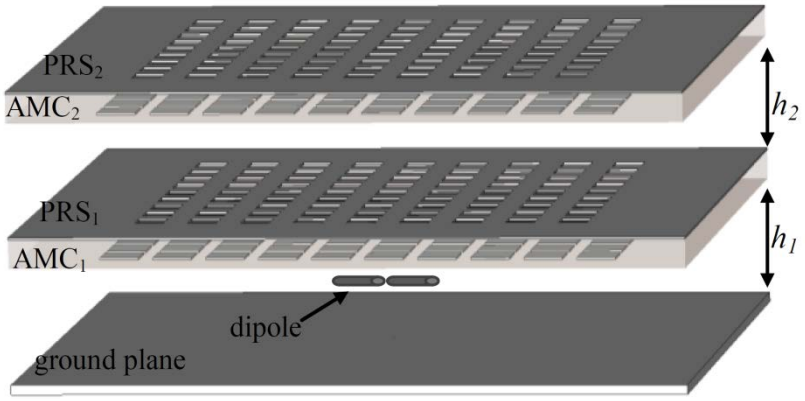

(a)

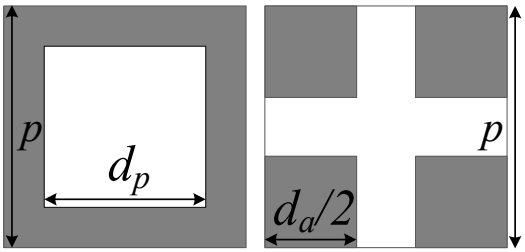

(b)

Fig. 5.1.1 (a) Schematic diagram of the proposed antenna (dimensions are not to scale), (b) PRS array (left) and AMC array (right).

5.1.1 Unit Cell Design of AMC-PRS

5.1.1.1 *Single-Layer AMC-PRS*

Initially, a single layer AMC-PRS structure is being studied. The AMC and PRS arrays are printed on both sides of a 1.5mm thick dielectric substrate with ε_r=2.2. The AMC array is formed by square metallic patches with a periodicity p=5.5mm, while the PRS array is formed by square apertures with the same periodicity, shifted with respect to the AMC array by p/2 in x and y-axis. The unit cell dimensions are shown in Fig. 5.1.1 (b) for the bottom (AMC) side and for the top (PRS) side, with d_p=3mm and d_a=4mm.

The basic concept of the investigated design is to achieve a near zero reflection phase for the desired operating frequency, with high reflection magnitude values. It is worth reminding here that high reflection magnitude values are required to obtain highly directive antennas. The reflection phase is controlled predominately by the dimensions of the AMC while the magnitude by the aperture size of the PRS. Therefore the dimensions of the unit cell have been carefully selected to obtain a reflection phase of zero degrees at 14GHz. Periodic boundary conditions are applied in the simulation software, assuming an infinite structure and the extracted reflection characteristics are presented in Fig. 5.1.2. It can be observed that high values of magnitude are obtained due to the highly reflective PRS. From the equation (2.1-8), substituting ϕ_R with zero degrees, the resulting cavity thickness is λ/4 which for 14GHz is 5.36mm.

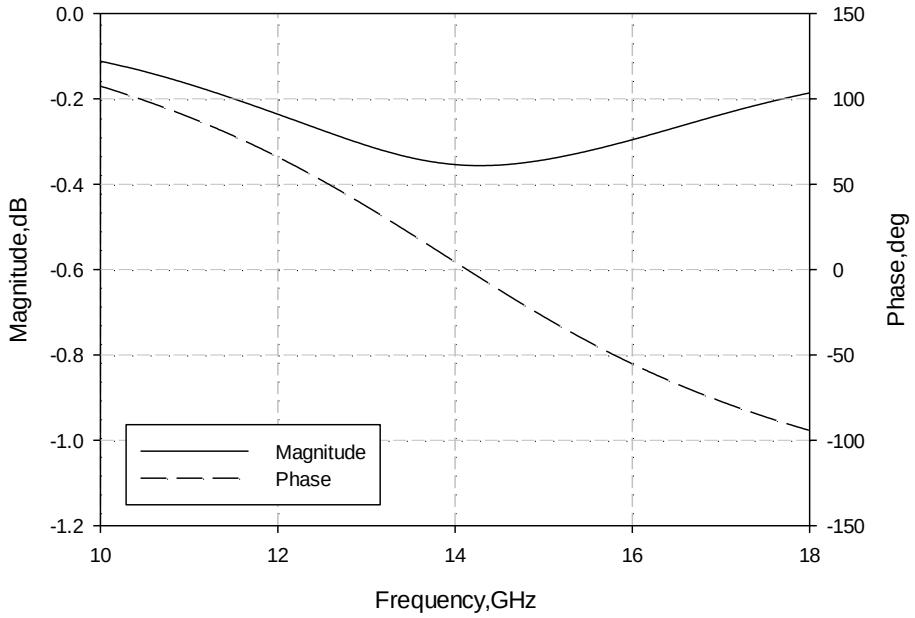

Fig.5.1.2 Reflection magnitude and phase of single layer AMC-PRS.

5.1.1.2 *Double-Layer AMC-PRS*

In this section, a multi-layer array structure is designed employing two pairs of composite AMC-PRS surfaces (Fig. 5.1.1). Again, the AMC and PRS arrays are printed on both sides of a 1.5mm thick dielectric substrate and the periodicity of the arrays is the same as in the case of the single-layer AMC-PRS structure, i.e. p=5.5mm. Initially the first AMC-PRS array is designed as explained in the previous section, such that high reflection magnitude values and a close to zero reflection phase are obtained for normal plane wave incidence from the AMC side. Next, a second double-layer array is added over the first one (Fig. 5.1.3). The resonance condition for the formed cavity with thickness h_2 (Fig. 5.1.3), is written in (5.1-1) where ψ_{R1} and ϕ_{R2} are the reflection coefficient phases as shown in the figure under normal incidence. The dimensions of the double-layer arrays are designed to achieve reflection phases ψ_{R1} and ϕ_{R2} respectively that satisfy (5.1-2) for a cavity thickness h_2 of about λ/4 at 13.7GHz.

Periodic boundary conditions are applied to the unit cell of the structure in CST Microwave Studio, assuming an infinite structure, and the reflection coefficients are extracted. The dimensions are shown in Fig. 5.1.3 with d_{p1}=3.4mm, d_{p2}=3.7mm, d_{a1}=d_{a2}=4mm and h_2=4.8mm. These dimensions are chosen after investigation based on the previous analysis. The phase (ψ_{R1}) and magnitude of the reflection coefficients under normal incidence at PRS_1 (first layer) are presented in Fig. 5.1.4. High magnitude values are obtained, while the reflection phase is 169^o at 13.7GHz. The complex reflection coefficient at AMC_2 is shown in Fig. 5.1.5. It can be observed that the reflection phase ϕ_{R2} is equal to -15^o at 13.7GHz. Substituting these values of ϕ_{R2} and ψ_{R1} in (5.1-2) results in a cavity thickness h_2 equal to 4.98mm, which is close to quarter wavelength and to the value that has been selected.

$$\phi_{R2} - \psi_{R1} - \frac{2\pi}{\lambda} 2h_2 = \pm 2N\pi \,, \quad N=0,1,2... \tag{5.1-1}$$

$$h_2 = (\frac{\phi_{R2}}{\pi} - \frac{\psi_{R1}}{\pi})\frac{\lambda}{4} + N\frac{\lambda}{2} \,, \quad N=0,1,2... \tag{5.1-2}$$

Then, the complex reflection coefficient of the multi-layer structure for normal incidence at AMC_1, is presented in Fig. 5.1.6. The reflection phase ϕ_{R1} is zero at 13.7GHz. Moreover, a phase increase is observed around zero degrees between 13.5GHz and 13.9GHz. Based on a ray optics analysis explained in Chapter 2.1, for a maximum directivity within a certain frequency range, a linearly increasing with frequency phase response is required. The theoretical ideal phase derived from ray theory is also included in the graph. It is expected that at the frequencies where the two phase responses intersect, the directivity will be maximum.

Finally, the multi-layer structure is placed over a ground plane and a primary source (dipole). The first cavity thickness is set at h_1=5.5mm (Fig. 5.1.1a) which is λ/4 at 13.7GHz, where the reflection phase is equal to zero. This will produce a dual quarter-wave resonant cavity antenna with a total profile of about λ/2.

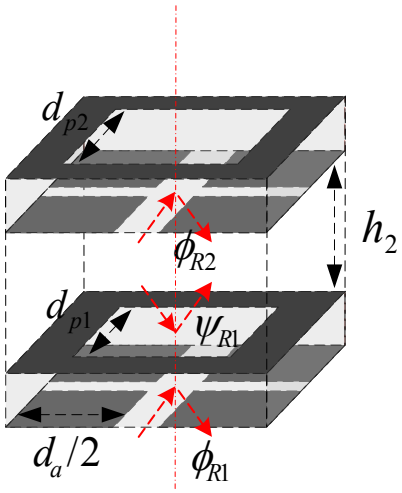

Fig. 5.1.3 Unit cell of the multi-layer structure.

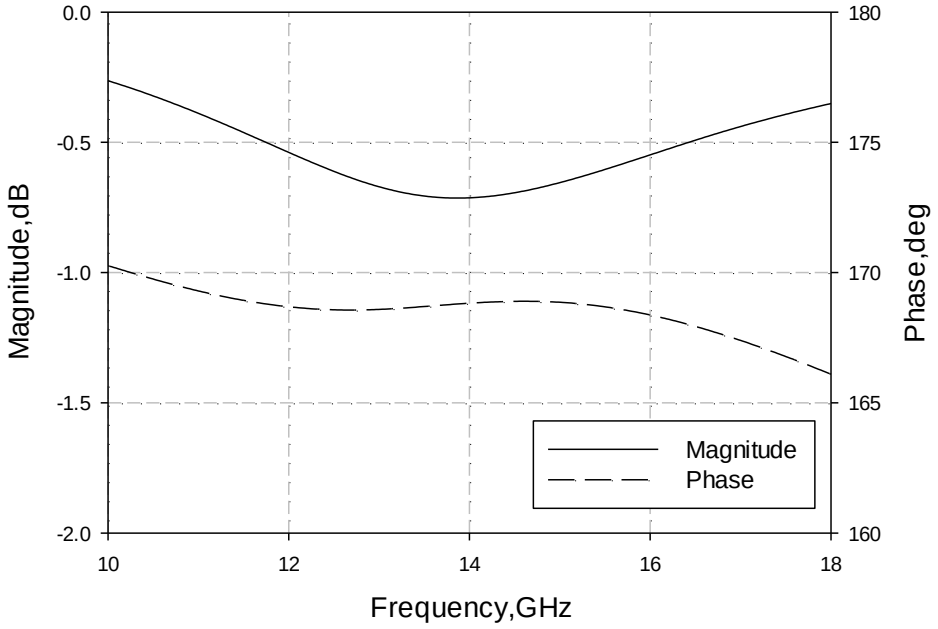

Fig. 5.1.4 Reflection magnitude and phase at PRS_1.

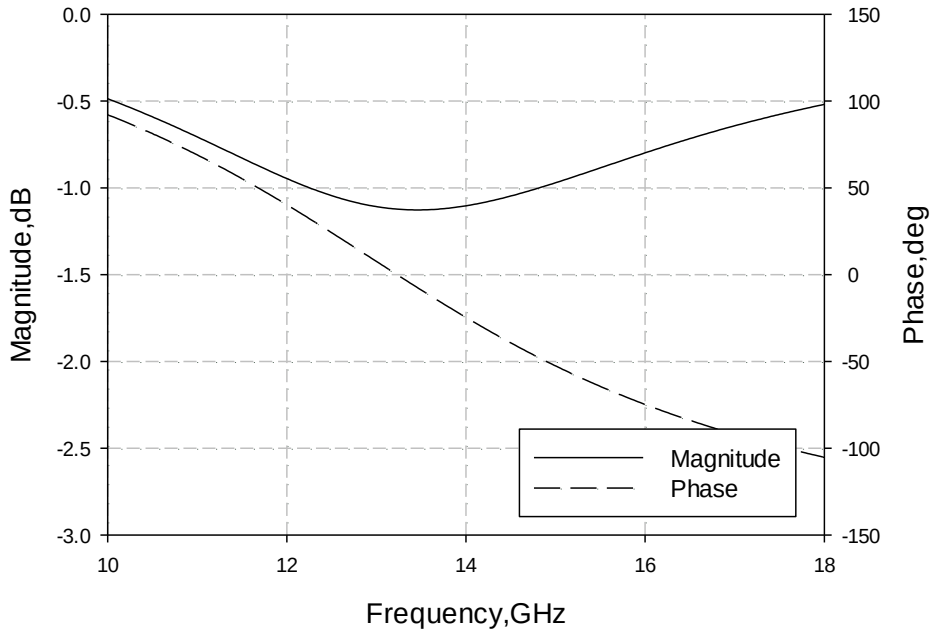

Fig. 5.1.5 Reflection magnitude and phase at AMC_2.

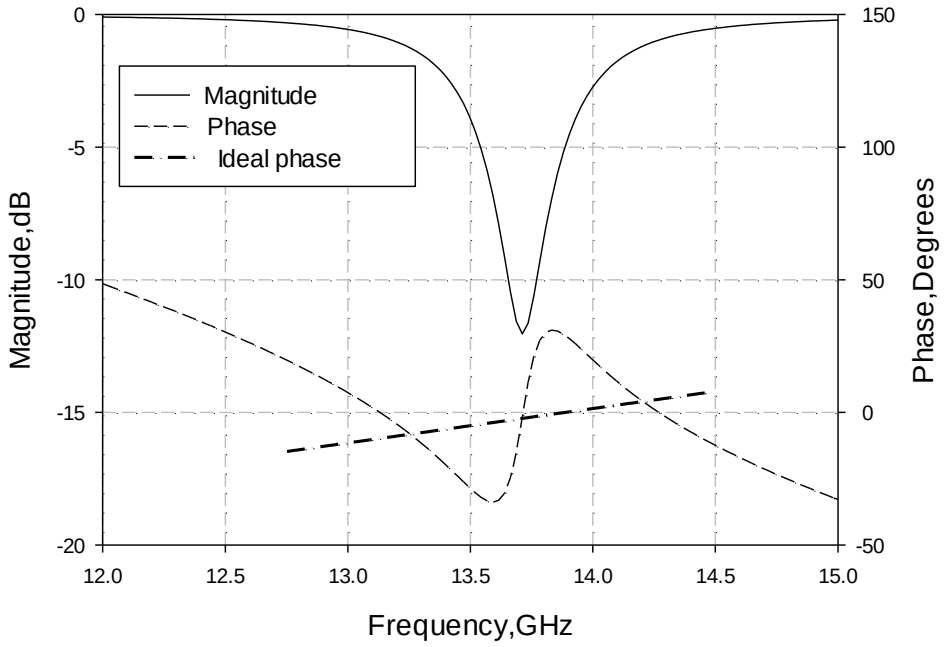

Fig. 5.1.6 Reflection magnitude and phase of the multi-layer AMC-PRS.

5.1.2 Finite Size Antennas

Based on the conclusions from the unit cell analysis in section 5.1.1.1, a finite size antenna is designed. It consists of employing the single-layer AMC-PRS array placed at distance h_1=5mm from a ground plane with 80 mm x 80 mm overall dimensions. The dimensions of the elements are as described in 5.1.1. An ideal dipole has been used as excitation. The antenna structure resembles the one depicted in Fig. 5.1.1, but with only one composite AMC-PRS layer instead of two. The simulated directivity versus frequency is presented in Fig. 5.1.7. A maximum of 18dBi is achieved at 14.3GHz. Although it is a finite size structure, the operation frequency agrees well with the ray analysis.

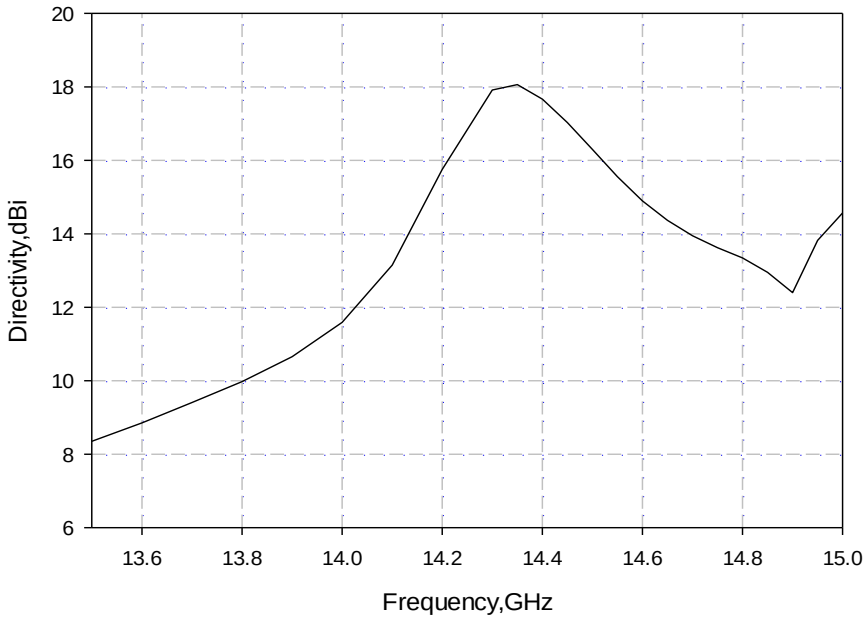

Fig. 5.1.7 Directivity vs frequency for the single layer finite size antenna.

Subsequently, a finite size antenna has been implemented based on the analysis of section 5.1.1.2, employing two double-layer AMC-PRS structures over a ground plane as shown in Fig. 5.1.1 (a). The overall lateral dimensions of the structure are again 80mm x 80mm, while the cavity distances and the dimensions of the periodic elements are those mentioned in 5.1.1.2. The profile of the antenna is thus h_1+h_2 plus 3mm which is the total thickness of the two dielectric substrates. So in total, the antenna profile is 13.3mm, which is just over λ/2 at the central frequency 13.7GHz. An ideal dipole has been used as excitation, placed in the middle of the first cavity. The simulated directivity versus frequency is presented in Fig. 5.1.8. Two peaks occur in the directivity which correspond approximately to the two intersection points between the reflection phase of the optimised multi-layer array and the ideal phase satisfying the resonant condition (see Fig. 5.1.6). A maximum of 18.3dBi is obtained at 14.05GHz. A broadband performance is achieved with a 3-dB radiation bandwidth of 8%. The simulated H- and E-plane radiation patterns are shown in Fig. 5.1.9 for four

frequencies within the operational bandwidth of the antenna. Good sidelobe level (below -10dB) is observed with the patterns deteriorating as the frequency increases which is a typical behaviour in le:

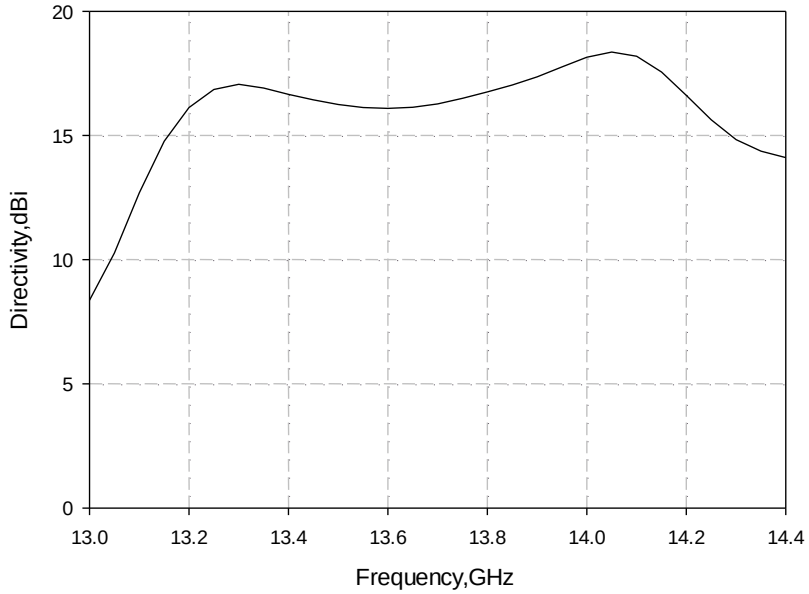

Fig. 5.1.8 Directivity vs frequency for the proposed multi-layer AMC-PRS antenna.

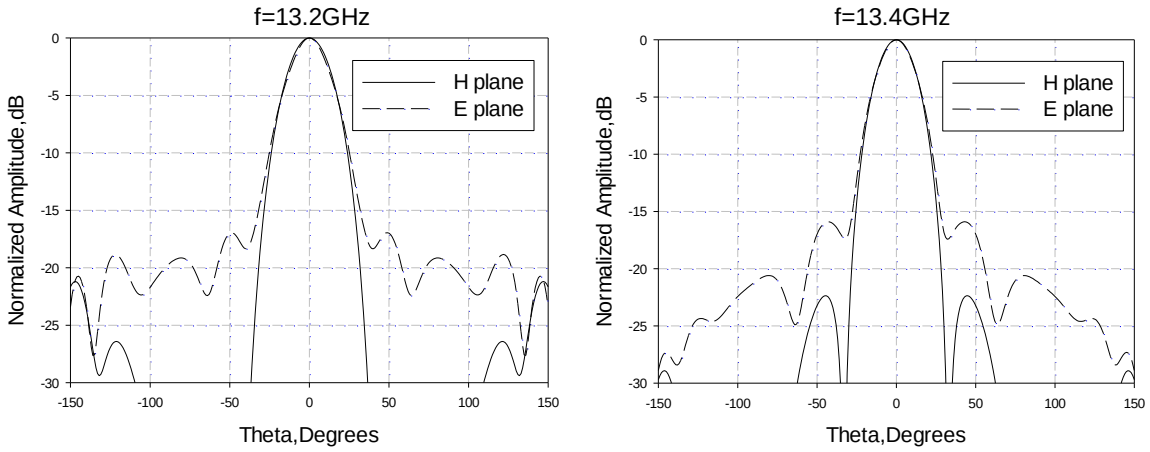

(a) (b)

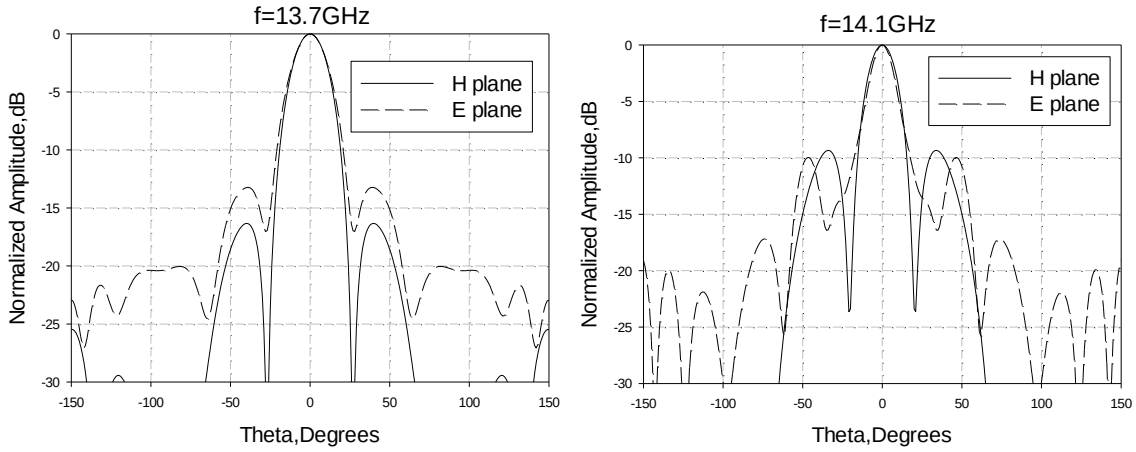

(c) (d)

Fig. 5.1.9 Simulated H- and E-plane radiation patterns at (a) 13.2GHz, (b) 13.4GHz, (c) 13.7GHz and (d) 14.1GHz.

5.1.3 Fabrication and Measurements

In order to fabricate and measure a prototype of the proposed sub-wavelength antenna, a practical feeding has been implemented. The two optimized composite double-layer AMC-PRS were then employed to design a finite size antenna as explained earlier but with a different feeding structure (Fig. 5.1.10). The feeding technique that has been initially introduced in Chapter 3.3 is used to excite the antenna comprising a dual slot at the ground plane, fed by a microstrip line. The feeding structure is dual resonant, resulting in a wideband matching. The dimensions of s_1 are 17.5mm x 1mm and of s_2 9.4mm x 1.5mm. Moreover from Fig. 5.1.10 (b), a=37.2mm and b=42.8mm while the length and width of the microstrip line are l=50.5mm and w=4.8mm respectively.

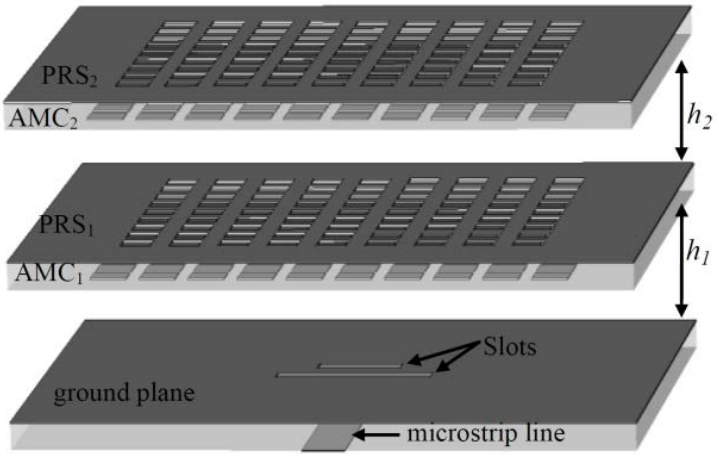

(a)

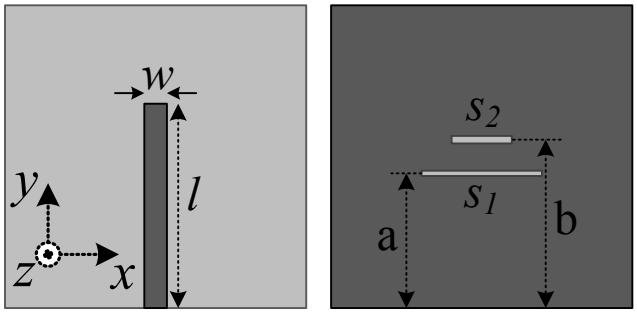

(b)

Fig. 5.1.10 (a) Schematic diagram of the proposed antenna (dimensions are not to scale) and (b) back and front view of ground plane with the microstrip line and slots.

The simulated gain of the antenna is presented in Fig. 5.1.11. A maximum gain of 16.1dBi is obtained at 13.5GHz. A broadband performance is achieved with a 3-dB gain bandwidth of 8.7%. The simulated S_{11} is also shown in the figure. Two minima occur at 13.46GHz and 14.1GHz due to the dual resonant feeding. It can be seen that the S_{11} is satisfactory across the antenna radiation bandwidth.

In order to validate the simulation results, a prototype of the proposed antenna was fabricated and experiments were carried out to measure the antenna's performance. Plastic spacers have

been used to define the air cavities between the AMC-PRS surfaces and the ground plane. The measured gain and S_{11} are also included in Fig. 5.1.11. A maximum gain of 16.9dBi has been measured with a 7.3% 3dB-bandwidth while the antenna's matching is well below -10dB from 13.65GHz to 14.55GHz. It can be observed that, the antenna's operation is slightly shifted towards higher frequencies compared to the simulated one. This discrepancy is attributed to fabrication tolerances of both the cavity thicknesses and the feeding slots dimensions. The simulated and measured H- and E-plane radiation patterns are shown in Fig. 5.1.12 for four frequencies across the operational bandwidth of the antenna. For the measured patterns at each frequency, an angular resolution of 1^{o} was obtained. Highly directive patterns and low sidelobe level is observed in both planes at the measured frequencies. Good agreement with the simulation results is obtained. An asymmetry is evident for both simulated and measured E-plane patterns, which is caused by the asymmetrical feeding at this plane (YZ). Nevertheless the patterns in both planes demonstrate a directive emission.

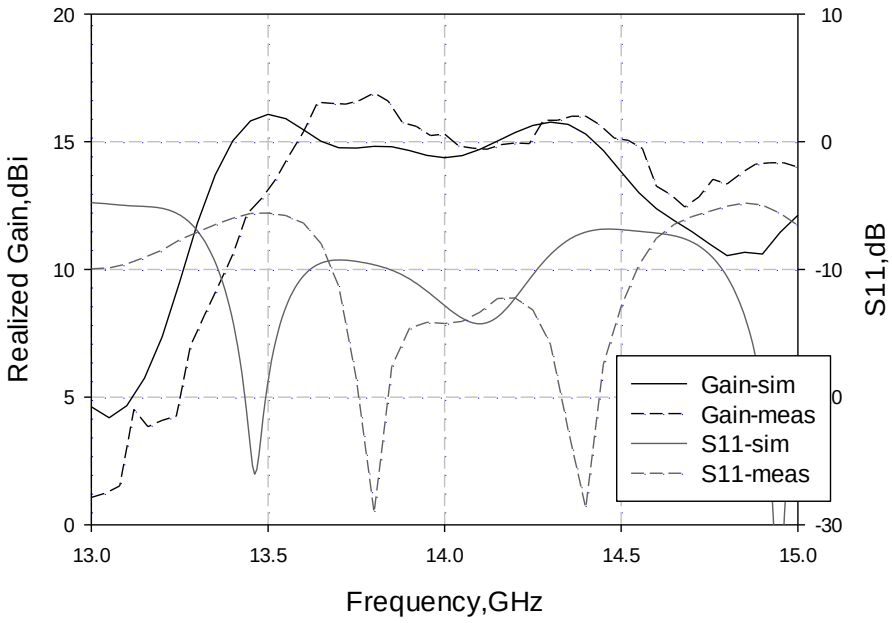

Fig. 5.1.11 Comparison of simulated and measured gain and S_{11} for the proposed multi-layer AMC-PRS antenna.

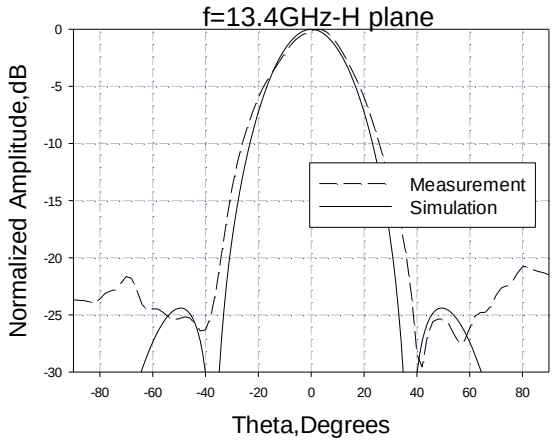
f=13.4GHz-H plane
Normalized Amplitude,dB
Theta,Degrees
Measurement
Simulation

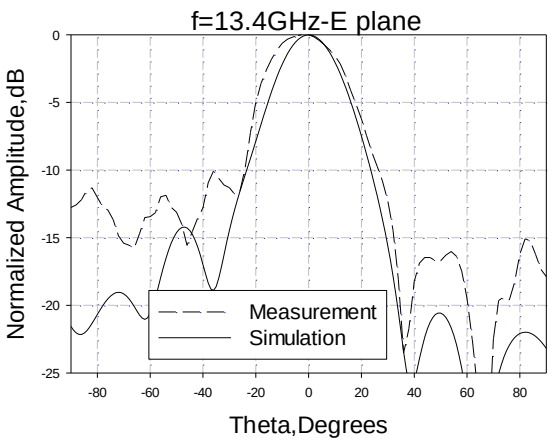
f=13.4GHz-E plane
Normalized Amplitude,dB
Theta,Degrees
Measurement
Simulation

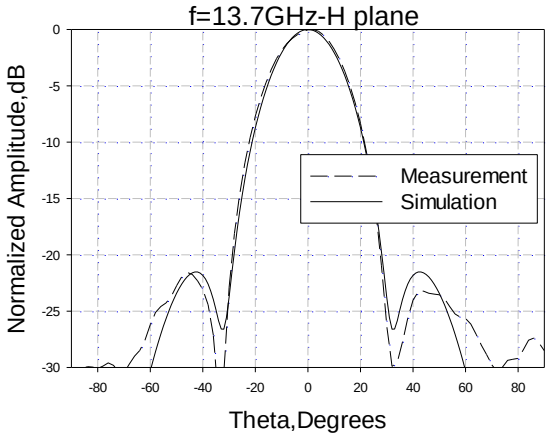
f=13.7GHz-H plane
Normalized Amplitude,dB
Theta,Degrees
Measurement
Simulation

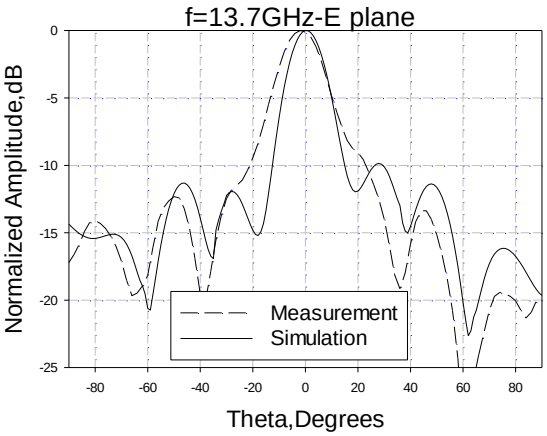
f=13.7GHz-E plane
Normalized Amplitude,dB
Theta,Degrees
Measurement
Simulation

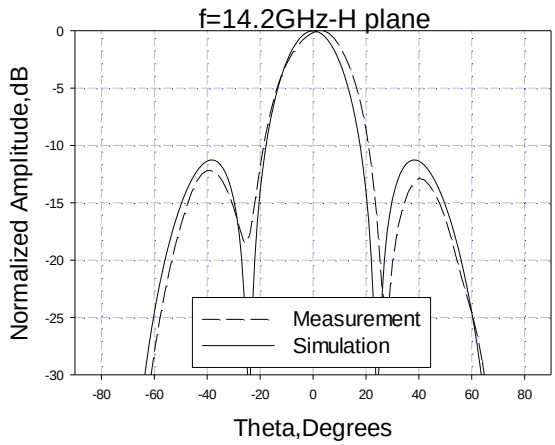
f=14.2GHz-H plane
Normalized Amplitude,dB
Theta,Degrees
Measurement
Simulation

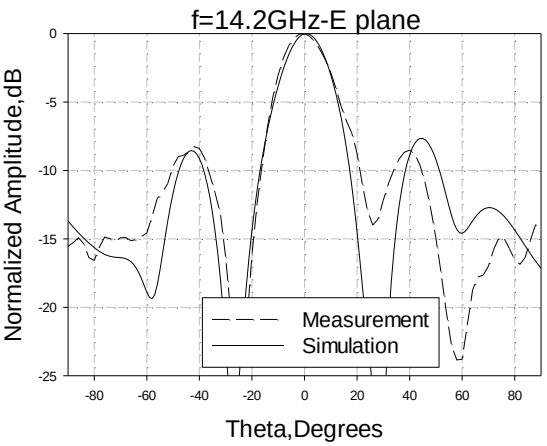
f=14.2GHz-E plane
Normalized Amplitude,dB
Theta,Degrees
Measurement
Simulation

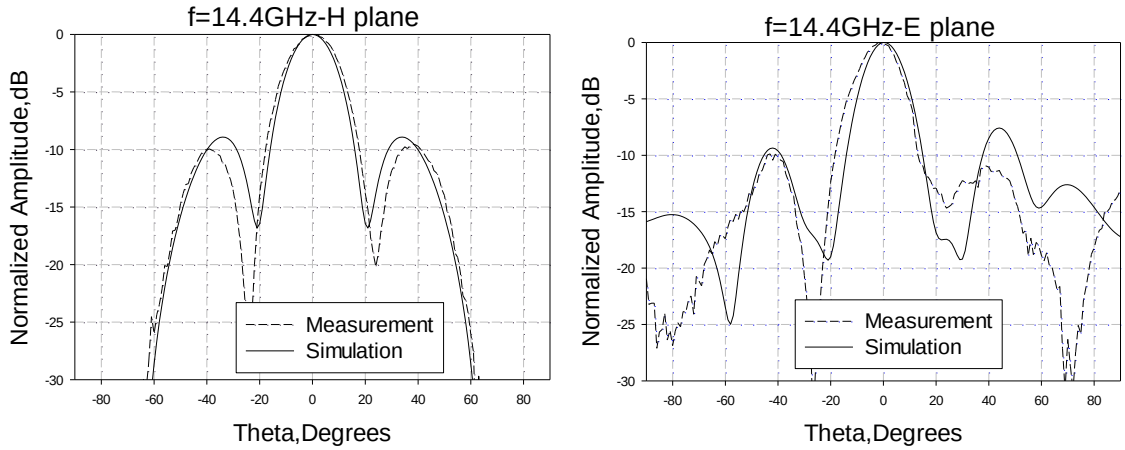

(a) (b)

Fig. 5.1.12 Comparison between simulated and measured (a) H- and (b) E-plane radiation patterns at 13.4GHz, 13.7GHz, 14.2GHz and 14.4GHz.

5.2 DESIGN OF PERIODIC AIS-PRS ARRAYS FOR λ/6 CAVITY

In this section we extend the concept of multilayer sub-wavelength profile FP antennas for further profile reduction keeping the increased bandwidth performance. Three double-sided arrays are employed each one consisting of an Artificial Impedance Surface (AIS) and a PRS surface with sub-wavelength unit cell dimensions printed on either sides of a dielectric substrate. The term AIS is used to differentiate from the AMC due to the fact that an AIS exhibits reflection phase values other than 0 degrees. Hence, after optimising their phase response, they are designed here to create λ/6 air cavities instead of λ/4. The design of the multilayer AIS-PRS structure is initially being studied and then three sub-wavelength finite size FP antennas are investigated using a single-layer, a double-layer and a three-layer AIS-PRS respectively, fed by the two optimised microstrip-fed slots that were used in the λ/4 case.

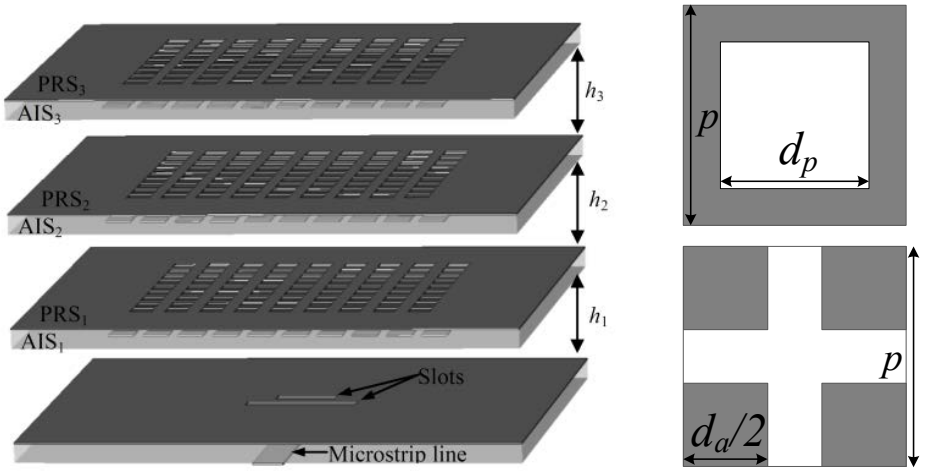

(a) (b)

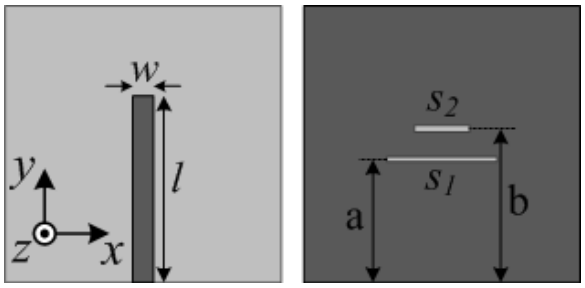

(c)

Fig. 5.2.1 (a) Schematic diagram of the proposed antenna (dimensions are not to scale), (b) top (PRS array) and bottom (AIS array) view of the unit cell, (c) back and front view of ground plane with the microstrip line and slots.

5.2.1 Unit Cell Design of AIS-PRS

5.2.1.1 *Single-Layer AIS-PRS*

Initially a single layer AIS-PRS structure is designed. The AIS and PRS arrays are printed on both sides of a 1.55mm thick dielectric substrate with ε_r=2.2. The AIS array is formed by square metallic patches with a periodicity p=5.5mm, while the PRS array is formed by square apertures with the same periodicity, shifted with respect to the AIS array by $p/2$ in x and y-

axis. The unit cell dimensions are shown in Fig. 5.1.1 (b) for the bottom (AIS) side and for the top (PRS) side, with d_p=3mm and d_a=4.4mm. In order to create a λ/6 cavity, the reflection phase of the structure ϕ_R has to satisfy (2.1-8) for h=λ/6 (π is the phase introduced by the total reflection at the ground), i.e. to be -60^o at the desired operating frequency, with high reflection magnitude values to achieve a high directivity antenna. Therefore the dimensions of the unit cell have been carefully selected to obtain the required reflection phase at 14GHz. Periodic boundary conditions are applied in the simulation software, assuming an infinite structure to extract the reflection coefficients. The simulated reflection characteristics are presented in Fig. 5.2.2. It can be observed that high values of magnitude are obtained due to the highly reflective PRS and a reflection phase of -60^o is obtained at 14GHz.

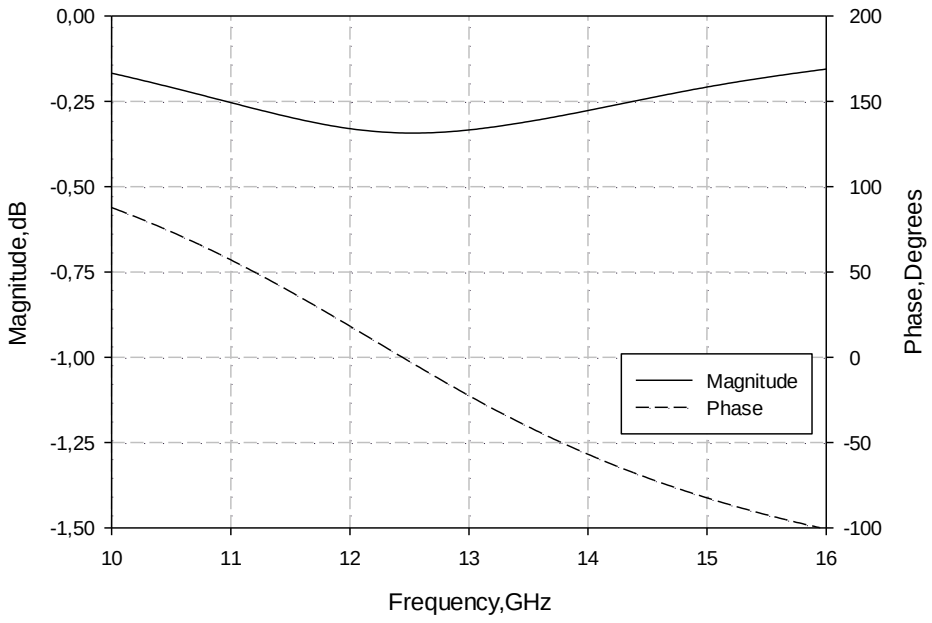

Fig. 5.2.2 Reflection magnitude and phase of single layer AIS-PRS.

5.2.1.2 *Double-Layer AIS-PRS*

Next, the concept of the sub-wavelength profile antenna is extended for multilayer structures. In this section, a double layer structure is designed employing two composite surfaces of AIS-

PRS. Initially the first layer is designed following the procedure that was followed for the design of the single AIS-PRS layer. The dimensions are chosen such that high reflection magnitude values and a reflection phase of -60^o are obtained. Next, a second layer is added at λ/6 distance from the first one. The resonance condition (5.1-1) for the second cavity is derived from (2.1-8) after replacing the reflection phase π from the ground plane with ψ_{R1} which is the reflection phase at the first layer from the PRS side. In this case, the reflection phase at the second layer from the AIS side is ϕ_{R2} (Fig. 5.2.3). Since ψ_{R1} is replacing the full reflection from the ground plane, the PRS of the first layer should be designed to achieve a phase of around π (180^o). Substituting h_2 with λ/6 in (5.1-2), the value of ϕ_{R2} can be calculated. For N=1 and ψ_{R1}=172^o, it can be extracted that ϕ_{R2} should be -68^o at the operational frequency for the equation to be satisfied.

Periodic boundary conditions are then applied to the unit cell of the multilayer structure and the reflection coefficients are extracted. The dimensions are shown in Fig. 5.2.3 with d_{p1}=3mm, d_{p2}=3.6mm, d_{a1}=d_{a2}=4.4mm and h_2=3.6mm. Furthermore the thickness of the first cavity is h_1=4mm. These dimensions are chosen after investigation, in order to obtain the desired values for the reflection phases ϕ_{R1}, ϕ_{R2} and ψ_{R1}. The phase and magnitude for reflection at the PRS_1 (first layer) are presented in Fig. 5.2.4. High magnitude values are obtained, while the reflection phase ψ_{R1} is stable at 172^o around the resonant frequency. For the second layer, the complex reflection coefficient at the side of AIS_2 is shown in Fig. 5.2.5. It can be observed that the reflection phase ϕ_{R2} is -70^o around 14GHz. Inserting the values of ψ_{R1} and ϕ_{R2} for f=14GHz at (5.1-2) the cavity distance is h_2=3.51mm which is in good agreement with the actual value that has been used. Finally, the complex reflection coefficient for incidence at AIS_1, including the complete double layer unit cell in the simulation, is

presented in Fig. 5.2.6. It should be noted at this point that the selection of the aperture size of the PRSs has been such that a phase increase would be achieved in the frequency range of operation. Indeed, from Fig. 5.2.6 it can be observed that a phase increase occurs for ϕ_{R1}, between 13.6GHz and 13.8GHz. The theoretical phase derived from (2.1-8) for h_1=4mm is also included in the graph. Moreover, the reflection phase ϕ_{R1} is -50^o at 13.7GHz, resulting in a cavity thickness of h_1=3.95mm from the ray optics analysis, which again is close to the actual value that has been used for the design.

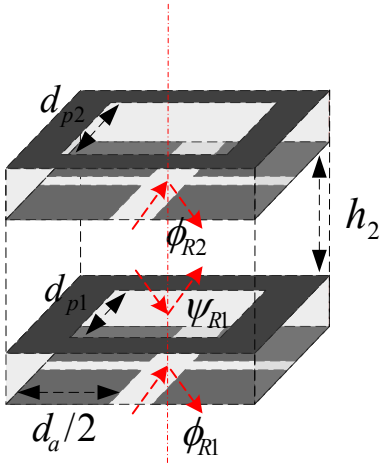

Fig. 5.2.3 Unit cell of the double layer structure.

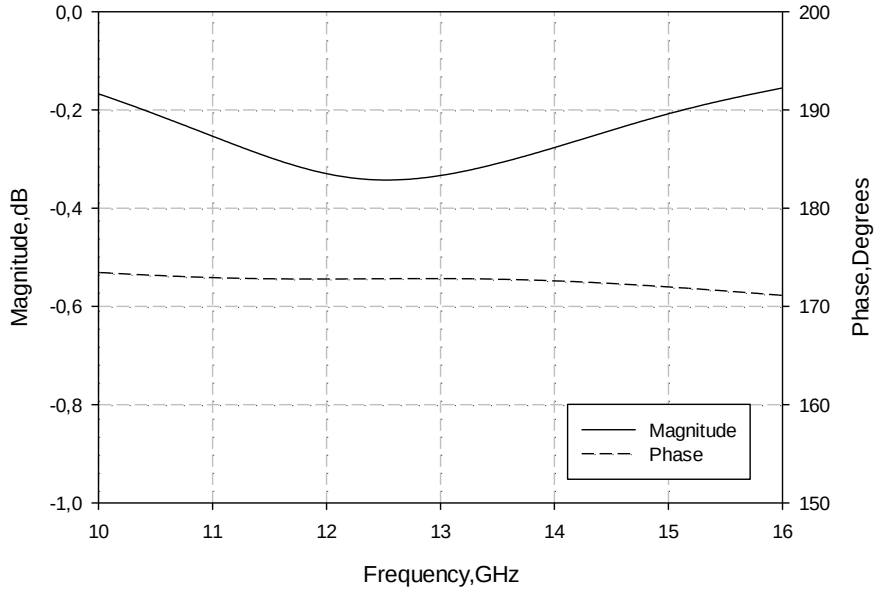

Fig. 5.2.4 Reflection magnitude and phase at PRS_1.

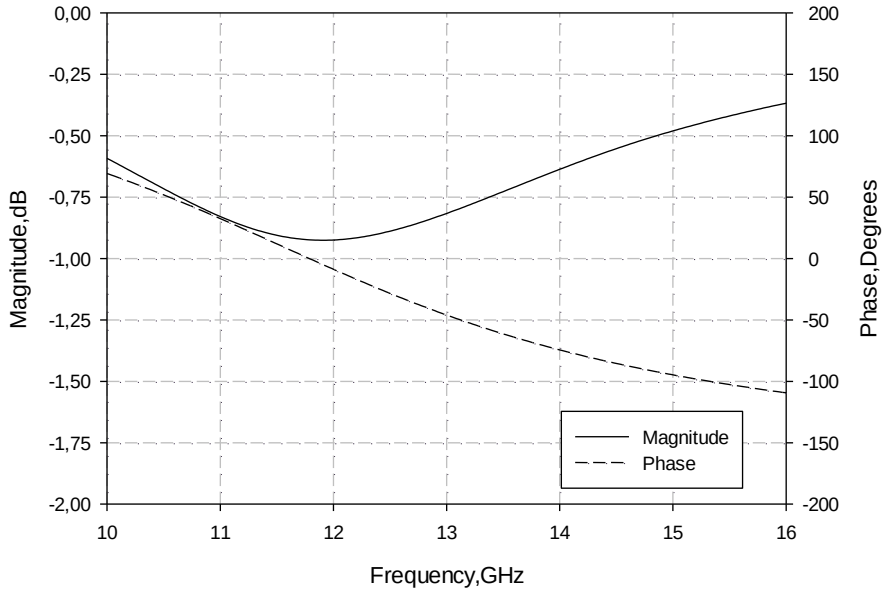

Fig. 5.2.5 Reflection magnitude and phase at AIS_2.

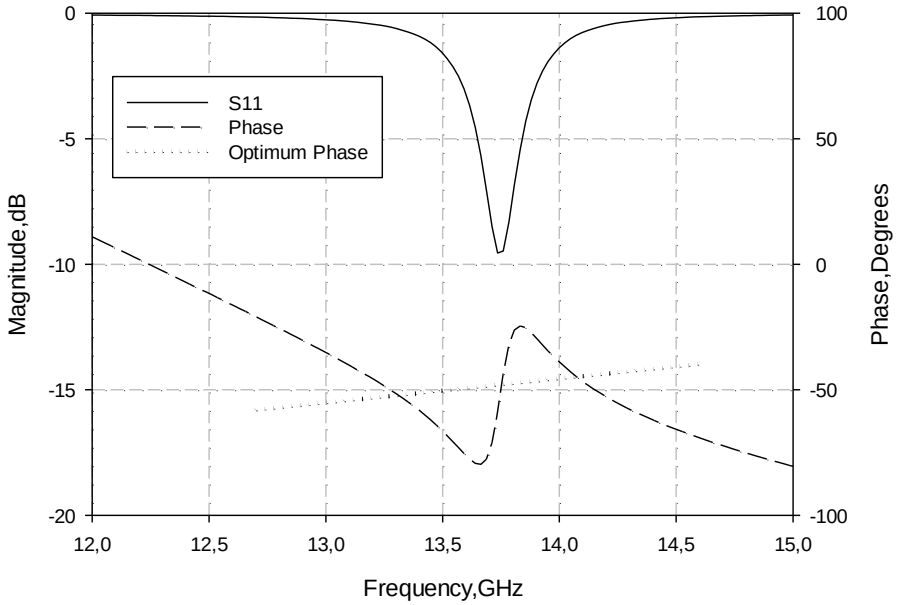

Fig. 5.2.6 Reflection magnitude and phase of the double layer AIS-PRS.

5.2.1.3 *Three-Layer AIS-PRS*

Based on the conclusion extracted from the analysis in Section 5.2.1.2, the concept is further extended to the design of three composite AIS-PRS layer sub-wavelength profile antenna. It must be emphasized that all three AIS-PRS layers in this design are different from the double-layer structure presented in the previous section. The unit cell of the structure is shown in Fig. 5.2.7. Again the first two layers are designed to satisfy (5.1-1) and (5.1-2) as described in the previous sections. For the third layer the dimensions are chosen such that the reflection phase ϕ_{R3} will result in a cavity of $h_3 = \lambda/6$ at the central frequency. The new optimised dimensions are d_{p1}=3.5mm, d_{p2}=3.1mm, d_{p3}=4.3mm, $d_{a1}=d_{a2}=d_{a3}$=4.4mm, h_2=3.9mm and h_3=2.64mm (Fig. 5.2.7). Also, the first cavity thickness h_1 is set at 3.65mm (Fig. 5.2.1a).

Periodic boundary conditions are applied to the unit cell of the structure and the reflection characteristics are calculated. For incidence at PRS_1, the magnitude and phase of the reflection coefficients are presented in Fig. 5.2.8. For incidence at the AIS_2 (second layer) the

reflection magnitude and phase are presented in Fig. 5.2.9. It can be seen from Fig. 5.2.8 and Fig. 5.2.9 that the reflection phases ψ_{R1} and ϕ_{R2} at 13.7GHz, are 171° and -53° respectively. These values correspond to a cavity thickness h_2=4.13mm which is close to the optimised one. In Fig. 5.2.10 and Fig. 5.2.11, the reflection coefficients for incidence at PRS_2 and AIS_3 are depicted respectively. In this case, the reflection phases ψ_{R2} at 13.7GHz is 188°, while ϕ_{R3}=-90° at the same frequency. Substituting these values in the resonance condition for the third cavity, gives h_3=2.5mm. Finally, the reflection coefficients of the complete structure, for incidence at the first layer (AIS_1) are shown in Fig. 5.2.12. It can be observed that a double reflection phase increase with frequency is obtained for ϕ_{R1} from 13.1GHz to 14.2GHz. The theoretical ideal phase for h_1=3.65mm is again included in the graph. The obtained phase follows closely the ideal phase indicating that a more broadband antenna performance for this optimised three layer structure is expected. Moreover, the reflection phase ϕ_{R1} is -65° at 13.7GHz, giving a cavity thickness of h_1=3.5mm which determines the distance from the ground plane (Fig. 5.2.1a).

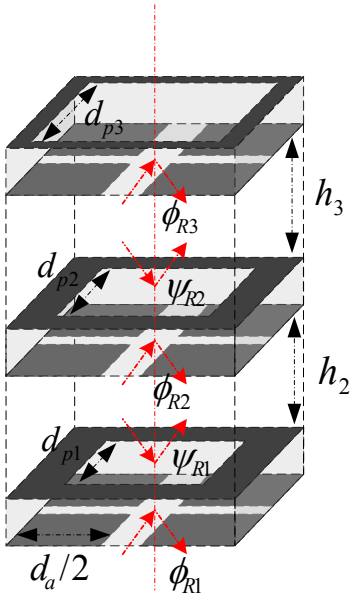

Fig. 5.2.7 Unit cell of the three layer structure.

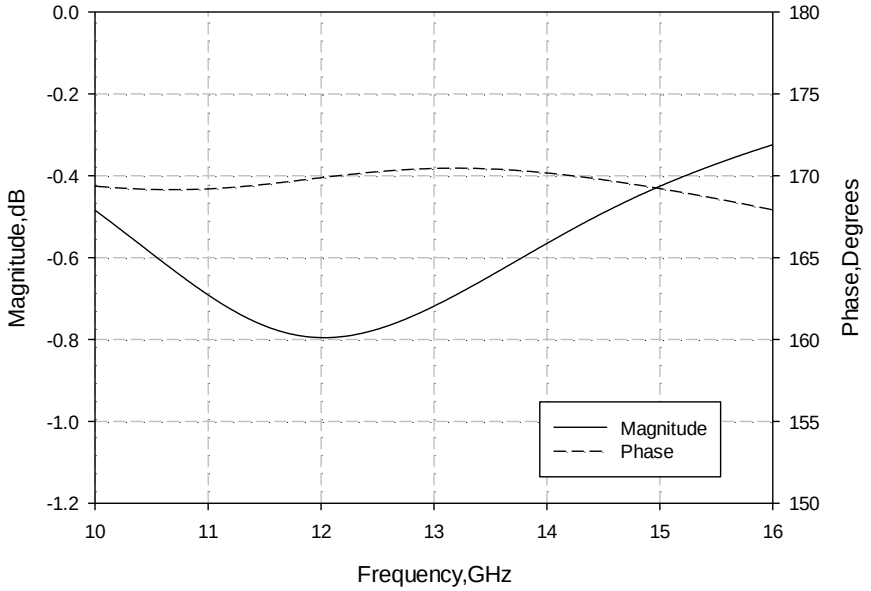

Fig. 5.2.8 Reflection magnitude and phase at PRS_1.

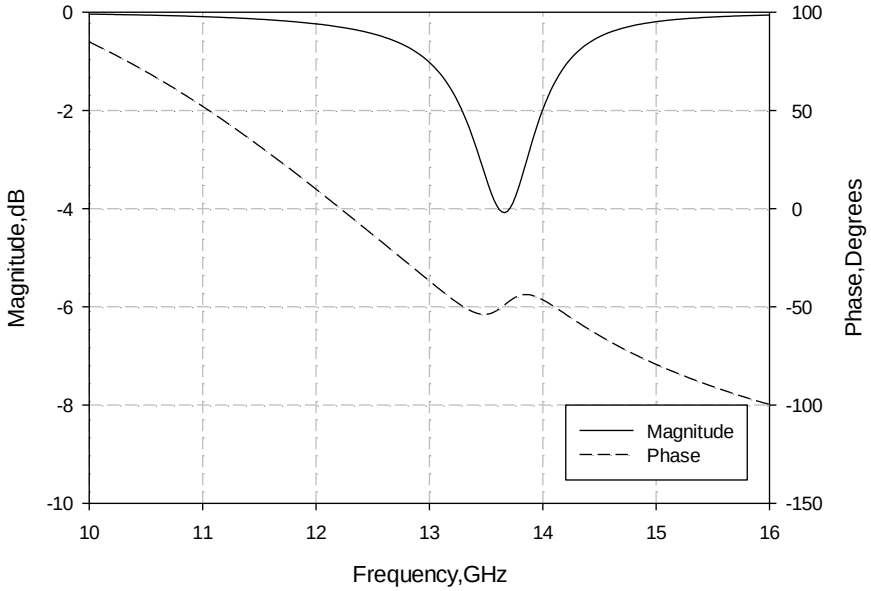

Fig. 5.2.9 Reflection magnitude and phase at AIS_2.

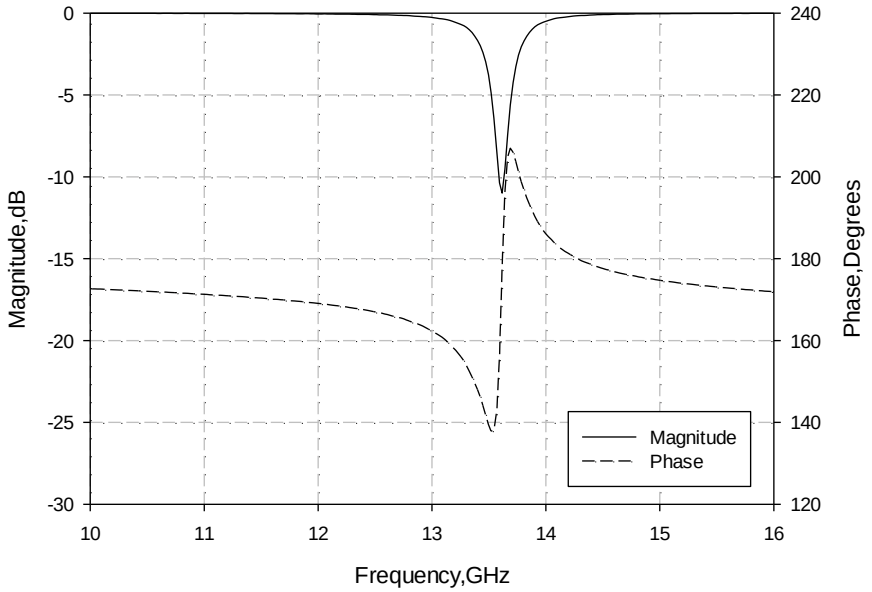

Fig. 5.2.10 Reflection magnitude and phase at PRS_2.

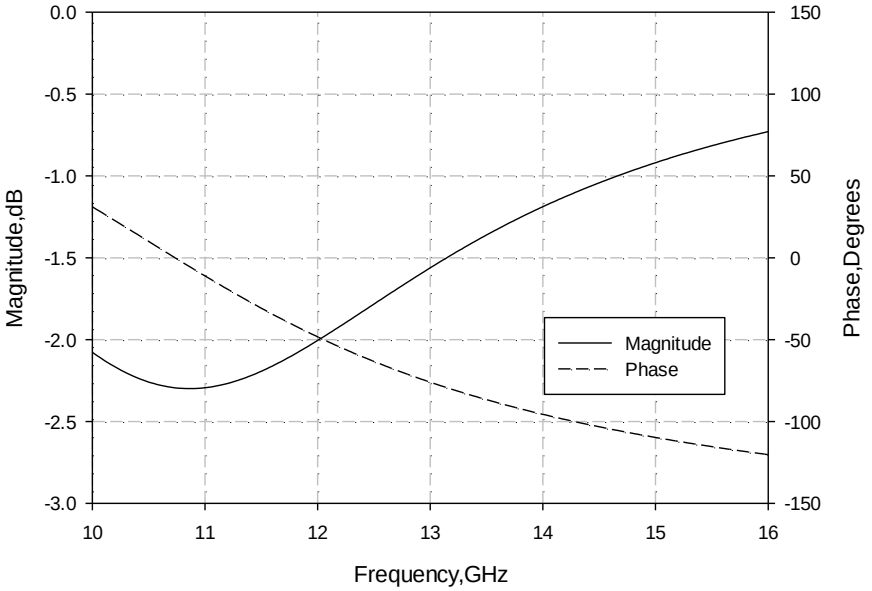

Fig. 5.2.11 Reflection magnitude and phase at AIS_3.

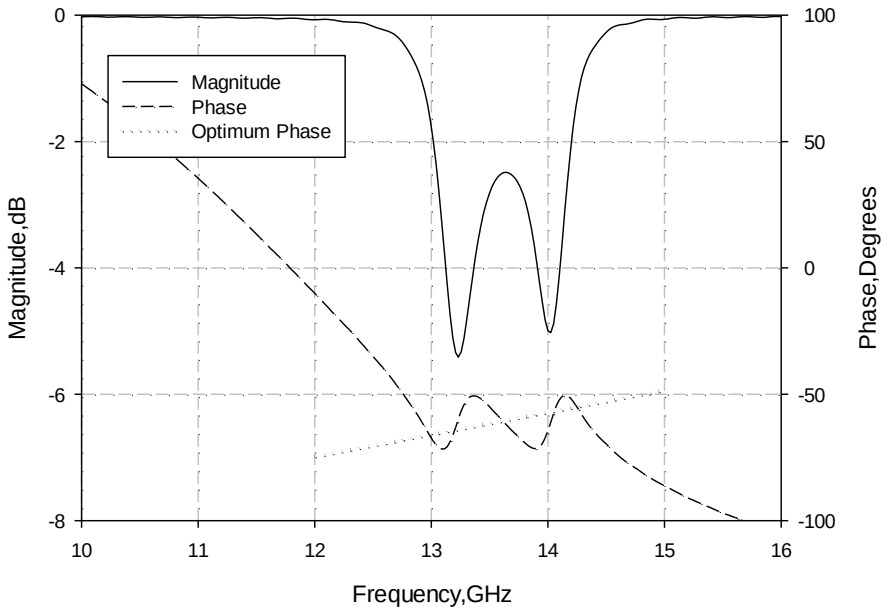

Fig. 5.2.12 Reflection magnitude and phase of the three layer AIS-PRS.

5.2.2 Finite Size Antennas

Based on the conclusions from the previous section, three sub-wavelength finite size antennas are designed: a single-layer AIS-PRS, a double-layer AIS-PRS and a three-layer AIS-PRS antenna. Each antenna has 80 mm x 80 mm overall dimensions. Initially the single-layer AIS-PRS antenna is designed consisting of an AIS-PRS array placed at distance h from a ground plane with d_p=3mm and d_a=4.4mm. The cavity distance is set at h=3.8mm to obtain an optimised performance which is slightly more than $\lambda/6$ at 14GHz (3.6mm). This small discrepancy between the ray optics analysis and the finite size antenna is due to the fact that the former assumes an infinite structure. The dual slot at the ground plane, fed by a microstrip line has been used to excite the antenna (Fig. 5.2.1c). The dimensions are as described in section 5.1.3. The ground plane and the microstrip line are printed on the same substrate (thickness 1.55mm and ε_r=2.2) as the composite AIS-PRS surfaces. The simulated directivity versus frequency is presented in Fig. 5.2.13. A maximum of 17dBi is achieved at 14.25GHz.

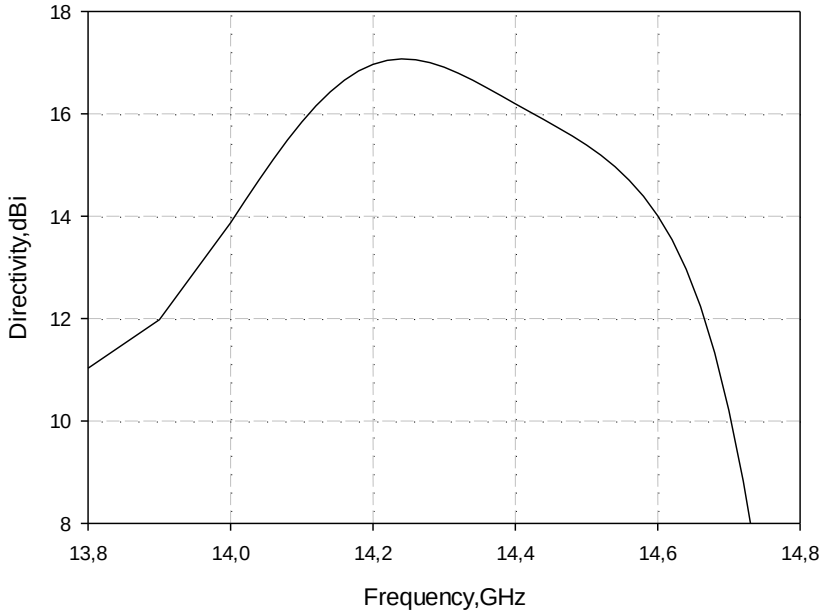

Fig. 5.2.13 Directivity vs frequency for the single layer AIS-PRS finite size antenna.

Subsequently, a finite size antenna has been implemented employing the double-layer AIS-PRS introduced in 5.2.1.2, over the ground plane. The overall lateral dimensions of the structure are 80mm x 80mm as in the single AIS-PRS layer antenna, while the cavity distances and the dimensions of the periodic elements are those mentioned in the corresponding subsection. The profile of the antenna is thus h_1+h_2 which is about $\lambda/3$. The simulated directivity of the antenna versus frequency is presented in Fig. 5.2.14. A maximum of 17.2dBi is achieved at 14.2GHz. It is interesting to note that two peaks appear in the directivity response, corresponding to the resonant modes of the two coupled cavities. It can be observed that an improved bandwidth performance is achieved with the proposed double AIS-PRS layer configuration compared to the single AIS-PRS layer antenna. A better comparison between the two designs is presented in Table I. This performance demonstrates that a broadband sub-wavelength profile, highly-directive antenna is feasible through the

introduction of extra optimised composite AIS-PRS layers. It should be emphasized that even with a profile of less than λ/2, high directivity and broad bandwidth is achieved.

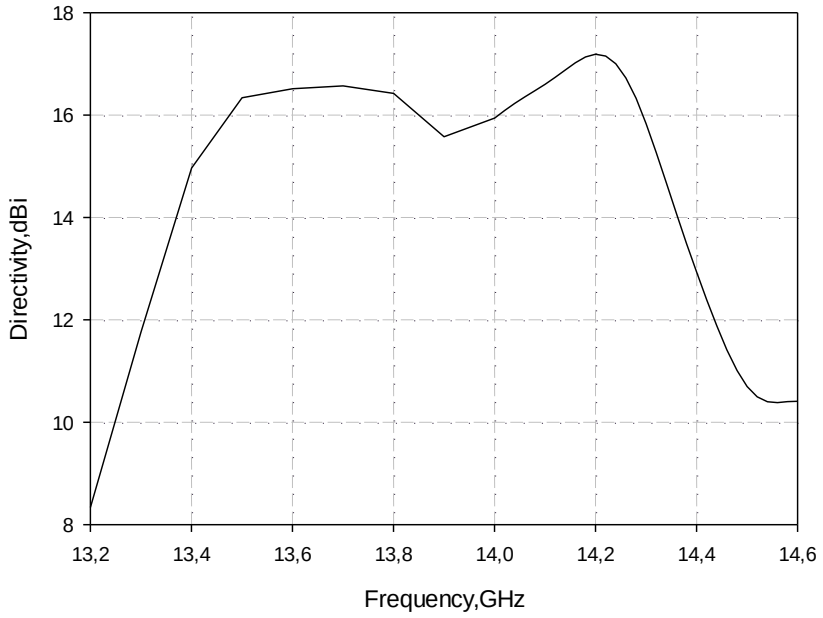

Fig. 5.2.14 Directivity vs frequency for the proposed double layer AMC-PRS antenna.

Finally, based on the periodic analysis of the three AIS-PRS layer structure, a finite size antenna has been implemented as shown in Fig. 5.2.1 (a). The antenna has the same overall lateral size like the previous two cases. The dimensions of the elements and the cavity distances are those mentioned in 5.2.1.3. The total profile of the antenna in this case is h_1+h_2+ h_3 which is approximately λ/2. The antenna is fed using the double-slot feeding structure which ensures a match covering the antenna's operation frequency range. The simulated directivity response of the antenna is presented in Fig. 5.2.15. A maximum of 16.9dBi is achieved at 13.8GHz with a 3dB radiation bandwidth of 10.7%. A fluctuation of less than 2dB is observed over the operational bandwidth. The antenna dimensions could be further optimised to achieve a more flat directivity response. Comparing the three aforementioned antenna designs presented in the figure, it is evident that the three AIS-PRS layer antenna achieves a more broadband performance. It can also be observed that three peaks occur in the

directivity curve in this case, corresponding to the three resonant modes. A more detailed comparison between the three designs in terms of maximum directivity and 3dB bandwidth is presented in Table I.

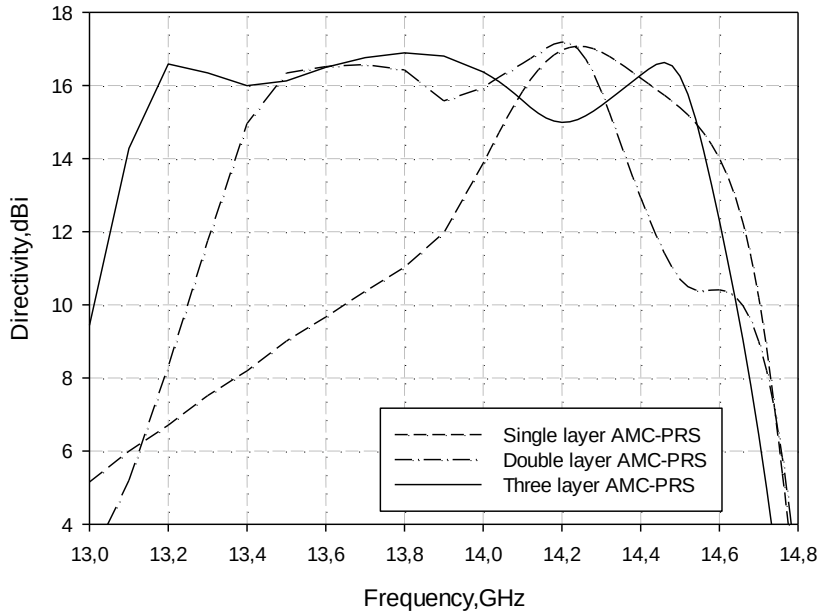

Fig. 5.2.15 Directivity vs frequency for the three proposed AMC-PRS antenna configurations.

TABLE I.

COMPARISON OF THE THREE AMC-PRS ANTENNA CONFIGURATIONS

Antenna Design	***Directivity max (dBi)***	***Bandwidth 3dB***
Single-Layer AMC-PRS	17	4.1%
Double-Layer AMC-PRS	17.2	7%
Three-Layer AMC-PRS	16.9	10.7%

5.2.3 Fabrication and Measurements

A prototype of the proposed three layer AIS-PRS antenna was fabricated and experiments were carried out to measure the antenna's performance and validate the simulation results. For each of the composite AIS-PRS surfaces, an array of 9x9 elements was etched off the copper to form the PRS side and an array of 10x10 patches was printed on the other side of a 1.55mm thick TLY-5 substrate to form the AIS (Fig. 5.2.16b). The same substrate was used for the ground plane comprising the two microstrip line fed slots (Fig. 5.2.16c). A photograph of the assembled antenna is shown in Fig. 5.2.16 (a). Plastic spacers have been used to define the air cavities between the AIS-PRS surfaces and the ground plane. The measured S_{11} of the fabricated prototype along with the corresponding simulation results are shown in Fig. 5.2.17. The fabricated antenna is well matched with S_{11} below -10dB from 13GHz to 14.5GHz which is in good agreement with the simulation result. The simulated and measured realized gain of the antenna is presented in Fig. 5.2.18. A maximum gain of 16.3dBi has been measured at 13.7GHz with a 10.9% 3dB-bandwidth. The simulated and measured H- and E-plane radiation patterns are shown in Fig. 5.2.19 for four frequencies across the operational bandwidth of the antenna. The small discrepancies between the simulation and measurement results are attributed to fabrication tolerances of both the cavity thicknesses and the feeding slots dimensions.

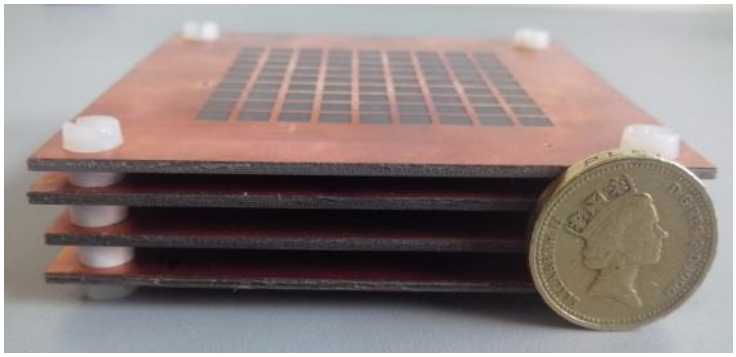

(a)

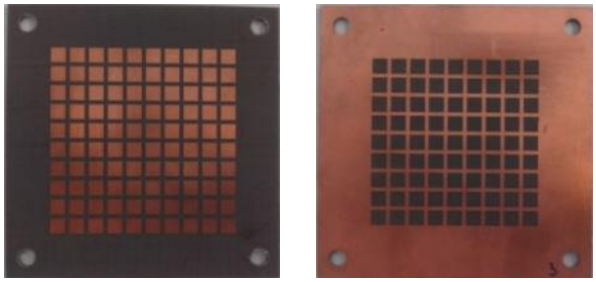

(b)

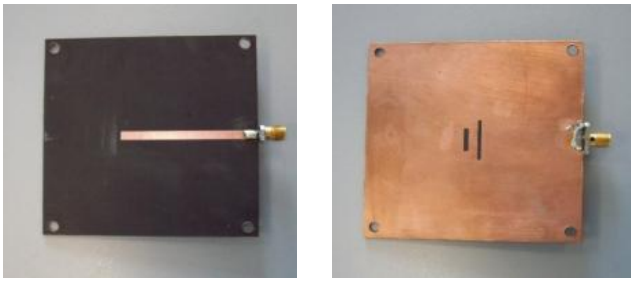

(c)

Fig. 5.2.16 (a) Photograph of the fabricated three layer AMC-PRS, (b) Both sides of AMC-PRS and (c) Both sides of the feeding structure.

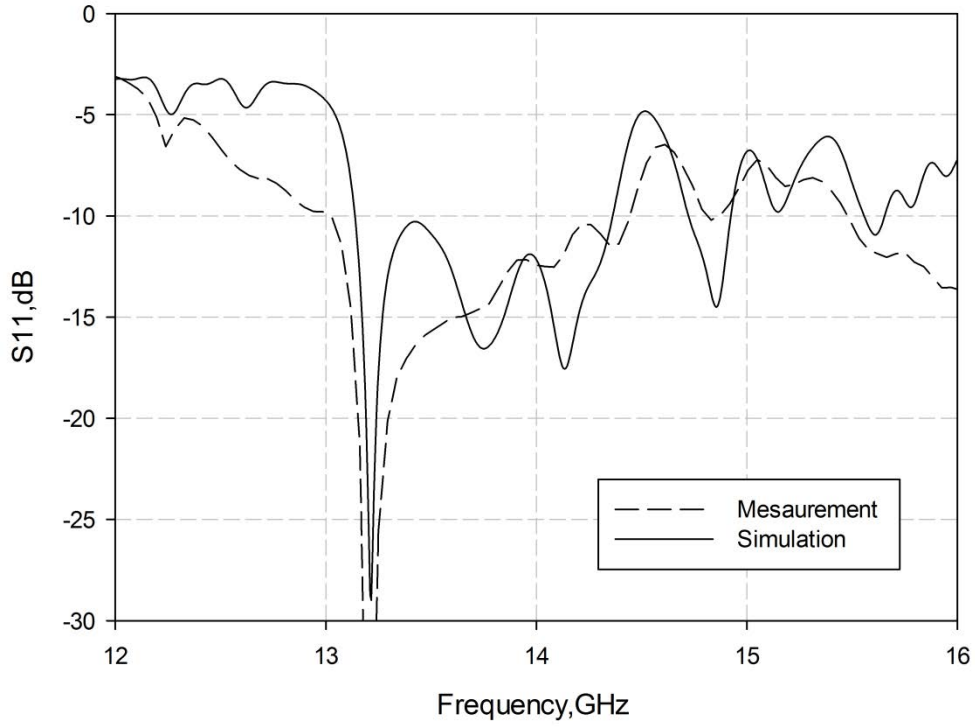

Fig. 5.2.17 Simulated and measured S_{11} of the proposed antenna.

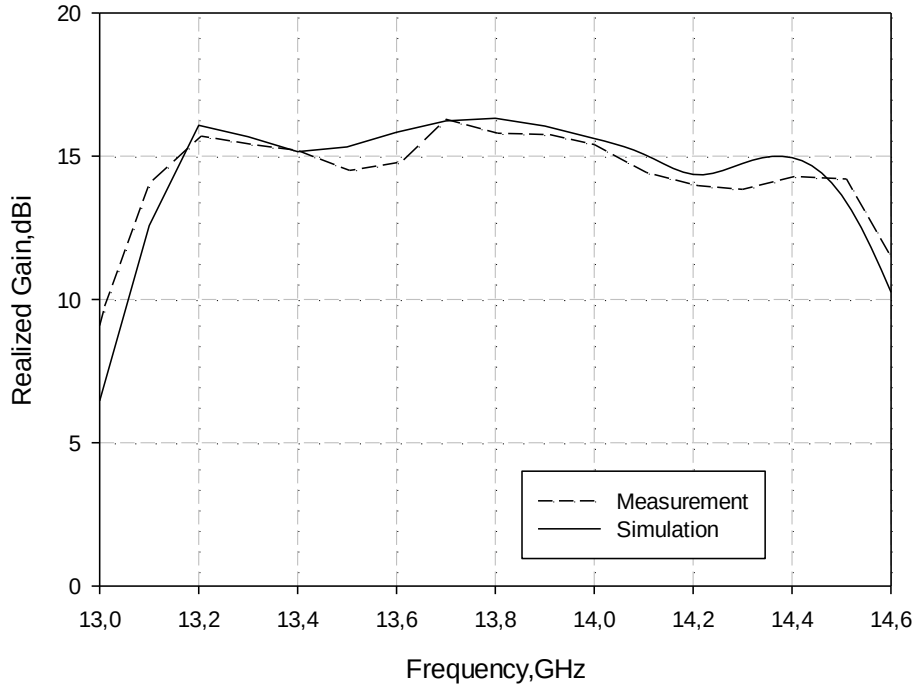

Fig. 5.2.18 Simulated and measured realized gain of the final antenna.

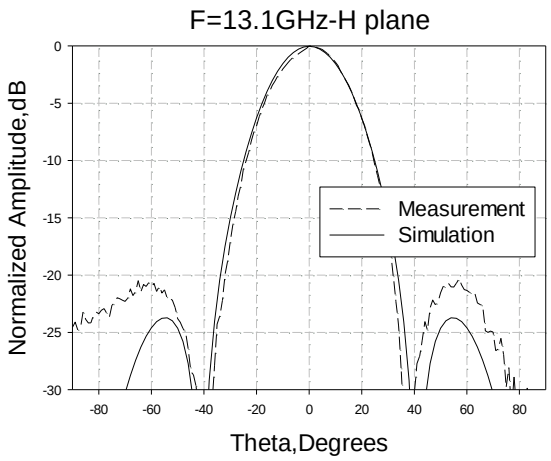
F=13.1GHz-H plane
Normalized Amplitude,dB
Theta,Degrees
Measurement
Simulation

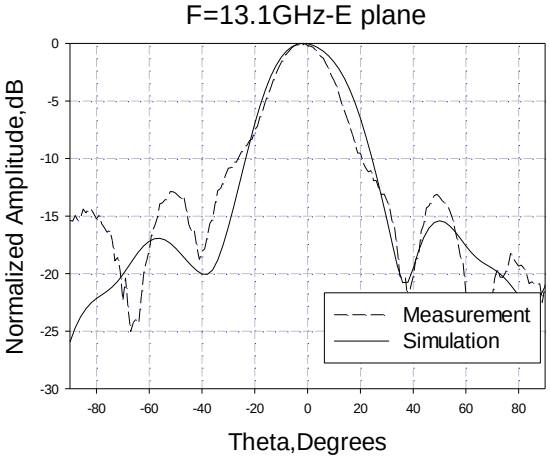
F=13.1GHz-E plane
Normalized Amplitude,dB
Theta,Degrees
Measurement
Simulation

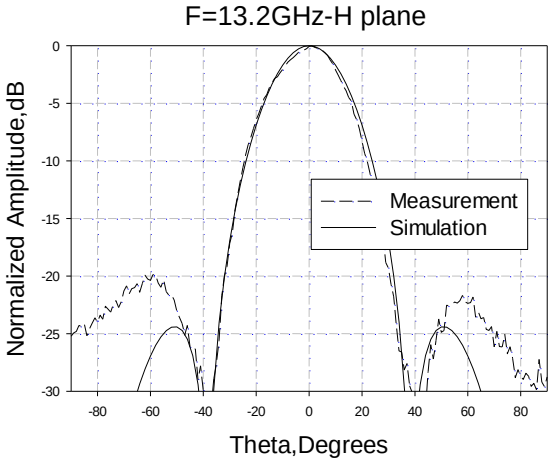
F=13.2GHz-H plane
Normalized Amplitude,dB
Theta,Degrees
Measurement
Simulation

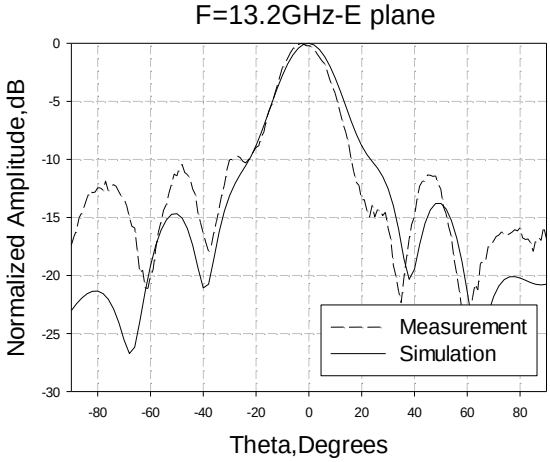
F=13.2GHz-E plane
Normalized Amplitude,dB
Theta,Degrees
Measurement
Simulation

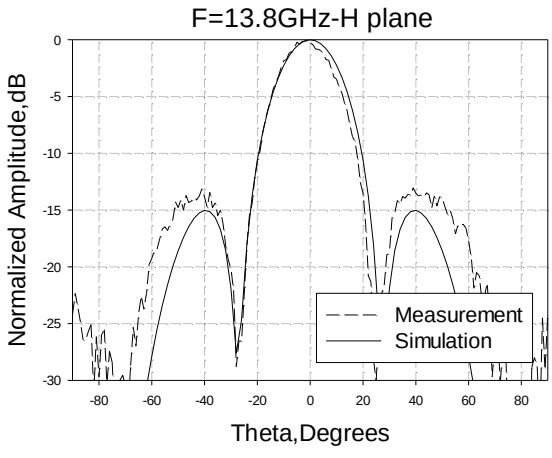
F=13.8GHz-H plane
Normalized Amplitude,dB
Theta,Degrees
Measurement
Simulation

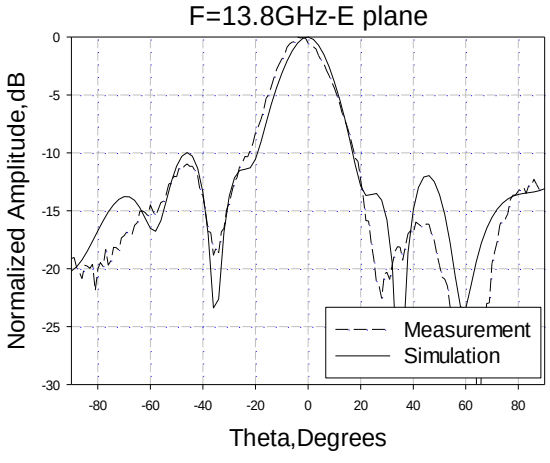
F=13.8GHz-E plane
Normalized Amplitude,dB
Theta,Degrees
Measurement
Simulation

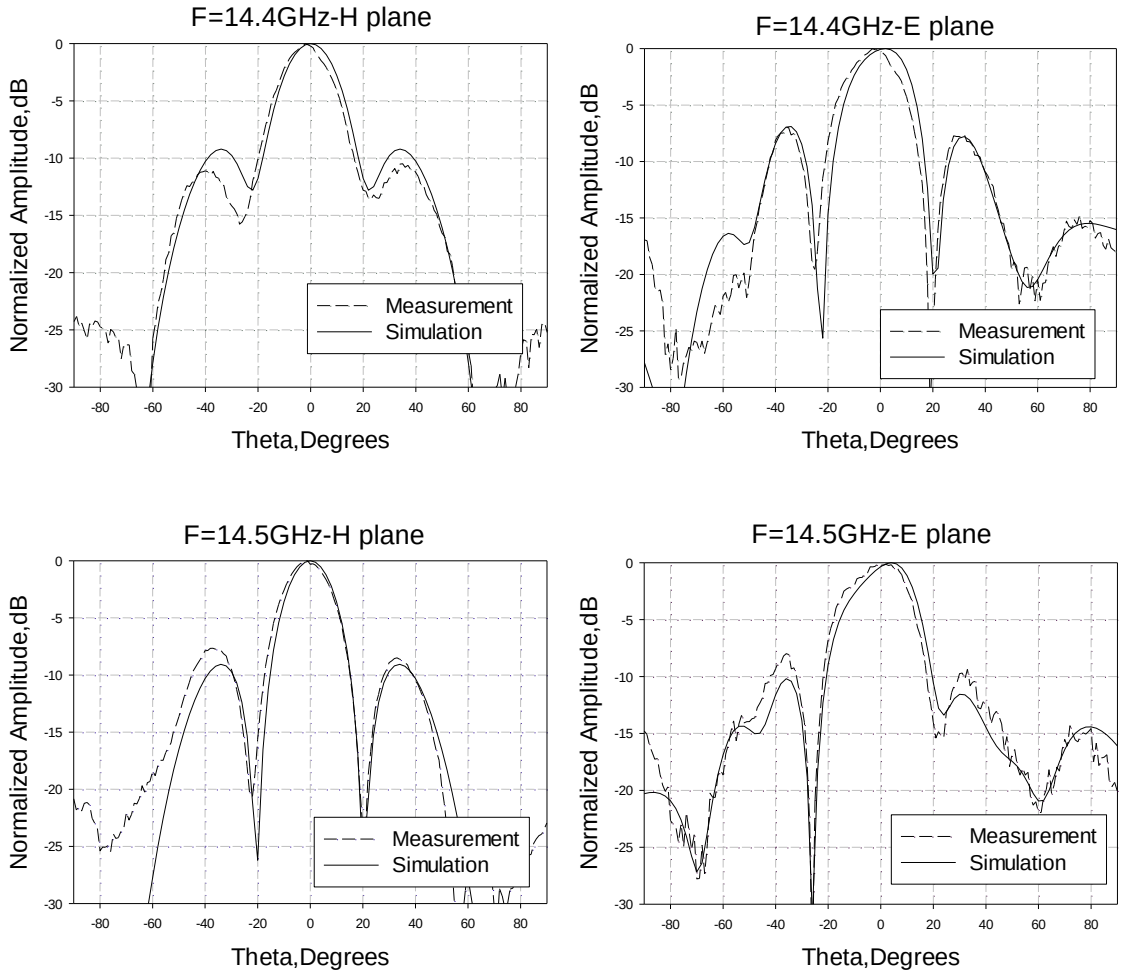

(a) (b)

Fig. 5.2.19 Simulated and measured radiation patterns for the (a) H-plane and (b) E-plane in five frequencies over the operational bandwidth of the antenna.

5.3 COMPARISON WITH A CONVENTIONAL FABRY-PEROT PRS ANTENNA

In this section, a comparison of the proposed three layer AIS-PRS antenna with a conventional λ/2 profile Fabry-Perot antenna is carried out. The antenna under study consists of one layer aperture PRS placed at half wavelength distance in front of a ground plane. It is fed using the same feeding technique comprising the microstrip line fed slots. The investigated structure has been designed to operate in the same frequency band and achieve

the same maximum directivity as the proposed antenna so that a fair comparison can be performed. In Fig. 5.3.1, the directivity versus frequency for the two evaluated designs is shown. The conventional Fabry-Perot antenna achieves a maximum directivity of 16.8dBi at 13.7GHz with a 3dB bandwidth of 5.6%. It can be extracted from the figure that the proposed three AIS-PRS layer antenna outperforms the single layer antenna in terms of bandwidth while keeping the same total profile ($\lambda/2$). Moreover, the directivity response of the proposed structure shows a faster roll-off. From Table II, it can be seen that the 2dB radiation bandwidth is more than doubled in the case of the proposed antenna compared with the single layer PRS antenna. Finally, the radiation patterns at the two edges of the operational bandwidth of the single layer antenna are shown in Fig. 5.3.2 for both antennas. As can be seen from the figure, a significantly improved sidelobe level is obtained with the proposed antenna, especially for the E-plane patterns. More specifically, the sidelobe level for the E-plane at 13.3GHz is -8dB and -13dB for the conventional antenna and the proposed antenna respectively. At 14.1GHz where higher order modes tend to deteriorate the radiation patterns of such type leaky wave antennas, the obtained improvement is more evident, with sidelobe levels of -3dB and -12dB for the single layer antenna and the three AIS-PRS layer antenna respectively.

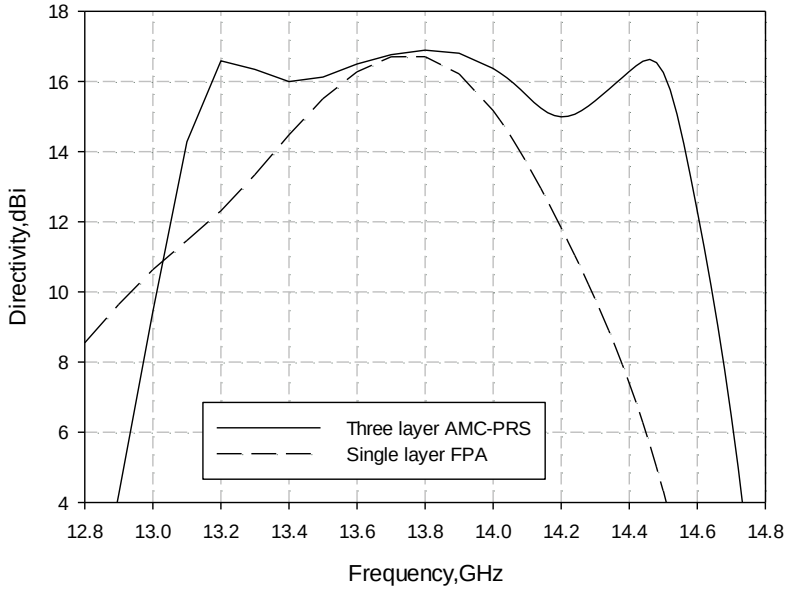

Fig. 5.3.1 Directivity vs frequency comparison between the proposed three layer AMC-PRS antenna and the single layer Fabry-Perot antenna.

TABLE II.

ANTENNA PERFORMANCE COMPARISON BETWEEN THE SINGLE LAYER FABRY-PEROT ANTENNA AND THE PROPOSED THREE LAYER AMC-PRS ANTENNA

Antenna Profile	***Directivity max (dBi)***	***Bandwidth (%)***	
		2dB	***3dB***
One Layer λ/2	16.8	4.5	5.6
Three Layer AMC PRS λ/6	16.9	10.3	10.7

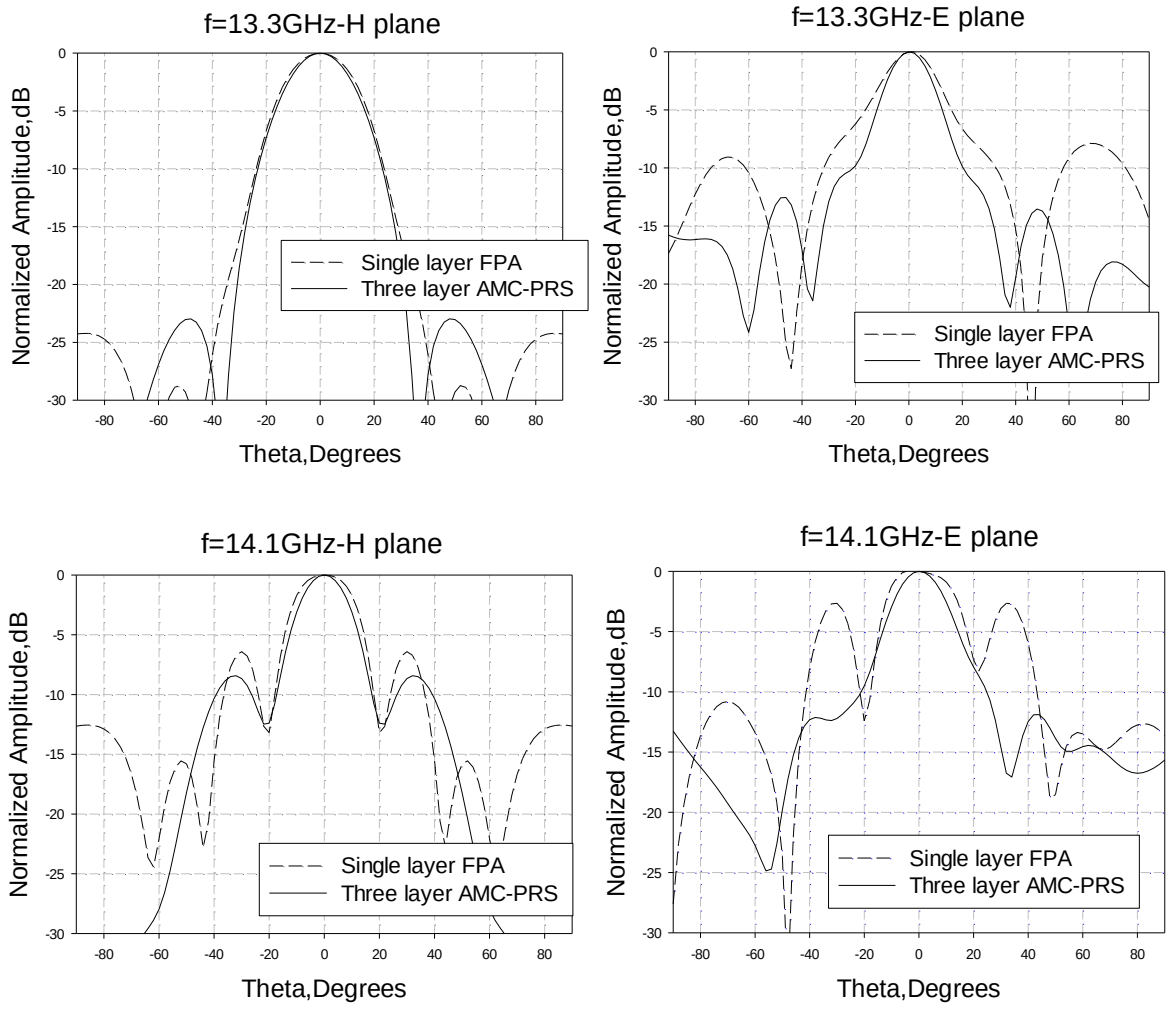

(a) (b)

Fig. 5.3.2 Simulated H- and E-plane radiation patterns for single layer Fabry-Perot antenna and the proposed three layer AMC-PRS antenna at (a) 13.3GHz and (b) 14.1GHz.

5.4 BROADBAND NEAR-ZERO METASURFACES

Over the past years metamaterials have been the subject of extensive study due to their extraordinary properties. They offer great flexibility for manipulating their electromagnetic and optical properties such as their effective refractive index. Negative-index metamaterials have been realised and experimentally demonstrated [6, 7]. More recently, numerous reports have appeared for metamaterials with near-zero refractive index (NZI) [8] and epsilon-near-

zero (ENZ) [9, 10] for visible and infrared wavelengths. Electromagnetic waves inside such materials experience no spatial phase change and extremely large phase velocity. These properties have led to a number of applications such as cloaking [11-13], super-reflection [14], tunnelling [15-17] and funnelling [18].

Metasurfaces [19, 20] are a 2D implementation of metamaterial structures, typically created by arrays of sub-wavelength scatterers. NZI metasurfaces have been employed in conjunction with low directive emission sources to achieve directivity enhancement [21-23]. In these studies, multiple layers of metasurfaces have been utilized resulting in a bulky profile. The design of sub-wavelength profile metasurfaces for directive emission has been also investigated [2, 24, 5] exploiting the unique property of Artificial Magnetic Conductor (AMC) surfaces to reflect electromagnetic waves with zero phase shift at a specific frequency. However, all the aforementioned antenna structures exhibit very narrow bandwidth due to the respectively narrowband NZI response.

In this section, we present a different approach of characterizing the sub-wavelength metasurfaces proposed in the previous sections of this chapter with respect to their constitutive parameters. As an example, the double-layer metasurfaces introduced in 5.1.1.2 are analyzed giving a broadband NZI response which is demonstrated experimentally by producing broadband directive emission combining the investigated multilayer metasurfaces with a single low directivity source. The retrieval parameters are extracted using the reflection and transmission characteristics of the metamaterial [25-27], demonstrating the broadband ENZ effect. The parameters have been extracted considering both isotropic and anisotropic homogeneous material. Introducing a low directive radiating source between a conducting plane and the proposed composite metasurfaces, a broadband directional antenna is generated which basically consists in the finite size antenna presented in 5.1.2. A validation of the

concept is also presented by comparing the radiation patterns of the antenna formed using the proposed metasurfaces, with the patterns calculated for a homogeneous material with the extracted effective retrieval parameters.

In Fig. 5.4.1, the structure of the antenna is depicted, with the metamaterial structure placed above a conducting plane and a radiating source as explained earlier. It is worth reminding here that the metamaterial consists of a combination of two double-layer arrays of scatterers with dissimilar subwavelength dimensions printed on either sides of a dielectric sheet and separated by an air cavity. Each composite double-layer structure comprises a capacitive and an inductive metasurface resulting in a total of four metasurfaces (Fig. 5.4.1). The dimensions and separation between the two composite metasurfaces are given in section 5.1.1.2.

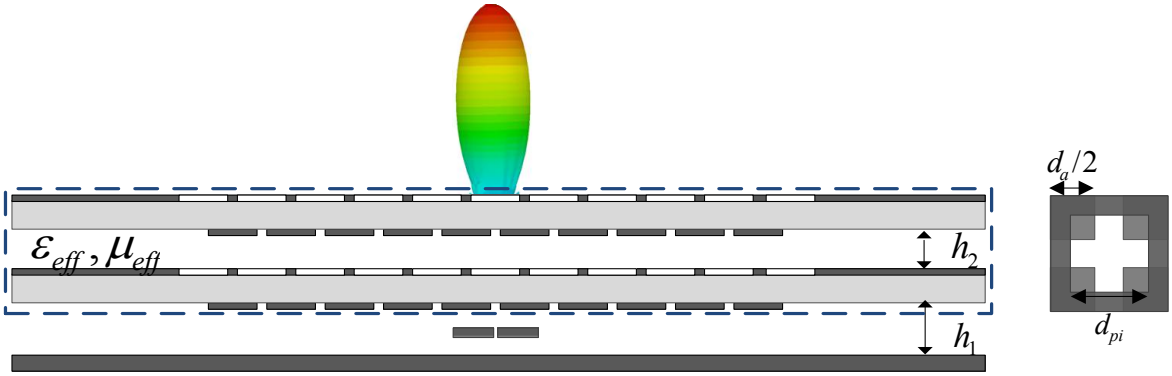

Fig. 5.4.1 Schematic diagram of the antenna generated utilizing the two pairs of composite metasurfaces. The effective homogeneous metamaterial is also illustrated with the blue dashed line, with effective parameters ε_{eff} and μ_{eff}.

5.4.1 Retrieval Parameter Extraction for Isotropic Medium

In order to evaluate the constitutive parameters of the designed metamaterial, we consider infinite size metasurfaces with the dimensions and separation described in 5.1.1.2. The composed metamaterial structure is modelled using electromagnetic simulation software and

the scattering parameters are extracted for normal plane wave incidence as shown in Fig. 5.4.2 (a). The real part of the reflection coefficient (*R*) experiences a resonance while both the imaginary part of the reflectance and the real part of the transmittance (*T*) show strong modulation. Subsequently, using the analytical expressions described in [25, 26] and in Chapter 2.4.1, considering an isotropic metamaterial, the refractive index as well as the electric permittivity ε and magnetic permeability μ are calculated. Only the real part of the parameters is shown. The permittivity undergoes an inverse spectral variation from 13.2GHz to 14.2GHz. The resulting fluctuation in the real permittivity values produces a second zero crossing with the values between the two zeros being very small. After this point epsilon continues increasing. A similar fluctuating response is observed in the magnetic permeability which is approaching zero at 13.5GHz. The combination of epsilon and mu values results in the refractive index shown in Fig. 5.4.2 (b). The real part of n has small values within the range of 0.5 and 0.8 in the area of interest, i.e. the area where the ENZ effect is obtained. It should be pointed out that this effect has been attained by engineering the properties of each metasurface and controlling their individual dimensions so that their specific combination will provide the presented broadband NZI response.

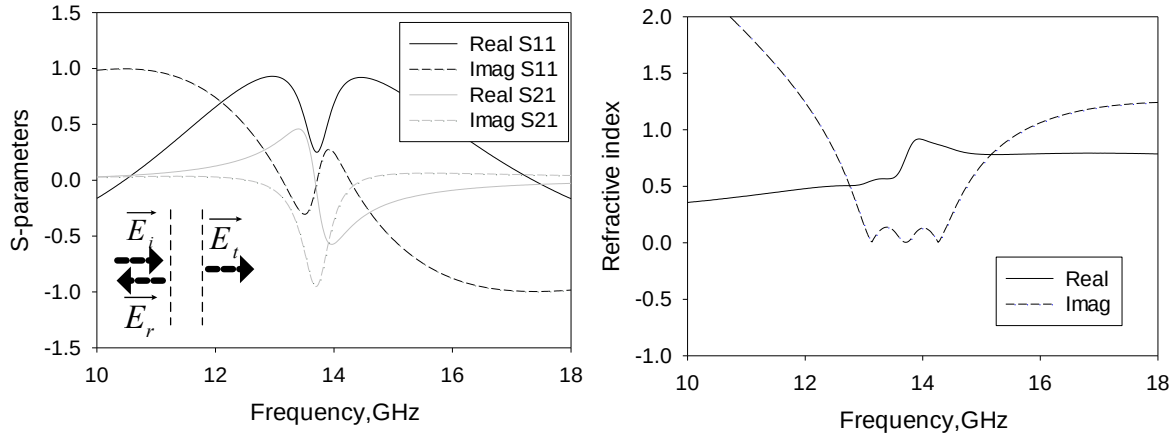

(a) (b)

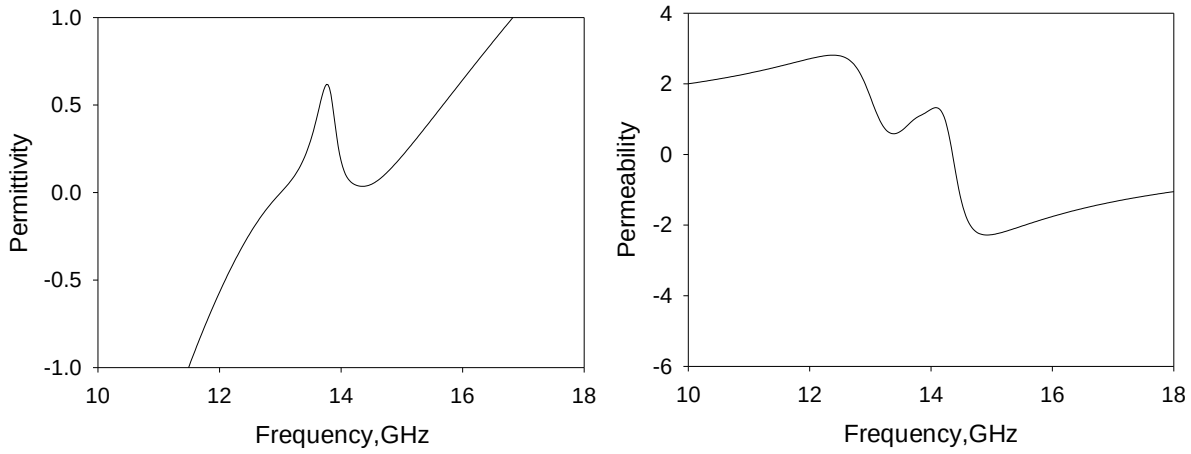

(c) (d)

Fig. 5.4.2 (a) Reflection (*R*) and transmission (*T*) coefficients under normal incidence for two metasurfaces of dissimilar reflectivities. (b)Refractive index n for the proposed metamaterial structure as calculated with the retrieval method for isotropic effective medium. (c) Effective electric permittivity and (d) Effective magnetic permeability.

5.4.2 Retrieval Parameter Extraction for Anisotropic Medium

The evaluation of the parameters presented in the previous section has been carried out under the hypothesis of an isotropic effective medium. A more accurate characterization of the proposed metasurfaces is carried out that takes into account the anisotropy of the proposed metamaterial in the x, y, z axes. In order to gauge the constitutive parameters for anisotropic materials, the modelled scattering parameters for two different angles of incidence where used as explained in [27], to obtain information for all three components of the electric and magnetic fields (Fig. 5.4.3). Again, we consider infinite size metasurfaces and the scattering parameters are extracted for incident angles of 0^o and 40^o for both transverse-electric (TE) and transverse-magnetic (TM) incident waves. The modified analytical expressions proposed in [27] and described in 2.4.2 are then used, and the electric permittivity ε and magnetic permeability μ tensors are computed and shown in Fig. 5.4.4. It can be observed, that the

obtained response for the three orientations exhibit qualitative similarities to the one of the isotropic case. In particular, in the x and y directions the ε and μ are very similar (Fig. 5.4.4a, c and b, d), as expected due to the symmetry of the structure in these directions. Once again, the permittivity undergoes an inverse variation around 13.8GHz, crossing zero at about 13GHz and 14.2GHz. This effect is observed for all three dimensions. However, for the z-axis, which is the one we are mostly interested in as it is the main direction of propagation, ε_{zz} assumes values closer to zero and for a slightly broader frequency range compared to x and y. Particularly, ε_{zz} is below 0.4 within the frequency range of interest, while for ε_{xx} and ε_{yy} the local maximum of the real part is 0.6. Additionally, the magnetic permeability experiences a fluctuation at the frequencies where ε shows the inverse variation with frequency. Specifically, for μ_{zz} the values are also close to zero (less than 0.5), while a discontinuity occurs above 15GHz which is outside our range of interest.

The ENZ effect could be extended to cover a broader bandwidth by altering the dimensions of the metasurfaces to adequately manipulate their total reflectivity. A reduced total reflectivity will result to a higher peak value of ε, leading to a more broadband behavior. On the contrary, an increase in the total reflectivity of the metamaterial structure will result in a lower peak value and narrower frequency range of ENZ. This property of the proposed metasurfaces can be further extended, keeping the same low value of ε, by adding extra layers of properly designed metasurfaces. However for the specific example, constrained by two pairs of composite metasurfaces, the optimum balance between a close to zero permittivity and bandwidth has been reached.

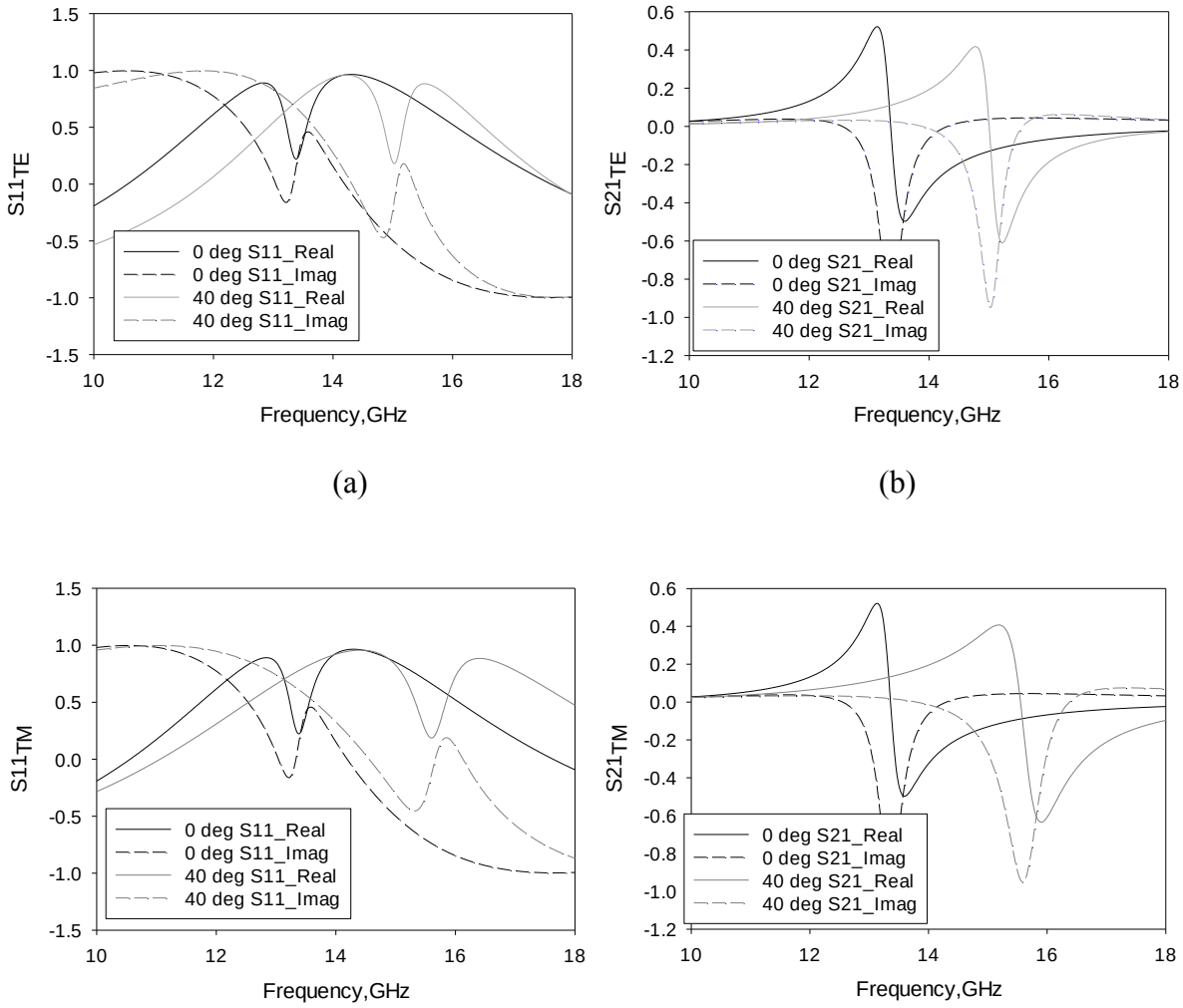

Fig. 5.4.3 (a) Reflection (S_{11}) and (b) transmission (S_{21}) coefficients under 0^o and 40^o TE incident waves and (c) Reflection (S_{11}) and (d) transmission (S_{21}) coefficients under 0^o and 40^o TM incident waves.

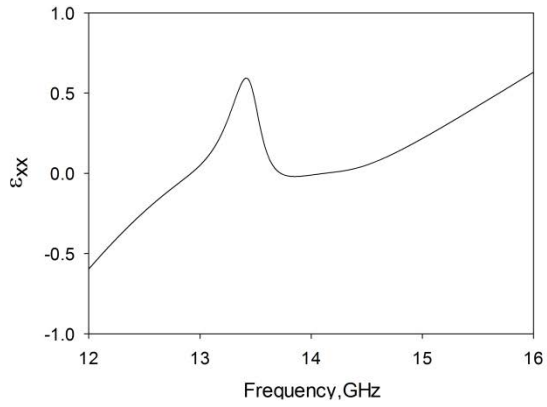
1.0
0.5
0.0
-0.5
-1.0
εxx
12
13
14
15
16
Frequency,GHz

(a)

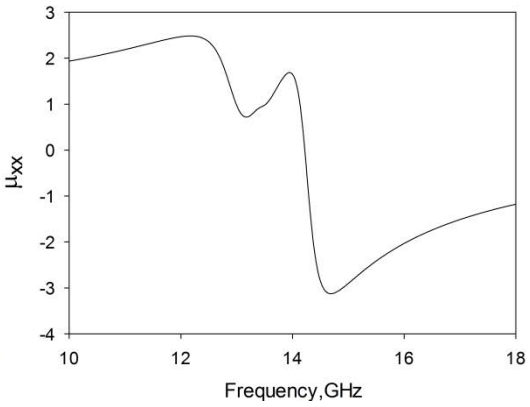
3
2
1
0
-1
-2
-3
-4
μxx
10
12
14
16
18
Frequency,GHz

(b)

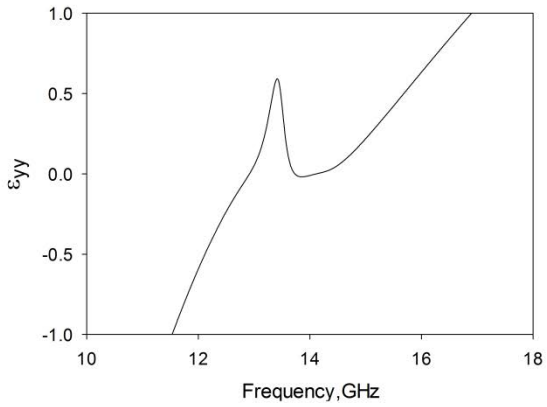
1.0
0.5
0.0
-0.5
-1.0
εyy
10
12
14
16
18
Frequency,GHz

(c)

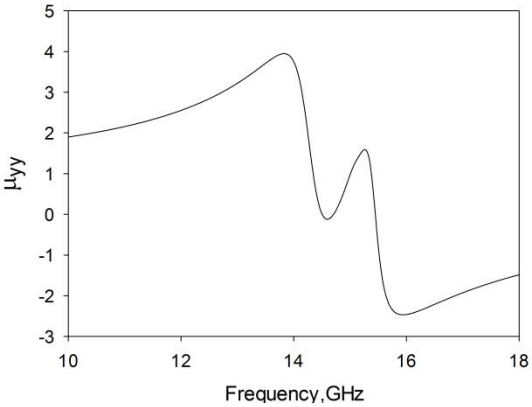
5
4
3
2
1
0
-1
-2
-3
μyy
10
12
14
16
18
Frequency,GHz

(d)


1.0
0.5
0.0
-0.5
-1.0
εzz
10
12
14
16
18
Frequency,GHz

(e)

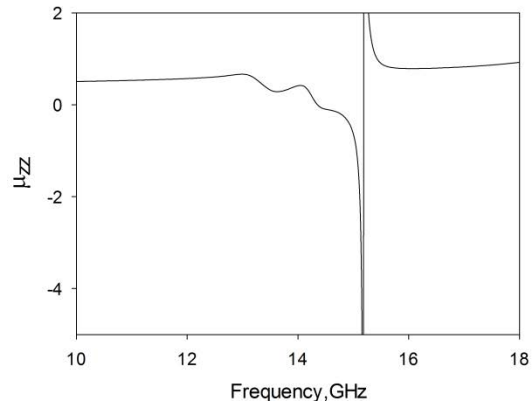
2
0
-2
-4
μzz
10
12
14
16
18
Frequency,GHz

(f)

Fig. 5.4.4 Effective electric permittivity (a) for the x direction, (c) for the y direction and (e) for the z direction of the optimized composite metasurfaces. The respective effective magnetic permeabilities are plotted in subfigures (b), (d) and (f).

5.4.3 Near-Zero Multi-Layer Metasurfaces for High-Gain Antenna

As an application of the proposed metasurfaces, which exploits the ENZ property, we incorporate them with a low directivity source in order to generate a highly directive antenna. This is one of the several potential applications of ENZ materials. The structure is shown in Fig. 5.4.1 and it consists of the designed metasurfaces placed above a conducting plane and a low directive radiating source. Due to the broadband ENZ response, a broad frequency range of high directive emission is obtained as demonstrated by the radiation patterns shown in Fig. 5.4.6 for 13.4GHz and 14GHz. The results were obtained by simulating the whole structure in CST. The value of the maximum directivity obtained by the modeled structure is 18.2dB. Furthermore, a homogeneous anisotropic material is modeled using the extracted constitutive parameter values plotted in Fig. 5.4.4. This effective material has replaced the multi-layer metasurfaces, shown in Fig. 5.4.1 with the blue dashed line, and the radiation patterns for this case have also been extracted. A comparison between the patterns produced by the proposed metasurfaces and the anisotropic effective medium is illustrated in Fig. 5.4.6. The same study has been carried out for an isotropic material and the radiation patterns are shown in Fig. 5.4.5. It is evident that taking into account the anisotropy of the structure, better agreement has been obtained.

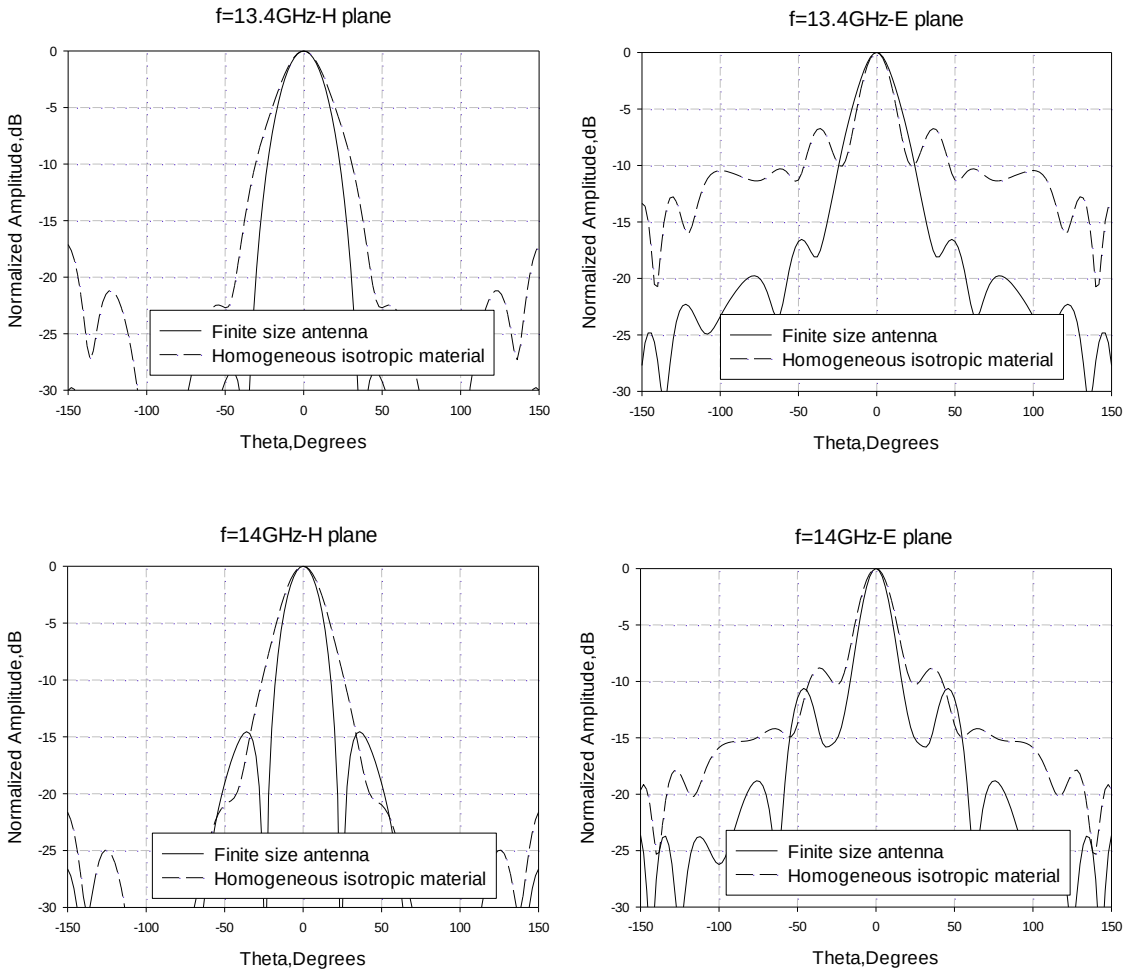

Fig. 5.4.5 Radiation patterns comparison between the proposed structure and homogeneous isotropic material for H-plane and E-plane at 13.4GHz and 14GHz.

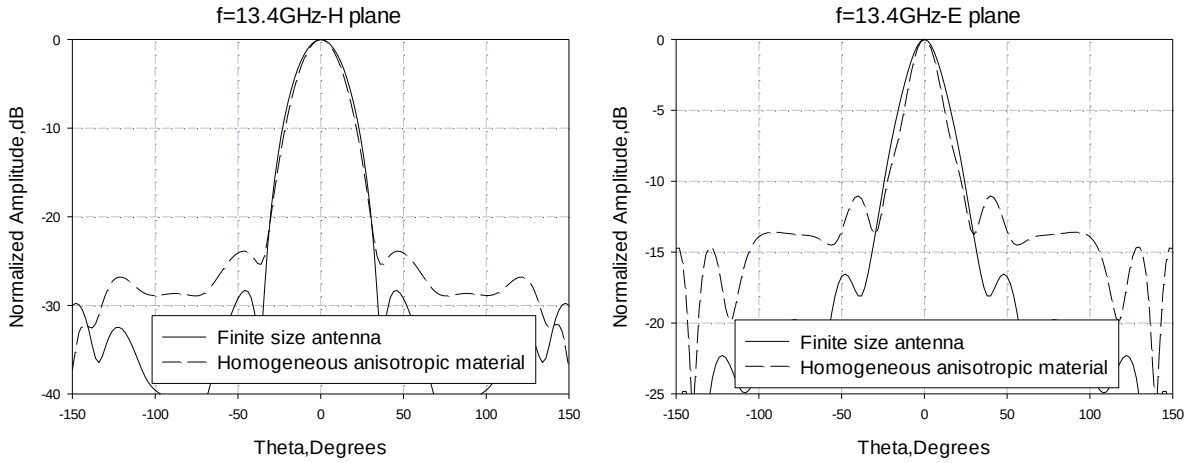

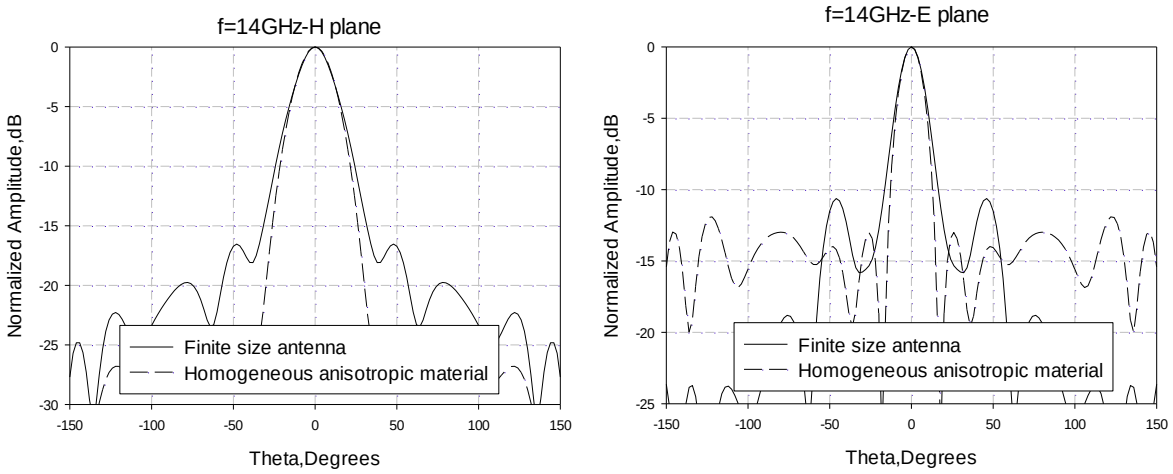

Fig. 5.4.6 Radiation patterns comparison between the proposed structure and homogeneous anisotropic material for H-plane and E-plane at 13.4GHz and 14GHz.

This concept has been experimentally demonstrated since a prototype of the proposed antenna has been fabricated and measured with the results presented in 5.1.3. It can be seen from Fig. 5.1.11 that a broadband performance is obtained employing the investigated metasurfaces. Furthermore, the radiation patterns extracted from the model for frequencies between 13.4GHz and 14.2GHz are presented and compared with the measured ones in Fig. 5.1.12. Very small discrepancies are observed, validating the proposed concept.

5.5 CONCLUSIONS

In this chapter, a technique for designing sub-wavelength profile antennas achieving broadband highly directive performance has been demonstrated through simulated and experimental results. This has been accomplished by employing multiple metasurfaces formed by optimized double-layer periodic arrays of dissimilar dimensions. Each double-layer array consists of a capacitive AMC layer and an inductive PRS layer printed on either side of a dielectric substrate. Five sub-wavelength antennas have been investigated based on optimised composite double-layer arrays, two with $\lambda/4$ separation between the meatasurfaces and three

with λ/6. A dual-resonant feeding mechanism was employed to cover the broad bandwidth of the antenna. The design of the antenna structures has been optimised using a combination of ray optics analysis and periodic full-wave simulations. The proposed antennas outperform conventional FP type antennas with the same profile. Finally, a new approach has been presented, demonstrating that the proposed composite metamaterial structures posses a broadband ENZ response which can be applied for the design of broad frequency range directive emission in the microwave regime.

REFERENCES

[1] D. Sievenpiper, Z. Lijun, R. F. Broas, N. G. Alexopoulos, and E. Yablonovitch, "High-impedance electromagnetic surfaces with a forbidden frequency band," *IEEE Trans. Microw. Theory Tech.*, vol. 47, no. 11, pp. 2059–2074, Nov. 1999.

[2] S. Wang, A.P. Feresidis, G. Goussetis, J.C. Vardaxoglou, "Low-profile resonant cavity antenna with artificial magnetic conductor ground plane," *Electron. Lett.*, vol.40, no.7, pp.405,406, 1 April 2004.

[3] A. P. Feresidis, G. Goussetis, S. Wang, and J. C. Vardaxoglou, "Artificial magnetic conductor surfaces and their application to low profile high-gain planar antennas," *IEEE Trans. Antennas Propag*., vol. 53, no. 1, pp. 209–215, Jan. 2005.

[4] C. Mateo-Segura, G. Goussetis, A. P. Feresidis, "Sub-Wavelength Profile 2-D Leaky-Wave Antennas With Two Periodic Layers," *IEEE Trans. Antennas Propag.*, vol.59, no.2, pp.416,424, Feb. 2011.

[5] A. Ourir, A. de Lustrac, and J.-M. Lourtioz, "All-metamaterial-based sub-wavelength cavities (λ/60) for ultrathin directive antennas," *Applied Physics Lett.*, vol. 88, no. 8, pp. 84103-1–3, Feb. 2006.

[6] Shuang Zhang, Wenjun Fan, N. C. Panoiu, K. J. Malloy, R. M. Osgood, and S. R. J. Brueck, "Experimental Demonstration of Near-Infrared Negative-Index Metamaterials", *Phys. Rev. Lett*. 95, 137404, (2005).

[7] X. Zhang, M. Davanc¸o, Y. Urzhumov, G. Shvets, and S. R. Forrest, "From Scattering Parameters to Snell's Law: A Subwavelength Near-Infrared Negative-Index Metamaterial", *Phys. Rev. Lett*. 101, 267401, (2008).

[8] P. Moitra, Y. Yang, Z. Anderson, I. Kravchenko, D. Briggs, and J. Valentine, "Realization of an all-dielectric zero-index optical metamaterial", *Nat. Photonics* 7, 791 (2013).

[9] R. Maas, J. Parsons, N. Engheta and A. Polman, "Experimental realization of an epsilon-near-zero metamaterial at visible wavelengths", *Nat. Phot*.. 7, 907 (2013).

[10] R. J. Pollard, A. Murphy, W. R. Hendren, P. R. Evans, R. Atkinson, G. A. Wurtz, A.V. Zayats, and V. A. Podolskiy, "Optical Nonlocalities and AdditionalWaves in Epsilon-Near-Zero Metamaterials", *Phys.Rev. Lett*. 102, 127405 (2009).

[11] T. Ergin, N. Stenger, P. Brenner, J. B. Pendry, and M. Wegener, "Three-Dimensional Invisibility Cloak at Optical Wavelengths", *Science* 328, 337 (2010).

[12] E. Kallos, C. Argyropoulos, Y. Hao, and A. Alú , "Comparison of frequency responses of cloaking devices under nonmonochromatic illumination", *Phys. Rev. B* 84, 045102 (2011).

[13] P. Y. Chen, C. Argyropoulos, and A. Alù, "Broadening the Cloaking Bandwidth with Non-Foster Metasurfaces", *Phys. Rev. Lett*. 111, 233001 (2013).

[14] J. Hao, W. Yan, and M. Qiu, "Super-reflection and cloaking based on zero index metamaterial", *Appl. Phys. Lett*. 96, 101109 (2010).

[15] R. Liu, Q. Cheng, T. Hand, J. J. Mock, T. J. Cui, S. A. Cummer, and D. R. Smith, "Experimental Demonstration of Electromagnetic Tunneling Through an Epsilon-Near-Zero Metamaterial at Microwave Frequencies", *Phys. Rev. Lett*. 100, 023903 (2008).

[16] M. Silveirinha and N. Engheta, "Tunneling of Electromagnetic Energy through Subwavelength Channels and Bends using ε-Near-Zero Materials", *Phys. Rev.Lett*. 97, 15740 (2006).

[17] B. Edwards, A. Alù, M. G. Silveirinha, and N. Engheta, "Reflectionless sharp bends and corners in waveguides using epsilon-near-zero effects", *J. Appl. Phys*. 105, 044905 (2009).

[18] D. C. Adams,S. Inampudi, T. Ribaudo, D. Slocum, S. Vangala, N. A. Kuhta, W. D. Goodhue, V. A. Podolskiy, and D. Wasserman, "Funneling Light through a Subwavelength Aperture with Epsilon-Near-Zero Materials", *Phys. Rev. Lett*. 107, 133901 (2011).

[19] F. Falcone, T. Lopetegi, M. A. G. Laso, J. D. Baena, J. Bonache, M. Beruete, R. Marqués, F. Martín, and M. Sorolla, "Babinet Principle Applied to the Design of Metasurfaces and Metamaterials", *Phys. Rev. Lett*. 93, 197401 (2004).

[20] N.Yu and F. Capasso, "Flat optics with designer metasurfaces", *Nat. Mat*., 13, 139 (2014).

[21] B. Temelkuaran, M. Bayindir, E. Ozbay, R. Biswas, M. M. Sigalas, G. Tuttle, and K. M. Ho, "Photonic crystal-based resonant antenna with a very high directivity", *J. Appl. Phys*., 87, 603–605, 2000.

[22] S. Enoch, G. Tayeb, P. Sabouroux, N. Guerin, and P. Vincent, “A metamaterial for directive emission”, *Phys. Rev. Lett.*, vol. 89, 2139021 (2002).

[23] E. Saenz, K. Guven, E. Ozbay, I. Ederra, R. Gonzalo, “Enhanced directed emission from metamaterial based radiation source”, *Appl. Phys. Lett.*, Vol. 92, 2041031 (2008).

[24] Zhou, H. Li, Y. Qin, Z. Wei, and C. T. Chan, “Directive emissions from subwavelength metamaterial-based cavities”, *Appl. Phys. Lett.*, Vol. 86, 1011011 (2005).

[25] D. R. Smith, “Analytic expressions for the constitutive parameters of magnetoelectric metamaterials”, *Phys. Rev. E* 81, 036605 (2010).

[26] D. R. Smith, D. C. Vier, Th. Koschny, and C. M. Soukoulis, “Electromagnetic parameter retrieval from inhomogeneous metamaterials”, *Phys. Rev. E* 71, 036617 (2005).

[27] Z. H. Jiang, J. A. Bossard, X. Wang, and D. H. Werner, “Synthesizing metamaterials with angularly independent effective medium properties based on an anisotropic parameter retrieval technique coupled with a genetic algorithm”, *J. Appl. Phys*. 109, 013515 (2011).

CHAPTER 6

MICROMACHINED TERAHERTZ FABRY-PEROT CAVITY ANTENNA

In recent years, there has been increased interest in the design and fabrication of periodic surfaces at millimetre-wave and sub-millimetre-wave/THz frequencies for numerous applications. Periodic surfaces have been developed as Frequency Selective Surfaces (FSS) and employed as demultiplexing elements in passive Earth observation THz radiometers traditionally employing a single mechanically scanned aperture antenna [1-5]. FSSs are used in the quasi - optical receiver of these advanced instruments to spectrally separate the signals that are collected by the scanning antenna [6]. Split slot ring based periodic surfaces have also been developed as thin linear to circular polarization converters [7-9]. Other applications of THz periodic surfaces include thin absorbers [10] and THz biosensors for chemical and biochemical materials [11].

THz frequencies offer new opportunities for communications, sensing and imaging applications [11, 12]. Sensing and imaging systems are required for both medical and security applications. For these applications, THz technology offers a lot of benefits due to the high resolution linked to the short wavelength at THz frequencies. Moreover, it has the advantage of non-ionizing radiation which is harmless for the human tissue, as opposed to X-rays. Furthermore, in automotive radar applications [13] such as adaptive cruise control, collision avoidance and blind spot detection, there is a trend towards higher frequencies which will provide better quality imaging of the scenery in front of the sensor, combining the high

resolution with beam-steered high-gain antennas. In addition, since all dimensions decrease as the frequency increases, the size of the antenna is miniaturized.

Such applications require high efficiency and high gain antennas to improve the overall system gain and enhance the signal-to-noise-ratio. At THz frequencies, reflector-based antennas [12] and horn antennas [14, 15] have been used. Despite their good radiation performance, they are bulky, which is an important drawback and furthermore they require complex, expensive and time-consuming fabrication techniques (e.g. CNC metal milling) in order to achieve the desired tolerances at these frequencies. Lenses have also been reported [16] as highly directive antennas for broadside radiation. Lens antennas are fabricated with laser silicon etching, which is not cost-efficient, and they normally have a profile of several wavelengths which is increased if a higher gain value is desired [17]. Although a profile of several wavelengths is not a problem at higher THz frequencies (over 1 THz) it can be problematic at the lower end of the THz spectrum (about 300GHz) particularly in the case of compact integrated systems. Planar antennas are therefore required for compact integrated systems at low THz frequencies [18]. In addition, planar antennas are readily compatible with micromachining techniques which lead to low-cost fabrication for mass production. Conventional microwave planar antennas employ microstrip patch arrays to achieve high gain. Nevertheless, patch arrays are not a viable solution for THz frequencies since they exhibit high losses, low efficiency and narrow bandwidth.

In this chapter, we present the design and implementation of a new type of micromachined terahertz planar highly directive antenna based on the FP antenna concept but adjusted to a specific micromachining fabrication process. The periodic surface and antenna are fabricated using SU-8 photoresist micromachining technology. A fully metalized micromachined PRS is placed at half wavelength distance over a metallic ground and a single waveguide-fed slot

(Fig. 6.1). The PRS is supported on a metalised SU-8 polymer ring. A resonant air cavity is thus formed with the metallic ground which leads to directive radiation patterns and high gain. The antenna, including a waveguide section feeding the resonant cavity, is implemented using micromachining fabrication techniques available at the University of Birmingham. SU-8 photoresist polymer is employed that has the advantages of high dimensional accuracy, high achievable structure aspect ratio and a capability of large scale inexpensive production. The proposed antenna supports a leaky wave mode within the cavity when excited by a single feed. A large radiating aperture is hence formed that produces directive patterns without the need for complex feeding network and associated losses. The directive beams can be broadside or tilted towards larger angles as it is demonstrated. The micromachining fabrication process employed to develop the proposed planar highly directive Fabry-Perot cavity antenna at approximately 300GHz is described. Simulations and measurements of the antenna performance are presented.

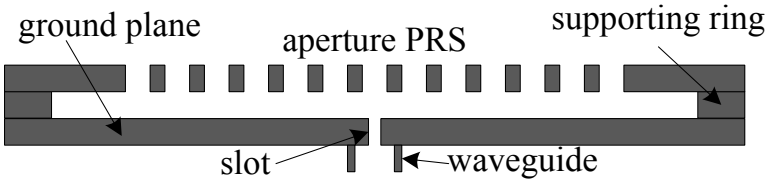

Fig. 6.1 Schematic diagram of the proposed antenna.

6.1 MICROFABRICATION TECHNIQUES AT TERAHERTZ FREQUENCIES

The demanded accuracy in fabrication techniques for THz frequencies, has led in adopting micromachining fabrication processes, since other available techniques such as metal milling or electrical discharge machining do not fulfil the dimensional accuracy requirements and have been proven to be time-consuming and expensive. Among the variety of reported micromachining fabrication techniques [19, 20], the most suitable for mass production are Si

deep reactive ion etching (DRIE) which belongs to a greater category called bulk micromachining, LIGA based thick layer electroplating and SU-8 photoresist. A quick overview of these techniques is given below.

Bulk micromachining refers to a micromachining process where the structure is formed by etching the materials from a bulk substrate, typically a silicon wafer. There are two types of etching methods that can be used, wet etching and dry etching. Wet etching is performed using a liquid chemical etchant to create a pattern controlled by a mask from the substrate. It is a rather simple and cheap technique but it offers poor control of the etch rate and the structure's dimensions. Dry etching on the other hand involves the use of gaseous etchants to pattern the substrate material underneath the mask. **Deep reactive ion etching (DRIE)** is the most popular dry etching technique since it is able to produce structures with arbitrarily defined features, high aspect ratio, critical dimension control and virtually vertical walls. This fabrication method consists at depositing silicon oxide (SiO_2) on both sides of the substrate wafer, so two layers of SiO_2 are created. The top layer is used to create the mask which will then be used for etching the substrate material, and the bottom layer is employed as a stop layer for the etching. To create the mask, a photoresist layer is used on top of the SiO_2 which is then patterned and developed. After the etching of the SiO_2 layer and the creation of the mask, the photoresist is removed and then the silicon substrate is etched. The two SiO_2 are finally removed from the substrate using a buffered oxide etch solution and the top is metallised with titanium and copper. The basic steps of this process are illustrated in Fig. 6.1.1. The drawbacks of bulk micromachining techniques are that the structure thicknesses are restricted by the commercially available silicon wafers and that for high aspect ratio structures the metallization of sidewalls is difficult.

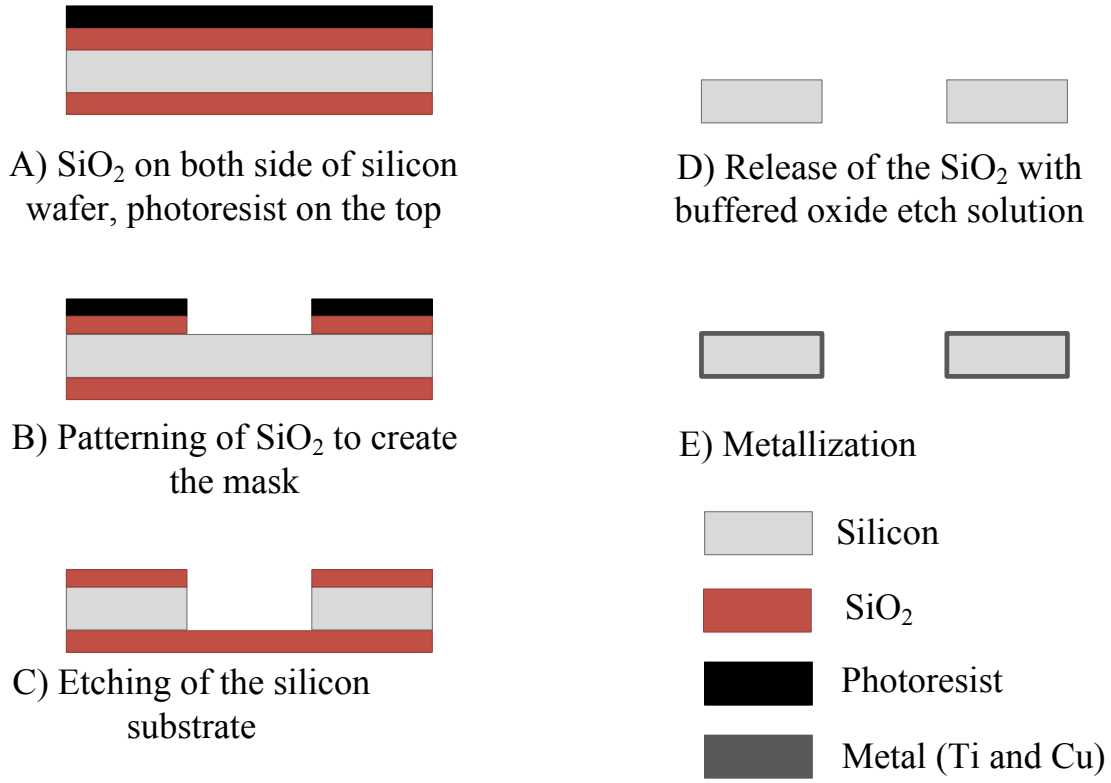

Fig. 6.1.1 Basic steps of the DRIE micromachining fabrication process.

LIGA process is a German acronym for Lithography, Electroplating, and Molding. The first step of the procedure is the coating of the substrate with an X-ray sensitive resist which is then patterned and developed. Subsequently, the resulting structure can be used as it is or it can be employed to produce a metal mould which is formed by electroplating the initial structure. Finally, the mould is utilized to form the final structure from a desired plastic material (Fig. 6.1.2). Due to the high penetrating capability of the X-rays, structures of the order of millimetres can be produced in a single step with high aspect ratios and almost vertical sidewalls. Nevertheless, this process is very expensive, mostly due to the required X-ray source.

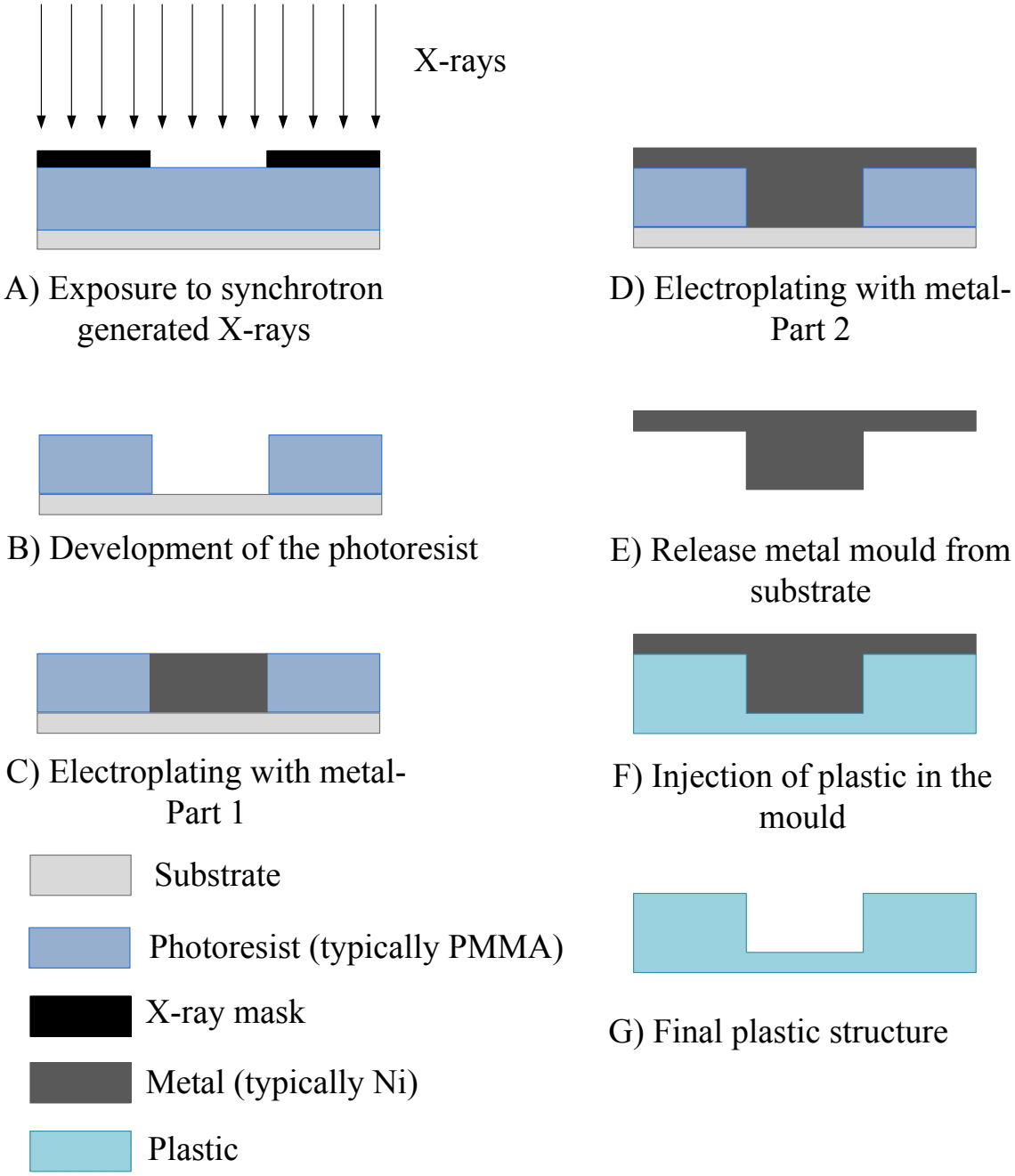

Fig. 6.1.2 Basic steps of the LIGA micromachining fabrication process.

6.1.1 In-House Fabrication Process

SU-8 is a negative epoxy-based photoresist that has been originally developed by the IBM-Watson Research Centre in 1989 [19, 20]. The thickness of the photoresist ranges from 1μm to 2mm with typical aspect ratio possible larger than 1:20. Due to its low optical absorption

in the UV (350-400nm) range, it makes it ideal for imaging near vertical sidewalls in very thick films. Therefore, SU-8 enables the use of a cheaper UV-lithography process. The general SU-8 fabrication process commonly involves the following steps: spin coat, soft bake, exposure under UV radiation, post exposure bake, development, hard bake and substrate removal, and metallization, which are described in detail below and illustrated in Fig. 6.1.3.

Spin coating: In the first step and prior to spin coating, a silicon wafer of 4-inch diameter with a desired thickness is chemically cleaned using Isopropyl alcohol (IPA) to remove any particulate matter on the surface and is dried with air. Then, the silicon wafer is weighed using precision weighing scales. An amount of SU-8 50 liquid photoresist is poured at the centre of the wafer which is placed at the spin coater. Then, the parameters are adjusted in order to achieve the desired SU-8 thickness. Due to the high-speed centrifugal whirling of the silicon wafer, the resist will cover the whole wafer. The higher the spin speed, the thinner the resist layer will be. The resulting wafer will be weighed and the measured weight of the silicon substrate will be subtracted. This will result in a systematic calibration method of the layer thickness after spin coating. As a rule of thumb, 83μm thickness corresponds to 1gr of SU-8. If the desired thickness is achieved, the wafer has to be cleaned from the back and placed on a perfectly levelled hotplate for ½ day for the liquid to be self-planarized. This is performed while covering the wafer with a glass taper and foil to prevent light reaching the SU-8.

Soft bake: Soft-baking is the step during which almost all of the solvents are removed from the SU-8. At this stage, a precision levelled hotplate is used at two temperature steps. Initially the resist is baked at 65^{o}C for 20 minutes, and then at 95^{o}C for 4.5 hours if 432μm thick layers are required or 6.5 hours for 635μm thicknesses. It is suggested to increase the temperature slowly in order to give a smooth transaction. Generally, the thicker the substrate the longer the

baking will be. The purpose of the pre-bake at 65^{o}C is to improve the thickness uniformity of the final SU-8 layers. Therefore, during this step it is necessary to occasionally rotate the wafer in order to distribute the SU-8 equally. The solvents during this step will be evaporated, and self-planarization will be achieved. The soft baking step at 95^{o}C is to dry out the solvent. During this step the wafer needs to be partly covered with a glass taper to allow solvent evaporation while at the same time protect the resist from dust particles. Finally, the wafer should be left for at least 2 hours until it cools down naturally.

UV exposure: One of the most important steps in the photolithography is the mask alignment. A mask is a square glass plate patterned with chromium on one side. As already mentioned, SU-8 is a negative photoresist so by projecting UV light onto the mask, the pattern is printed to the photoresist, since glass is transparent under UV light while chromium is opaque. Exposure to UV light causes the negative SU-8 resist to become polymerized and therefore more difficult to dissolve. Exposure time depends on the exposure energy required by the desired SU-8 wafer. It was mentioned previously that SU-8 has very low absorption at 350-400nm which enables multiple exposures for thick layers. Exposure of the SU-8 is carried out by placing the wafer under a mercury lamp UV source of a Canon PLA-510 mask aligner. Two filters are used at this stage, the L39 optical filter and the PL360 filter. The former is employed to filter out signals with lower than 400nm. The PL360 filter on the other hand is used to filter out signals under 360nm. The filtering is performed so that more efficient penetration of the UV light is achieved. Multiple exposure steps of 40 seconds are used in order to reduce the heat between the mask and the SU-8. Each exposure is followed by 2 minutes of ‘rest’, waiting for the surface to cool down. Then, the SU-8 photoresist is exposed for another 3 intervals of 40 seconds each, for cross-linking.

Post exposure bake: At this step, post exposure bake is carried out in order to produce the cross-linked reactions. For this procedure, the wafer is placed again on the hotplate whose temperature is carefully controlled in order to minimise stress and thus avoid cracks of the SU-8. The post exposure bake is carried out at 65^{o}C for 2 minutes and then at 95^{o}C for 30 minutes. Again, the wafer should be left for at least 2 hours until it cools down naturally. After that, the regions of the sample that are exposed become cross-linked and thus insoluble in the developer.

Development: One of the last steps in the photolithographic process is development. At this step the wafer is immersed into EC solvent for 15-25 minutes. Stirring of the developer is necessary due to the thick size of the SU-8. Development time and speed are a function of temperature, geometry and thickness of the specific substrate. Every 3-5 minutes the wafer should be taken out to check if it is developed. When the developed sample is taken out, it is rinsed with running EC solvent to clear the possible SU-8 leftovers. Then, IPA is poured onto the wafer (both sides) for about a minute which is then blow dried with a Nitrogen gun. At this stage, the wafer needs to be inspected using an optical microscope and if it is not perfectly developed it should be placed again into the EC solvent for a few minutes.

Hard bake and substrate removal: Hard bake is the final step of the photolithographic process. This step is necessary in order to harden the photoresist. Changes in the SU-8 may occur if the operating temperature is higher than previously encountered. Therefore, the wafer is placed on the levelled hotplate for approximately 20 minutes at 120^{o}C which will extend its operating temperature. Hard baking is also useful to eliminate surface cracks which may appear after development. The release is achieved by immersion of the wafer in sodium hydroxide (NaOH) solution in a 2lt volumetric flask at elevated temperature of 68^{o}C. After a few hours of immersion, the SU-8 pieces will be released from the wafer and will float. After

release, the SU-8 pieces are cleaned with running de-ionized water and they are subjected to ultrasonic cleaning bath for 10 minutes. Finally, they are blow dried with the Nitrogen gun.

Metallization: The released SU-8 pieces are then put onto a sample holder of a Cressington 308 sputtering and evaporation metal coat chamber. The procedure that is involved provides a thin adhesive layer (~5nm) of chromium and a 2μm silver coating of the SU-8 pieces. The SU-8 pieces are stuck using double sided tape on the sample holder which can be tilted at a given angle and can be rotated continuously during the sputtering and evaporation in order to achieve good metallization at the sidewalls of the pieces. An evaporation crucible at the bottom holds the charge of silver pieces. After pumping out the chamber, a procedure called Plasma-cleaning takes place in which Oxygen plasma is used to remove a few nm of the pieces' surfaces and give them a clean surface. Next, chromium sputtered in order to improve the adhesion between the silver and SU-8. Finally, the evaporation is carried out, where again the sources are heated slowly in a few steps in order to allow smooth silver evaporation. When this procedure is completed, the samples are turned over and the process is repeated to provide metallization of the other side. At the end of this procedure, the resulting metalized pieces are removed from the evaporator, stacked on top of each other and carefully aligned using alignment pins and precision screws.

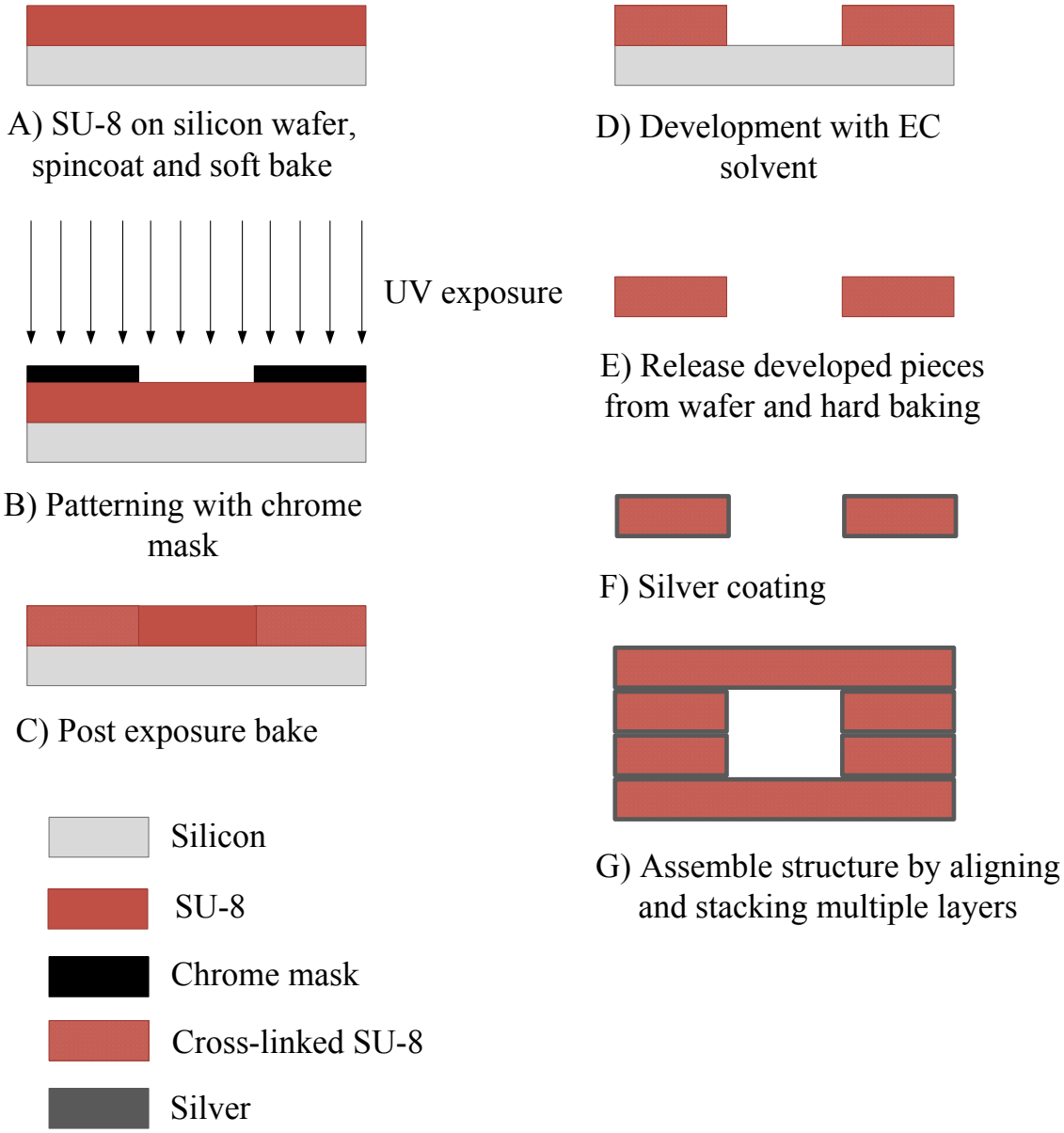

Fig. 6.1.3 Basic steps of the SU-8 micromachining fabrication process.

6.2 DESIGN OF THZ PERIODIC SURFACE

In this section the design of the proposed periodic PRS is described. Full-wave periodic analysis is employed using CST Microwave Studio^{TM} simulation software. Periodic boundary conditions are applied to the unit cell of the structure, assuming an infinite size of the periodic surface, and reduce the calculations of the complete structure into a single unit cell. The

performance of the FPC antennas that are described in later sections has already been explained in previous chapters. The analysis described in [21] shows that a high PRS reflection coefficient magnitude will result in high antenna directivity and a slow variation of the PRS reflection phase with frequency will result in improved antenna bandwidth. Thus, the proposed PRS is designed according to the aforementioned requirements.

A square aperture PRS element has been chosen for the design. The elements are etched in a 0.432mm thick SU-8 layer which is then silver plated as described later in section 6.4. The dimensions of each element are 0.48x0.48mm^2 and the periodicity is 0.6mm (Fig. 6.2.1). The thickness of the layer was chosen in order to facilitate the micromachining fabrication process while the periodicity and the size of the aperture were selected so that the desired phase response was achieved. The simulated reflection coefficient (magnitude and phase) is obtained for normal incidence and is shown in Fig. 6.2.1. A slow variation of the phase with frequency is observed. High values for the reflection coefficient magnitude are obtained for the chosen unit cell dimensions which indicate high antenna directivity.

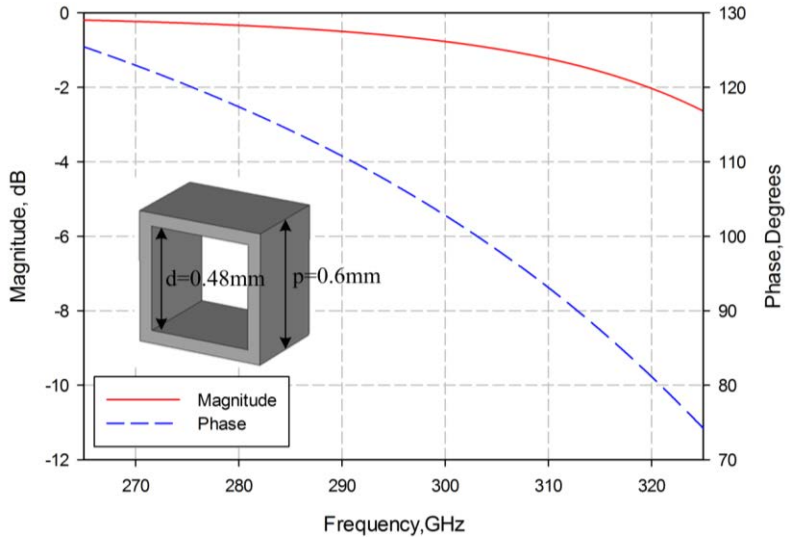

Fig. 6.2.1 Unit cell dimensions and simulated complex reflection coefficient of the proposed PRS.

6.3 ANTENNA DESIGN

Subsequently, based on the unit cell analysis that has been performed, a Fabry-Perot type antenna is designed formed by the proposed PRS array placed at half wavelength distance over a ground plane. An H-plane waveguide bend used for the interconnection between the antenna and the feeding waveguide is also described. The antenna performance is being studied including and excluding two supportive brass plates that hold all the layers together. Finally the simulated input matching and radiation performance for the proposed design are presented.

The H-plane bend is shown as an inset in Fig. 6.3.1. The bend is designed in order to provide a direct and accurate connection interface with the standard waveguide [22]. It is composed of two back-to-back bends and a straight waveguide section. One end of the bend is connected to the antenna and the other end directly to the waveguide flange. In total it was initially formed by four micromachined layers each of which contains holes to allow precision alignment pins and screws of the waveguide flange to pass through. The dimensions of the holes match the ones of the flange. The length of the straight section is 13.55mm, and has been chosen in order to permit fair separation between the flange and the antenna. This ensures that the pins and screws are not blocked from the other side and do not interfere with the antenna. The simulated response of the bend is given in Fig. 6.3.1. A broadband match is achieved with a return loss of at least -20dB over a frequency range from 220GHz to 330GHz.

The complete antenna structure comprises six metalized SU-8 layers and two brass plates placed on the top and bottom to support and hold the structure together (Fig. 6.3.2). Starting from the bottom, layers 1 to 3 form the waveguide bend described above, and layers 4 to 6 form the FPC antenna. When incorporating the antenna and the waveguide bend, the fourth

layer of the H-plane bend was removed in order to simplify the fabrication procedure and reduce the losses, since this change did not significantly affect the response.

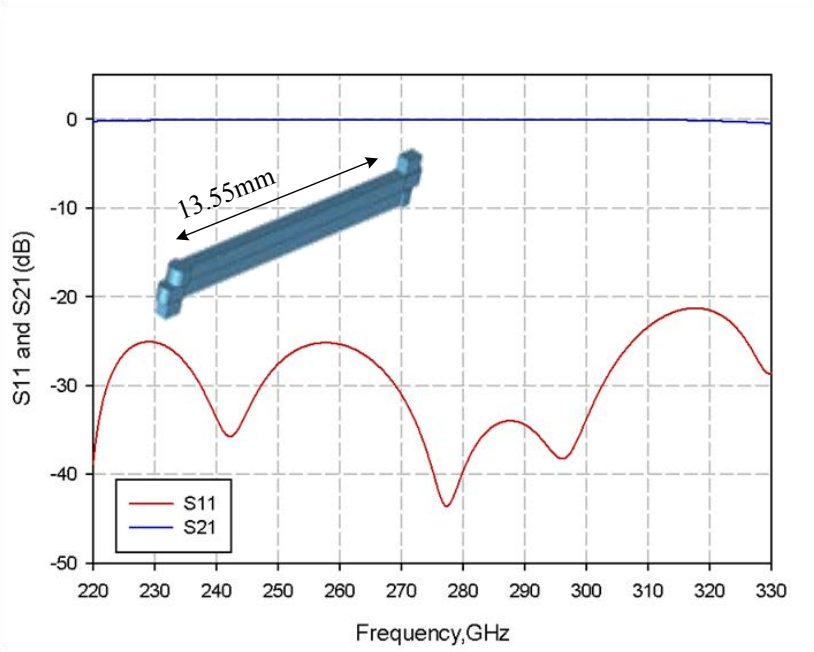

Fig. 6.3.1 Illustration of 4-layer H-plane waveguide bend and simulated S-parameters of H-plane waveguide bend.

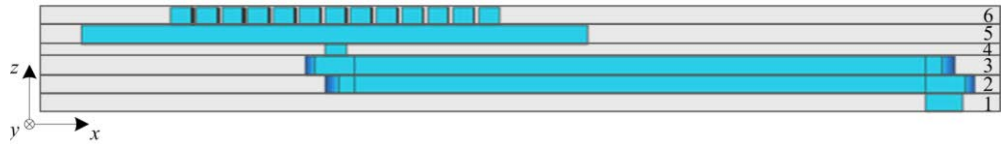

(a)

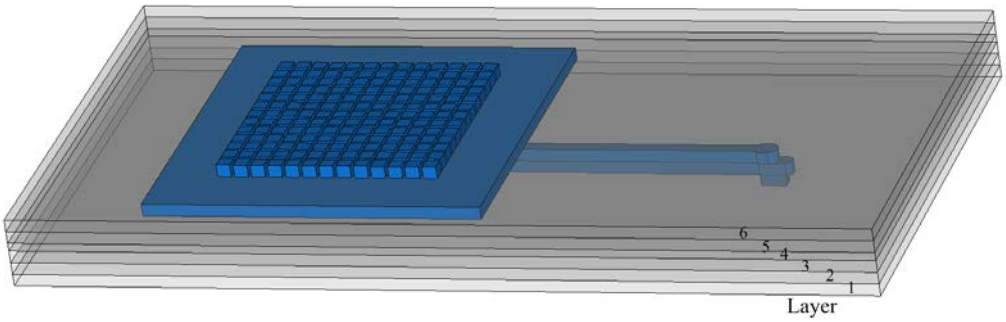

(b)

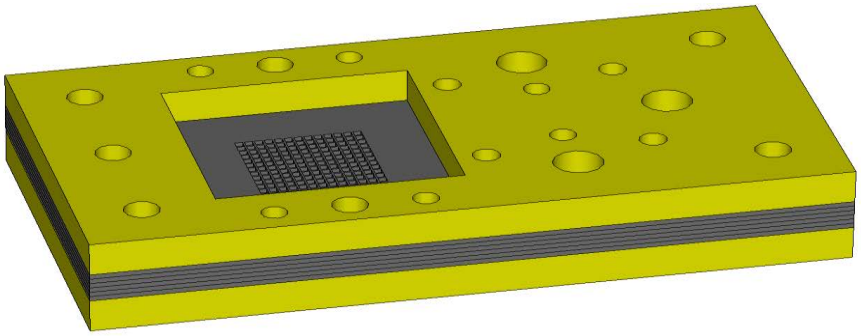

(c)

Fig. 6.3.2 Diagrams of the assembled antenna. (a) Cross section and (b) perspective of the structure (The blue part represents the hollow space and the surrounding conductors were made transparent to offer a clearer view). (c) Complete structure including brass plates and holes for alignment pins and screws.

A top view of all three layers forming the bend is shown in Fig. 6.3.3 (a), showing the area of interest and excluding the holes for the alignment pins and screws. In the same figure, the other three layers of the structure are shown which form the FPC structure. Five of the six layers have the same thickness, equal to 0.432mm to simplify the fabrication. However, due to restrictions to be explained in section 6.4, the thickness of the ground plane was reduced to the minimum available thickness which is 0.288mm. The antenna's design is based on the creation of Fabry-Perot type resonant cavity as mentioned in the introduction. It is formed of a slotted ground plane (layer 4), a supporting ring that defines the air cavity thickness (layer 5) and the PRS (layer 6). The values of the parameters shown in the Fig. 6.3.3 (a) are given in Table I.

The two brass plates used to support the structure are shown in Fig. 6.3.3 (b). The holes have different diameters corresponding to the diameter of the screws used for clamping the structure and the pins that assure the alignment of the antenna's layers and waveguide flange.

A rectangular aperture is etched for the radiation side, large enough so that it will not interfere with the performance of the antenna. From the feeding side, a circular aperture is made to fit the SU-8 device to the waveguide flange. The brass plates have a thickness of 3mm in order to make the whole structure rigid. The rest of the dimensions are also given in Table I. It is important to note that the brass plates are only used to clamp the SU-8 layers together and strengthen the structure and form no part in the alignment of the layers or waveguide flange.

As explained in the beginning of this section, the antenna has been formed using the optimized aperture PRS layer studied in 6.2, placed on top of the supporting layer in front of the ground plane. An air cavity is thus created of approximately half wavelength at 300GHz (0.432mm). The slot in the ground plane fed from the waveguide bend is used as a single feeder of the antenna. The dimensions of the slot in the ground plane were selected such that a good matching in the frequency range of interest is achieved. For the PRS, a total of 13x13 array elements are etched into the SU-8 layer, whose total length corresponds to about 8λ at 300GHz. Although it is a finite size structure, it is electrically large enough for the edge effects to be negligible in the calculation of the reflection coefficient. Moreover the distance of the supporting walls from the end of the PRS array is about 4λ. This was carefully studied by simulation to ensure that the antenna performance and the radiation patterns are not deteriorated.

The complete structure of the proposed antenna has been simulated in CST Microwave Studio and the obtained directivity and gain are presented in Fig. 6.3.4. A maximum directivity of 22.8dBi has been achieved at 283.8GHz with a 3dB radiation bandwidth of approximately 4.5GHz. The return loss is also shown in Fig. 6.3.4 with a minimum of around -20dB at 281.8GHz, whereas at the central frequency, 284GHz, $|S_{11}|$ is -7.5dB. This performance could not be further optimized due to the fabrication limitations in terms of the minimum dimension

of the feeding slot. Thinner feeding slots have produced S_{11} values below -15dB. Moreover, less reflective arrays could give better performance in terms of matching, but a lower directivity would be obtained. The impedance mismatch and material losses give a deviation of 1.5dB between directivity and gain at the central frequency.

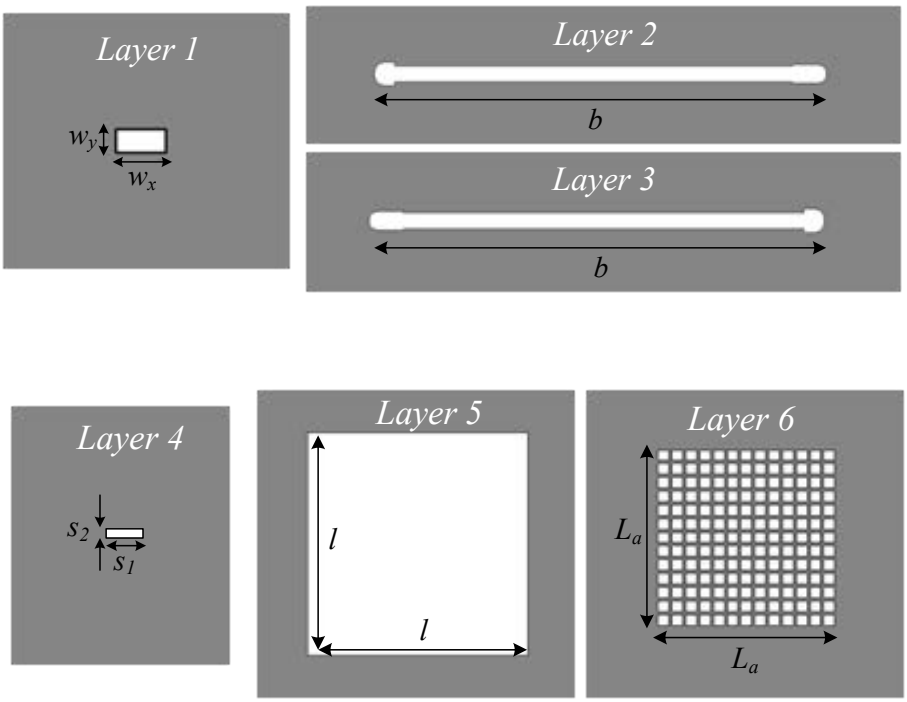

(a)

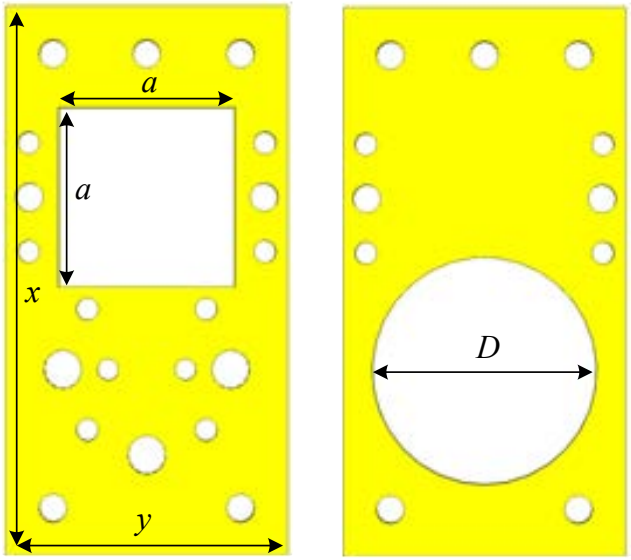

(b)

Fig. 6.3.3. (a) Illustration of the 6 layers forming the complete antenna structure (top view), white colour represents the air and grey the silver, (b) Top and bottom brass plate layers.

The effect of the brass plates in the antenna's performance has also been evaluated. A comparison of the directivity and realized gain for the structure including and excluding the brass plates is shown in Fig. 6.3.5. It can be observed that the directivity is increased by 0.3dB for the complete structure, while the gain drops by 0.2dB at the central frequency. Also, a small frequency shift towards higher frequencies is observed for the structure without the brass plates. Finally, an efficiency comparison was carried out in simulations. Both total and radiated efficiency are similar with and without the brass plates. At the central frequency, a radiation efficiency of 85% is observed for the complete structure while an 88% is obtained without the brass plates.

TABLE I

ANTENNA DESIGN DIMENSIONS FROM FIG. 6.3.3

Parameter	α	x	y	D	w_x	w_y
Value (mm)	13	46	24	19.05	0.8636	0.4318

Parameter	b	s_1	s_2	l	L_a
Value (mm)	15.4	0.5	0.09	11.8	7.68

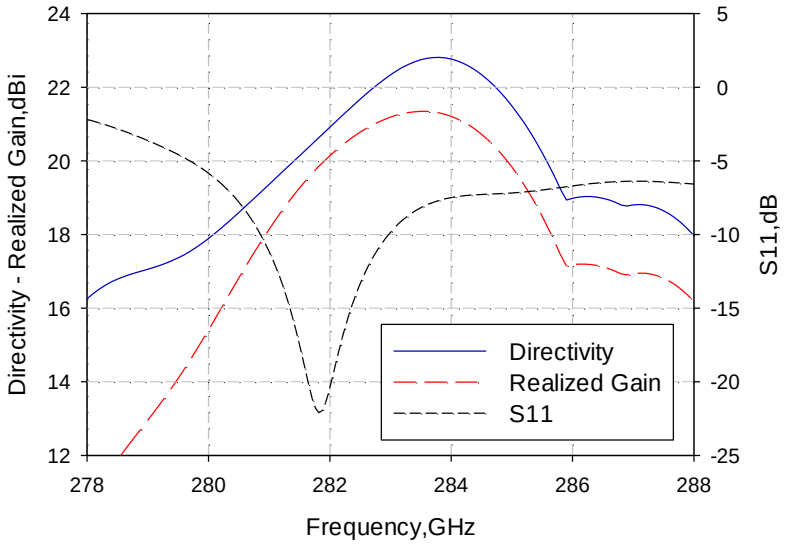

Fig. 6.3.4 Simulated directivity, realized gain and return loss of the proposed antenna.

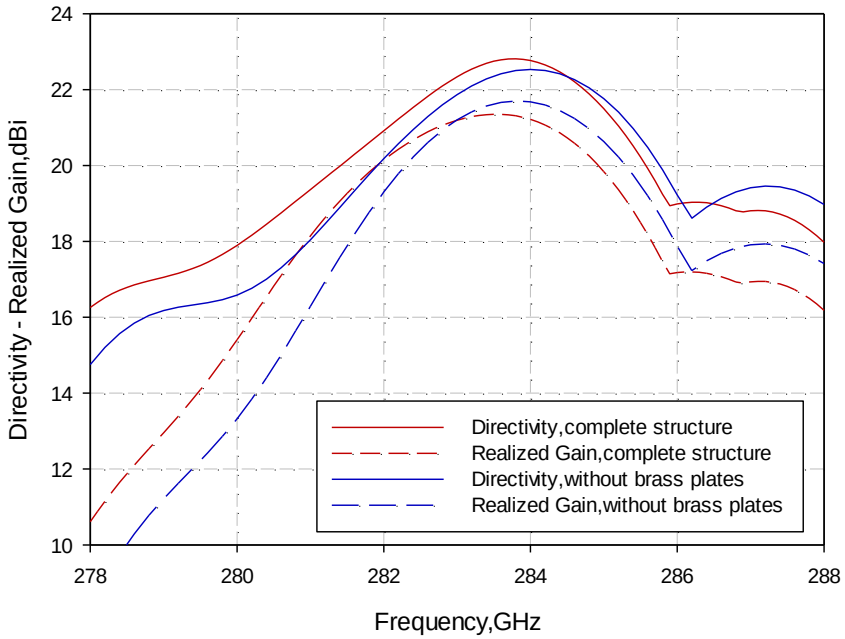

Fig. 6.3.5 Directivity and realized gain comparison between complete structure and antenna without brass plates.

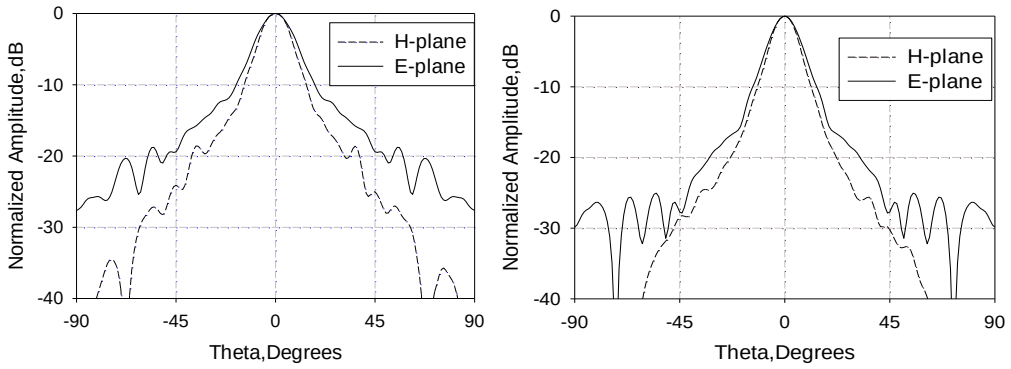

(a) (b)

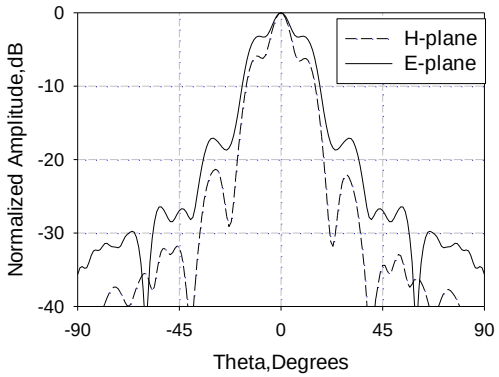

(c)

Fig. 6.3.6 Simulated H- and E-plane radiation patterns for: (a) 281GHz, (b) 283GHz and (c) 285GHz.

In Fig. 6.3.6 the H-plane and E-plane radiation patterns are shown for three frequencies over the operating band. Broadside directive beams are observed with a side lobe level below -20dB at the lower and central frequency whereas at the upper edge the beam becomes narrower with slightly higher sidelobes due to the frequency scanning and beam splitting effect which is typical in leaky-wave type antennas. This becomes more obvious at higher frequencies, were a split beam is obtained and the maximum radiation angle increases with frequency; this again is typical for leaky-wave antennas and could be useful in certain applications requiring multi-beam and beam scanning designs. This effect is investigated in section 6.3.2.

6.3.1 Multiple Slots for Broadband Matching

An endeavour to improve the matching performance of the proposed antenna has been carried out and is presented in this section. It consists in employing multiple slots etched off the ground plane instead of one. Namely, three parallel rectangular slots of the same size were used. The dimensions of each slot are s_x=0.92mm and s_y=0.05mm (Fig. 6.3.7). while the distance between the adjacent slots is s_d=0.1mm. These dimensions and spacing of the slots

were selected after investigations in order to obtain the optimum matching performance. As it can be seen from Fig. 6.3.8, in the case of three feeding slots, the S_{11} is significantly improved and thus so is the gain.

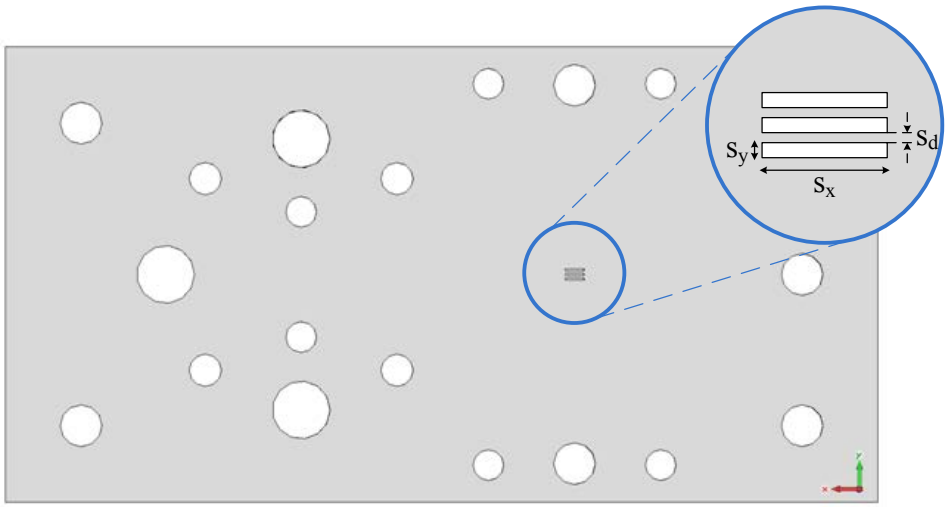

Fig. 6.3.7 Illustration of the three feeding slots (top view).

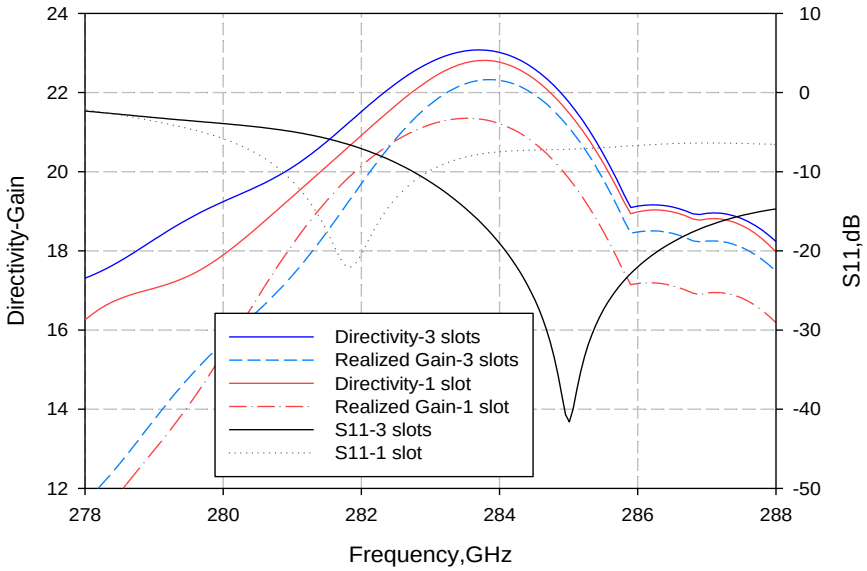

Fig. 6.3.8 Comparison of simulated directivity, realized gain and S_{11} for one and three feeding slots.

6.3.2 Beam-Steering Application

Based on the beam-splitting effect that has been observed in the proposed antenna for higher frequencies it can be deduced that, if a straightforward change in the position of the feeding slot towards one side of the antenna is performed, a single beam radiation pattern is obtained. To validate this concept, three slot positions were considered as shown in Fig. 6.3.9 (a). The simulated S_{11} for all the cases is presented in Fig. 6.3.9 (b), showing a good matching between around 294GHz and 305GHz, revealing a second possible operational band of the proposed antenna. The corresponding radiation patterns for operation at 302GHz are shown in Fig. 6.3.10. It can be observed that for position 1 (Fig. 6.3.10a) there are two beams at -40^{o} and $+40^{o}$. As the slot is moved towards one edge of the antenna, one of the two beams is suppressed, as expected, resulting in a single beam at 32^{o} with good side lobe level for position 3 (Fig. 6.3.10c). Furthermore, an angle scan of 12^{o} with frequency is obtained within the frequency band where good matching is observed.

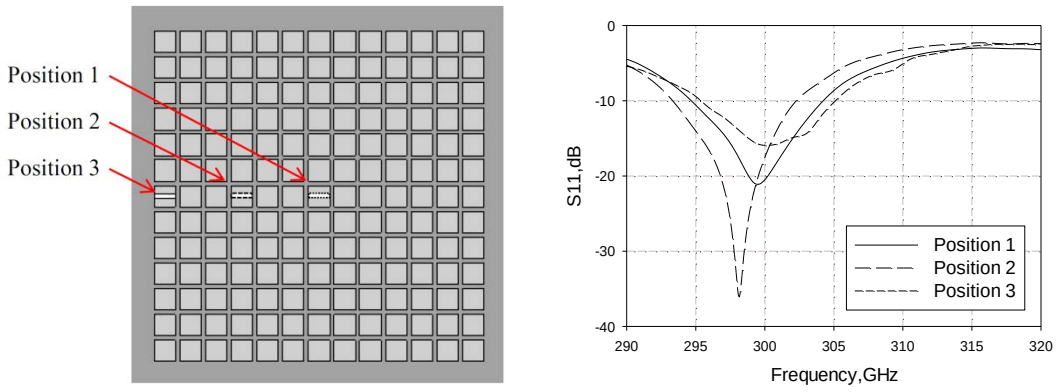

(a) (b)

Fig. 6.3.9 (a) Illustration of the three feeding slot positions (top view), (b) Simulated S_{11} for three slot positions.

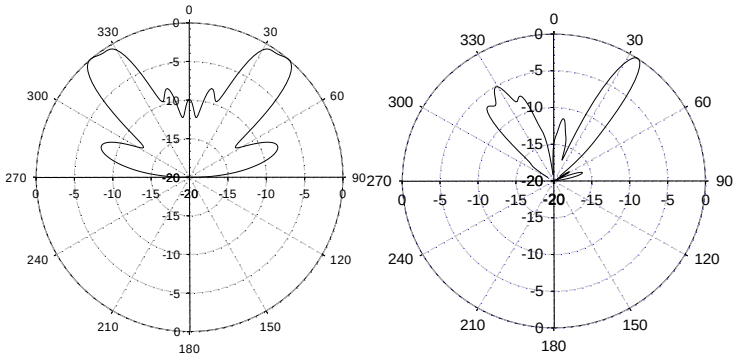

(a) (b)

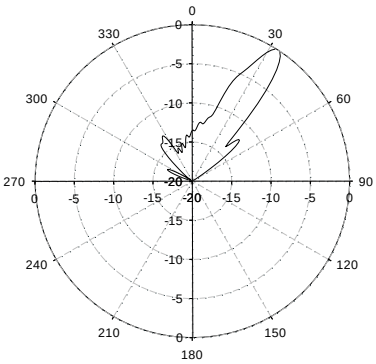

(c)

Fig. 6.3.10 Simulated H-plane radiation patterns at 302GHz for: (a) position 1, (b) position 2, and (c) position 3 (from Fig. 6.3.9).

6.4 FABRICATION

The proposed antenna described in the previous section has been fabricated using the in-house microfabrication process based on SU-8. The antenna has been designed using a square aperture PRS in a silver plated SU-8 layer. SU-8 is a UV-sensitive photoresist and able to form structures of high aspect ratio [23, 24]. The required accuracy at such high frequencies imposes the use of micromachining fabrication techniques so SU-8 is chosen as a suitable solution for this technique. A simple process is involved which can be exploited for volume production. Furthermore, the losses in silver plated SU-8 waveguiding structures are similar to those in solid metal structures and the cost of the material is low [24].

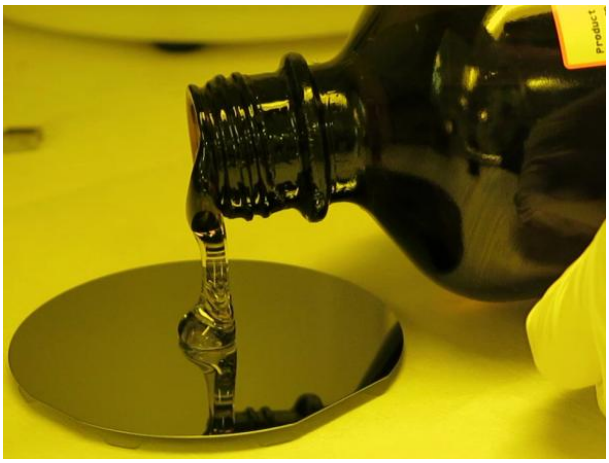

(a)

(b)

(c)

(d)

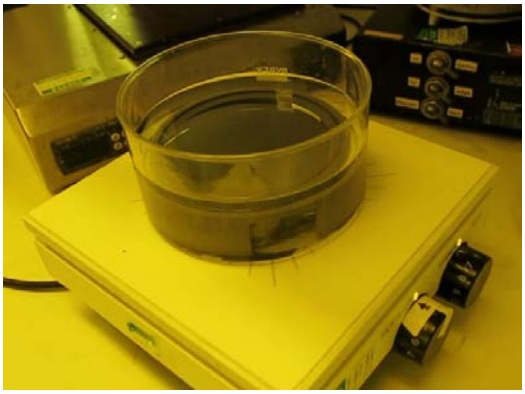

(e)

Fig. 6.4.1 Photographs of the fabrication process steps in the clean room. (a) SU-8 deposition, (b) spin coating, (c) soft baking, (d) UV exposure, and (e) development.

As mentioned in section 6.3, the designed antenna consists of 6 layers (Fig. 6.3.3a) and each layer was originally designed to be 432μm thick. However, in order to achieve better metallization inside the narrow waveguide slot, layer 3 was reduced to 288μm, to allow the silver to be coated thoroughly over all the sidewalls. All the layers were fabricated through an ultra-thick SU-8 photo-resist based micromachining process. First, SU-8 50 photo-resist was deposited (Fig. 6.4.1a) and spin coated (Fig. 6.4.1b) on a 100mm silicon wafer and the edge bead was removed immediately. For the layers with different thickness, the amount of the SU-8 disposed on wafer and spin coating parameters were adjusted to achieve the desired thickness. Then, the wafer rested on a carefully levelled stage for few hours to allow the liquid resist to be self-planarized. This step is critical to harvest a smooth and uniform surface. After that, the wafer was baked at 65^{o}C and 95^{o}C subsequently (Fig. 6.4.1c) and thereafter patterned with the designed mask in a Cannon PLA-501 mask aligner (Fig. 6.4.1d). For the 288μm layer the baking time was 30min at 65^{o}C and 2 hours and 40min at 95^{o}C. For the 432μm layers the baking time was 30min and 4 hours and 30min at 65^{o}C and 95^{o}C respectively. Post exposure bake was conducted at 70^{o}C, which was lower than the previous bake, to reduce the thermal stress accumulated in the thick SU-8 layer. The pieces were developed in EC solvent (Fig. 6.4.1e) and released from the silicon wafer using KOH solution. Finally, the SU-8 pieces were metalized with 2μm thick silver in a Cressington 308R vacuum evaporator (Fig. 6.4.2a, b). The previous steps take place in a Clean room environment while the release of the SU-8 pieces from the wafer and the metallization are carried out at the process room.

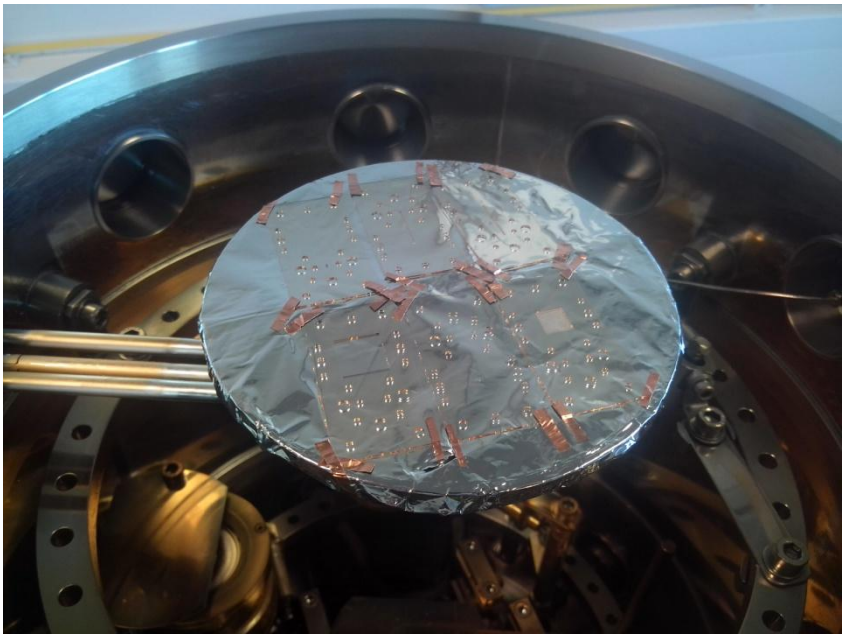

(a)

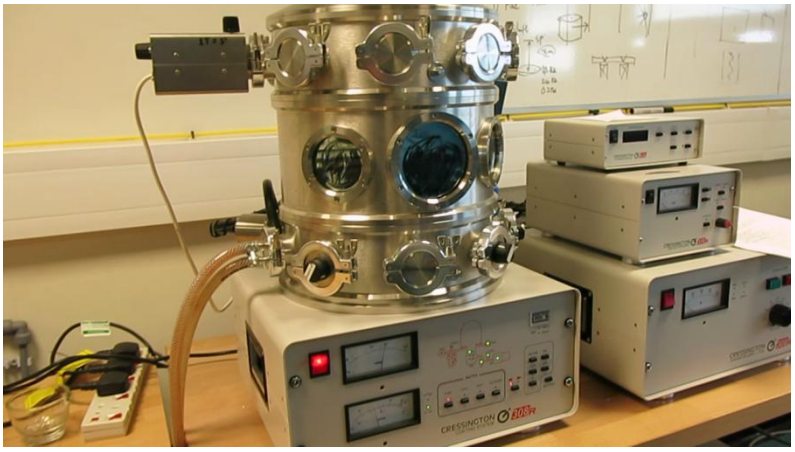

(b)

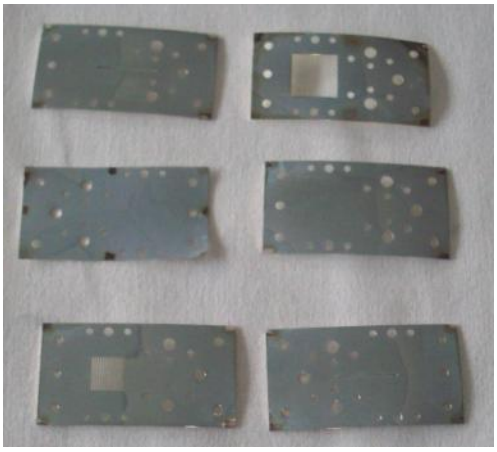

(c)

Fig. 6.4.2 Photographs of the fabrication process steps in the process room. (a) SU-8 pieces secured on the sample holder of the evaporator, (b) Cressington 308R vacuum evaporator, (c) silver-coated SU-8 layers of the proposed structure.

Finally, the antenna was assembled by stacking the six silver-coated SU-8 layers shown in Fig. 6.4.2 (c) and clamping between two brass plates, as illustrated in Fig. 6.3.2 (b). A careful alignment of the layers had been carried out using two metallic pins with precise diameter which also acted as the dowel pins to fit into the standard waveguide flange. A photo of the assembled circuit is shown in Fig. 6.4.3.

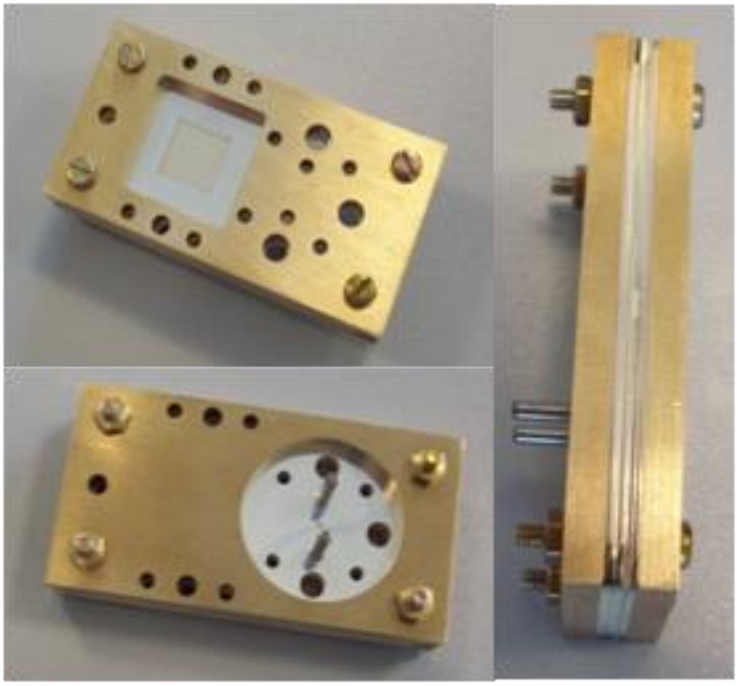

Fig. 6.4.3 Photograph of fabricated antenna comprising six layers of metallised SU-8 and brass plates.

6.5 MEASUREMENTS

In this section measurements of the fabricated prototype are presented. Initial measurements demonstrated that the operation of the antenna was shifted to a lower frequency than the expected one shown in Section 6.3. This fact suggested that some of the dimensions of the fabricated antenna did not match the proposed design due to fabrication inaccuracies. An error of up to ±20μm can be expected with the employed fabrication procedure, which has a significant effect in this frequency band. Another factor that could have contributed in this altered behaviour is the possible imperfect flatness of the SU-8 layers, and in particular the top radiating PRS layer. Based on the above, the antenna was simulated again in an effort to achieve better agreement with measurements and hence account for the altered fabricated dimensions.

Only two parameters were changed for this 'redesigned' antenna. The parameter that most significantly affects the antenna's operating frequency is the thickness of layer 5 which defines the height of the air cavity. This was increased by 30μm. It is worth noting that the 30μm added to the cavity height can be attributed partly to the fabrication tolerance in the thickness of layer 5 and partly to the slight curvature of layers 5 and 6. The new value of the cavity height is 462μm. Also, the aperture size of the PRS was increased by 20μm so the new value of d is 500μm.

In Fig. 6.5.1, the simulated realized gain and S_{11} is presented for the new structure. The maximum broadside gain is now shifted to 267GHz with a value of 19.1dBi. The matching has deteriorated, achieving only around -2dB within the operating bandwidth. However, at higher frequencies where the beam splitting effect is observed, good matching is obtained from 294GHz to 305GHz. The maximum gain at this frequency band is 13.4dBi. However for a single beam operation with the feeding slot at one edge of the ground plane as described in section 6.3.2, the maximum gain has been calculated to be 15.9dBi which is expected since the radiated power is almost doubled.

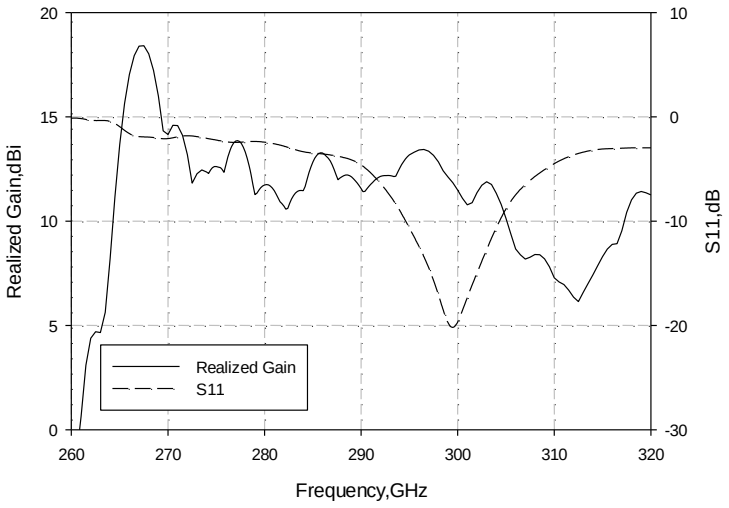

Fig. 6.5.1 Simulated realized gain and S_{11} of the redesigned antenna.

The S-parameters were measured using an Agilent N5250A network analyzer with OML WR-3 extension head. The measurements were subject to a Short-Offset-Load-Offset-Load (SOLOL) calibration. The radiation patterns were measured in an automated anechoic chamber of 60x60x90cm^3 dimensions available at the Rutherford Appleton Laboratory, Didcot, UK. A WR-2.8 corrugated feed horn was used as a receiver placed at a distance of 22cm from the antenna under test as shown from the photograph in Fig. 6.5.2. The patterns were measured only at a small number of frequencies in order to validate the simulation predictions. At each frequency a dynamic range of more than 40dB was achieved for the patterns measurement. The angular coverage of the measurement was limited from the dimensions of the chamber to -50^o and 50^o with a step of 0.5 degrees. Only H-plane patterns were measured.

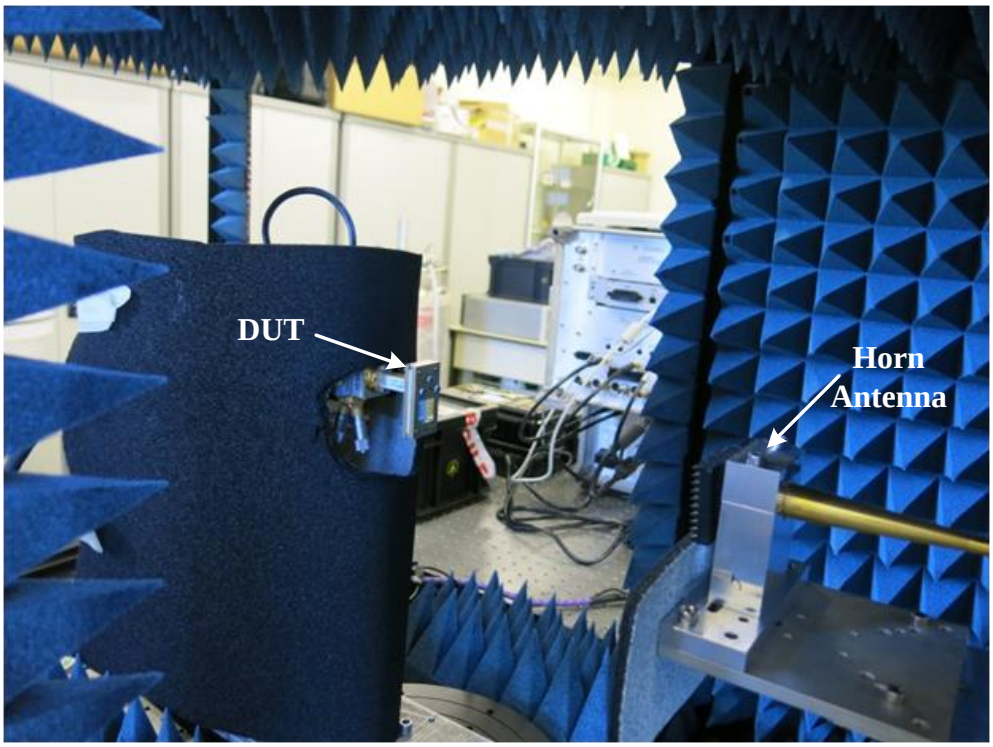

Fig. 6.5.2 Photograph of the measurement set up in the anechoic chamber.

In order to validate the performance of the waveguide-fed slot in the ground plane (layer 4), comparison was made of the simulated and measured S_{11} for the device after removal of layers 5 and 6, as shown in Fig. 6.5.3. The good agreement between simulation and measurements (less than 2% frequency shift) indicates that the dimensions of the coupling slot were only slightly altered from the designed values.

The measured S_{11} response of the complete antenna structure in comparison with the simulated one for the original and the redesigned antenna is depicted in Fig. 6.5.4. There is a good agreement between the measured and the simulated response of the redesigned antenna. For frequencies around 267GHz, where the antenna is expected to operate, there is a discrepancy of about 1dB which is attributed to losses.

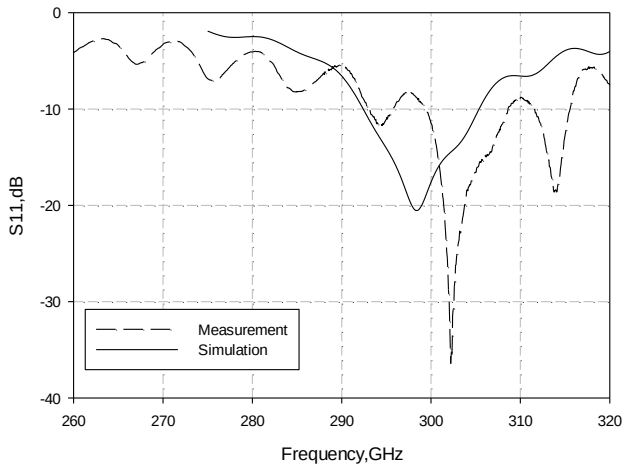

Fig. 6.5.3 Measured S_{11} in comparison with simulation of ground plane with a slot.

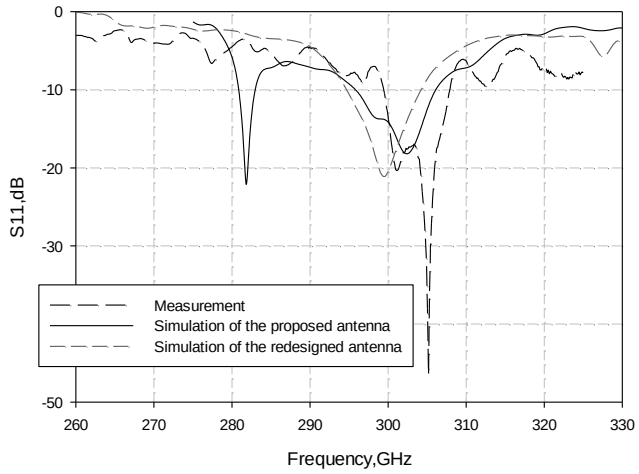

Fig. 6.5.4 Measured S_{11} in comparison with simulation of proposed and redesigned antenna.

In Fig. 6.5.5 the normalized measured H-plane patterns are shown for four different frequencies. It can be observed that there is a very good agreement with the simulations. Nevertheless, a consistent asymmetry is evident at the measured patterns, which is not present in the simulation. This is attributed to unwanted reflections at the relatively bulky positioning structure that was supporting the antenna in the measurements set-up. The patterns were measured for a small number of frequencies due to allocated time limitations. Also, at the time of the radiation pattern measurements we lacked the exact information about the dimensional discrepancies of the fabricated antenna, which as explained above led us to the redesigned antenna simulation model. However, a good directive pattern was obtained at 268GHz, i.e. very close to the central frequency of maximum broadside gain. The slightly distorted main beam is typical of this type of leaky-wave FPC antennas when operated above the central frequency as explained in section 6.3. It is interesting to note that in the frequencies where the split beam is observed, i.e. around 302GHz, the antenna is well matched (Fig. 6.5.4). This means that it could be used for beam scanning applications applying the change in the position of the feeding slot as proposed in 6.3.2.

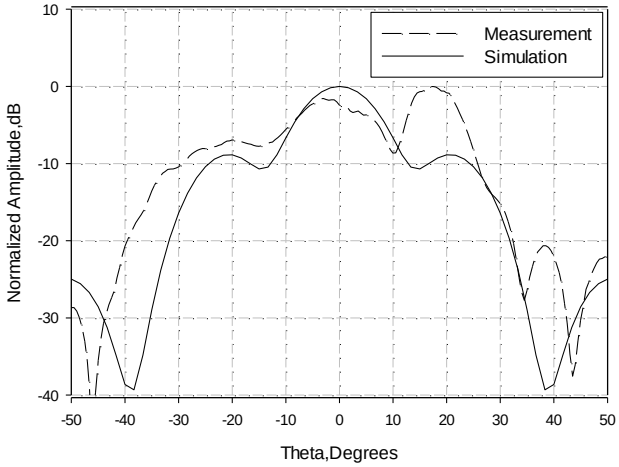
Measurement
Simulation
Normalized Amplitude,dB
Theta,Degrees
10
0
-10
-20
-30
-40
-50
-40
-30
-20
-10
0
10
20
30
40
50

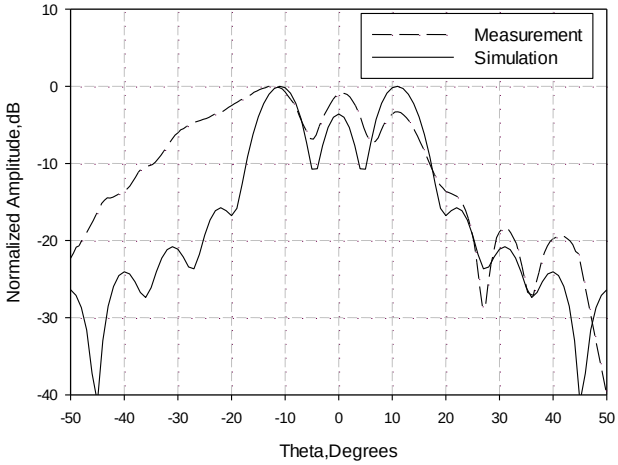
Measurement
Simulation
Normalized Amplitude,dB
Theta,Degrees
10
0
-10
-20
-30
-40
-50
-40
-30
-20
-10
0
10
20
30
40
50

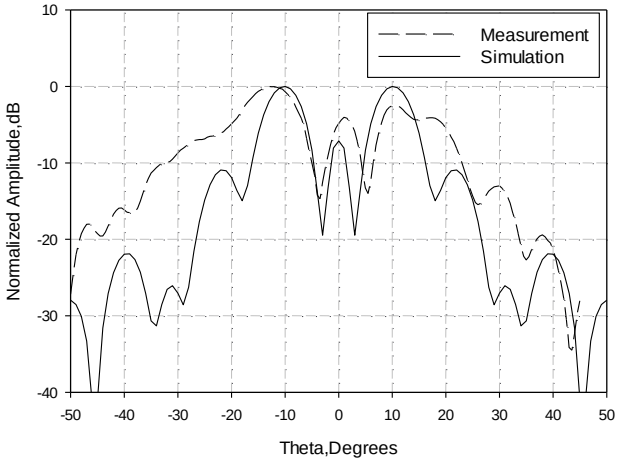
Measurement
Simulation
Normalized Amplitude,dB
Theta,Degrees
10
0
-10
-20
-30
-40
-50
-40
-30
-20
-10
0
10
20
30
40
50

(c)

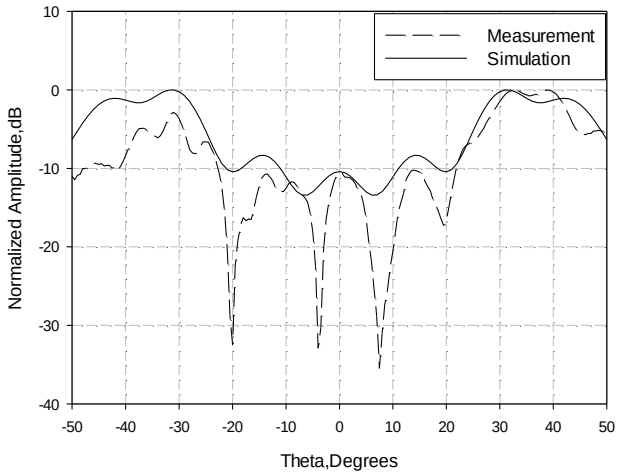

(d)

Fig. 6.5.5 Simulated and measured H-plane radiation patterns for: (a) 268GHz, (b) 270GHz, (c) 272GHz and (d) 302GHz.

Finally, the factors that could contribute to the losses of the fabricated antenna have been investigated. Firstly, a reduced conductivity of the silver caused by the imperfection of the metal coating will lead to losses. More specifically, for a surface roughness of 200nm, 51% reduction of the conductivity has been calculated leading to a total loss of 0.25 dB [23]. However, in order to account for an extreme case scenario, assuming 1% silver conductivity for a 15.4-mm-long waveguide wall a loss of 3.5 dB is estimated, while another 4.5 dB is attributed to the 11.8 x 11.8 mm^2 metallic walls supporting the PRS layer [22, 23]. Reduced silver conductivity is more likely at the corners of the square apertures and the feeding slot. Furthermore, the presence of even tiny air gaps between SU-8 layers will result in significant power dissipation at these frequencies and hence will contribute to the total losses of the structure. In order to achieve a better performance in terms of losses, a newly developed fabrication technique producing fully cross-linked metalized SU-8 layers [24] is currently being developed.

6.6 BROADBAND FABRY-PEROT TERAHERTZ ANTENNA

The Fabry-Perot type antenna that has been presented in this Chapter is based on a single layer highly reflective PRS and as such it possesses a narrow bandwidth. This issue could be addressed introducing a second PRS layer employing the technique described in Chapter 3. Therefore, the unit cell of the double layer PRS is initially analyzed applying periodic boundary conditions. The unit cell dimensions of the PRS are d_1=0.37mm and d_2=0.48mm for the first and the second layer respectively with a periodicity p of 0.6mm for both layers (Fig. 6.6.1). From the extracted reflection coefficients shown in Fig. 6.6.2, high reflection magnitude values and a reflection phase increase are observed around 294GHz. This indicates a broadband antenna operation when the proposed double layer PRS is employed above a ground plane.

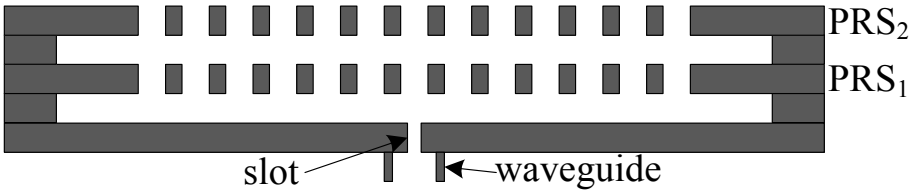

Fig. 6.6.1 Cross section of the proposed multilayer design.

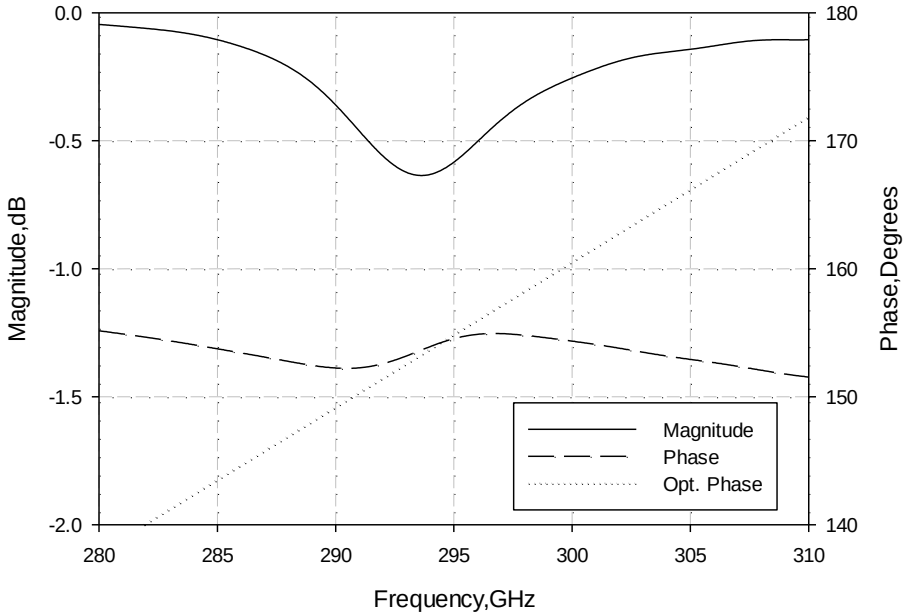

Fig. 6.6.2 Unit cell simulated complex reflection coefficient of the proposed double layer PRS.

Subsequently, the finite size antenna structure shown in Fig. 6.6.1 is designed and described here. It comprises a ground plane, two supporting rings and two PRS aperture arrays. Each PRS slot array consists of 13x13 square elements. A waveguide-fed slot is used in the ground plane. The size of the coupling aperture is 0.51mm x 0.08mm. These dimensions were selected such that a good matching in the frequency range of interest is achieved. The overall dimensions of the antenna are 15mm x 15mm. The first cavity is 0.476mm which is the thickness of the supporting ring, while the second is 0.382mm.

A maximum directivity of about 23dBi has been achieved at 289GHz as shown in Figure 6.6.3. The 3dB radiation bandwidth is 3.7%. In the same graph the directivity response of a single PRS layer antenna designed to operate in the same frequency band is also depicted for comparison. It can be observed that the proposed double layer antenna is significantly more broadband. A more detailed comparison of the two antennas is presented on Table II. Finally,

in Figure 6.6.4, the H-plane and E-plane are shown for the central frequency and the frequencies at the two edges of the operating band. Good suppression of the side lobes is observed with a side lobe level below -20dB at the lower and central frequency whereas at the upper edge a beam splitting effect is again observed.

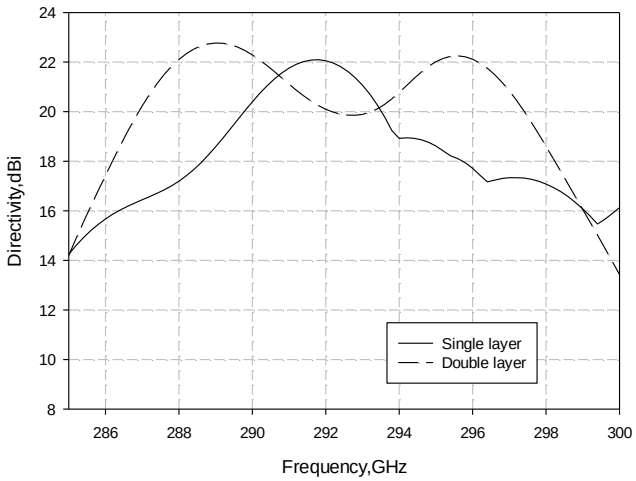

Fig. 6.6.3 Comparison of the simulated directivity between the single and the double layer antenna.

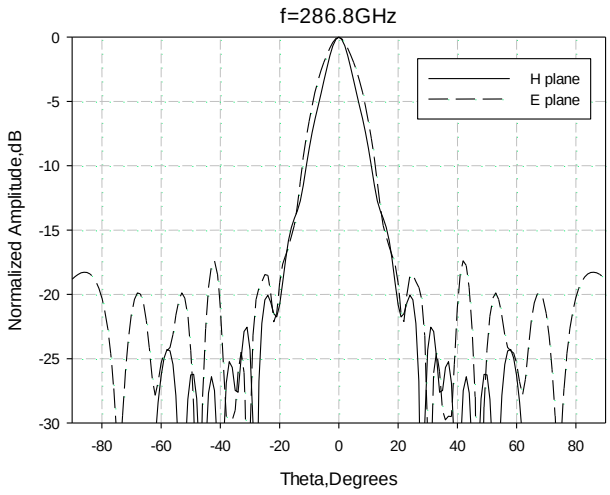

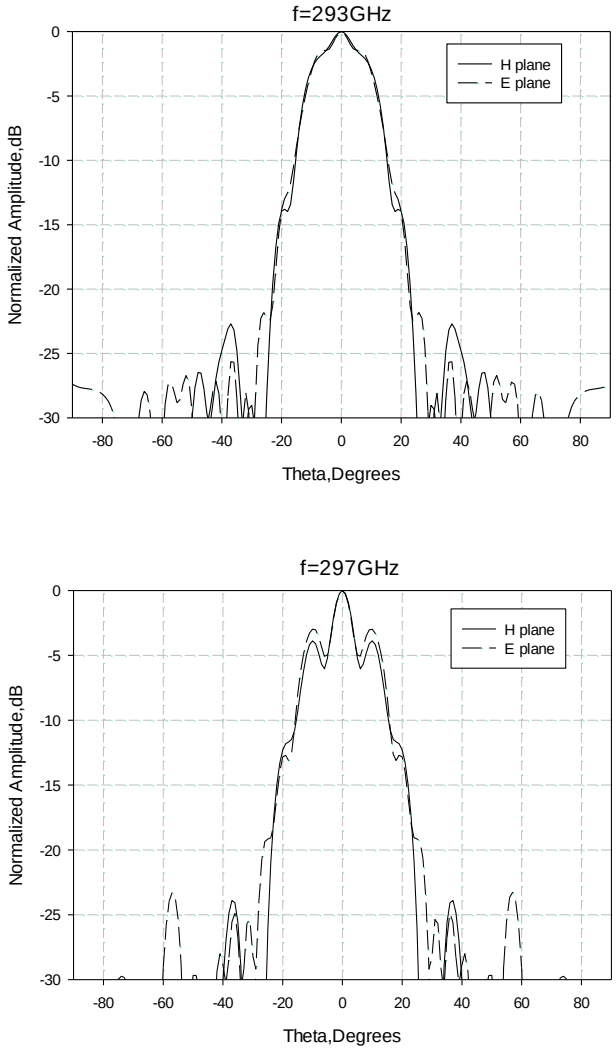

Fig. 6.6.4 Simulated radiation patterns of the proposed double layer antenna at frequencies over the operating bandwidth.

TABLE II

ANTENNAS CHARACTERISTICS COMPARISON

Design	***Maximum Directivity (dBi)***	***-3dB Bandwidth (%)***	***Directivity – Bandwidth Product***
Single-layer	22.1	1.6	0.35
Double-layer	22.7	3.7	0.84

6.7 CONCLUSIONS

A micromachined periodic surface based antenna has been proposed operating at low THz frequencies. An initial design for broadside operation at 284GHz is presented. Moreover, at higher frequencies a split beam is obtained and a beam scanning application is proposed by changing the position of the feeding slot leading to a single beam operation. A prototype is fabricated and experimentally tested validating the simulations. The frequency shift compared to the original design is attributed to inaccuracies of the fabrication process which have a significant effect in this frequency band. Moreover, alternative designs have been investigated for matching improvement employing multiple feeding slots, for beam scanning applications changing the feeding slot position and for more broadband performance employing two PRS layers.

REFERENCES

[1] B. A. Munk*, Frequency Selective Surfaces Theory and Design*. Hoboken, NJ: Wiley, 2000.

[2] W. J. Padilla, M. T. Aronsson, C. Highstrete, M. Lee, A. J. Taylor, R. D. Averitt, "Novel Electrically Resonant Terahertz Metamaterials" Phys. Rev. B, Rapid 2007, 75, 041102.

[3] R. Dickie, R. Cahill, V. Fusco, H. S. Gamble, N. Mitchell, "THz Frequency Selective Surface Filters for Earth Observation Remote Sensing Instruments*," IEEE Transactions on Terahertz Science and Technology*, vol. 1, no. 2, Nov. 2011.

[4] R. Dickie, R. Cahill, H. S. Gamble, V. F. Fusco, A. Schuchinsky, and N. Grant, "Spatial demultiplexing in the sub-mm wave band using multilayer free-standing frequency selective surfaces," *IEEE Trans. Antennas Propag.*, vol. 53, no. 6, pp. 1903–1911, Jun. 2005.

[5] R. Dickie, R. Cahill, H. S. Gamble, V. F. Fusco, M. Henry, M. L. Oldfield, P. G. Huggard, P. Howard, N. Grant, Y. Munro, and P. de Maagt, "Submillimeter wave frequency selective surface with polarization independent spectral responses," *Proc. IEEE Antennas and Propagation*, vol. 57, pp. 1985–1994, Jul. 2009.

[6] R. J. Martin and D. H. Martin, "Quasi-optical antennas for radiometric remote sensing," *Electron. Commun. Eng. J.*, vol. 8, pp. 37–48, Feb. 1996.

[7] M. Euler, V. F. Fusco, R. Cahill, and R. Dickie, "325 GHz single layer sub-millimeter wave FSS based split slot ring linear to circular polarization convertor," *IEEE Trans. Antennas Propag.*, vol. 58, no. 7, pp. 2457–2459, Jul. 2010.

[8] B. Y. Toh, R. Cahill, and V. F. Fusco, "Understanding and measuring circular polarization," *IEEE Trans. Edu.*, vol. 46, no. 3, pp. 313–319, Aug. 2003.

[9] M. Euler, V. F. Fusco, R. Cahill, and R. Dickie, "Comparison of FSS based linear to circular polarization converter geometries," *Proc. IET Microw. Antennas and Propag.*, vol. 4, pp. 1764–1772, Nov. 2010.

[10] C. Argyropoulos, K. Q. Le, N. Mattiucci, G. D'Aguanno, and A. Alù, "Broadband Absorbers and Selective Emitters Based on Plasmonic Brewster Metasurfaces," *Physical Review B*, Vol. 87, No. 20, 205112 (6 pages), May 10, 2013.

[11] C. Debus, P. Haring Bolívar, "Terahertz biosensors based on double split ring arrays," *Proc. SPIE 6987*, Metamaterials III, 69870U, April 23, 2008.

[12] N. Llombart, K. B. Cooper, R. J. Dengler, T. Bryllert, and P. H. Siegel, "Confocal ellipsoidal reflector system for a mechanically scanned active terahertz imager," *IEEE Transactions Antennas and Propagation*, on,vol. PP, no. 99, pp. 1 –1, 2010.

[13] W. Menzel, A. Moebius, "Antenna Concepts for Millimeter-Wave Automotive Radar Sensors", *Proc. IEEE*, vol.100, No. 7, July 2012.

[14] J.W. Britton, J. P. Nibarger, K.W. Yoon, J. A. Beall, D. Becker, H.-M Cho, G. C. Hilton, J. Hubmayr,M. D. Niemack, and K. D. Irwin, "Corrugated silicon platelet feed horn array for CMB polarimetry at 150 GHz," in *SPIE Proc*., San Diego, CA, USA, Jun. 2010, vol. 7741, p. 77410T.

[15] Ziran Wu, Min Liang, Wei-Ren Ng, M. Gehm, Hao Xin, "Terahertz Horn Antenna Based on Hollow-Core Electromagnetic Crystal (EMXT) Structure," *IEEE Transactions on Antennas and Propag.*, vol.60, no.12, pp. 5557-5563, Dec. 2012.

[16] M. Alonso-DelPino, N. Llombart, G. Chattopadhyay, C. Lee, C. Jung- Kubiak, L. Jofre, and I. Mehdi, "Design guidelines for a terahertz silicon micro-lens antenna," *IEEE Antennas Propag. Lett.*, vol. 12, pp. 84–87, 2013.

[17] D. F. Filippovic, S. S. Gearhart, and G. M. Rebeiz, "Double slot on extended hemispherical and elliptical silicon dielectric lenses," *IEEE Trans. Microw. Theory Tech.*, vol. 41, no. 10, pp. 1738–1749, Oct. 1993.

[18] N. Zhu, and R. W. Ziolkowski, "Progress toward THz antenna designs with high directivity and high efficiency," *Antennas and Propagation Society International Symposium (APSURSI), 2013 IEEE* , vol., no., pp. 2271, 2272, 7-13 July 2013.

[19] Hsu Tai-Ran, MEMS and Microsystems: Design, Manufacture, and Nanoscale Engineering (2nd edition, Wiley).

[20] Gentili E., Tabaglio L., Aggogeri F.: 'Review of Micromachining Techniques,' *Proceedings of the 7th International Conference on Advanced Manufacturing Systems and Technologies*, 2005.

[21] A. P. Feresidis and J. C. Vardaxoglou, "High gain planar antenna using optimised partially reflective surfaces," *IEE Proc. Microw. Antennas Propag*., vol. 148, no. 6, pp. 345-350, Dec. 2001.

[22] X. Shang, M. Ke, Y. Wang, and M. J. Lancaster, "Micromachined W-band waveguide and filter with two embedded H-plane bends," *IET, Microw., Antennas Propag.*, vol. 5, no. 3, pp. 334-339, 2011.

[23] Y. Wang, M. Ke, M.J. Lancaster, J. Chen, "Micromachined 300-GHz SU-8-Based Slotted Waveguide Antenna," *Antennas and Wireless Propagation Letters, IEEE* , vol.10, no., pp.573-576, 2011.

[24] X. Shang, M. Ke, Y. Wang, M.J. Lancaster, "WR-3 Band Waveguides and Filters Fabricated Using SU8 Photoresist Micromachining Technology," *Terahertz Science and Technology, IEEE Transactions on*, vol.2, no.6, pp.629-637, Nov. 2012.

CHAPTER 7

CONCLUSIONS AND FUTURE WORK

High-gain planar antennas have been extensively investigated thus far since they are required for various applications in communication, sensing and imaging systems, as briefly described in Chapter 1. The scope of this PhD dissertation has been to investigate and propose novel highly-directive Fabry-Perot type antennas with significantly enhanced bandwidth performance based on periodic metasurfaces. Various topologies have been proposed based on multiple layer periodic surfaces and metasurfaces, forming FP type antennas achieving the desired broadband high-directive operation at millimetre and sub-millimetre wave frequencies. Moreover, different analysis tools have been employed, which are introduced in Chapter 2, to efficiently design the proposed structures, while some newly developed tools have been presented throughout this thesis.

In Chapter 3, multi-layer FP antennas using PRSs of dissimilar elements separated by half wavelength air cavities from the ground plane and from each other have been presented. The antennas have been designed to achieve broadband highly-directive response outperforming earlier designs based on double-layer topologies. Two prototypes have been fabricated and measured comprising different feeding techniques and the obtained simulated and measured results have proven the validity of the concept. Consequently, the work carried out in this chapter has led to the generalization of the directivity-bandwidth product enhancement concept by adding appropriately designed PRS layers in FP type antennas.

In Chapter 4, the limitations of the technique described in Chapter 3 have been evaluated through studying the dispersion characteristics of the modes supported in multi-layer FP LWAs**.** The extraction of the complex propagation constant for the leaky modes has been achieved by a new technique developed in the framework of this PhD. A validation of the dispersion analysis has also been presented by comparing the radiation patterns at different frequencies as extracted through full wave simulations and employing the array factor approach using the extracted values of α and β. The achieved agreement has demonstrated that the performed analysis provides a full interpretation of the operation of multi-layer Fabry-Perot LWAs.

Thus far, the implementation of multi-layer FP antennas has dealt with the inherent narrow band performance of FP antennas but at the expense of increasing the antenna profile. Consequently, the next step has been to achieve improved bandwidth performance while keeping a low antenna profile. This has been carried out in Chapter 5, where a new concept of designing sub-wavelength profile multi-layer FP antennas by replacing the conventional PRSs with optimized composite metasurfaces has been demonstrated. Various antennas have been implemented of which two have been fabricated and measured validating the concept and outperforming previous designs of the same profile.

Finally, in Chapter 6, a report of FP antenna operating at sub-millimetre wave frequencies has been presented. The novelty of this work stems from the fact that this is the first design and implementation of a FP antenna based on micromachined fully metalized SU8 at around 300GHz. An in-house fabrication process has been employed imposing several design considerations which make this antenna different to the lower frequency prototypes reported in the literature. This work offers an interesting new solution for planar high-gain low cost

antennas for such high frequencies. A prototype has been fabricated and experimentally tested validating the simulations.

Future development of this work could be to investigate alternative designs achieving more broadband operation while at the same time making the antenna less sensitive to fabrication inaccuracies. High precision spacers could be used by bonding and sealing the gap between the PRS and the ground plane compensating the tolerances from the micromachining process. High gain and broadband FP antennas using a simple source could be implemented employing the multi-layer technique presented throughout this thesis. However, further increase of the antenna's gain could also be achieved by the incorporation of a waveguide slot array as a primary feed of a FP antenna. This could lead to a low cost and low fabrication complexity high gain antenna since the structure will be based on a micromachining process.

Moreover, tuning techniques for such type antennas suitable for THz frequencies could be the subject of future investigation. The research presented in this thesis paves the way for the development of new class THz antennas with low losses and electronically reconfigurable radiation patterns if integrated with a suitable reconfiguration technique. Piezoelectric actuators could be integrated to displace one of the surfaces and alter the resonance condition controlling thus the pointing angle of the antenna's radiation beam for a fixed frequency. Moreover, another technique to achieve beam scanning could be employed using an array of photomixers as the antenna's source. The array would be controlled such that only one element would radiate at a time, resulting in a virtual change of the feeding position which in turn will produce a beam at a different angle.

The results of this dissertation have been presented at several international conferences such as IEEE Antennas and Propagation Symposium (APS), European Conference on Antennas and Propagation (EuCAP), European Microwave Conference (EuMC) and Metamaterials Congress (Metamorphose). Moreover, parts of this work have already been published in IEEE Transaction on Antennas and Propagation (TAP), Antennas and Wireless Propagation Letters (AWPL) and IET Microwaves, Antennas and Propagation.